

ABSTRACT

This research involves an effort to study and compare the residual microstructures and dynamic behavior of two metallic targets of finite thicknesses, namely OFHC (oxygen-free high-conductivity) copper and 7039 aluminum, subjected to ballistic impact and perforation by a tungsten heavy alloy (WHA) projectile. Also included in this work is an attempt to validate mathematical modelling of experimental results through the use of a computer hydrocode, AUTODYN-2D, which allows for the simulation of ballistic penetration/perforation events and possible differentiation of fundamental mechanisms through validation strategies. These targets represent two very different FCC materials. The 7039 aluminum is extremely hard in contrast to a softer, ductile copper. The "failure" mechanisms appear to be different on a macroscopic scale, but may be similar on a microscopic scale.

A preliminary investigation of the residual penetration channels in these two targets revealed significant microstructural differences. In the 7039 aluminum target there is a limited extent of microstructural deformation seen through optical microscopy, though numerous shear bands are observed near the channel wall and at the spalled region. Observations of the OFHC target, on the other hand, show a narrow region of recrystallized grains adjacent to the crater wall, beyond which is an extensive area of microband clusters. Similar features have been observed previously in connection with hypervelocity impact cratering in copper.

This investigation will attempt to provide clues to the fundamental issues involved in the differing dynamic behavior of the two FCC materials. A detailed analysis of microstructures and their evolution will be conducted through metallography and transmission electron microscopy. Microhardness measurements will be performed to correlate the results of ballistic computer simulations through residual stress and hardness profiles. Computational modeling will be used to simulate the impact behavior of the two target materials and will be corroborated by experimental results to establish a validation of perforation geometry and residual stress mappings which can be related to actual residual hardness maps constructed experimentally.

This study is an attempt to correlate microstructural issues with computer simulations and especially validation of these simulations to improve predictive models and general ballistic and hypervelocity perforation behavior in metal targets.

FINAL REPORT JUNE 1, 1997 to DECEMBER 31, 2000

U.S. Army Research Office: AASERT Program - DAAG 55-97-1-0238

BASIC SCIENCE OF PENETRATION: TRANSMISSION ELECTRON MICROSCOPY AND
MODELLING OF COPPER AND ALUMINUM TARGETS

L. E. Murr and Christine Kennedy (AASERT Trainee)
Department of Metallurgical and Materials Engineering
The University of Texas at El Paso
El Paso, Texas 79968

Ph.D. Dissertation by Christine Kennedy
entitled: Ballistic Perforation of OFHC Cu and 7039 Al Targets:
Microstructural and Hydrocode Study, Submitted Dec., 2000.

To: U.S. Army Research Office
AASERT Program/Materials Science Div. (Box 12211)
Research Triangle Park, NC 27709-2211



January, 2001

NARRATIVE

Ms. Christine Kennedy completed her multi-disciplinary Ph.D. program in Materials Science and Engineering at the University of Texas at El Paso in December, 2000 and received the Ph.D. degree. She accepted a position with Phillips Electronics in Albuquerque, New Mexico. She was aided in her research program by two outstanding undergraduate (minority students): Ms. Rocio Avalos and Andy Bujanda. Christine's Ph.D. dissertation forms the bulk of this final report because it in fact is the essence of this traineeship. The work proposed has been completely developed far beyond our original expectations and she has made significant contributions to ballistic knowledge. Important aspects of her work were presented at EXPLOMET 2000 - Fundamental Issues and Applications of Shock-Wave and High-Strain Rate Phenomena - held in Albuquerque, New Mexico in June, 2000. This International Conference was also supported by ARO. Her paper, "Tungsten - Heavy Alloy Ballistic Rod Penetration into a Copper Target: Microstructural Analysis and Computer Simulations" was provided in a previous report and will be published in the Conference Proceedings book in 2001 (by Elsevier Science, BV). A comprehensive paper dealing with a summary of dissertation research is in preparation and will also be submitted for publication. All publications, presentations, etc. have acknowledged ARO-AASERT support. Publications and presentations by Ms. Kennedy are listed at the conclusion of the attached dissertation.

AUGMENTATION AWARDS FOR SCIENCE & ENGINEERING RESEARCH TRAINING (AASERT)
REPORTING FORM

The Department of Defense (DoD) requires certain information to evaluate the effectiveness of the AASERT Program. By accepting this Grant which bestows the AASERT funds, the Grantee agrees to provide 1) a brief (not to exceed one page) narrative technical report of the research training activities of the AASERT-funded student(s) and 2) the information requested below. This information should be provided to the Government's technical point of contact by each annual anniversary of the AASERT award date.

1. Grantee identification data: (ARO Proposal Number and Grant numbers found on Page 1 of Grant)

- a. University of Texas at El Paso
University Name
- b. DAAG55 -97-1-0238
Grant Number
- c. -----
ARO Proposal Number
- d. L.E. Murr
P.I. Name
- e. From: June 1, 1997 To: Dec. 31, 2000
AASERT Reporting Period

NOTE: Grant to which AASERT award is attached is referred to hereafter as "Parent Agreement."

2. Total funding of the Parent Agreement and the number of full-time equivalent graduate students (FTEGS) supported by the Parent Agreement during the 12-month period prior to the AASERT award date.

- a. Funding: \$ 45,000
- b. Number FTEGS: 2 M.S. Degrees)

3. Total funding of the Parent Agreement and the number of FTEGS supported by the Parent Agreement during the current 12-month reporting period.

- a. Funding: \$.-----
- b. Number FTEGS: -----

4. Total AASERT funding and the number of FTEGS and undergraduate students (UGS) supported by AASERT funds during the current 12-month reporting period.

- a. Funding: \$ 152,000
- b. Number FTEGS: 1 (Ph.D.)
- c. Number UGS: 2 (1 Senior, 1 Freshman)

VERIFICATION STATEMENT: I hereby verify that all students supported by the AASERT award are U.S. citizens.

[Signature]
Principal Investigator

1/4/2001
Date

FINAL REPORT JUNE 1, 1997 to DECEMBER 31, 2000

U.S. Army Research Office: AASERT Program - DAAG 55-97-1-0238

BASIC SCIENCE OF PENETRATION: TRANSMISSION ELECTRON MICROSCOPY AND
MODELLING OF COPPER AND ALUMINUM TARGETS

L. E. Murr and Christine Kennedy (AASERT Trainee)
Department of Metallurgical and Materials Engineering
The University of Texas at El Paso
El Paso, Texas 79968

Ph.D. Dissertation by Christine Kennedy
entitled: Ballistic Perforation of OFHC Cu and 7039 Al Targets:
Microstructural and Hydrocode Study, Submitted Dec., 2000.

To: U.S. Army Research Office
AASERT Program/Materials Science Div. (Box 12211)
Research Triangle Park, NC 27709-2211



January, 2001

NARRATIVE

Ms. Christine Kennedy completed her multi-disciplinary Ph.D. program in Materials Science and Engineering at the University of Texas at El Paso in December, 2000 and received the Ph.D. degree. She accepted a position with Phillips Electronics in Albuquerque, New Mexico. She was aided in her research program by two outstanding undergraduate (minority students): Ms. Rocio Avalos and Andy Bujanda. Christine's Ph.D. dissertation forms the bulk of this final report because it in fact is the essence of this traineeship. The work proposed has been completely developed far beyond our original expectations and she has made significant contributions to ballistic knowledge. Important aspects of her work were presented at EXPLOMET 2000 - Fundamental Issues and Applications of Shock-Wave and High-Strain Rate Phenomena - held in Albuquerque, New Mexico in June, 2000. This International Conference was also supported by ARO. Her paper, "Tungsten - Heavy Alloy Ballistic Rod Penetration into a Copper Target: Microstructural Analysis and Computer Simulations" was provided in a previous report and will be published in the Conference Proceedings book in 2001 (by Elsevier Science, BV). A comprehensive paper dealing with a summary of dissertation research is in preparation and will also be submitted for publication. All publications, presentations, etc. have acknowledged ARO-AASERT support. Publications and presentations by Ms. Kennedy are listed at the conclusion of the attached dissertation.

AUGMENTATION AWARDS FOR SCIENCE & ENGINEERING RESEARCH TRAINING (AASERT)
REPORTING FORM

The Department of Defense (DoD) requires certain information to evaluate the effectiveness of the AASERT Program. By accepting this Grant which bestows the AASERT funds, the Grantee agrees to provide 1) a brief (not to exceed one page) narrative technical report of the research training activities of the AASERT-funded student(s) and 2) the information requested below. This information should be provided to the Government's technical point of contact by each annual anniversary of the AASERT award date.

1. Grantee identification data: (ARO Proposal Number and Grant numbers found on Page 1 of Grant)

- a. University of Texas at El Paso
University Name
- b. DAAG55 -97-1-0238
Grant Number
- c. -----
ARO Proposal Number
- d. L.E. Murr
P.I. Name
- e. From: June 1, 1997 To: Dec. 31, 2000
AASERT Reporting Period

NOTE: Grant to which AASERT award is attached is referred to hereafter as "Parent Agreement."

2. Total funding of the Parent Agreement and the number of full-time equivalent graduate students (FTEGS) supported by the Parent Agreement during the 12-month period prior to the AASERT award date.

- a. Funding: \$ 45,000
- b. Number FTEGS: 2 M.S. Degrees)

3. Total funding of the Parent Agreement and the number of FTEGS supported by the Parent Agreement during the current 12-month reporting period.

- a. Funding: \$. -----
- b. Number FTEGS: -----

4. Total AASERT funding and the number of FTEGS and undergraduate students (UGS) supported by AASERT funds during the current 12-month reporting period.

- a. Funding: \$ 152,000
- b. Number FTEGS: 1 (Ph.D.)
- c. Number UGS: 2 (1 Senior, 1 Freshman)

VERIFICATION STATEMENT: I hereby verify that all students supported by the AASERT award are U.S. citizens.

Principal Investigator

1/4/2001
Date

BALLISTIC PERFORATION OF OFHC Cu AND 7039Al TARGETS:

A MICROSTRUCTURAL AND HYDROCODE STUDY

by

CHRISTINE KENNEDY, B.S., M.S.

DISSERTATION

Presented to the Faculty of the Graduate School of

The University of Texas at El Paso

in Partial Fulfillment

of the Requirements

for the Degree of

DOCTOR OF PHILOSOPHY

Materials Science and Engineering

Materials Research Institute

THE UNIVERSITY OF TEXAS AT EL PASO

December 2000

*Be not afraid of greatness:
some men are born great,
some achieve greatness,
and some have greatness thrust upon them.*

- Shakespeare

Dedicated to my sister Cindy;
may she one day discover the greatness within her.

ACKNOWLEDGEMENTS

I would like to recognize above all others a person who commands my deepest respect and gratitude, my advisor Dr. Lawrence E. Murr. I thank you for being the brilliant, inspiring and encouraging educator that you are.

I'd also like to thank the staff of the Metallurgical and Materials Engineering department who have provided so much help and support over the years. They include Faye Eckberg, Diana Gutierrez, Lori De Los Santos and David Brown. The members of my dissertation committee, Drs. Roy Arrowood (MME), Russell Chianneli (Chemistry) and Dwight Russell (Physics), also deserve recognition for their much appreciated time and efforts.

Dr. Fred I. Grace (Army Research Laboratory – Aberdeen Proving Ground, MD) should be acknowledged for providing the Cu and 7039Al targets, as well as the flash x-ray radiographs. Mr. Bence I. Gerber and Dr. Chris Quan are greatly appreciated for their support of the AUTODYN software. This research was supported by a Defense Augmentation Award (DAAG55-97-1-0238) for Science and Engineering Training through the U. S. Army Research Office (ARO).

Friends and colleagues have provided immeasurable support, and these include my dear friends Sridhar Pappu and Everaldo Ferreyra (together, we've been the three amigos!). Also, discussions and technical help from Drs. Elizabeth Trillo and Stella Quinones are highly appreciated. I'd like to thank you both for being such excellent role models for future female engineers and scientists; I believe you have provided a great deal of inspiration for these young female hopefuls.

All those in connection with the MME department, including students, faculty and staff, have greatly contributed to an environment that is caring, friendly, and highly conducive to the nurturing and growth of the mind. I cannot possibly mention every name, but I am truly grateful for every individual I have been in contact with.

The UTEP Pandemonium Steel Drum Band under the direction of Mr. Larry White has been a thrill for me these past four years and I'd like to thank both the old and new members for being a part of this incredible experience.

My heartfelt gratitude goes out to my parents for their enduring love and endless patience. A special thank you to my sister Cindy, and also to my nephew Jacob for being such a wonderful source of joy.

Family, love and God are truly the key to great happiness in life.

Christine Kennedy

This dissertation was submitted to the committee on November 3, 2000.

ABSTRACT

This research involves an effort to study and compare the residual microstructures and dynamic behavior of two metallic targets of finite thicknesses, namely OFHC (oxygen-free high-conductivity) copper and 7039 aluminum, subjected to ballistic impact and perforation by a tungsten heavy alloy (WHA) projectile. Also included in this work is an attempt to validate mathematical modelling of experimental results through the use of a computer hydrocode, AUTODYN-2D, which allows for the simulation of ballistic penetration/perforation events and possible differentiation of fundamental mechanisms through validation strategies. These targets represent two very different FCC materials. The 7039 aluminum is extremely hard in contrast to a softer, ductile copper. The "failure" mechanisms appear to be different on a macroscopic scale, but may be similar on a microscopic scale.

A preliminary investigation of the residual penetration channels in these two targets revealed significant microstructural differences. In the 7039 aluminum target there is a limited extent of microstructural deformation seen through optical microscopy, though numerous shear bands are observed near the channel wall and at the spalled region. Observations of the OFHC target, on the other hand, show a narrow region of recrystallized grains adjacent to the crater wall, beyond which is an extensive area of microband clusters. Similar features have been observed previously in connection with hypervelocity impact cratering in copper.

This investigation will attempt to provide clues to the fundamental issues involved in the differing dynamic behavior of the two FCC materials. A detailed analysis of microstructures and their evolution will be conducted through metallography and transmission electron microscopy. Microhardness measurements will be performed to correlate the results of ballistic computer simulations through residual stress and hardness profiles. Computational modeling will be used to simulate the impact behavior of the two target materials and will be corroborated by experimental results to establish a validation of perforation geometry and residual stress mappings which can be related to actual residual hardness maps constructed experimentally.

This study is an attempt to correlate microstructural issues with computer simulations and especially validation of these simulations to improve predictive models and general ballistic and hypervelocity perforation behavior in metal targets.

STATEMENT OF THE PROBLEM

In studies involving penetration and perforation of metal targets by long rod projectiles, detailed microstructural analyses performed through transmission electron microscopy (TEM) are generally absent or. An analysis of this nature is imperative to the understanding of fundamental issues involved in the dynamic behavior of metal and alloy targets.

The two target materials chosen for this investigation, OFHC copper and 7039Al, exhibit considerably different failure phenomena. Though both are FCC, the initial and residual microstructures of the two target materials are markedly dissimilar. In a recent study by Huang et al. [1], optical microscopy observations of the initial microstructures of 7039 Al revealed heavy deformation (a result of manufacture processing) with an extremely small grain structure and heavy precipitation rendering the material relatively hard (140 VHN) in contrast to the copper. Shear bands were prominent in the residual microstructure, and there were very limited deformation-induced microstructural changes extending away from the penetration channel wall. OFHC copper, on the other hand, exhibited a relatively simple, equiaxed grain structure initially, while perforation of the material by a projectile resulted in a rather extensive microstructural evolution extending from the channel wall into the target.

A systematic and thorough analysis, utilizing optical and transmission electron microscopy, as well as microhardness testing, may lead to the identification of the particular mechanisms involved in the differing dynamic behavior of the two materials.

In the simplest case, these behaviors include a rather "brittle-like" failure for the aluminum alloy in contrast to a classical ductile failure for the copper. Moreover, validation of a computer hydrocode, AUTODYN-2D, via comparisons of stress profile maps between simulated and experimental results will serve to improve the predictive capability and usefulness of ballistic simulations.

Reference:

1. W. Huang, L. E. Murr, C.-S. Niou, N. L. Rupert, F. I. Grace and S. J. Bless, 16th International Symposium on Ballistics, Ballistics '96:

JUSTIFICATION OF IMPORTANCE

With the emerging threat of improved kinetic energy penetrator materials technology, a need arises for the development of more effective armors (target materials). Yet in order to improve upon the effectiveness of modern metal armors, it first becomes necessary to gain a better understanding of the material's behavior under such rigorous dynamic (impact) conditions, characteristic of extreme strains and extreme strain rates.

Advances in theoretical penetration mechanics have produced a large body of knowledge about penetration and perforation, yet certain aspects of the process have not been adequately addressed. This includes the nature of target deformation in terms of changes in microstructure of the material [1]. In a recent study of the impact of a tungsten projectile into both an RHA (rolled homogeneous armor) and a titanium alloy (Ti-6Al-4V) target, the experimental results revealed significant differences in penetration characteristics [2], with a higher efficiency of the Ti alloy against the projectile. This fundamental difference was shown to be reflected in significantly different residual microstructures associated with the perforated channel wall by Huang et al. [3], whose work has become one of the first efforts to systematically observe and compare residual target microstructures associated with ballistic penetration/perforation phenomena.

Computational modelling of ballistic impact is currently an active field of endeavor [4] and can serve as a cost-efficient tool for providing realistic results from the simulation of ballistic events. The validation of existing computer codes and their

associated simulations of dynamic events, through the incorporation of material response (such as hardness as it relates to specific microstructure), can greatly improve the predictive capability and usefulness of these mathematical models.

This study attempts to shed more light on the microstructural issues associated with ballistic impact and in particular to pinpoint the differing mechanisms of penetration-related failure occurring in OFHC copper and 7039 aluminum. Computer simulations will be performed using a hydrocode (AUTODYN-2D) in an attempt to mathematically replicate the behavior of the target materials seen in the experimental evidence, and to use the intrinsic issues embedded in the corresponding constitutive equations to elucidate the mechanisms of rod penetration and target failure.

References:

1. N. L. Rupert, F. I. Grace, W. Huang, L. E. Murr and C.-S. Niou, Army Research Laboratory Report (ARL-TR-1453) August 1997
2. N. L. Rupert and F. I. Grace, Metallurgical and Materials Applications of Shock-Wave and High-Strain-Rate Phenomena, L. E. Murr, K. P. Staudhammer and M. A. Meyers, eds., Elsevier Science B. V., 1995, p257
3. W. Huang, L. E. Murr, C.-S. Niou, N. L. Rupert, F. I. Grace and S. J. Bless, 16th International Symposium on Ballistics, Ballistics '96 :
4. G. T. Camacho and M. Ortiz, *Comput. Methods Appl. Mech. Engrg.*, **142**, 1997, p269

MATERIALS SCIENCE AND ENGINEERING STATEMENT

In the most simplistic terms, materials are atoms that have been joined in the solid state, and the bulk properties of a material are determined by its atomic architecture. One group of materials in particular, metals, is the primary structural material of technology. Its principal use in military applications include a variety of armors (tank armor, body armor, etc.) as well as high-velocity projectiles. The defeat of structures through projectiles is of great importance, likewise the mechanisms by which armor can protect these structures is equally important [1]. Ballistic impact research, therefore, involves the parallel efforts of both armor improvement and armor defeat. Hence it becomes necessary to fully understand the behavior of metals under such high-velocity, high-strain-rate impact conditions.

It is the purpose of this research to elucidate the mechanisms by which dynamic deformation occurs in the ballistic perforation of two materials, 7039 aluminum and oxygen-free, high conductivity (OFHC) copper. A comparison of the two residual targets, both perforated by an identical tungsten-alloy sub-scale projectile, reveals distinct differences in crater geometry and features, as well as differences in deformation-induced microstructures at the crater edge. This contrast in behavior, as well as the underlying mechanisms involved, may be attributed in part to the dissimilarities in properties between the two materials, though both share a face-centered cubic crystal structure. The aluminum alloy possesses higher yield strength (0.48 GPa) and hardness (140 VHN)

compared to that of copper (yield stress is 0.27 GPa, hardness is ≈ 80 VHN), though its density (2.9 g/cm^3) is roughly a third of that of copper (8.9 g/cm^3).

In concurrence with the experimental portion of this study, numerical simulations will be performed in an attempt to replicate experimental results. Validation of the hydrocode, AUTODYN, will occur through the comparison of simulated stress profiles to experimental microhardness profiles by the empirical relationship $\sigma_y = H / 3$. Therefore, residual stress maps ($f(\sigma_y)$) are simply and linearly related to residual hardness maps ($f(H)$).

Reference:

1. M. A. Meyers, Dynamic Behavior of Materials, John-Wiley & Sons, Inc., New York, 1994

TABLE OF CONTENTS

Acknowledgements.....	iv
Abstract.....	vi
Statement of the Problem.....	viii
Justification of Importance.....	x
Materials Science and Engineering Statement.....	xii
Table of Contents.....	xiv
List of Tables.....	xviii
List of Figures.....	xix
Chapter 1: Introduction.....	1
1.1 Dynamic Processes.....	2
1.2 Kinetic Energy Anti-armor Warheads.....	8
1.3 Projectile / Target Interactions.....	15
1.4 Theories of Penetration / Perforation Phenomena.....	18
1.5 Research Goals.....	25
Chapter 2: Shock Waves and Materials Effects.....	26
2.1 Shock Wave Phenomena.....	26
2.2 Dynamic Fracture and Spalling.....	28
2.3 Shock Wave Generated Microstructure.....	32
2.3.1 Dynamic Recovery and Dynamic Recrystallization.....	35
2.3.2 Microbands and Microtwins.....	39

	2.3.3 Shear Bands.....	46
2.4	Characterization of Target Materials.....	50
	2.4.1 Plane-wave and Oblique Shock-loading.....	50
	2.4.2 Hypervelocity Impact-Cratering.....	54
	2.4.3 Ballistic Penetration / Perforation.....	55
Chapter 3:	Hydrocode Analysis of Dynamic Impact.....	59
	3.1 Hydrocodes.....	59
	3.1.1 Numerical Processors.....	62
	3.1.2 Constitutive Models.....	65
	3.2 Modelling of Ballistic Impact.....	68
Chapter 4:	Research Objectives.....	71
Chapter 5:	Experimental Procedures.....	74
	5.1 Target Materials.....	74
	5.2 Ballistic Impact Set-Up.....	76
	5.3 Metallography.....	80
	5.3.1 Macrography.....	80
	5.3.2 Micrography.....	80
	5.4 Microhardness Testing.....	85
	5.5 Electron Microscopy.....	86
	5.5.1 SEM Analysis.....	86
	5.5.2 TEM Characterization.....	87
	5.6 AUTODYN-2D Computer Simulations.....	88

Chapter 6:	Results and Discussion.....	95
6.1	Macrostructural Failure Features.....	95
6.1.1	SEM Analysis.....	98
6.1.2	Properties of Cu and 7039Al.....	100
6.2	Microstructural Examination of OFHC Cu.....	102
6.2.1	Initial Microstructure.....	102
6.2.2	Residual Microstructure.....	104
6.3	Microstructural Examination of 7039 Al.....	118
6.3.1	Initial Microstructure.....	118
6.3.2	Residual Microstructure.....	122
6.4	Comparison of Target Deformation Behavior.....	140
6.4.1	Penetration Channel Analysis.....	140
6.4.2	Residual Microstructure Comparison.....	143
6.4.3	Mechanisms of Failure.....	149
6.4.4	Hardness Profiles of Cu and Al.....	150
6.5	Computer Modelling of Cu.....	152
6.5.1	X-Ray Radiography Validation.....	152
6.5.2	Geometry-Based Validation.....	153
6.5.3	Property-Based Validation.....	161
6.5.4	Additional Hydrocode Predictions.....	161
6.6	Computer Modelling of 7039Al.....	164
6.7	Geometry-Based Validation of Monolithic Target.....	167

Property-Based Validation of Monolithic Target.....	173
6.7.1 Impact in the Two-Layer Configuration.....	176
Chapter 7: Summary and Conclusions.....	181
References.....	187
Appendix.....	196
Curriculum Vitae.....	202
Publications.....	203
Presentations.....	206

LIST OF TABLES

Table 1.1:	Ballistic results for the impact of RHA and Ti-6/4 targets.....	22
Table 1.2:	Calculated values for the impact of RHA and Ti-6/4 targets.....	23
Table 1.3:	Energy partitioning in the RHA and Ti-6/4 targets.....	24
Table 1.4:	Energy rates and displaced mass in the RHA and Ti-6/4 targets.....	24
Table 3.1:	Principal Hydrocodes used in the United States.....	60
Table 3.2:	Lagrangian and Eulerian forms of conservation equations.....	62
Table 5.1:	Comparison of experimental target properties.....	75
Table 6.1:	Comparison of penetration channel geometry.....	142
Table 6.2:	Comparison of deformation-induced microstructure.....	145
Table 6.3:	Comparison of Cu geometrical parameters.....	160
Table 6.4:	Comparison of Al geometrical parameters (Euler).....	169
Table 6.5:	Comparison of Al geometrical parameters (SPH).....	172

LIST OF FIGURES

Figure 1.1:	Military applications where high-strain-rate phenomena are important [2].....	3
Figure 1.2:	Civilian applications where high-strain-rate deformation of materials occur [2].....	5
Figure 1.3:	Sequential views of high velocity penetration and perforation of a thick plate by a long-rod (length/diameter $\cong 10$) projectile [4].....	6
Figure 1.4:	Schematics of : a) detonating shaped charge, where dashed lines depict the metal liner cone and arrows denote the detonation propagation, and b) a backward folding EFP, formed upon the detonation of high explosives (H.E.) [4].....	7
Figure 1.5:	Crater formation in the hypervelocity regime (>5 km/s), where u_0 is the impact velocity, d_p is penetrator diameter, D_c is crater, and p is depth of penetration [4].....	9
Figure 1.6:	Aerodynamic forces separate the petals of the sabot from a 120 mm kinetic energy penetrator following launch [8].....	11
Figure 1.7:	Components of a typical modern-day 120 mm KE projectile [3].....	12
Figure 1.8:	The penetration of armor by a kinetic energy (or long-rod) projectile; pressure contours are shown at the projectile/target interface [11,12].....	14
Figure 1.9:	The various mechanisms involved in defeating armor include: a) spalling, b) plugging, c) ductile hole growth, d) conoid formation, e) melting/vaporization and plume formation, f) concurrent erosion of projectile and target, g) petalling and h) comminution/cracking [2].....	17
Figure 1.10:	High-velocity penetration of projectile into target; the projectile is consumed as it penetrates [2].....	20
Figure 2.1:	Ideal representation of a shock wave traveling through a solid material with a peak pressure (P) and pulse (Δt) [2].....	27

Figure 2.2:	Schematic of a sharp, step shock wave front [2].....	29
Figure 2.3:	The branching of cracks as they propagate dynamically ($t_0 < t_1, t_2$) [27].....	31
Figure 2.4:	a) Distance-time plot showing propagation of the wave in the target and projectile after impact and spalling. b) Stress profiles at times t_1, t_2 , and t_3 . c) Stress histories at positions x_1, x_2 and x_3 [2].....	33
Figure 2.5:	Schematic diagrams of recrystallization by a) high angle boundary migration through a partially-recovered microstructure, and b) subgrain rotation and coalescence [36].....	37
Figure 2.6:	Schematic of a twin where the atomic arrangement on one side of the twin boundary is a mirror reflection of that on the other side [49].....	41
Figure 2.7:	Schematic representation of a) a deformation microtwin (or twin-fault) and b) a microband in the (110) grain surface orientation of an fcc crystal [50].....	42
Figure 2.8:	Location of twin spots (T) for twinning along the $[\bar{1}12]$ direction on a (110) fcc surface orientation resulting from a rotation of the matrix pattern about the $[1\bar{1}1]$ direction [54].....	44
Figure 2.9:	Schematic illustration of microband formation model according to Huang and Gray [46]. a) Coarse slip band on primary slip planes showing random dislocations, b) coarse slip band after generation of polarized dislocations, c) double-wall-like features formed after annihilation of polarized dislocations, d) secondary dislocations are activated by internal stresses and Lomer-Cottrell locks form between primary and secondary dislocations, e) microband with stable dislocation arrays in the double walls.....	45
Figure 2.10:	Stacking fault-free energy vs. pressure for several fcc materials [55]....	47
Figure 2.11:	The formation of shear bands in dynamic deformation events (military applications): a) defeat of armor by plugging, b) shear bands breaking up projectile, c) shear bands determining fracture in exploding cylinders [2].....	48
Figure 2.12:	Schematic of the planar shock-loading assembly developed by Murr [33].....	51

Figure 2.13:	Cylindrical shock-loading assembly.....	53
Figure 2.14:	Schematic of the various effects related to impact crater formation including a spherical shock wave. Note the large strains or strain zones experienced by the target material [49].....	56
Figure 3.1:	Examples of a) Eulerian and b) Lagrangian computational grids [13].....	64
Figure 3.2:	Profile of Taylor test specimen (iron, impacted at 221 m/s) plotted as radial strain vs. distance; the experimental result is compared with the Johnson-Cook and Zerilli-Armstrong constitutive equations [2].....	67
Figure 5.1:	a) Macrograph of a WHA (tungsten-heavy alloy) right-circular cylinder projectile. b) Microstructure of WHA, consisting of tungsten particles embedded in a Ni-Fe matrix.....	77
Figure 5.2:	Geometrical parameters of target and projectile before impact.....	78
Figure 5.3:	Experimental set-up for high-speed (flash) x-ray radiography [25].....	79
Figure 5.4:	Surface view of perforation a) entrance and b) exit in the OFHC copper target perforated by a tungsten-alloy rod at a velocity of 1.5 km/s.....	81
Figure 5.5:	Surface view of the perforation a) entrance and b) exit in the 7039Al target plate impacted by a WHA rod at 1.5 km/s impact velocity.....	82
Figure 5.6:	Half-section views of the a) 7039 aluminum and b) copper target, revealing the penetration channels.....	83
Figure 5.7:	Half-sections of the residual al-mg alloy pre-target (front block), and the 7039Al primary target in a two-layer arrangement.....	84
Figure 5.8:	AUTODYN material status plot for the impact of an RHA plate by a WHA rod [87].....	90

Figure 5.9:	Set-up plot for the computer simulation of impact in the copper target by a WHA long-rod projectile at 1.5 km/s impact velocity.....	92
Figure 5.10:	Initial set-up plot for the computer simulation of the perforation of 7039Al by a WHA long-rod projectile in the a) monolithic and b) two-layer configuration in an Euler subgrid.....	93
Figure 5.11:	Set-up plot for the computer simulation of aluminum impact in the a) monolithic and b) two-layer configurations using the SPH subgrid.....	94
Figure 6.1:	Half-section of the impacted 7039Al plate; target is enlarged to show the fracture characteristics of the penetration channel.....	96
Figure 6.2:	Enlarged half-section of the impacted copper target revealing the penetration channel.....	97
Figure 6.3:	SEM view of the numerous WHA erosion products embedded along the crater wall in the region of the exit rim.....	99
Figure 6.4:	SEM views of the fracture features on the crater wall of the 7039Al showing a) cleavage as well as b) ductile dimpling.....	101
Figure 6.5:	Initial microstructure characteristic of annealed copper consisting of a) large equiaxed grain structures and b) dislocations.....	103
Figure 6.6:	Microstructural map from a region of the residual copper target, revealing the evolution of deformation from the WHA particle at the channel edge to 6 mm into the surrounding material.....	106
Figure 6.7:	a) Cross-sectional view of a WHA erosion product along the channel wall, arrow indicates direction of perforation. b) Enlarged view of the exaggerated zone of dynamic recrystallization surrounding the particle.....	107
Figure 6.8:	TEM bright-field image of dynamic recrystallization in 7039Al confirmed by the polycrystalline nature of the diffraction pattern.....	108
Figure 6.9:	a) Layers of dynamically recrystallized grains in the reconstruction of the copper entrance rim b) Reconstruction of the exit rim cross-section showing very little plastic flow and more fracturing than the entrance rim.....	109

Figure 6.10:	TEM image showing a mixture of recrystallized grains and subgrains from an area 1 mm away from the crater edge. SAD pattern shows a range of misorientations.....	111
Figure 6.11:	Bright-field image of elongated subgrains located 1 mm from the crater edge.....	112
Figure 6.12:	a) TEM bright-field image of a microband lying coincident with a (111) plane in the [110] direction for a (110) surface orientation. b) The dark-field image corresponding to a), obtained from the reflection circled on the SAD pattern insert.....	113
Figure 6.13:	Bi-directional microbands observed in the impacted copper target. These are coincident with {111} planes and run along $\langle 022 \rangle$ directions.....	115
Figure 6.14:	TEM image of an intermixing of microtwins and microbands in a (110) grain where the SAD pattern clearly illustrates misorientations (M) of $\sim 3.5^\circ$, as well as twin spots ($\frac{1}{3}[111]$) perpendicular to the direction of twinning marked T.....	116
Figure 6.15:	Schematic illustrating residual microstructure of copper in connection with shock geometry. a) Planar shock-loading produces twinning (T), b) hypervelocity impact cratering results in microbands (M), and c) ballistic impact by a long-rod projectile produces a mixture of microbands and twinning (M + T).....	117
Figure 6.16:	Optical view of the starting microstructure for work-hardened 7039Al showing a) elongated grains, oriented in the direction of deformation, mixed with clusters of small grains, seen more clearly in the b) enlarged view.....	119
Figure 6.17:	Micrographs of a) small grains and precipitates in the initial work-hardened microstructure of 7039Al and b) heavy dislocation density, approaching saturation, within the small grains....	120
Figure 6.18:	a) TEM view of a large, elongated grain in the aluminum alloy. b) High dislocation density within the grain, consistent with work-hardening.....	121
Figure 6.19:	General stress-strain diagram illustrating work-hardening behavior in metals and the effect of saturation.....	123

Figure 6.20:	Microstructural map of a segment of the penetration channel in the residual 7039Al target. Limited plastic flow is seen close to the channel edge, also, shear bands and associated cracks are revealed.....	124
Figure 6.21:	Micrograph of a narrow shear band located 4 mm from the channel wall.....	125
Figure 6.22:	a) Optical view of two shear bands propagating in the shear direction and terminating at a crack. b) View of the re-oriented microstructure alongside a crack.....	126
Figure 6.23:	Bright-field image of a narrow region of possible localized deformation associated with a shear band. The corresponding SAD pattern shows high misorientations related to subgrains and recrystallized grains, and also shows texturing of the microstructure.....	128
Figure 6.24:	Micrograph of dynamically recrystallized grains located on the surface of the 7039Al channel. This is confirmed by the large misorientations in the corresponding SAD.....	129
Figure 6.25:	Microstructure from the surface of the 7039Al penetration channel consisting of a) microbands as well as b) recrystallized grains and subgrains.....	131
Figure 6.26:	Dense dislocation cells and subgrains from the surface of the 7039Al penetration channel.....	132
Figure 6.27:	a) Dense dislocation cells observed in the region >2 mm from the channel edge.....	133
Figure 6.28:	a) Bright-field image of microband parallel to the trace of a (111) plane in the [121] direction. b) The corresponding SAD pattern shows the reflection (circled) of small misorientation ($\sim 3^\circ$) characteristic of microbands.....	134
Figure 6.29:	TEM image of a microband with a characteristic width (0.2 μ m) located 3mm from the crater edge. The SAD pattern shows a (123) zone axis, with the microband lying in the [523] direction.....	135
Figure 6.30:	TEM image illustrating the long, string-like behavior of microbands in the residual 7039Al target.....	137

Figure 6.31:	Optical view of deformation bands a) within elongated grains, and b) within the region of the fractured shear lips.....	138
Figure 6.32:	a) TEM image of band-like features that may correspond to the deformation bands observed in figure 6.33. b) SAD insert shows large misorientations associated with the microstructure.....	139
Figure 6.33:	Comparison of the geometries of the penetration channels in the a) 7039Al and b) OFHC copper target.....	141
Figure 6.34:	a) Stress-strain curves illustrating the different tensile behaviors of the copper and aluminum alloy starting materials. b) Comparison of hardness variations with distance from the channel wall in both residual targets.....	144
Figure 6.35:	Computer generated yield stress contour plots for a) the OFHC Cu and b) 7039Al target. Aluminum shows limited variation in yield stress than Cu, consequently, deformation is localized.....	151
Figure 6.36:	Flash x-ray radiograph sequence for a tungsten-alloy projectile perforating an OFHC copper plate at a velocity of 1.5 km/s, which shows a) the projectile leaving the sabot at impact velocity...	154
Figure 6.36:	(con't) b) the tungsten-alloy rod exiting the rear surface of the target in a debris cloud.....	155
Figure 6.36:	(con't) c) the final shape of the target alloy rod compared with the initial rod. Erosion products from the initial rod have been observed to be embedded along the channel wall of the copper target.....	156
Figure 6.37:	A comparison of a) the x-ray radiograph of the projectile leaving the back surface of the copper target, with b) the computer simulation of the same.....	157
Figure 6.38:	A comparison of a) the experimental half-section of the copper target and b) the computer simulated half-section.....	158
Figure 6.39:	A comparison of the fracture features in the exit rim formation of the a) experimental (enlarged) and b) computer simulated crater....	159

Figure 6.40:	a) Copper hardness profile showing variations in hardness with respect to deformed microstructure. b) Computer simulated yield stress contour plot for comparison with a) in a validation that is based on material property.....	162
Figure 6.41:	Computer plot showing the location of selected targets points on the initial copper target. The target points will provide histories for selected variables.....	163
Figure 6.42:	History plots of a) pressure vs. time and b) effective plastic strain vs. time showing the respective variations at the selected target points.....	165
Figure 6.43:	a) History plot of temperature vs. time for the perforation of copper. b) Temperature contour plot at 75 μ s after impact.....	166
Figure 6.44:	Comparison of a) the experimental 7039Al penetration half-section to b) the predicted half-section (Euler).....	168
Figure 6.45:	Comparison of a) the experimental 7039Al penetration half-section to b) the predicted half-section (SPH).....	170
Figure 6.46:	Time-sequence for the perforation of a) 7039Al (Euler), b) 7039Al (SPH), and c) OFHC copper.....	171
Figure 6.47:	a) 7039Al hardness profile showing slight softening near the penetration edge and maximum hardness at the breakout region. b) Simulated yield stress contour plot (Euler) showing limited variation similar to a).....	174
Figure 6.48:	Comparison of a) 7039Al hardness profile with b) the predicted yield stress contour plot for the SPH subgrid, which shows some softening at the channel edge, but too much variation with distance from the crater.....	175
Figure 6.49:	Comparison of the simulated (Euler) impact of 7039Al in the a) two-layer and b) monolithic configuration. The same parameters were used for 7039Al in both cases.....	178
Figure 6.50:	Comparison of the simulated (SPH) impact of 7039Al in the a) two-layer and b) monolithic configuration, using the same input parameters for 7039Al.....	179

Chapter 1

INTRODUCTION

A projectile is a missile designed to be fired from a gun (e.g. tank gun). The design, engineering, fabrication and use of missiles in modern warfare has become a highly specialized and highly skilled art and science. Projectile/target interaction has fascinated and inspired the ingenuity of weapons designers, resulting in the development of numerous concepts and combinations. As this interaction in materials involves the combination of high velocity, high strains and high-strain-rates, it is termed dynamic.

Materials will behave in a dynamic manner as they become subjected to rapidly changing loads. The type of loading that occurs when one body impacts against another can be termed impulsive, or dynamic, and is distinguishable from a conventional load primarily by its suddenness of application and its brevity of duration. The resulting intensity is usually of sufficient magnitude to produce extensive fracturing and large permanent distortions in the body upon which it acts [1].

It is highly important to understand the dynamic response of a material. The following is a simple equation relating kinetic energy to the velocity of a mass, which can be applied to all applications that involve the dynamic behavior of materials :

$$E_c = \frac{1}{2} mv^2 \quad (1)$$

As the square of its velocity increases, so does the energy of a mass. An object of mass m delivers energy to a target through the expression:

$$dE = F dl ; F = m a \quad (2)$$

where dl is the length over which the force F acts. The kinetic energy is translated into damage in both projectile and target.

One other important concept to consider is the understanding of the fundamental differences between static (or quasi-static) and dynamic deformation. Quasi-static deformation constitutes a situation of static equilibrium at any given time, where any element in the body has a summation of forces acting on it close to zero. As deformation is applied from the outside at a very high (dynamic) rate, one portion of the body becomes stressed while the other portion has not experienced this stress yet. Therefore, stress (and strain) must travel through the body and does so at specified velocities that can be calculated fairly accurately. These are known as shock waves.

Therefore, dynamic deformation often involves shock wave propagation, whereas quasi-static deformation can be considered as a sequence of states of equilibrium that can be treated by the equations of mechanics of materials [2].

1.1 Dynamic Processes

There are a wide range of phenomena and applications where dynamic processes play an important role. Civilian applications are generally intended at producing something, whereas military applications have the intention of either defeating or protecting [2]. A summary of common military applications where dynamic deformation is involved is shown in figure 1.1. High velocity projectiles that can defeat armored structures hold great importance. Likewise, the mechanisms by which armor can protect

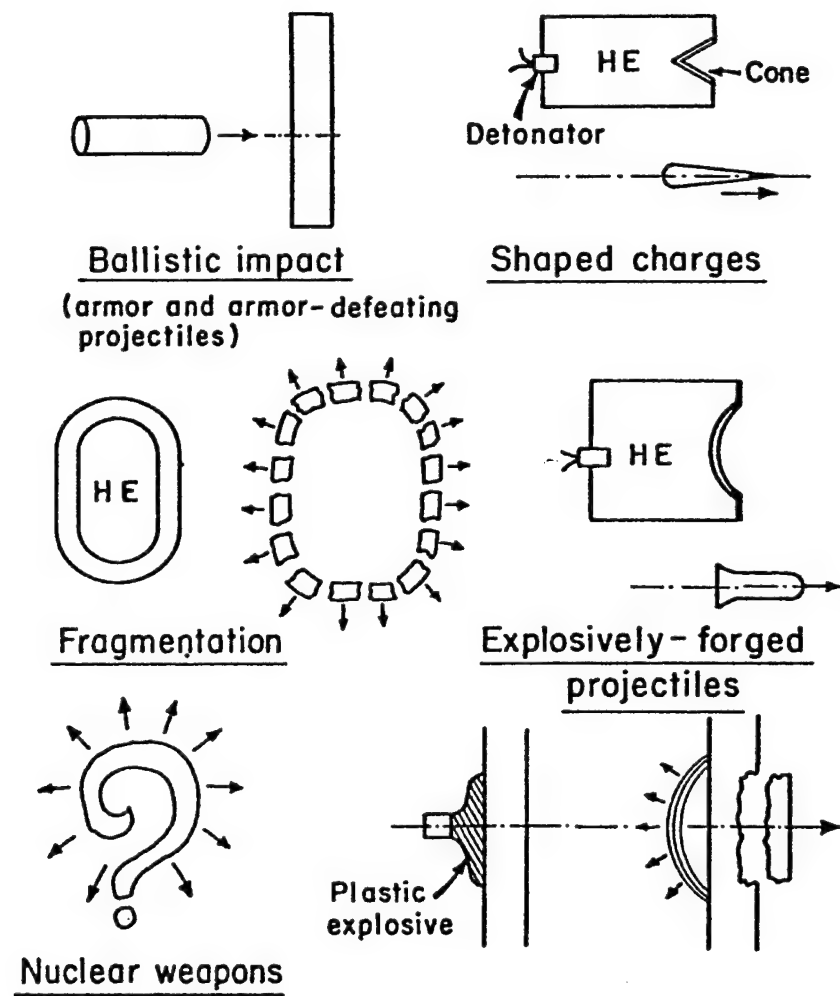


Figure 1.1: Military applications where high-strain-rate phenomena are important [2].

these structures are equally important. Figure 1.2 summarizes the common civilian applications where dynamic deformation may be applied.

Of the military applications, these processes may be classified as either kinetic energy or chemical energy projectiles. Kinetic energy penetrators are those in which gun or rocket propellants accelerate metal penetrators to lethal (perforation) velocities. Chemical energy projectiles (or warheads) are high-explosive devices in which damage to the target is caused by the action of an explosive that accelerates metal [3].

Figure 1.3 shows the sequential views of the high velocity impact and subsequent perforation of a thick target by a kinetic energy, or long-rod, penetrator. This schematic illustrates the “eroding rod model”, where the projectile is consumed as it penetrates. In the family of high-explosive, chemical energy warheads, two are of greatest importance: the shaped charge and the explosively formed penetrator (EFP). The shaped charge is essentially an explosive with a geometrical shape such as a cone that serves to focus the detonation energy [4].

A simple schematic of a shaped charge is shown in figure 1.4(a). Upon detonation, a shock wave approaching 100 GPa pressure is produced, which collapses the liner cone and forms a jet [5]. In the jet elongation, the strains can exceed 1000%, and the associated strain rates are usually in the range of 10^5 to 10^7 s^{-1} [6]. EFPs are similar to shaped charges, but only a slug is formed because of differences in liner geometry. In this process, a metal liner becomes “forged” into a rod, or slug, on detonating with an explosive charge [7]. The schematic development of an EFP is illustrated in figure 1.4(b). The slug does not form by the uniform, extreme plastic strain characteristic of the

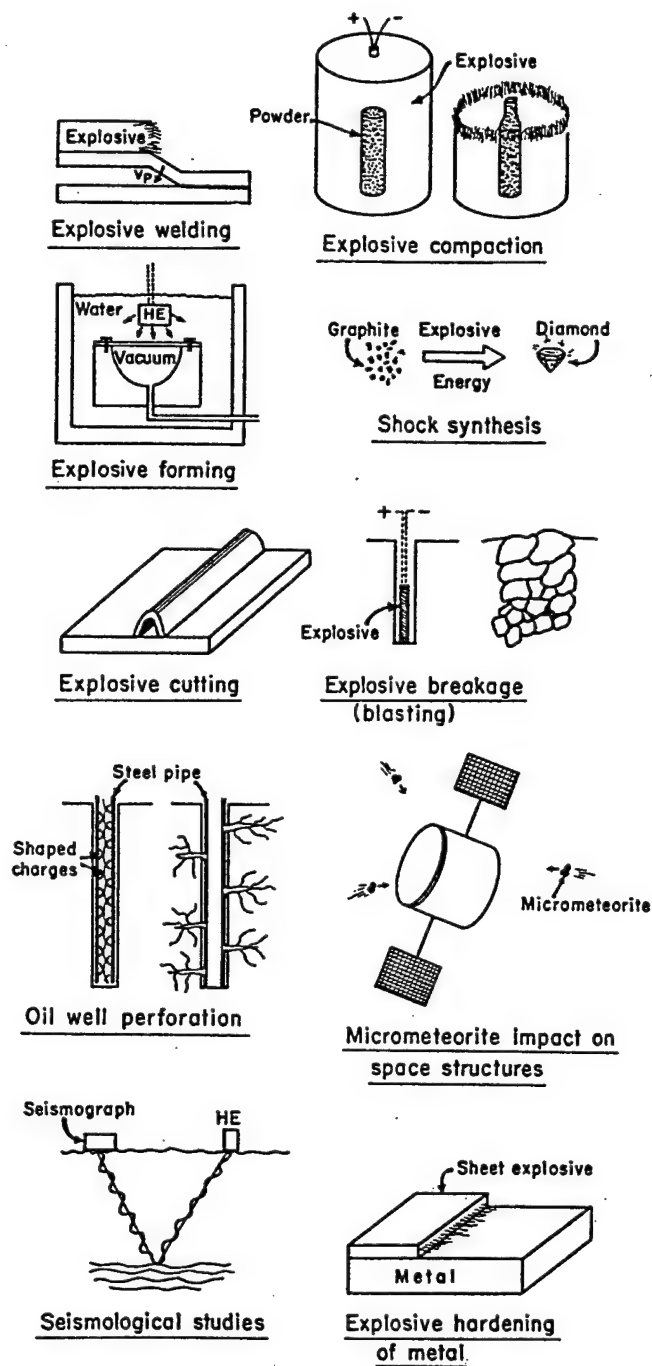


Figure 1.2: Civilian applications where high-strain-rate deformation of materials occur [2].

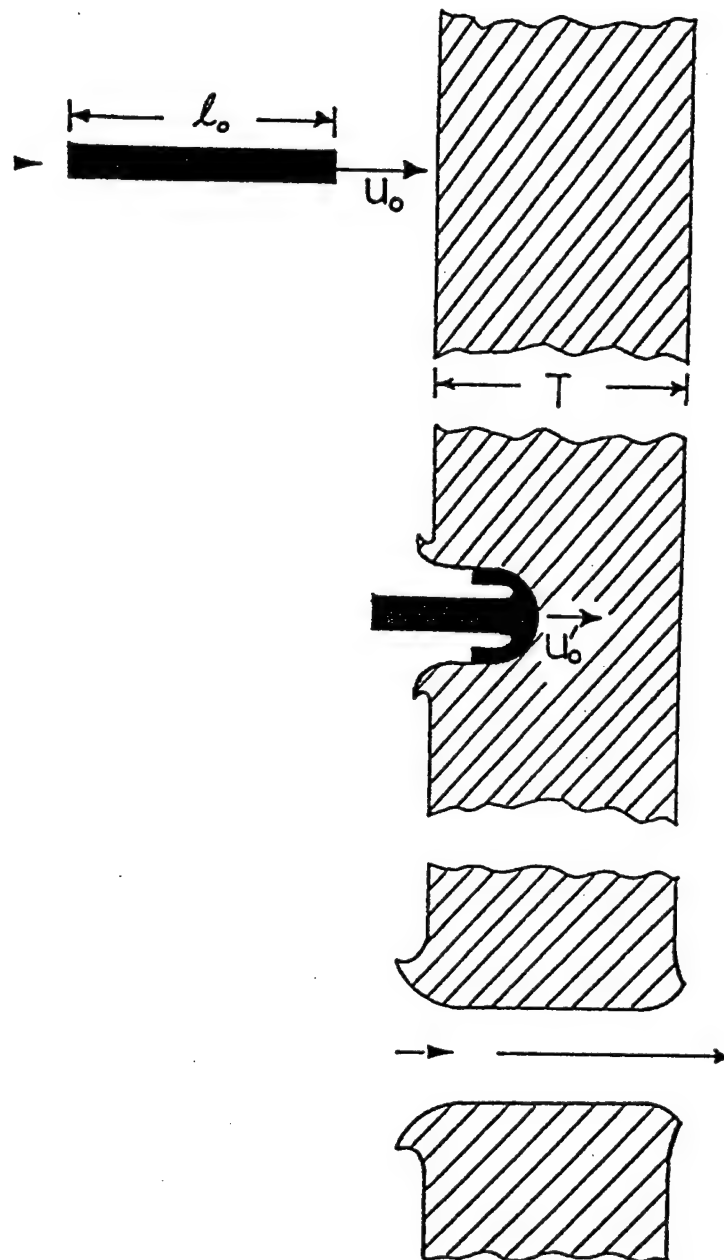


Figure 1.3: Sequential views of high velocity penetration and perforation of a thick plate by a long-rod (length/diameter $\cong 10$) projectile [4].

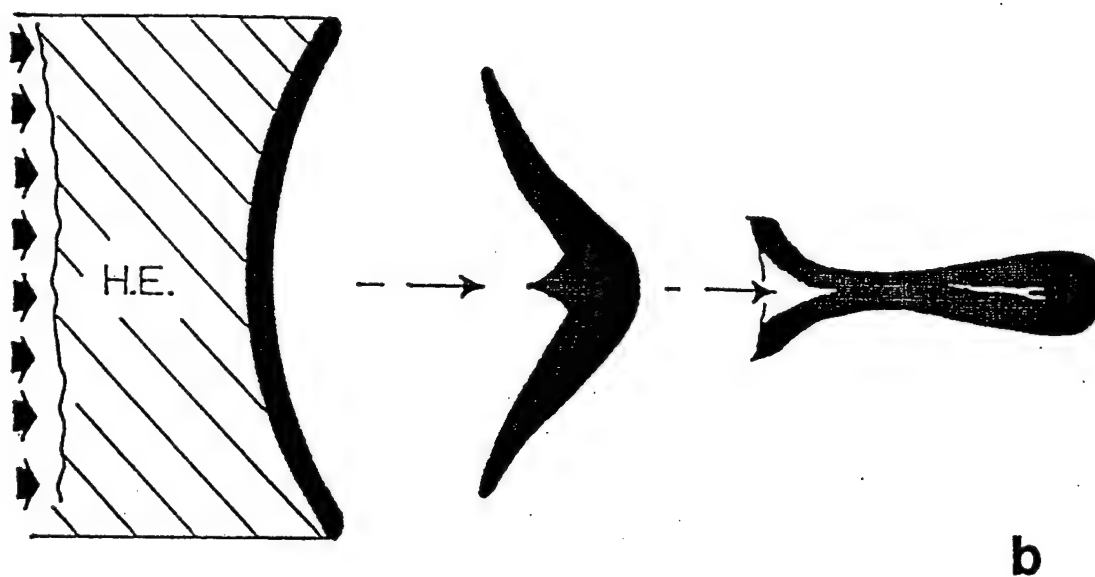
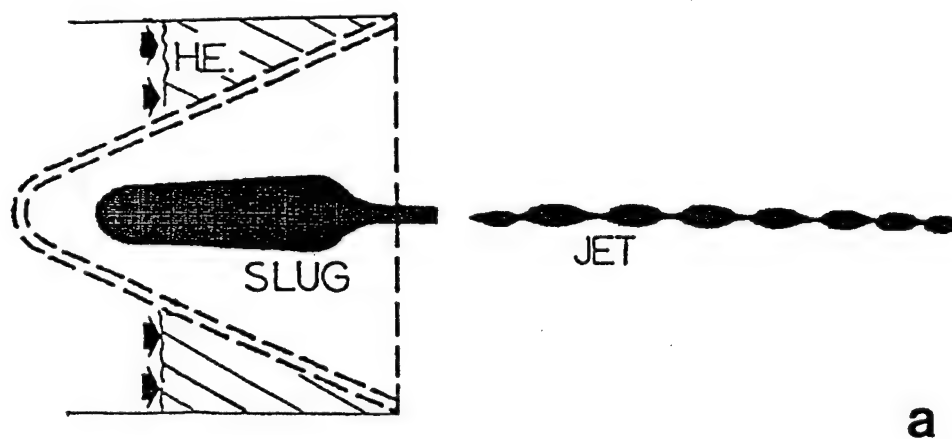


Figure 1.4: Schematics of : a) detonating shaped charge, where dashed lines depict the metal liner cone and arrows denote the detonation propagation, and b) a backward folding EFP, formed upon the detonation of high explosives (H.E.) [4].

shaped charge, and the strains within the EFP usually do not exceed a true strain of 4 (~400%). The strain rate is somewhat lower than the shaped charge jet (10^4 s^{-1}) [7].

Dynamic events occurring in space have, of late, become a major concern. Particles moving around the earth at high velocities, such as micrometeoroids, interplanetary dust and man-made debris, have been recognized as a threat to manned space operations [8]. Researchers have attempted to reproduce these hypervelocity impact conditions by using gas guns to accelerate a spherical particle up to 10 km/s towards a metal target, leaving behind an impact crater. Figure 1.5 shows the formation and geometry of such a crater.

1.2 Kinetic Energy Anti-armor Warheads

The most effective anti-tank defeat mechanisms have traditionally been, and continue to be, kinetic energy projectiles fired from high pressure cannons, the main armament of all modern-day battle tanks [2]. These projectiles differ from the chemical energy projectiles (i.e., shaped charges and EFPs) in that they derive their kinetic energy from the high-pressure gases within a confined volume (the barrel of a gun) rather than a chemical (explosive) source [1].

A descendant of the solid shot of an ancient cannon, the typical modern day kinetic-energy projectile is a sub-caliber, discarding sabot-launched, high L/D (length to diameter), high-density-metal, fin-stabilized, long-rod or arrow projectile, typically

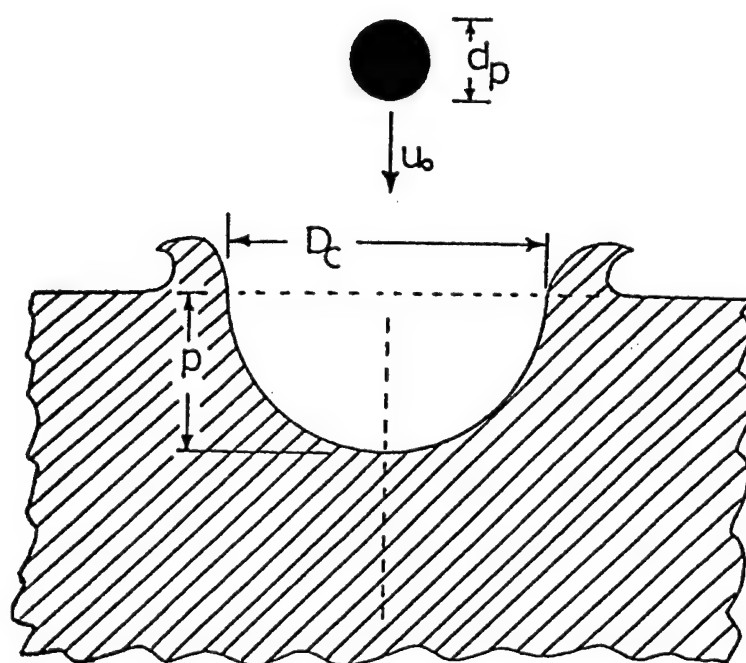


Figure 1.5: Crater formation in the hypervelocity regime (>5 km/s), where u_0 is the impact velocity, d_p is penetrator diameter, D_c is crater, and p is depth of penetration [4].

referred to as APFDS (armor-piercing, fin-stabilized, discarding sabot). Figure 1.6 shows the petals of a sabot falling away from the penetrator immediately after launch [9]. The two most popular materials employed for this application include tungsten alloys and depleted uranium (because of their high density), though the latter is known to have serious environmental hazards. These may be used either as the main penetrator, or as a composite with another metal (e.g., steel) housing the high-density penetrator.

The projectiles are typically driven to velocities in excess of 1.5 km/s by the cannon propellant charges. At such velocities, the trajectories are flat and the time it takes to reach the target is very short. Massive and complex armor arrays are required to defend against such high-energy kinetic energy penetrators. The behind armor effect of the residual penetrator consists of high-density metals from both the projectile and the armor spall, ricocheting about the target interior.

Figure 1.7 illustrates a typical modern-day KE projectile to be fired from the cannon of a tank gun [10]. In this example, a high-density tungsten penetrator is housed in a steel carrier that has external ribs to interface with and lock into a three-piece, multisector, discardable sabot fabricated from light metals such as magnesium or aluminum. This particular projectile was designed for a 120-mm smooth bore cannon.

The mechanisms by which kinetic energy penetrators defeat armor are varied and depend on a number of factors. Prominent among these is the velocity of the projectile, since the kinetic energy is proportional to the square of the velocity. As the velocity of impact is increased, the region of damage decreases, and one progresses from structural effects to local effects. The stresses and strains produced by external tractions travel

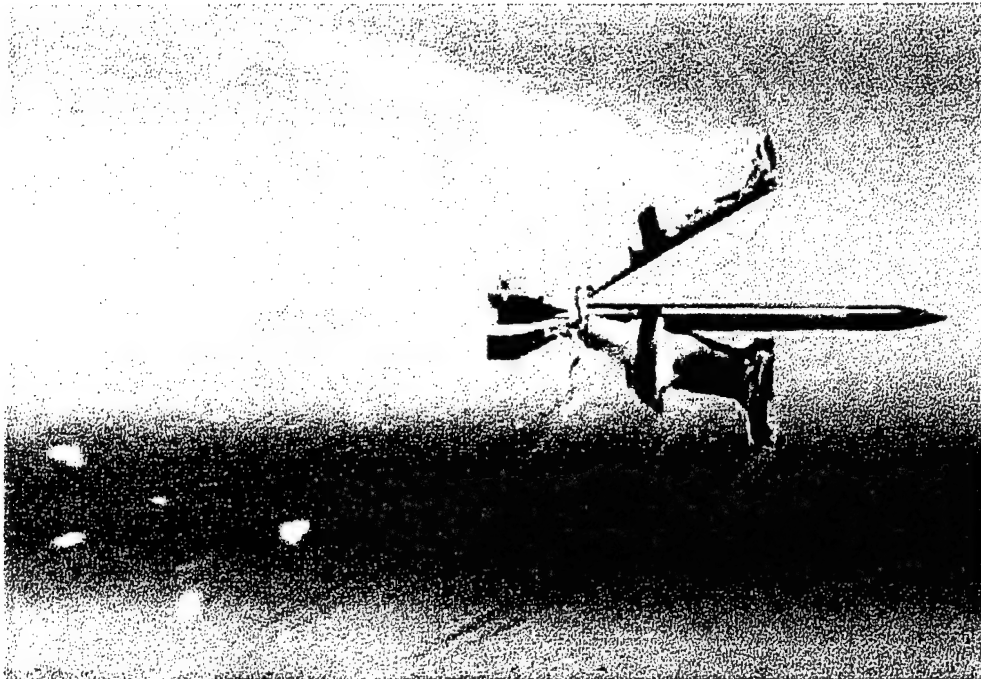


Figure 1.6: Aerodynamic forces separate the petals of the sabot from a 120 mm kinetic energy penetrator following launch [9].

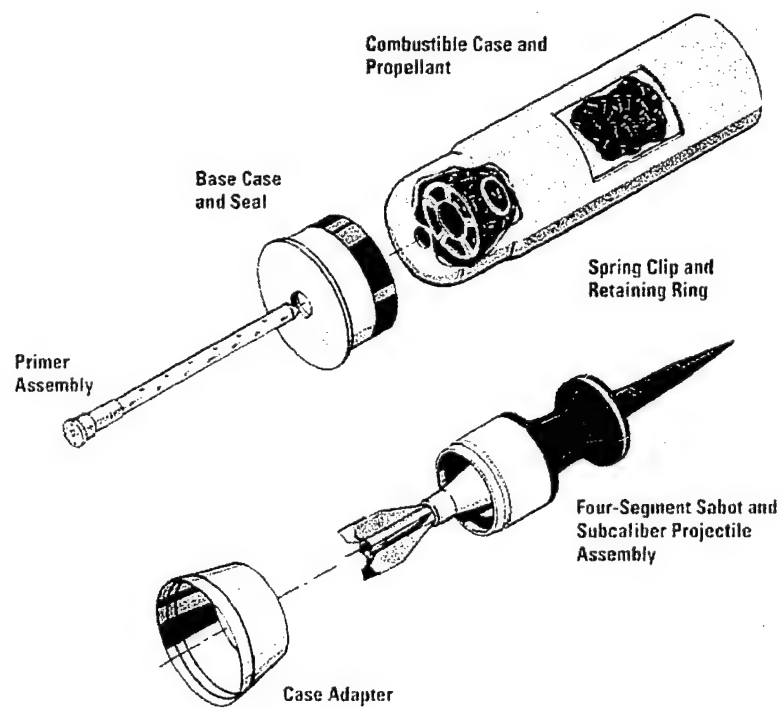
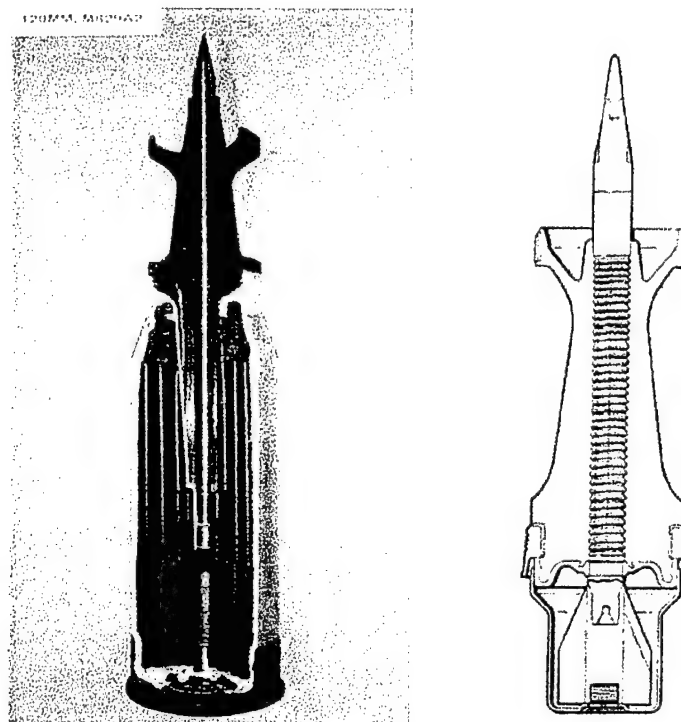


Figure 1.7: Components of a typical modern-day 120 mm KE projectile [10].

through a material at sonic speeds. Thus quasi-static tractions create a situation of equilibrium. The externally applied loads are countered by internal stresses throughout the body. In high-velocity impact, the externally applied tractions can reach their maximum and decay long before the entire body has experienced the reactive stresses; thus, a hole is formed, as opposed to large-scale plastic deformation [2].

Long-rod penetrators interact with targets in a manner in which there is simultaneous deformation of both. The features of this deformation process can be seen in figure 1.8. The initial contact between penetrator and armor materials results in peak stresses and strain rates. These quickly decrease as relief waves return from free surfaces. The stresses that are generated by the deceleration of the penetrator and subsequent acceleration and displacement of the armor material are greater than the strengths of both penetrator and target materials, deforming both plastically [12].

As the armor in the path of the projectile is pushed aside, the high-density penetrator core becomes inverted and eroded at the moving penetrator-target interface. This process ends when the penetrator is either brought to rest, or is completely consumed by erosion. The deformation to both penetrator and armor materials will be localized to regions on either side of the penetrator-target interface due to the relatively slow propagation rates of plastic strains [13]. These regions are deformed to large plastic strains at strain rates of up to 10^6 s^{-1} [12,14].

Hydrostatic pressures in excess of 5 GPa are generated at the head of the penetrator due to the inertia of each material and the constraint of the surrounding volume of armor which resists expansion of the penetrator cavity. These pressures work to

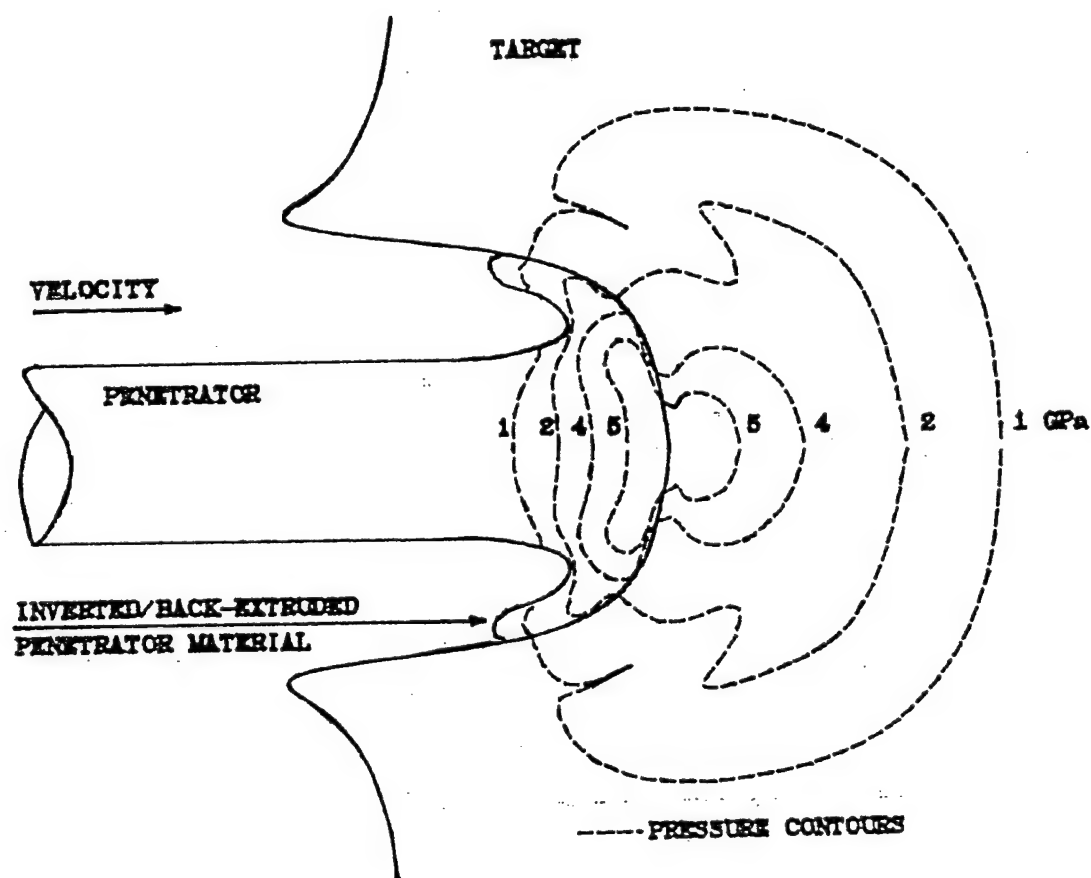


Figure 1.8: The penetration of armor by a kinetic energy (or long-rod) projectile; pressure contours are shown at the projectile/target interface [11,12].

suppress fracture failures at the head of the penetrator. Fractures, however, occur more easily along the outside of the mushroomed head as the pressures begin to diminish radially away from the penetrator-target interface.

1.3 Projectile / Target Interactions

A kinetic energy penetrator takes the form of a long rod, and is generally cylindrical in shape, with either a conical, ogival, hemispherical or flat nose. When such a projectile strikes a target, strong compressive shock waves propagate into both bodies. If the impact velocity is sufficiently high, relief waves will propagate inward from the lateral free-surfaces of the projectile and cross at the centerline, creating a region with high tensile stress. The initial compression wave in the target is followed quickly by a release wave. When the initial compressive wave reaches a free boundary in the target, an additional release wave is generated. If the combination of load intensity (tensile) and duration exceeds a critical value for the target material, failure will be initiated [15].

Targets are best classified following Backman and Goldsmith [16]. A target is said to be:

1. Semi-infinite if there is no influence of the distal boundary on the penetration process.
2. Thick if there is influence of the distal boundary only after substantial travel of the projectile into the targets.

3. Intermediate if the rear surface exerts considerable influence on the deformation process during nearly all of the penetrator motion.
4. Thin if stress and deformation gradients throughout its thickness do not exist.

Impacted materials may fail in a variety of ways. The actual mechanisms will depend on such variables as material properties, impact velocity, projectile shape, method of target support, and relative dimensions of projectile and target [15]. Depicted in figure 1.9 are some modes of projectile-target interactions. Spalling (a), plugging by shear band formation (b), and ductile hole growth (c) occur in ductile materials.

When the target is brittle (e.g., glass), a projectile creates a conoid, which is ejected [1.9(d)]. Impacts at hypervelocities (>3000 m/s) can melt and even vaporize the target or create a thin plume of fragments traveling at much lower velocities; this is shown schematically in figure 1.9(e).

Long-rod penetrators, traveling at velocities of 1-2 km/s, interact with targets in a mode in which there is concurrent deformation of both. When the pressure at the deformation interface exceeds significantly the dynamic flow stress of the material(s), deformation can be assumed to be guided by fluid dynamics, and one develops patterns similar to the ones of figure 1.9(f).

When the target is very thin, it usually fractures in a star pattern called "petaling" after it has been stretched [1.9(g)]. A ceramic target responds quite differently than a metallic one, as seen in figure 1.9(h). As the ceramic experiences damage by the stresses due to the projectile, the projectile tip is plastically deformed at the same time. The

comminuted ceramic is ejected from the target through the orifice created by the projectile, creating room for the continued penetration of the projectile [2].

1.4 Theories of Penetration/Perforation Phenomena

Historically, the impact of long-rod penetrators with targets of finite thickness, or plate targets, has been investigated extensively and many theories have been established [17]. Penetration analyses can be dated back to the 1800's when cannonball experiments by the French military in Metz were the first attempt to instill science into this area [2]. The equation that was developed as a result of these experiments, also known as de Marre's equation, correlates the kinetic energy of the projectile ($\frac{1}{2}MV^2$) to the maximum thickness of the target:

$$M V^2 = C D^\beta T^\alpha \quad (3)$$

Where C , α , and β are empirical parameters, T is maximum target thickness, and D is projectile diameter. More recently, Bruchey [18] proposed a more complex expression:

$$(\rho_p V^2 / E_p) (L_o / D) = C (T \sec \theta / D)^\alpha E_p^\beta / E_t (\rho_p / \rho_t)^\gamma \quad (4)$$

The subscripts p and t refer to projectile and target, respectively; L_o and D are the initial length of the projectile and its diameter, respectively; ρ_p and ρ_t are the densities; T is the target thickness, θ is the angle at which the projectile strikes the target; and α , β , γ and C are the empirical parameters. When values for the parameters are obtained through experimentation, then curves may be developed from which the ballistic limit can be

predicted. The ballistic limit is simply the velocity above which a projectile perforates a target, and below which it will not.

The above equations consider only the kinetic energy of the projectile, yet studies have been performed in which the physical mechanisms of penetration are analyzed in greater detail. The penetration of a long cylinder into a metallic target has been treated in a very preliminary manner by Birkhoff et al [19]. They considered, simply a semi-infinite target impacted by a long-rod of length L at a velocity V . Figure 1.10 shows the advance of the tip of the projectile during penetration; its velocity is U , the densities of the projectile and target are ρ_p and ρ_t , respectively. By changing the coordinate system so that the stagnation point (interface between target and projectile) is at the origin, the target is then moving from right to left at a velocity $V - U$. It was assumed that the pressure created at the interface was much higher than the strength of the materials which could then be treated as fluids by applying Bernoulli's equation:

$$P = \frac{1}{2} \rho_p (V - U)^2 = \frac{1}{2} \rho_t U^2 \quad (5)$$

From this expression, a simple expression for rod penetration can be derived:

$$p = \alpha L (\rho_p / \rho_t)^{1/2} \quad (6)$$

Though this is an oversimplified representation of the penetration process, it is significant in that it predicts 1) that the depth of penetration is equal to the projectile length if the two materials have the same density, and 2) that the penetration increases with the ratio ρ_p / ρ_t (ratio of projectile and target densities) [2]. Other analyses by Backman and Goldsmith [20] as well as Zukas [15] have provided in-depth treatments of the physical processes which depend on the impact velocity, shape of the penetrator, and materials of

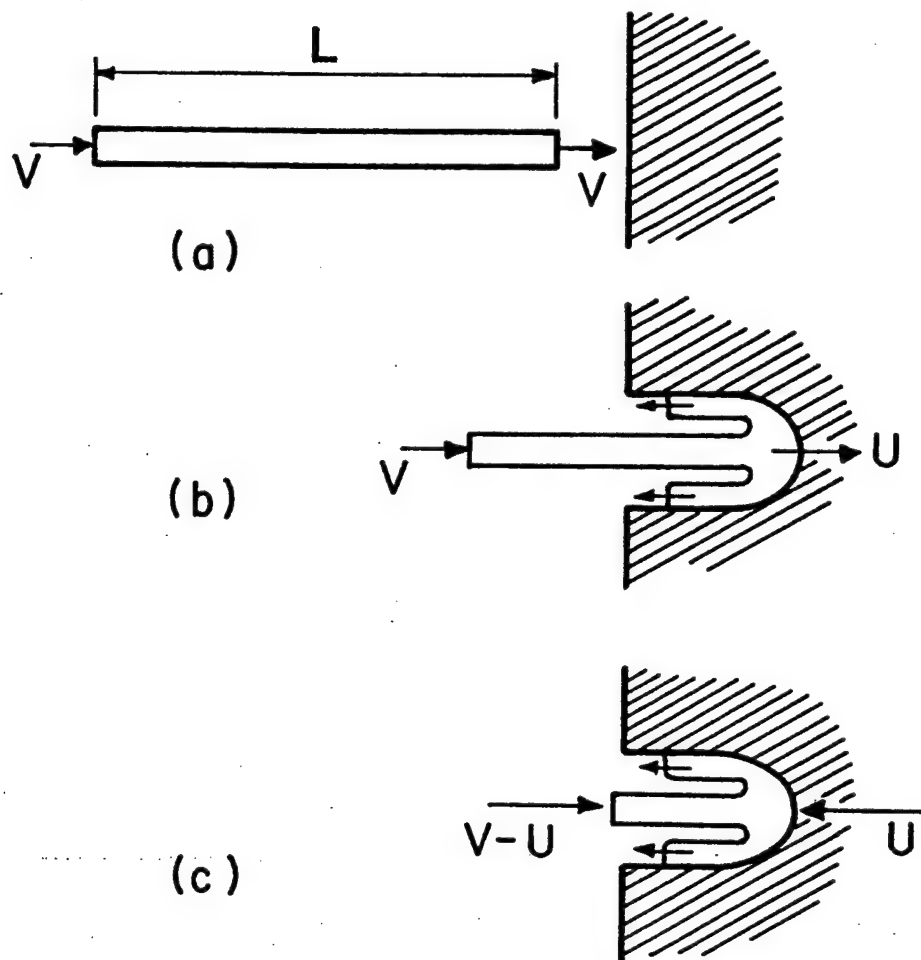


Figure 1.10: High-velocity penetration of projectile into target; the projectile is consumed as it penetrates [2].

the penetrator target. A semi-empirical equation developed by Lambert and Jonas [21] has provided a means to estimate residual properties.

Mechanistic models developed by Recht and Ipson [17] Awerbuch and Bodner [22], Woodward and de Morton [23] and Woodward et al [24] have provided more insight into the perforation of a plate at relatively low impact velocities. Ravid and Bodner [25] have outlined the various stages of plate perforation into three main events: (1) initial penetration into the target, wherein the rod and target undergo erosion, (2) failure of the uneroded target material during perforation, and (3) a momentum or energy exchange between the uneroded rod and target masses.

Recently, Grace [26] developed a one-dimensional, non-steady theory for long-rod penetration into targets of finite thickness based on experimental observations and analytical studies. In this formulation, a solution for the problem where both rod and target simultaneously undergo acceleration and erosion is obtained from momentum considerations without resorting to Bernoulli's equation.

The model has been used to monitor specific details of the penetration events throughout the impact, penetration and perforation phases [27]. In the impact of a tungsten-heavy alloy (WHA) projectile against finite thickness targets of titanium alloy (Ti-6/4) and rolled homogeneous armor (RHA) steel, this approach allowed the energetics of the individual phases to be examined theoretically and provided an explanation for the observed penetration response differences between Ti-6/4 and RHA [28].

Table 1.1 presents the actual differences in ballistic results for the Ti6/4 and RHA targets tested. Table 1.2 presents the results of calculations made using the model developed by Grace to predict penetration/perforation of finite targets. In comparison, the residual penetrator characteristics such as striking velocity, residual rod length and residual rod velocity appear to be in very good agreement with the experimental observations [29]. This provided a valid basis for the energy analysis. The calculations addressing the model-predicted energetics are presented in Tables 1.3 and 1.4. Table 1.3 lists the summation.

Table 1.1

Ballistic Results for the Impact of RHA and Ti-6/4 Targets

Target	Pitch (degrees)	Yaw (degrees)	Striking Velocity (m/s)	Residual Rod Length (mm)	Residual Rod Velocity (m/s)
RHA	-0.25	0.75	1,507	39.7	1,297
	-0.50	0.00	1,510	38.6	1,297
Ti - 6/4	-0.5	0.25	1,501	26.1	1,110
	-0.50	0.25	1,501	26.5	1,118

Table 1.2
Calculated Values

Target	Striking Velocity (m/s)	Residual Rod Length (mm)	Residual Rod Velocity (m/s)	Plug Mass (g)
RHA	1,507 (1,507) ^a	39.14 (39.7) ^a	1,292 (1,297) ^a	10.39
	1,510 (1,510) ^a	39.21 (38.6) ^a	1,297 (1,297) ^a	10.27
Ti - 6/4	1,501 (1,501) ^a	26.27 (26.1-26.5) ^a	1,127 (1,110-1,118) ^a	15.16

^a Experimentally measured values from Table 1.

of energy attributed to the various aspects of the penetration process, while table 1.4 provides the results of energy rate calculations and target mass estimates. The quantities of interest include the initial rod KE before impact, and its KE after erosion and deceleration following penetration into the target (first phase). Also of interest are the KE of accelerated target mass at the end of the first phase, the KE of the residual rod and target mass (plug) after perforation (second phase), and the fracture energy required to separate the plug from the target (fracture energy of breakout).

The amount of KE dissipated during rod erosion is that which is lost by the rod during penetration (first phase), and is based on the difference between its KE before impact and that at the end of the penetration phase. Table 1.3 shows that the rod loses

Table 1.3
Energy Partitioning in the RHA and Ti-6/4 Targets

Target	Striking Velocity (m/s)	Initial Rod KE (J)	KE Dissipated during Rod Erosion (J)	Plug KE before Breakout (J)	Fracture Energy at Breakout (J)	Residual Rod KE (J)	Plug KE after Breakout (J)
RHA	1,507	75,206	42,231	3,316	124	27,492	8,675
	1,510	75,506	42,331	3,328	121	27,754	8,628
Ti - 6/4	1,501	74,609	55,173	5,692	1,460	14,040	9,628

Table 1.4
Energy Rates and Displaced Mass for the RHA and Ti-6/4 Targets

Target	Striking Velocity (m/s)	KE Dissipated: Time (J/ μ s)	KE Dissipated: ←-----→ Penetrator Target	length (J/mm)	KE Dissipated: ←-----→ Penetrator Target	mass (J/g) -----→ Target	Displaced Target Mass in Penetration Channel (g)
RHA	1,507	678.12	1,067.52	1,048.33	1,268.50	830.22	50.87
	1,510	682.09	1,071.94	1,040.63	1,273.76	831.17	50.93
Ti-6/4	1,501	566.62	1,052.32	982.08	1,250.44	1,221.56	45.17

more KE when penetrating the Ti-alloy than it does in the RHA plate. As a result of this analysis, two conclusions were drawn to explain the penetration differences between the

two materials: 1) the Ti6/4 target causes the penetrator to dissipate significantly more energy during the initial penetration phase, and 2) the energy required for the plug to fracture during breakout is an order of magnitude greater for the Ti-6/4 target [27].

1.5 Research Goals

The goal of this study is to observe and make comparisons of the deformation-related features of two target materials, 7039 aluminum and OFHC copper, that have been perforated by a kinetic energy, tungsten-alloy (WHA) projectile at an impact velocity of 1.5 km/s. The two materials share a similar crystal structure (FCC), yet have different properties and as such exhibit very different failure modes.

To date, a detailed and comparative analysis of the two distinctly failing materials to determine fundamental mechanisms of deformation has not been done. In fact, little effort has been made to understand the materials-related issues involved in the ballistic impact and penetration of metal targets. This systematic study will involve TEM and optical microscopy as well as microhardness measurements.

Computer modelling of the perforation events will also be performed, with the intention of validating the hydrocode that will be used through a microstructural-based comparison. This will be an important feature of the work, since numerical simulations hold much potential for revealing many details of the penetration/perforation phenomena, yet are lacking in the fact that microstructural aspects have been ignored.

Chapter 2

SHOCK WAVES AND MATERIALS EFFECTS

2.1 Shock Wave Phenomena

A shock wave is essentially a plastic wave with a very sharp front having a thickness independent of time as the shock wave propagates. This sharp front creates a discontinuity in pressure, temperature (or internal energy), and density between two adjacent regions within the material [30]. Shock waves are generally produced either by the detonation of explosives or through high velocity impact phenomena [4]. A shock wave propagating into or through a material, with respect to time and pressure, can be illustrated in the schematic of figure 2.1. The shock pressure is shown as a region where the material is subjected to increasing pressure (stress) up to the peak shock pressure. The time of application of the peak shock pressure (P) is indicated as the shock pulse duration, Δt . As the pressure of the wave declines or is attenuated, the shock wave is characterized by a rarefaction wave (or wave portion) [31].

The mathematical treatment of shock waves was originally developed by Rankine and Hugoniot for fluids. The hydrodynamic treatment was later extended to shock waves propagating into gas, liquid, or solids. Shock waves require a state of uniaxial strain, where $\epsilon_x \neq 0$, $\epsilon_y, \epsilon_z = 0$, which results in the build-up of the hydrostatic component of stress to high levels [2]. When the hydrostatic component becomes greater by several

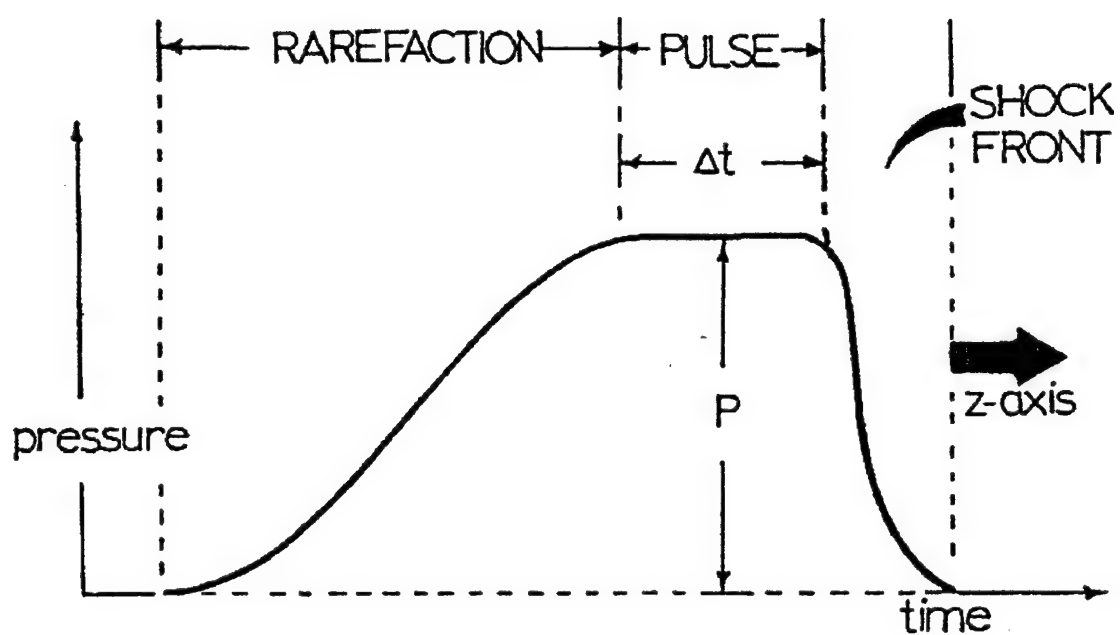


Figure 2.1: Ideal representation of a shock wave traveling through a solid material with a peak pressure (P) and pulse (Δt) [2].

factors than the dynamic flow stress in a material, it can be assumed that the solid has no shear resistance ($G = 0$). Therefore, the calculation of shock wave parameters are based upon the Rankine-Hugoniot [32,33] conservation equations, which utilize the fundamental assumption that $G = 0$. The equations are developed by considering regions immediately ahead of, as well as behind, the shock front. Figure 2.2 illustrates a shock front. Conservation laws require that mass, momentum and energy arrive at the shock front from the undisturbed material at the same rate at which these quantities leave the shock front in the compressed region [30]. The conservation equations can then be arrived at:

$$\text{Conservation of mass:} \quad \rho_o U_s = \rho (U_s - U_p) \quad (7)$$

$$\text{Conservation of momentum:} \quad (P - P_o) = \rho_o U_s U_p \quad (8)$$

$$\text{Conservation of energy:} \quad E - E_o = \frac{1}{2} (P + P_o) (V_o - V) \quad (9)$$

These equations are based on the assumption that the amplitude of the stress is many times larger than the elastic limit of the material, thus the material responds to the wave as a fluid. Therefore, use of these equations is restricted to conditions of a very high pressure, or an equivalent stress, which exceeds the yield stress.

2.2 Dynamic Fracture and Spalling

Dynamic fracture refers to the rapid formation and propagation of many cracks during high rates of loading. The feature that distinguishes dynamic fracture from quasi-

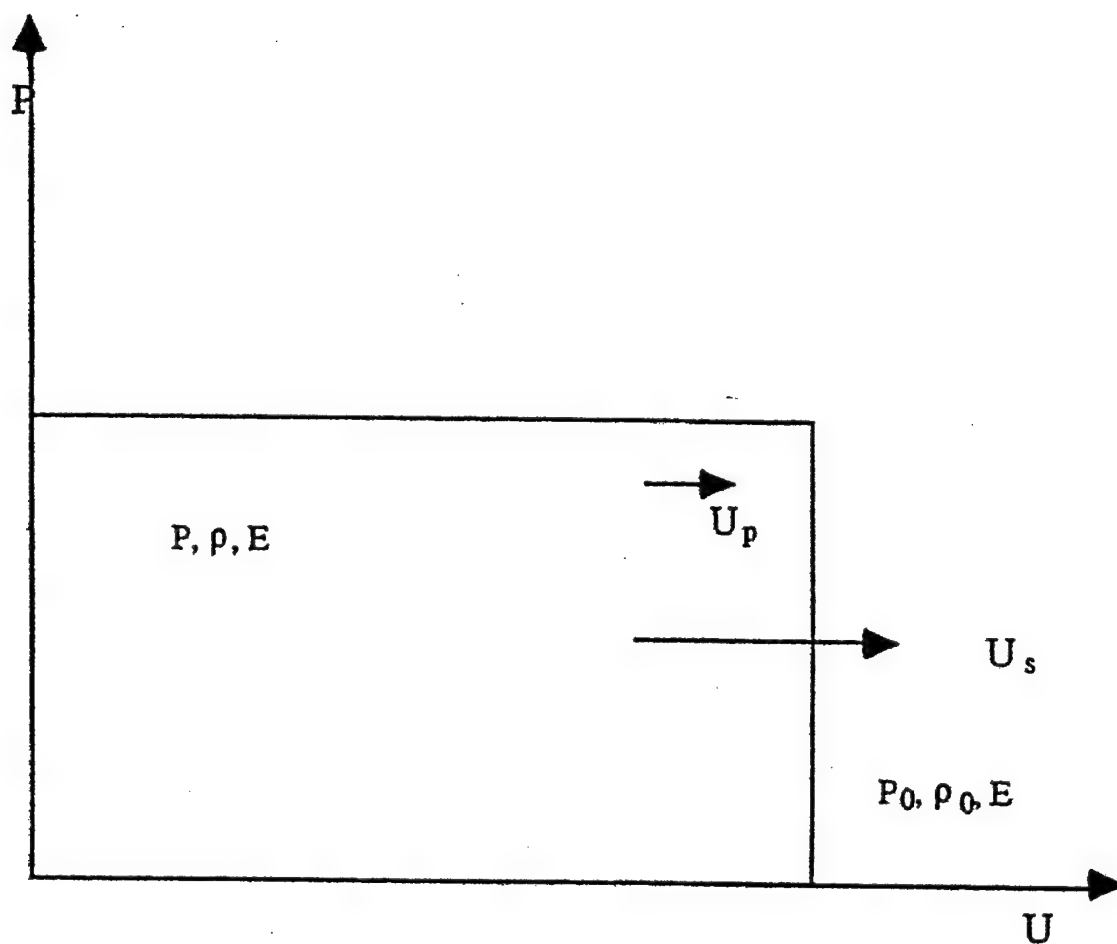


Figure 2.2: Schematic of a sharp step shock wave front [2].

static behavior is the presence of stress waves. These waves arise due to either the stresses released from the crack tip at fracture or externally applied loads. When stress waves, reflected from free boundaries, return to the crack tip, they alter the crack tip stress state, and this can result in a change of crack speed or cause crack branching if the intensity of the stress waves is sufficiently high [2].

Dynamic fracture is independently nucleated at many sites, thus forming many cracks. The stresses will travel along the crack tips and can travel at a maximum velocity at the crack surface. At a certain critical velocity cracks tend to branch out (bifurcate) in order to decrease the overall energy of the system as shown in figure 2.3. When many cracks are formed and grow simultaneously, the body is eventually divided into many parts and fragmentation occurs. Thus, quasi-static failure will result in the propagation of a single crack, dividing a part into two, whereas dynamic crack propagation can produce fragmentation [29].

Spalling can be defined as a dynamic material failure that occurs due to tensile stresses generated by the interaction (collision) of two rarefaction, or reflected, waves. First, compressive waves are generated at the interface between the impacted target and the projectile and travel along the thickness of both materials [34]. Upon reaching the free surface (back end) of both, projectile and target, the waves are reflected back into the materials as tensile waves. The collision of these waves (tensile and compressive) produces damage, or a spall.

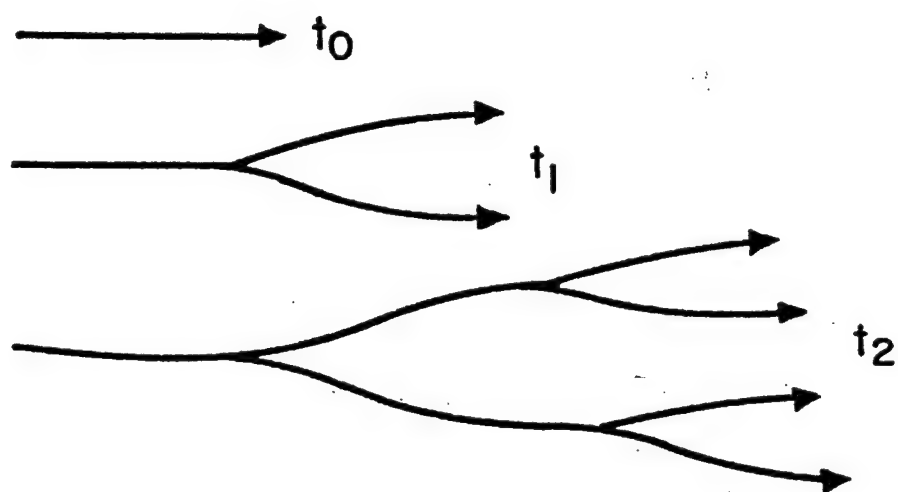


Figure 2.3: The branching of cracks as they propagate dynamically ($t_0 < t_1, t_2$) [27].

The distance-time typified by figure 2.4(a) is helpful in understanding spalling. The left-hand side represents the projectile, while the right-hand side represents the target. At time $t = 0$, the projectile impacts the target. Elastic waves are first emitted into both projectile and target; they are followed by plastic waves. In figure 2.4(a) the inverse of the slope of the diagonal lines gives the velocities of the waves; it can be seen that the elastic precursor has a higher velocity than the shock wave. As the elastic and plastic waves encounter the free surfaces of target and projectile, they reflect back. The first region to feel the tensile pulse is the one marked (x_0, t_0) . It is presently known that spalling is dependent both on the amplitude and on the duration of the reflected tensile pulse. If this pulse is of sufficient magnitude to produce spalling, it should occur. Spalling will produce release waves at the newly created internal surfaces (spall surfaces) that alter the subsequent configuration of pulses. In figure 2.4(a) an incubation time for the onset of spalling was assumed and is indicated. As spalling initiates, release pulses emanate from the newly created free surfaces and decrease the tensile stresses. When the projectile and target consist of the same material, the distance of the spall from the free surface will be roughly equal to the thickness of the projectile [2].

2.3 Shock-Wave Generated Microstructure

Essentially all explosively driven processes and impact phenomena involve the creation of shock waves that travel as a geometrical demarcation (or shock front) in the

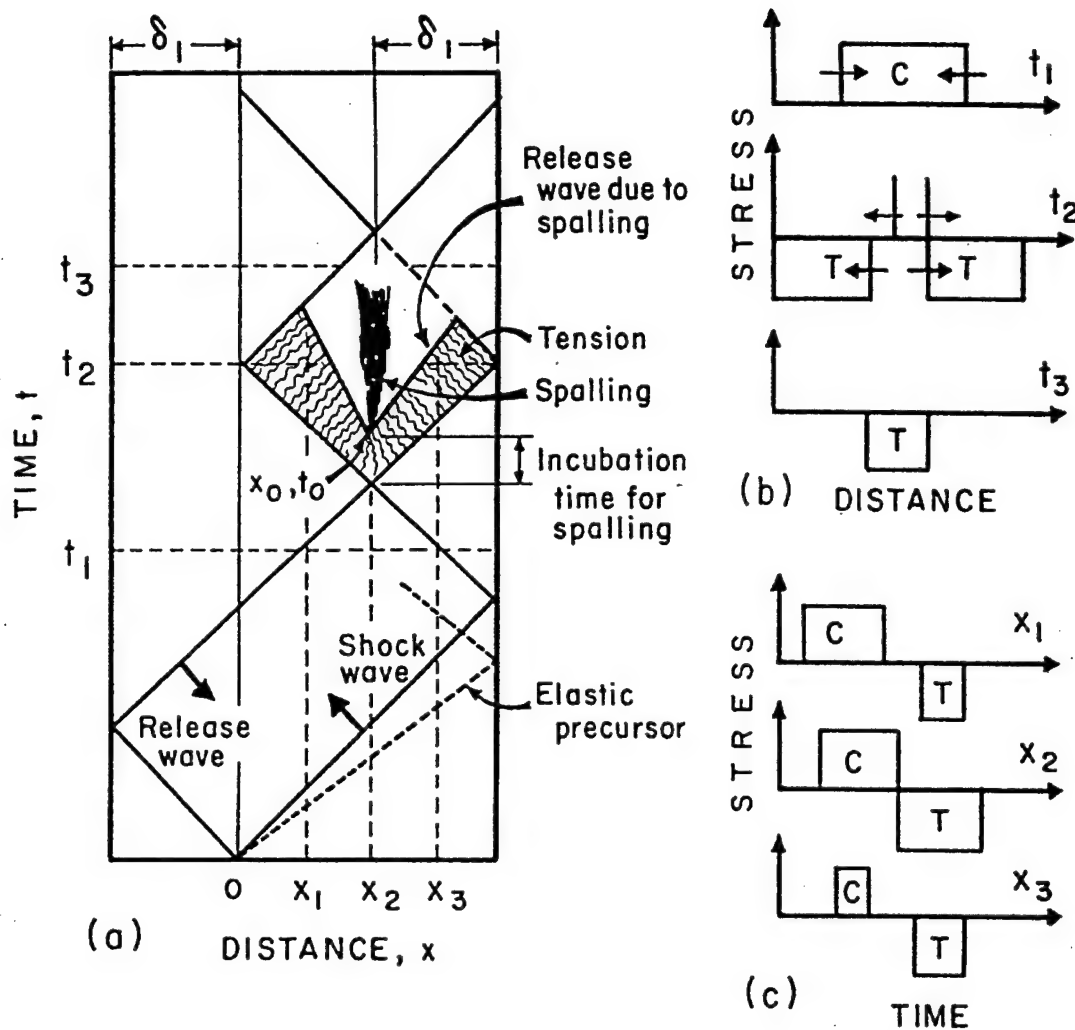


Figure 2.4: a) Distance-time plot showing propagation of the wave in the target and projectile after impact and spalling. b) Stress profiles at times t_1 , t_2 , and t_3 . c) Stress histories at positions x_1 , x_2 and x_3 [2].

associated materials or materials systems. In crystalline or polycrystalline materials, the advancing shock front creates lattice defects that alter the microstructure [6]. For many polycrystalline metals and alloys, the dislocation density increases with increasing peak shock pressure [35]. While dislocations may be involved in a range of metallurgical effects, there are also the mitigating and controlling effects of temperature, strain, strain-rate and the strain (or stress) state [31]. The changes in dislocation density are simply related to changes in stress (or strain) through expressions of the form:

$$\sigma = \sigma_0 + K\sqrt{\rho} \quad (10)$$

$$\rho = \rho_0 + A\varepsilon \quad (11)$$

where σ_0 , K and A are constants and ρ is the dislocation density (ρ_0 is the initial dislocation density). This equation elucidates that residual yield stress, or flow stress, will be increased by the creation of dislocations. Yield stress in polycrystalline metals and alloys can also be related to grain size, or other microstructural partitioning (such as twin spacing), through the Hall-Petch relation:

$$\sigma = \sigma_0 + K\sqrt{D} \quad (12)$$

where D is the grain size. This can be written in a more general expression:

$$\sigma_y = K' + K'' \sum_j (\lambda^G)^{m_j} \quad (13)$$

where K' and K'' are interrelated constants, λ^G is the deformation gradient wavelength (or spacing associated with a particular microstructure) and m_j varies from 0.25 to 1 depending upon the particular microstructure (j). Therefore, λ^G can be set equal to grain

size (D), dislocation cell diameter (d), or the spacing between twins (Δ). If all these microstructures were to contribute to a change in stress, then the previous equation can be written out as:

$$\sigma_y = \sigma_0 + K_1 \rho^{1/2} + K_2 V_C d^{-1} + K_3 V_T \Delta^{-1/2} + K_4 D^{-1/2} \quad (14)$$

where V_C and V_T denote the volume fractions of dislocation cells (C) and twin faults (T), respectively. In essence, microstructures which can be characterized as interfaces (such as sub-grain, grain or twin boundaries) contribute to hardening and strengthening by acting both as sources for dislocations, and as barriers to their motion.

Consequently, hardness and yield strength are usually increased when a shock wave passes through a crystalline or polycrystalline material. Because a shock wave will move at bulk sound velocity, it is a precursor to plastic deformation. Also, the associated plastic deformation will involve the shock-wave-altered microstructure [6]. For shock-loading-related phenomena, the corresponding strain rates are very large (10^6 - 10^8 s⁻¹). Thus temperature in deforming materials can be raised by increasing the strain, and by adiabatic heating at high-strain-rates [31]. These features – high strain, high-strain-rate, and associated high temperatures – are, of course, conducive to dynamic recovery and recrystallization of microstructures created in the shock front [6].

2.3.1 Dynamic Recovery and Dynamic Recrystallization

Recovery and recrystallization are generally considered as restoration mechanisms through which deformed metals or alloys are partially or completely returned to their original condition before deformation [36]. Restoration mechanisms can

be classified as either static or dynamic processes. During the static process, the materials are typically cold-worked and then annealed at elevated temperatures in the absence of stress or strain. During the dynamic process, on the other hand, dislocations are created continuously under concurrent stress, strain, and high temperature [29]. Both dynamic recovery and dynamic recrystallization generally occur during hot working or extreme plastic deformation at high-strain-rates, such as shock loading.

Recovery is a process during which mutual annihilation as well as rearrangement of dislocations into more stable (low-energy) configurations occurs (without the mitigation of high angle boundaries) [37]. Dislocation cells, or subgrains, can be formed during this process, and these are characterized by coarse, heavily dislocated cell boundaries having a small misorientation with respect to the grain matrix [30]. The cell size tends to decrease and subgrain misorientation tends to increase with increasing strain rate or decreasing temperature [38]. Recrystallization, the process in which new grains are formed within the parent matrix, takes place by a combination of nucleation of strain-free grains and the growth of these nuclei to absorb the entire deformed material [36].

Several nucleation mechanisms for recrystallization have been proposed and examined [39]. Bailey and Hirsch [40] have further developed a theory, first proposed by Beck and Sperry [41], known as strain-induced boundary migration (SIBM). SIBM is believed to occur as a result of differences in dislocation density across an existing high-angle grain boundary in a cold-worked metal. This is shown schematically in figure 2.5(a). In materials of medium to high stacking fault energy, such as copper, the high density of dislocations generated during deformation will rearrange into a lower energy

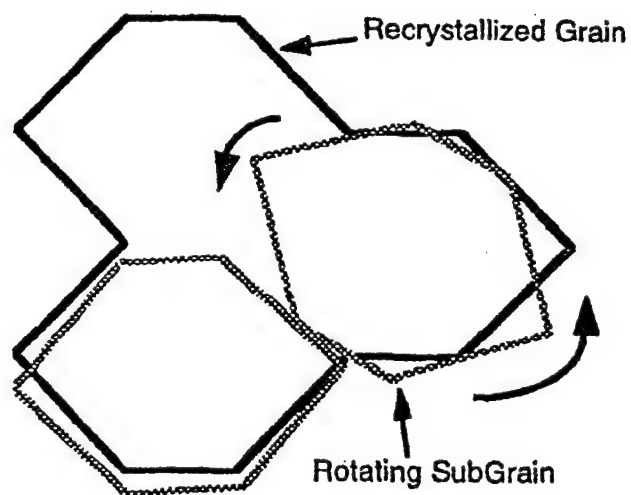
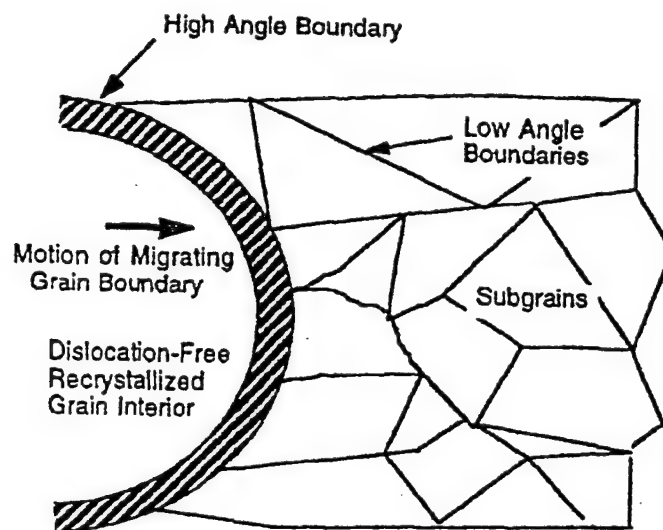


Figure 2.5: Schematic diagrams of recrystallization by a) high angle boundary migration through a partially-recovered microstructure, and b) subgrain rotation and coalescence [36].

configuration, often a cellular structure and eventually subgrains. Some subgrains contain fewer dislocations in their interiors than others, consequently, if two subgrains are adjacent to a high angle boundary and one subgrain has a lower dislocation density, the driving force associated with the strain energy difference will cause a portion of the high angle boundary to migrate into the subgrain with the higher dislocation density. As the strain is imposed on the material, and the high angle boundary moves through the subgrain, it eliminates dislocations and creates a small, strain-free nucleus, which will continue to grow through grain boundary migration [42].

The process of subgrain coalescence is another heterogeneous nucleation mechanism, first proposed by Li [43] and later demonstrated by Hu [45]. This mechanism (shown in figure 2.5(b)) involves two adjacent subgrains which attempt to lower their surface energy by rotating into coincidence and eliminating the low-angle boundary that separates them. This process involves the collective climb and glide of the low angle boundary dislocations for the rotation of the boundary to the new configuration and for the elimination of the boundary once coincidence is obtained [45]. The rotation of certain subgrains will also produce larger misorientations with adjacent subgrains yielding high-angle grain boundaries, thereby forming new recrystallized grains [37].

In a study of shock-loaded copper by Andrade et al. [46], where it was observed that the microstructure within shear band regions were recrystallized grains, it was concluded that recrystallization occurred during deformation and not subsequent to it. A recrystallization model for high-strain-rate phenomena was proposed that consisted of elements of both boundary migration and subgrain coalescence. However, in a similar

study of shock-loaded copper by Hines and Vecchio, it was found that both the classical recrystallization mechanisms were kinetically too slow (being diffusion-rate controlled) to account for the recrystallization behavior either during, or subsequent to deformation under high-strain, high-strain-rate conditions [42]. It was therefore concluded that another mechanism, possibly a mechanically-assisted subgrain rotation/coalescence, may be necessary to account for dynamic recrystallization at high-strain-rates.

2.3.2 Microbands and Microtwins

Microbands can be defined as bands of localized shear deformation, which often resemble elongated subgrains [47]. They are cell blocks, or domains of contiguous dislocation cells which have an orientation that is coincident with a primary slip system. Huang and Gray [48] have asserted that the dislocation walls, which distinguish microbands, behave similar to a very low-angle ($\leq 1^\circ$) boundary, such as a dislocation cell boundary, hence the resemblance to subgrains.

Observations of microbands in OFHC copper by Murr et al. [47] revealed that the microbands consist of double dislocation walls (DDW), which are spaced approximately 0.1 - 0.4 μm in width, and are coincident with traces of $\{111\}$ planes. They were found to be misoriented 1 to 3° with respect to the surrounding matrix. They are often referred to as second-generation microbands [49] to differentiate them from similar, non-coincident, elongated, dislocation cell related microbands referred to as first-generation microbands. These microband observations have been typical of many similar observations in a variety of both fcc and bcc metals and alloys over the past two decades. Microbands

increase in volume fraction with increasing grain size and increasing shock pressures, and do not appear to be noticeably influenced by stacking-fault free energy (SFE) [29].

In FCC materials, deformation twins and microbands each occur as linear bands, or traces, that are coincident with traces of $\{111\}$ planes intersecting corresponding grain surfaces [50]. Their features are hardly distinguishable by surface microscopy, if in fact they are observable at all [48].

Twinning may be defined as the shearing of planes of atoms within a specific (twinning) plane, such that the twinned portion lies on a different orientation and appears as a mirror image of the parent matrix that surrounds it (figure 2.6). Figure 2.7 shows a schematic comparing the crystallography and geometry of deformation twins and microbands. Twins, like microbands, increase with increasing peak shock pressure, or an equivalent stress [48,53]. Both tend to increase in density with an increase in grain size [54-56], and at some critically small grain size, deformation twins and microbands are prevented from forming [55,56].

Though there are similarities between the two, they are obviously crystallographically distinct since the volume of a microband is only misoriented a few degrees at most from its surrounding matrix [49]. In addition, deformation microtwins are often only $0.01\text{ }\mu\text{m}$ thick [35], while microbands are at least an order of magnitude thicker. Transmission electron microscopy (TEM) and selected-area diffraction (SAD) analysis has proven to be vital tools in the unambiguous characterization of, and distinction between, microbands and microtwins. Not only is TEM required to see features and geometries, but corresponding SAD is necessary to uniquely identify the

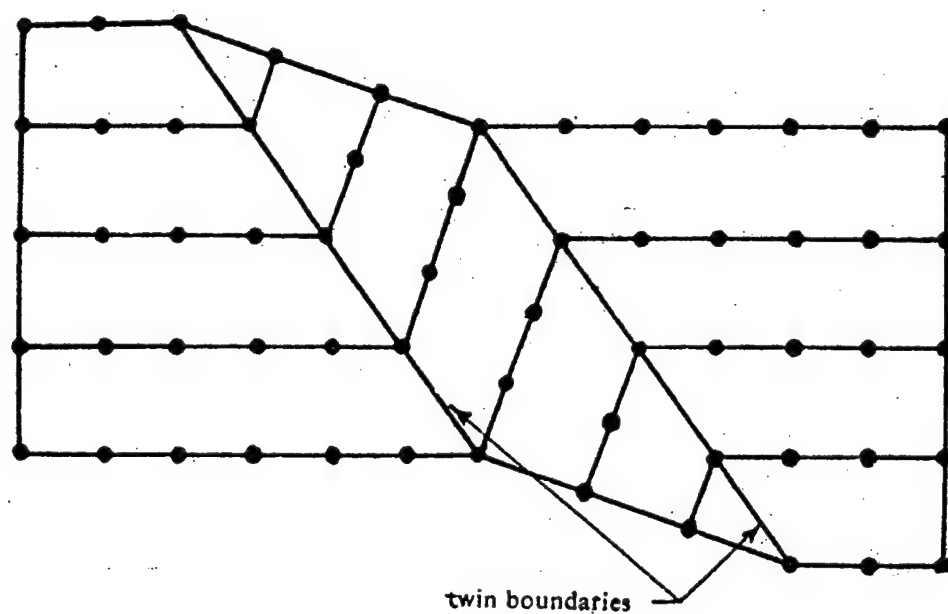


Figure 2.6: Schematic of a twin where the atomic arrangement on one side of the twin boundary is a mirror reflection of that on the other side [49] .

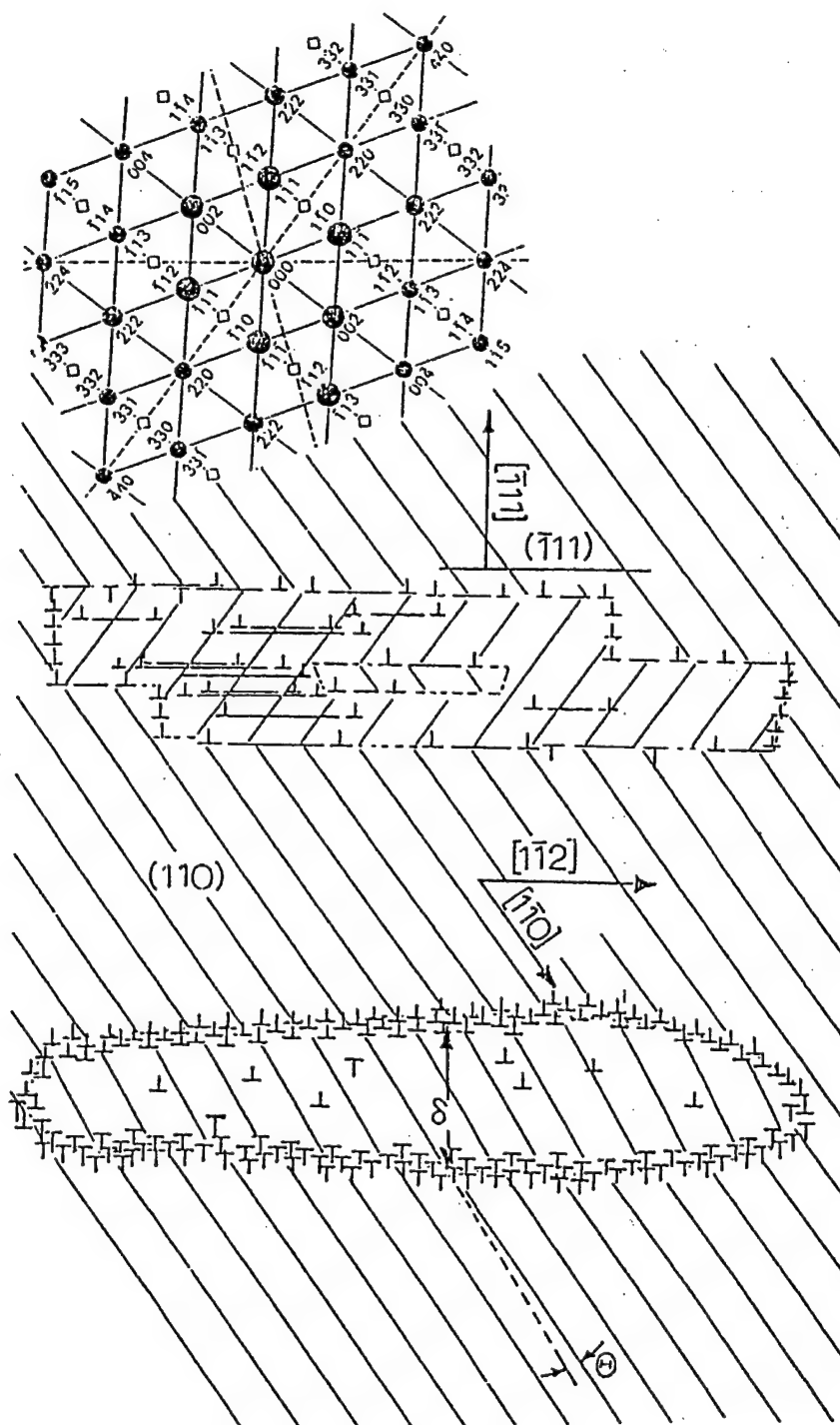


Figure 2.7: Schematic representation of a) a deformation microtwin (or twin-fault) and b) a microband in the (110) grain surface orientation of an fcc crystal [50].

diffracted reflections and crystallographic directions. The intrinsic nature of twins produces reflections which occur in the diffraction pattern, and have a fixed relationship to the allowed matrix spots. In fcc crystals, the twin spots can occur as $\frac{1}{3}(hkl)$, where (hkl) is a particular diffraction condition (a diffracting plane which produces a diffraction spot in the SAD) [28]. Figure 2.8 illustrates a typical diffraction pattern which shows the location of twin spots (T) for twinning along the $[\bar{1}12]$ direction of a (110) grain surface orientation of an fcc material [57]. Microbands produce diffracted spots which are misoriented to matrix spots by $2-3^\circ$.

The mechanism of microband formation is fundamentally different from that of deformation twins. Huang and Gray [48] proposed a mechanism for the formation of microbands based on a study of shock-loaded and quasi-statically deformed metals. This is shown in figure 2.9. When strain is initially applied, primary (and parallel) slip planes become activated and form coarse slip bands, along which dense dislocations can travel (figure 2.9(a)). As the stress increases, dislocations will distribute in a "polarized" arrangement (dislocations of opposite signs forming pairs) as illustrated in figure 2.9(b). As these polarized dislocations become annihilated (opposite signs will cancel each other out) in the central region of the slip band, this ultimately leads to a double-wall configuration of a dislocation band structure with a relatively vacant center region (figure 2.9(c)). Since the dislocation wall is mechanically and thermally unstable, secondary dislocations will react with the primary dislocation array within the slip bands, and this interaction creates Lomer-Cottrell locks (barriers to the free movement of dislocations) as shown in figure 2.9(d). Figure 2.9(e) shows the final morphology of the microband.

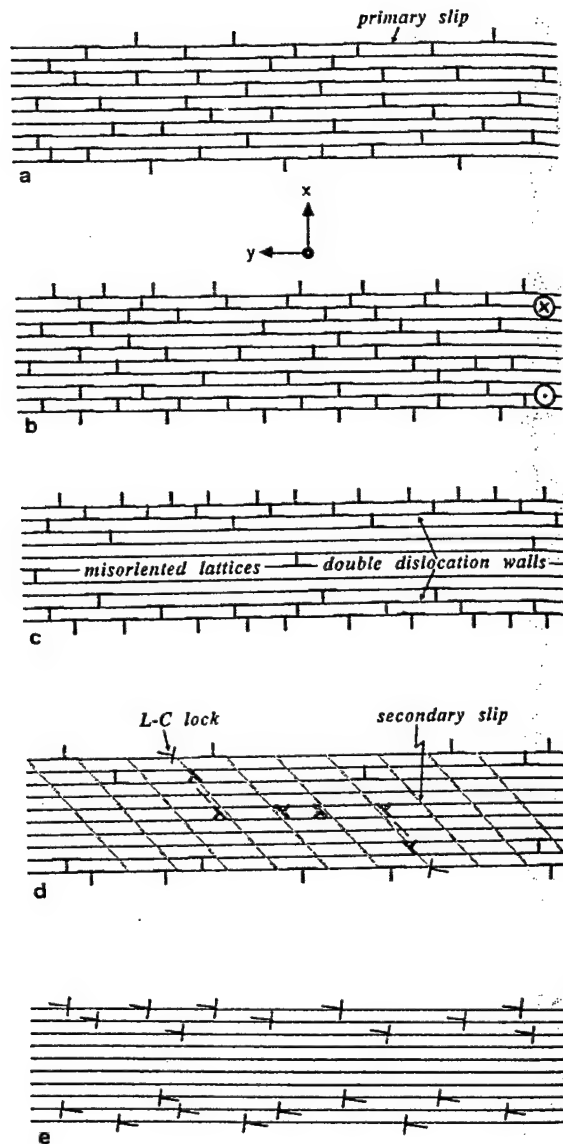


Figure 2.9: Schematic illustration of microband formation model according to Huang and Gray [46]. a) Coarse slip band on primary slip planes showing random dislocations, b) coarse slip band after generation of polarized dislocations, c) double-wall-like features formed after annihilation of polarized dislocations, d) secondary dislocations are activated by internal stresses and Lomer-Cottrell locks form between primary and secondary dislocations, e) microband with stable dislocation arrays in the double walls.

Twinning in fcc materials occurs by the dissociation of $a\langle 110 \rangle/2$ dislocations into two partials of the form $a\langle 112 \rangle/6$. They become extended under an applied stress and eventually form intrinsic stacking faults (these are faults in the stacking sequence of atoms), or single layer twins. When these stacking faults overlap on every $\{111\}$ plane, the twin becomes multi-layered and will appear broader, or thicker. In high-strain-rate deformation, this process is very irregular, and the twins develop as illustrated in the schematic of figure 2.7(a).

Though Huang and Gray [48] have noted that microbands do not appear to be noticeably influenced by stacking fault free energy, in contrast, twinning is SFE dependent. The critical twinning pressure in plane-wave shock-loading is stacking fault free energy dependent, as shown in figure 2.10 for several fcc materials. In the case of copper, which has an SFE of $\approx 78 \text{ mJ/m}^2$, twinning occurs at a critical twinning pressure of 20 GPa. It can also be seen that twin fault density increases with decreasing stacking fault free energy at constant shock pressure [2,35,59].

2.3.3 Shear Bands

Shear bands, which are narrow regions of highly localized plastic deformation, can be extremely important in the dynamic deformation of materials because they are often a precursor to fracture. They are of great interest to the ballistic performance of armors since they provide an easy crack propagation path [60]. In the penetration of a target by a projectile, the formation of a shear concentration, as seen in figure 2.11(a),

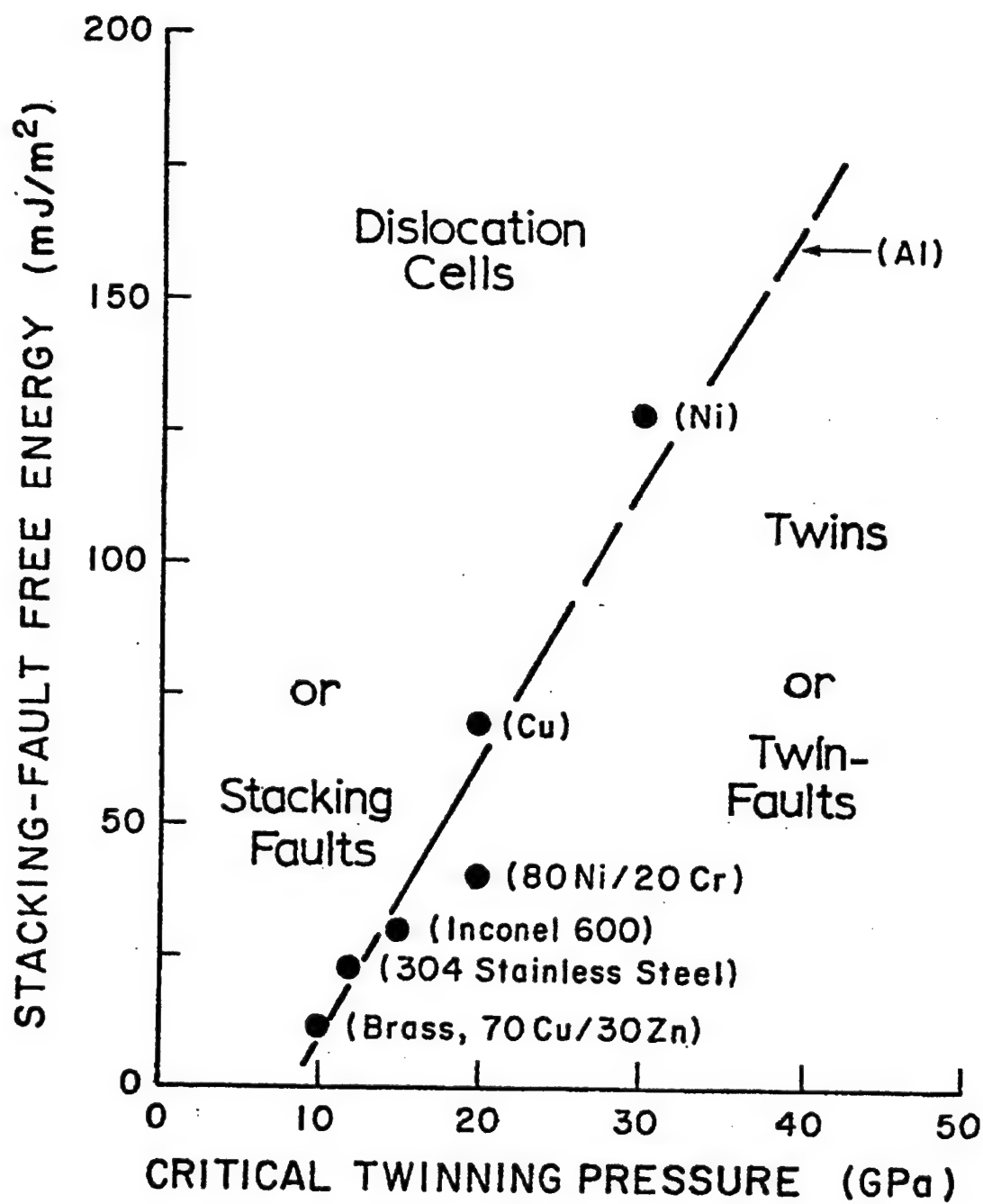


Figure 2.10: Stacking fault-free energy vs. pressure for several fcc materials [55].

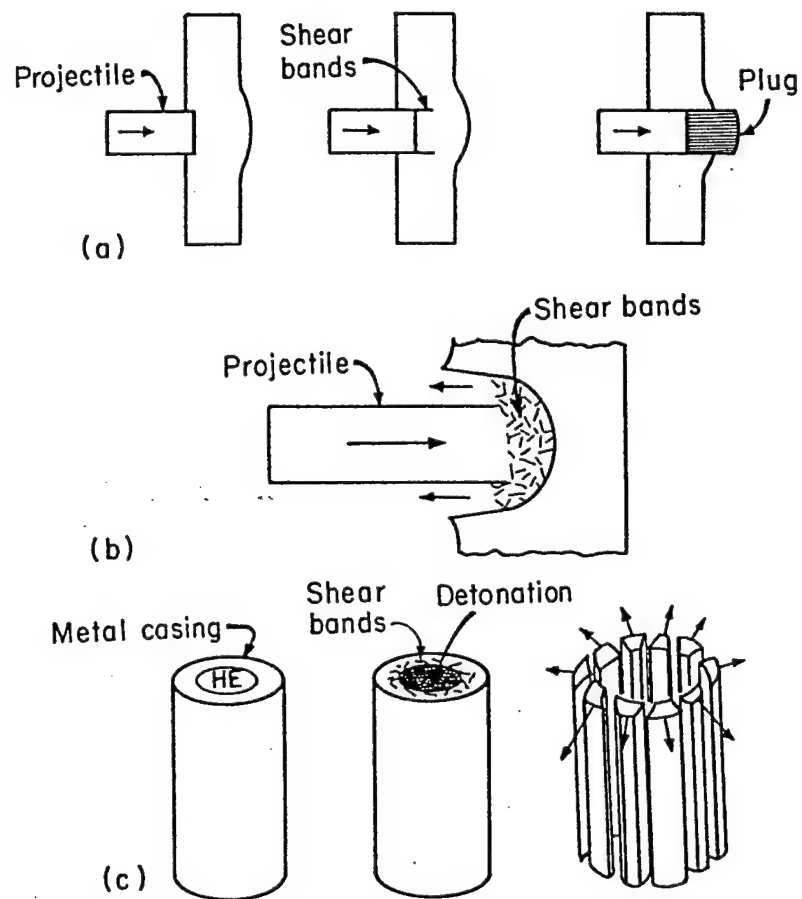


Figure 2.11: The formation of shear bands in dynamic deformation events (military applications): a) defeat of armor by plugging, b) shear bands breaking up projectile, c) shear bands determining fracture in exploding cylinders [2].

alters the defeat mechanism. If no shear bands are formed, plastic deformation is better distributed. The formation of the shear band establishes the shear failure path and is responsible for the "plugging" of the target. In a similar manner, the projectile is fragmented by means of shear cracks preceded by shear bands [Fig. 2.11(b)] [2].

Adiabatic shear bands are a specific type of shear band that can form during high-strain-rate deformation [42]. The term "adiabatic shear" is attributed to a 1944 report of Zener and Hollomon on shear banding in steel [61]. They proposed that when plastic deformation occurs in a material, a large proportion of the plastic work is converted into heat. If the strain rate in a region is sufficiently high, there may not be enough time for heat to conduct away from the deforming zone, causing a significant local temperature rise. If the strength loss due to thermal softening becomes greater than the increase in strength due to strain or strain-rate hardening, the plastic deformation will become unstable and give way to a localized band-like deformation mode (i.e. shear bands). Shear band formation is therefore a complex function of strain, strain rate, and temperature [42].

During the past decade, the presence of recrystallized grains in adiabatic shear bands has been reported in a number of different materials [46,58-66]. Based on these observations of shear bands, it appears that the deformation and/or associated temperature rise during shear band formation is sufficient to produce a new recrystallized microstructure in the shear bands. However, the mechanism for recrystallization under the extreme conditions of high-strain-rate and rapid temperature change present in shear bands is unclear. It has been shown by Hines and Vecchio [42], that the existing kinetic

models for recrystallization cannot account for the formation of these grains in the time scale and temperature history for adiabatic shear band formation and subsequent cooling. The temperature rise, and its duration in shear bands, is generally lower than normally associated with static recrystallization [2]; as such, recrystallization mechanisms relying on diffusional processes may be too slow to account for the observed recrystallized microstructures. Based on this assessment, a mechanically driven subgrain rotation mechanism was proposed. This mechanism can be divided into three components: subgrain formation, subgrain rotation, and subgrain boundary refinement [38] which is characteristic of dynamic recrystallization. Consequently, the fundamental mechanism of shear bands involves dynamic recrystallization.

2.4 Characterization of Target Materials

2.4.1 Plane-wave and Oblique Shock-loading

It was revealed in the previous discussion that the combined effects of high-strain-rate and high plastic strain on metals can generate a broad range of microstructural changes: work hardening, dynamic recovery, dynamic recrystallization, twinning, shear banding, etc. These changes can take place through the introduction of a planar shock-wave, generated through an explosively driven flyer plate arrangement, such as the one shown in figure 2.12 which was developed by Murr [35]. This will impose strong planar waves over different metals or alloys [58,67-68]. As the flyer plate impacts the plane

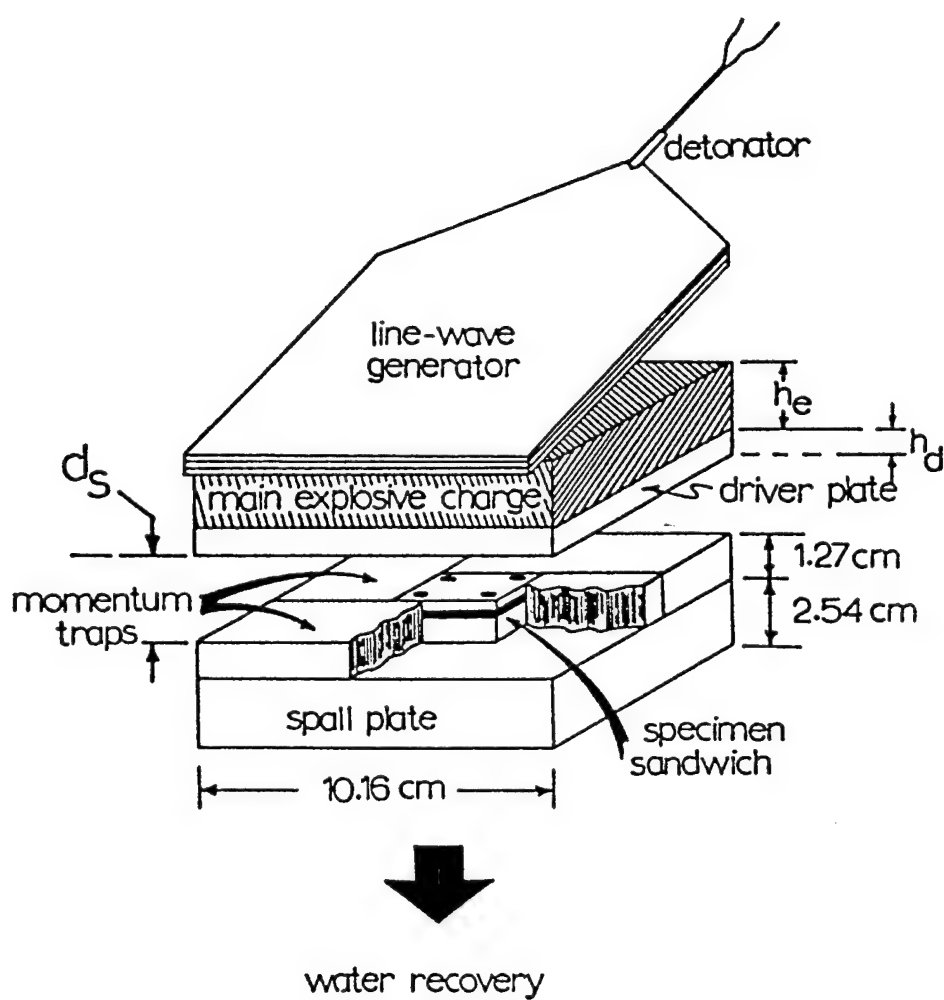


Figure 2.12: Schematic of the planar shock-loading assembly developed by Murr [33].

(parallel) surface, a shock wave is created with a peak shock pressure of:

$$P_s = \rho_t (C_t + S_t U_{pm}) U_{pm} \quad (15)$$

where ρ_t is the target density, C_t is the bulk sound velocity in the target, S_t is a material constant, and U_{pm} is the modified projectile (or flyer plate) velocity in the compressed region after impact [6].

When materials have been plane-wave shock-loaded, the residual microstructures are highly influenced by the stacking fault free energy (especially in fcc materials), in addition to the peak shock pressure and pulse duration of the shock-wave. Typically, dislocation cell structures are formed in shock-loaded materials when the SFE is greater than 60 mJ/m^2 (figure 2.10 illustrates this) [35]. For energies below 40 mJ/m^2 , planar arrays of dislocations, forming stacking faults and other planar microstructures (such as twins), result. Since face-centered cubic metals are normally characterized by high stacking fault free energies ($>60 \text{ mJ/m}^2$), dislocation cell structures will predominate. Though aluminum is the highest SFE fcc metal (168 mJ/m^2), when shock-loaded it does not normally exhibit recognizable cell structure, partly due to its low melting temperature (660°C). In plane-wave shock-loaded copper, twinning will occur when a critical twinning pressure of 20 GPa is reached.

The nature of residual microstructures will be affected by complex geometries; this was demonstrated in a recent study by Sanchez, et al. [69]. Experiments were performed to shock-load copper rods in an oblique manner, using the cylindrical shock-loading assembly shown in figure 2.13. The assembly allows for loading at an oblique

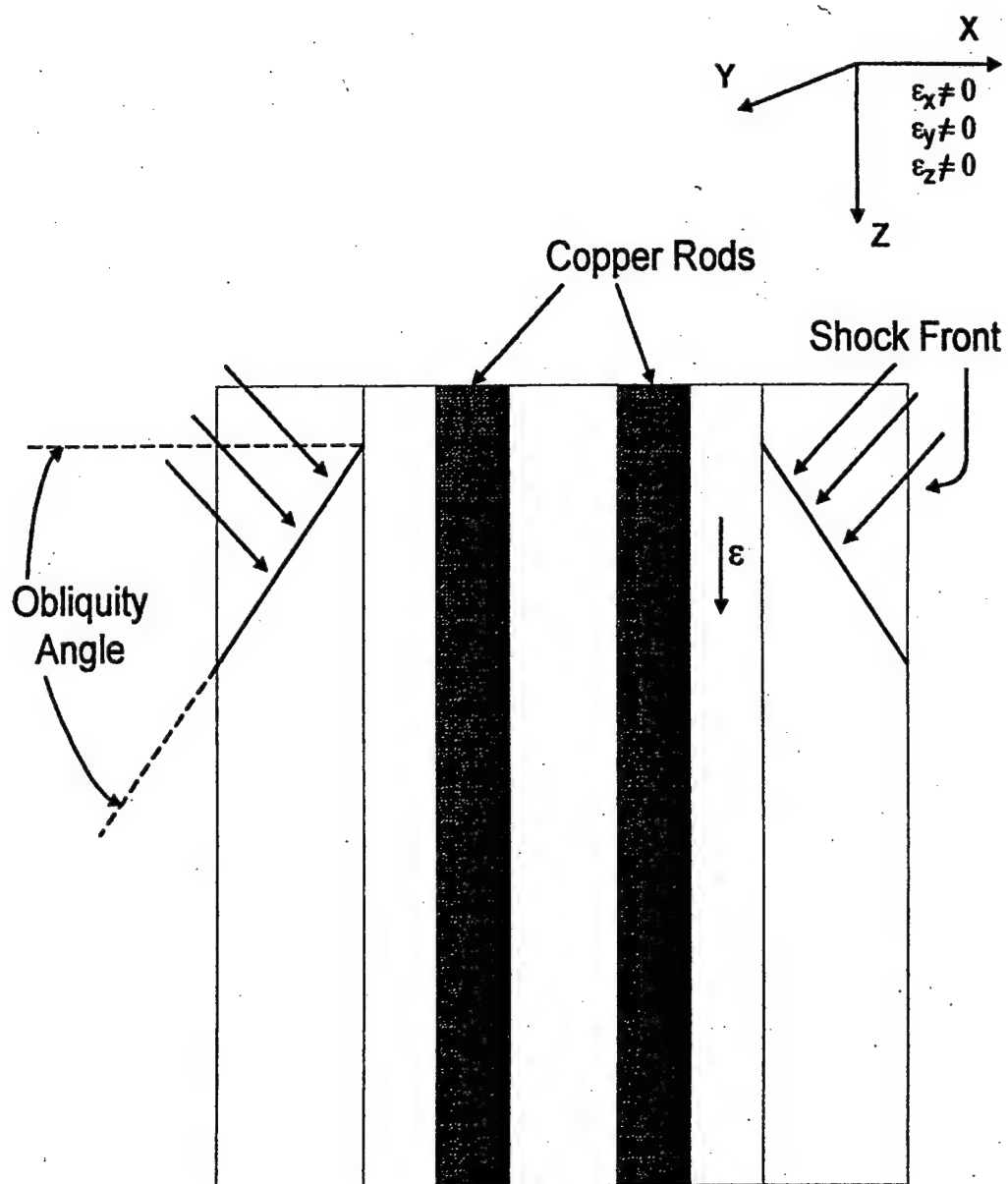


Figure 2.13: Schematic of oblique shock-loading assembly showing the angle of obliquity at the shock front.

angle (roughly 50° relative to the rod axes) and allowed for pressure variations across the rod cylinder [69]. It was discovered that the microstructure of the shock-loaded copper rods consisted of microbands (coincident with traces of $\{111\}$) intermixed with deformation twins [30]. In addition, profuse twinning was observed at a pressure of 11 GPa, whereas a minimum pressure of 20 GPa is required for the presence of twins in plane-wave shock-loaded copper.

2.4.2 Hypervelocity Impact-Cratering

The microstructural features resulting from the hypervelocity impact craters have been well documented for several materials [30,70-74]. In these studies, the residual microstructures of the impact-formed craters had been analyzed at the level of the transmission electron microscope for the first time. Many interesting phenomena were investigated, and some micromechanisms for the formation of the craters were explored. For an OFHC copper target, a recrystallized zone is formed near the crater wall, especially at the rim of the crater, and is followed by a zone of heavily (plastically) distorted grains, which extends into a less distorted region of grains containing linear defects. These linear features were confirmed to be microbands which are coincident with $\{111\}$ slip planes, and usually have a small misorientation of $1\sim 3^\circ$. However, there is a complete absence of deformation twinning, despite the fact that the associated shock pressures far exceed the critical twinning pressure [47]. The assumption is that the nature of the shock wave has an effect, since a spherical projectile impacting a plane target surface would produce a spherical shock-wave as the crater is formed, as shown in figure

2.14. Consequently, shock-deformation geometry appears to be a very critical feature in determining the occurrence (or propensity) of twinning [75]; an oblique shock wave results in twinning, whereas a spherical wave produces no twinning. Microhardness measurements were also developed in the cratering research work, which appears to correspond very well with the microstructures described above. Different impact conditions, such as impact velocity, original structure of the target material, the size and material of the impact ball used in the experiment, can also cause variations in the residual microstructures [29].

2.4.3 Ballistic Penetration/Perforation

There have been few examples of studies involving residual target microstructures associated with the ballistic penetration/perforation phenomena. An examination of the residual microstructure of a perforated copper plate by Huang et al. [76], and Murr et al. [77], was borne out of the speculation that the principal features of hypervelocity crater-related residual microstructure may also be observed in the complete penetration of a target by a ballistic projectile. In fact, it was indeed found that the penetration of copper is characteristically similar to the impact cratering of copper. A very thin, dynamically recrystallized zone was observed at the crater wall, and was concluded to be a prominent mechanism in the penetration process as it is associated with solid state plastic flow [77]. Also, it was found that deformation microbands dominate the residual target microstructure radiating outward from the penetration channel wall into the target. As in the case of impact cratering of copper, no deformation twins were observed.

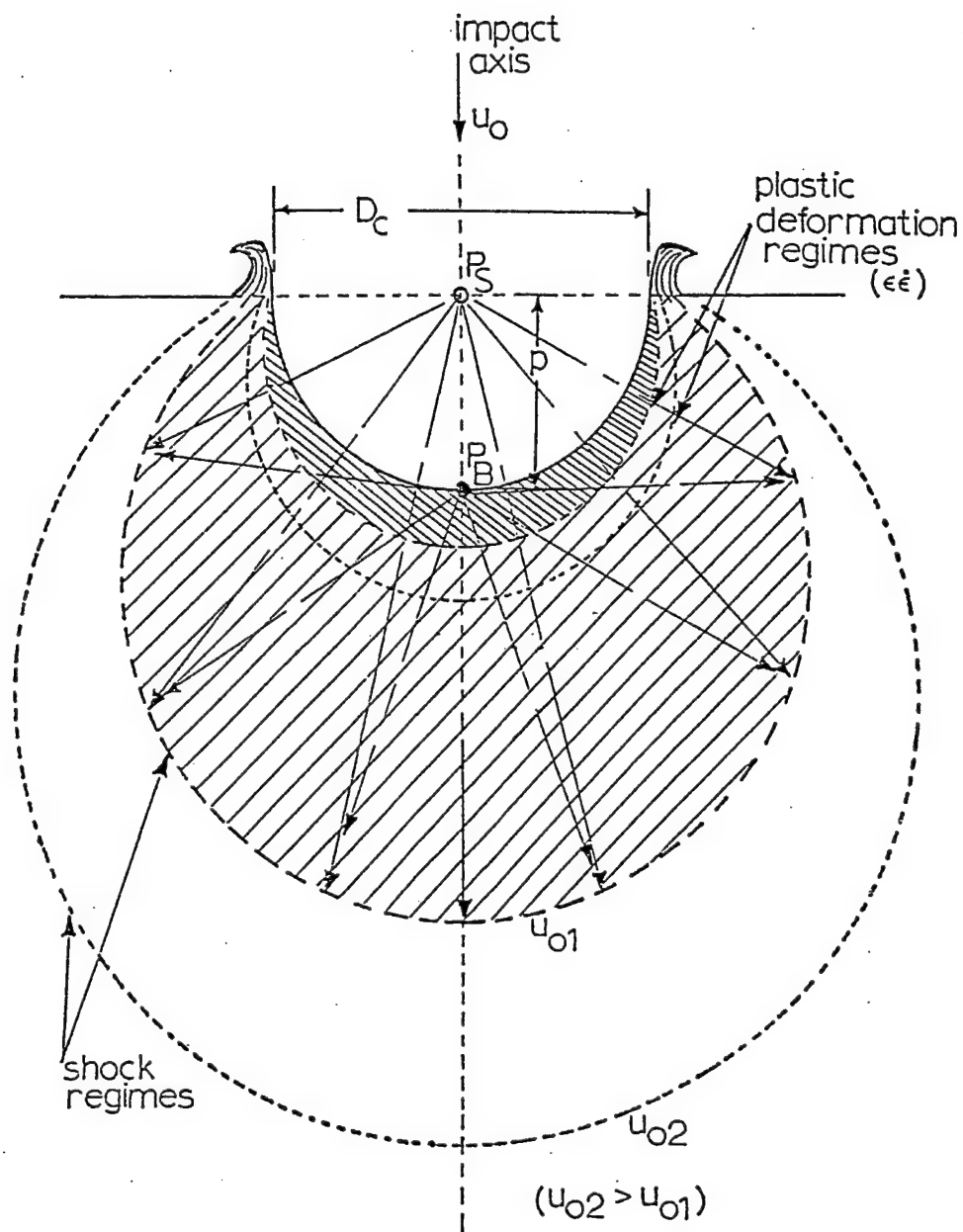


Figure 2.14: Schematic of the various effects related to impact crater formation including a spherical shock wave. Note the large strains or strain zones experienced by the target material [49].

In the study by Huang, et al. [76], a systematic examination and comparison of the characterization of the residual microstructures was carried out in targets of finite thicknesses that were impacted by WA projectiles. The target materials examined included the OFHC copper, as well as 7039Al, Ti-6Al-4V, RHA steel and iron. Each represented different crystal structures, initial microstructures and densities. In the 7039Al target, a limited extent of deformation was revealed. Some plastic distortion (deformation) and recovery were seen near the channel wall, as well as numerous shear bands intermixed with the microstructure and associated with cracks. Microhardness measurements revealed little hardening in the target outward from the penetrated channel wall. The observations were in contrast to the residual copper microstructure, which as stated earlier, showed a very narrow zone of dynamic recrystallization extending from the channel wall followed by a heavily deformed zone which extends into a less distorted region of grains containing microbands coincident with $\{111\}$ slip planes.

The experimental test results obtained by Huang were used in a study by Rupert and Grace [27], to understand target penetration and perforation through energy partitioning. Through a comparison of both the experimental work and an energy analysis of the ballistic process, the authors were able to conclude that Ti-6/4 is a substantially more mass-efficient target material than RHA due to higher energy dissipation by the WA projectile in that target material. The associated calculations indicated that length-based KE dissipation rates were similar in the formation of penetration channels in both Ti-6/4 and RHA, yet metallurgical observations of the

channel wall showed a difference in the process. The Ti-6/4 target did not exhibit the gross plastic deformation seen in RHA, rather evidence of brittle failure was observed and since it is plausible that Ti-6/4 undergoes extensive fracturing, such a process would require that much more energy be expended. This approach takes into account an aspect of the penetration process which has not been adequately addressed, namely the nature of target deformation in terms of changes in microstructure of the material. The results stress the importance of materials characterization as a comparative tool in the study of perforation/penetration.

From the above discussion, it can be seen that there are a variety of microstructural features and mechanisms, and failure modes active in the high-strain, high-strain-rate regime. It obviates the need for a detailed, extensive microstructural characterization of the penetrator and target in order to understand the fundamental mechanisms operating in the complex projectile/target interaction regime. Only an understanding of the phenomena at the fundamental levels can help improve the armor and anti-armor materials. Such a detailed microstructural characterization of long-rod projectiles and impacted targets has previously not been carried out. In this study, we are attempting to characterize OFHC copper and 7039 aluminum targets perforated by tungsten-heavy alloy rods in order to understand the mechanisms that operate in the different behavior of these targets.

Chapter 3

HYDROCODE ANALYSIS OF DYNAMIC IMPACT

3.1 Hydrocodes

Computer programs which are used to numerically simulate dynamic events in solid mechanics, particularly those which involve shocks, are commonly referred to as hydrocodes [78]. These programs were originally developed to study the behavior of materials under hypervelocity impact conditions, primarily with impacts above the speed of sound in the colliding objects (5-6 km/s for metals) [79]. Under these conditions, pressures are generated that exceed material strengths by 10-1000 and material response was governed solely by an equation of state (EOS). In this regime, solids could be treated as fluids, and hence the expression 'hydrodynamic computer code' came about, and was eventually shortened to 'hydrocode'. Some of the common hydrocodes currently in use have been listed in table 3.1. In general, these codes contain the following components [2]:

1. Conservation equations: Equations of mass, momentum and energy.
2. Constitutive equations: These equations describe the material behavior in elastic, plastic and shock (hydrodynamic) regimes.

Table 3.1
Principal Hydrocodes Used in the United States^a

Code	Origin*	Numerical Method	Dimensional Capability	Numerical Coordinate Scheme
SWAP		MC	1-D	Lagrangian
WONDY		FD	1-D	Lagrangian
TOUDY	SNL	FD	2-D	Lagrangian
DUFF		FD	1-D	Lagrangian
HEMP	LLNL	FD	1, 2, 3-D	Lagrangian
STEALTH	SAIC	FD	1, 2, 3-D	Lagrangian
PRONTO	SNL	FD	2, 3-D	Lagrangian
MESA	LANL	FD	2, 3-D	Eulerian
PAGOSA	LANL	FD	3-D	Eulerian
JOY	LLNL	FD	3-D	Eulerian
DYNA	LLNL	FE	2, 3-D	Lagrangian
CALE	LLNL	FD	2-D	Lagrangian
CAVEAT	LANL	FD	2, 3-D	
CTH	SNL	FD	2, 3	Eulerian
PICES	Phys. Intl.	FD	2, 3-D	Coupled Lagrangian/ Eulerian
CRALE		FD	1, 2-D	Arbitrary Lagrangian/ Eulerian
AFTON		FD	1-D	
CSQ II	SNL	FD	2-D	Eulerian
EPIC-2	Honeywell	FE	2-D	Lagrangian
EPIC-3	Honeywell	FE	3-D	Lagrangian
NIKE-2D, 3D	LLNL	FE	2, 3-D	
Codes for personal computers				
ZEUS	Segletis/Zukas			Lagrangian
AUTODYN		FE	2-D	
TDL MADER	C. Mader	FD	2-DD	Lagrangian

^aAbbreviations: MC, method of characteristics; FD, finite differences; FE, finite elements.

*SNL: Sandia National Labs; LLNL: Lawrence Livermore National Labs.; SAIC: Science Appl. Inc.; Phs. Intl: Physics International.

3. Equation of State (EOS): An equation that describes the extremely high pressures generated in a collision.
4. Failure Models: These deal with fracture, spalling and shear band formation.

The coupling of conservation equations with the material descriptions results in a set of coupled nonlinear partial differential equations. The two common algorithms used to solve these equations in all production hydrocodes are the finite-element and finite-difference methods. Regardless of the method chosen, the net result is a set of algebraic equations, which are solved at a discrete number of time intervals to provide information on the nature of colliding objects.

Once the geometry, material data, and initial and boundary conditions have been specified, computations are then performed that solve the conservation equations together with a material constitutive model at each point in the geometry. These solutions will provide new positions, velocities, material stresses, etc., which will act as the initial conditions for the next computational cycle. Cycles are repeated until the desired termination time is reached. The final phase of the process lies in the interpretation of the results; information concerning material displacements, velocities, accelerations, material strains, pressures, stresses, temperatures and energies at any point in the geometry can be generated.

The accuracy and utility of hydrocodes is limited by the material descriptions embodied in their constitutive equations; the numerical simulations can only be as accurate as the material models [78]. A poor agreement between computer model and

experiment generally requires abandoning the constitutive model or accepting the results with caution. Excellent results have been obtained for situations where material behavior is well understood and characterized – the better the description of material behavior at the strain rates encountered experimentally and of its failure modes at those strain rates, the better the computational results [15].

3.1.1 Numerical Processors

The bulk of computer codes used on a production basis for impact studies commonly fall into two categories: Lagrangian and Eulerian. These numerical processors each provide a different mathematical treatment in obtaining a solution for a problem. Table 3.2 gives the Lagrangian and Eulerian forms of the conservation equations [78].

Table 3.2

Lagrangian and Eulerian Forms of Conservation Equations

	Lagrangian	Eulerian
Conservation of Mass	$\frac{D\rho}{Dt} + \rho \frac{\delta v_i}{\delta x_i} = 0$	$\frac{\delta \rho}{\delta t} + \frac{\delta}{\delta x_i}(\rho v_i) = 0$
Conservation of Momentum	$\frac{Dv_i}{Dt} = f_i + \frac{1}{\rho} \frac{\delta \sigma_{ji}}{\delta x_j}$	$\frac{\delta v_i}{\delta t} + v_j \frac{\delta v_i}{\delta x_j} = f_i + \frac{1}{\rho} \frac{\delta \sigma_{ji}}{\delta x_j}$
Conservation of Energy	$\frac{De}{Dt} = f_i v_i + \frac{1}{\rho} \frac{\delta}{\delta x_j}(\sigma_{ij} v_{ij})$	$\frac{\delta e}{\delta t} + v_i \frac{\delta e}{\delta x_i} = f_i v_i + \frac{1}{\rho} \frac{\delta}{\delta x_j}(\sigma_{ij} v_i)$

These differential equations relate material density (ρ), velocity (v_i), specific total energy (e), the stress tensor (σ_{ij}), and external body forces per unit mass (f_i) (subscripts represent standard tensorial notation).

The Eulerian description is a spatial description, the Lagrangian description is a material description [78]. Lagrangian codes follow the motion of fixed elements of mass. The computational grid is fixed in the material and will deform with it. A typical example of a Lagrangian grid is shown in figure 3.1(a). The Lagrange formulation tends to be faster computationally, compared to the Eulerian approach, as no transport of material through the mesh needs to be calculated. Moreover, material interfaces, free surfaces, and history dependent material behavior are generally easier to follow in the Lagrange framework. The major disadvantage of Lagrange is that if excessive material movement occurs, the numerical mesh may become highly distorted leading to an inaccurate and inefficient solution. Because of its inherent efficiency the Lagrange processor is typically used whenever the deformation and boundary conditions permit [80].

For problems in which large deformations predominate or where mixing of materials (which were initially separated) occur, an Eulerian description of material behavior is necessary. In the Eulerian approach, the computational grid is fixed in space while material passes through it (figure 3.1(b)) [4]. An Euler formulation is ideally suited to handling large deformations and fluid flow. However, it is more difficult to track free surfaces, material interfaces, and history dependent material behavior [80].

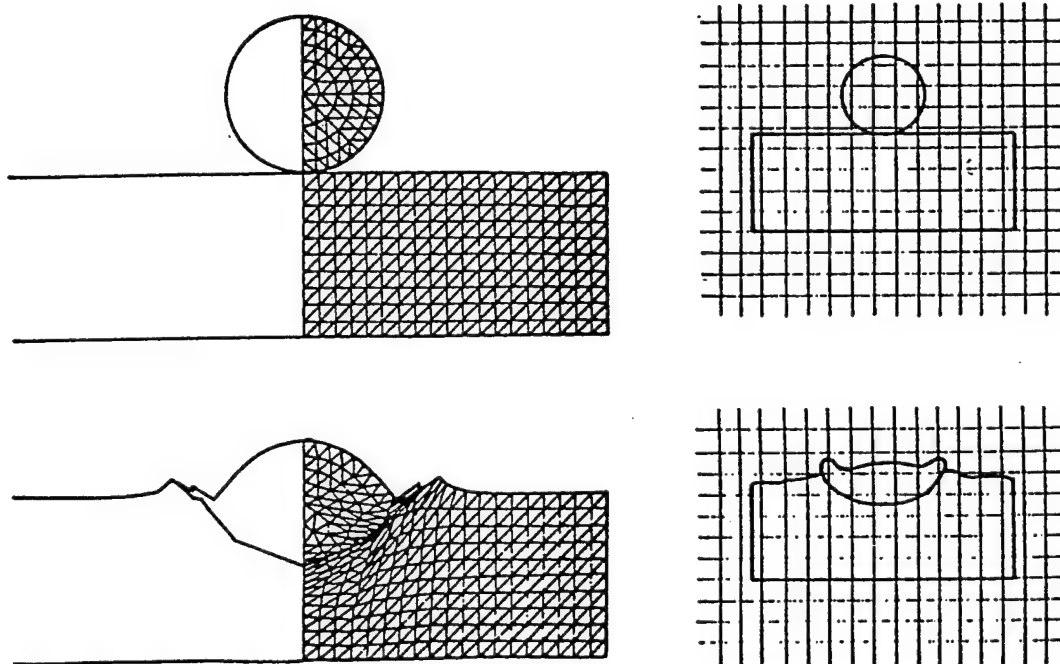


Figure 3.1: Examples of a) Eulerian and b) Lagrangian computational grids [13].

3.1.2 Constitutive Models

Constitutive equations, or models, are used to describe the high-strain-rate deformation of materials [2]. The stress in such a case can be expressed as a function of strain (ϵ), strain rate ($\dot{\epsilon}$), and temperature (T):

$$\sigma = f(\epsilon, \dot{\epsilon}, T) \quad (16)$$

Since dynamic deformation is the result of the complex interrelationships between stress, stress state, strain, strain rate, and temperature, the changes in plastic stress in a uniaxial stress state can be written as [31]:

$$d\sigma = \left(\frac{\partial \sigma}{\partial \epsilon} \right)_{\epsilon T} d\epsilon + \left(\frac{\partial \sigma}{\partial \dot{\epsilon}} \right)_{\epsilon T} d\dot{\epsilon} + \left(\frac{\partial \sigma}{\partial T} \right)_{\epsilon \dot{\epsilon}} dT \quad (17)$$

A number of equations have been proposed to describe the plastic behavior of materials subjected to large strains, high-strain-rates and high temperatures [2]. One of the most successful and more commonly used constitutive equation, known as the Johnson-Cook equation, has the form:

$$\sigma = [\sigma_0 + B\epsilon^n] [1 + C \ln \dot{\epsilon}^*] [1 - T^{*m}] \quad (18)$$

where ϵ is the effective (or equivalent) plastic strain, $\dot{\epsilon}^*$ is the normalized effective plastic strain rate, and σ_0 , B , C , n , and m are experimentally determined parameters. The term T^* is the homologous, or normalized temperature and is calculated as:

$$T^* = (T - T_r) / (T_m - T_r) \quad (19)$$

Where T_r is the reference temperature at which σ_0 is measured, and T_m is the melting temperature. The parameters (σ_0 , B , C , n , m) must be determined experimentally by subjecting materials to high-strain-rate mechanical testing over a range of temperatures and strain rates. Since the Johnson-Cook equation has been the most widely used, the parameters are known for a large number of materials. Once the parameters have been determined, the constitutive models can then be validated through experimental testing by comparing experimental values to predicted values.

Though the Johnson-Cook equation successfully predicts the behavior of most materials tested, it was, however, acknowledged that the results for OFHC (oxygen-free high-conductivity) copper did not agree well [80]. Seeking to improve on the Johnson-Cook approach, Zerilli and Armstrong proposed a more sophisticated constitutive relation based on dislocation dynamics. They analyzed the temperature and strain rate response of BCC and FCC materials and noticed significant differences between the two, such as a higher temperature and strain rate sensitivity in BCC metals. The important point made by Zerilli and Armstrong is that each crystal structure will have its own constitutive behavior, which will be dependent on the dislocation characteristics for that particular structure. As a consequence, two constitutive equations were proposed:

$$\text{FCC : } \sigma = \sigma_G + C\epsilon^{1/2} \exp(-C_3T + C_4T \ln \epsilon) + kd^{-1/2} \quad (20)$$

$$\text{BCC : } \sigma = \sigma_G + C_1 \exp(-C_3T + C_4T \ln \epsilon) + C_5 \epsilon^n + kd^{-1/2} \quad (21)$$

The main difference between the two equations lies in the fact that the plastic strain is uncoupled from strain rate and temperature for BCC metals. Figure 3.2 shows a comparison of the Zerilli-Armstrong and Johnson-Cook predictions with the

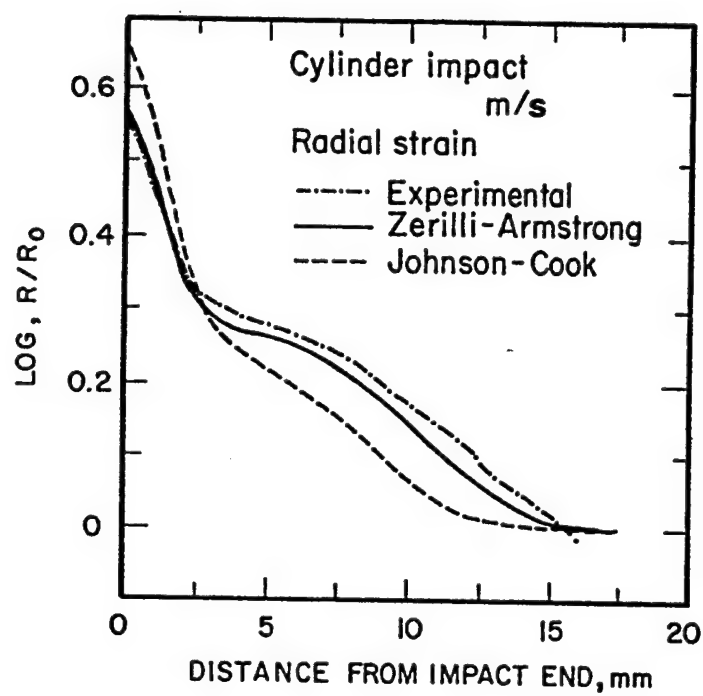


Figure 3.2: Profile of Taylor test specimen (iron, impacted at 221 m/s) plotted as radial strain vs. distance; the experimental result is compared with the Johnson-Cook and Zerilli-Armstrong constitutive equations [2].

experimental results obtained through a Taylor test (the impact of a cylinder against a rigid wall). For the BCC metal in this case (Fe), the Zerilli-Armstrong model shows a better correlation to the experimental results. For FCC materials, the two models are comparable.

The equations discussed previously are but two of the numerous strength models developed over the years, though they are two of the more sophisticated and most successful treatments available. Along with a constitutive equation, another expression is required to express the relationship between pressure, volume, and internal energy [78]. This is known as an equation of state (EOS) or shock Hugoniot, and it is used to describe the shock response of materials. These are experimentally determined, and the simplest form for the shock Hugoniot is the linear equation:

$$U_s = C_o + SU_p \quad (22)$$

where U_s is shock velocity, U_p is particle velocity, C_o is the sound velocity in the material, and S is an empirical parameter. EOS data have been determined for most pure metals and most of the important alloys (e.g. 304 stainless steels, Al alloys, etc.).

3.2 Modelling of Ballistic Impact

The penetration of a finite thickness target (plate) by a kinetic energy projectile is a complex process that has not been solved analytically yet; as a consequence, numerical simulation tools are primarily employed for the purpose of furthering penetration mechanics. The penetration of metallic targets using numerical simulations (through a

variety of hydrocodes) has been studied fairly extensively during the past decade. The validation technique generally involves establishing a relationship between the residual properties and the initial conditions of the problem, such as rod and target geometries, and rod striking velocity, for example [81]. The impact of a finite thickness target has been a difficult endeavor for hydrocode analysis as discussed by Anderson and Bodner [82], particularly for the perforation part of the problem, which depends critically upon having material failure in the code [83].

Anderson et al. have utilized computer modeling in numerous studies to amass data on many different aspects of penetration mechanics. Included in these works are numerical simulations to determine target resistance into semi-infinite targets [82], simulations to quantify strain-rate effects [81], and simulations to examine penetration as a function of impact velocity [84]. J. E. Reaugh has performed computer modelling to study the effect of target steel strength on perforation by a WA [83], as well as the effect of adiabatic heating on penetration by WA and DU alloy rods [84], among many other studies.

While the emphasis of these studies centers on the macromechanical aspects of penetration, the micromechanical behavior of the materials has been severely neglected. Observations of material microstructure for penetration-related phenomena could provide a basis for further refinement of computer hydrocodes as well as penetration theories [29]. Yet, not enough work has been performed to better understand and characterize material behavior in the high-strain-rate regime for the purpose of obtaining realistic computational results. In studies involving the numerical modeling of long-rod

penetration/perforation, it is usually common to find a good agreement between experimental and simulated crater geometries such as penetration depth, residual penetrator length and crater diameter. Validation of a hydrocode rarely, if ever, takes into account the microstructural changes induced by the high-velocity, high-strain-rate deformation. This might be accomplished by comparing the residual stress profiles of the simulated event to the experimental residual microstructure and corresponding hardness profile through the empirical relationship $\sigma \cong H / 3$, where σ is yield stress and H is hardness.

Chapter 4

RESEARCH OBJECTIVES

The focus of this study will center on two target materials, OFHC copper and 7039Al, subjected to ballistic impact and perforation by a tungsten-alloy projectile. A thorough analysis and comparison will be made of the dynamic behavior of the residual targets as a consequence of impact. The impacting kinetic energy penetrator microstructures, etc., will also be examined. Though both target materials show a similar crystal structure (FCC), their initial microstructures, densities and yield strengths vary considerably. As a result, there are significant differences in the deformation-related features of both target materials.

Observations of perforation-related microstructures in ballistically impacted OFHC Cu have been documented by Huang et al. [76] and Rivas [77], and the microstructure of 7039Al documented by Huang et al. [76] in a cursory investigation, though an in-depth and complete analysis is lacking in the literature. The effort at hand will attempt to resolve the fundamental issues associated with the impact behaviors of each of the target materials, which are strikingly different. A systematic investigation, utilizing optical and transmission electron microscopy, as well as a microhardness tester, will be conducted to pinpoint the mechanisms responsible in each case.

In concurrence with the experimental research, a computer hydrocode (AUTODYNTM-2D) will be used to simulate the perforation events in an effort to replicate actual results.

The results garnered from this research will be applied towards the validation of the computer hydrocode in numerically simulating the impact of an OFHC copper and 7039 aluminum target by a tungsten-alloy projectile. Specifically, experimental microhardness profiles will be compared to the simulated yield stress profiles, based on the empirical relationship $\sigma_y \cong H/3$, to more accurately predict microstructural changes in the target due to perforation. A comparison of actual and simulated geometries of the residual targets will also be performed in the hopes of contributing to the refinement of hydrocodes.

This dissertation will attempt to accomplish the following:

- ◆ A meticulous comparison of both macrostructure and microstructure of the WHA impacted aluminum and copper targets using metallography, TEM and microhardness testing.
- ◆ A differentiation of the fundamental failure mechanisms responsible for the dynamic behaviors of the two FCC materials.
- ◆ The construction of microhardness maps for both targets to separate zones of differing hardness as a result of microstructural changes.
- ◆ Computer simulations of the ballistic impact events for both materials using the AUTODYN hydrocode.
- ◆ Establish a validation of the hydrocode through perforation geometry and residual stress mappings (where it can be related to residual hardness maps constructed experimentally in an attempt to correlate microstructural issues with the computer simulations).

In effect, this dissertation represents a modern example of the emerging field of computational materials science and engineering.

Chapter 5

EXPERIMENTAL PROCEDURES

The experiments performed in this study were focused on two target materials, a 7039 aluminum alloy and an Oxygen-Free High-Conductivity (OFHC) copper, both impacted by a tungsten-heavy alloy (WHA) projectile. Following impact, the targets were sectioned and analyzed through the following techniques: optical microscopy, microhardness testing, scanning electron microscopy (SEM) and transmission electron microscopy (TEM). The results were then used to provide a basis for the microstructural validation of computer simulations, generated through the AUTODYNTM hydrocode.

5.1 Target Materials

The properties of both 7039Al and OFHC Cu have been listed in Table 5.1 [87,88]. The properties of aluminum have been measured from random plates used at the U.S. Army Research Laboratory (ARL) over the past ten years [87]. The development of 7039Al to military specification by the Al industry occurred as a result of the evolution of aluminum armor during World War II. The alloy itself has demonstrated improved protection against kinetic energy ammunition, and has since become the standard aluminum armor for the Army.

According to the designation system for wrought aluminum, adopted by the American Standards Association, a 7XXX series indicates an aluminum alloy with zinc as a major alloying element [89]. The 0 in 7039 indicates the number of impurities that are controlled, and the last two digits serve to identify the different alloys in the group as registered.

The thick, rectangular aluminum target plate (of 7.6cm thickness) was arranged in a 2-layer configuration before impact; the first layer being composed of an Al-Mg alloy plate with a finite thickness of 3.9cm, the second layer was composed of the 7039Al plate. Copper, on the other hand, was monolithic in configuration and cylindrical in shape with a plate thickness of 3.5cm.

Table 5.1

Comparison of Experimental Target Properties

PROPERTIES	7039Al	OFHC Cu
Composition	4.0%Zn, 2.8%Mg, 0.27%Mn and 0.2%Cr	99.99% Cu
Crystal Structure	FCC	FCC
Density (g/cm^3)	2.7	8.9
Stacking Fault Energy (mJ/m^2)	~78	~160
Melting Temperature ($^{\circ}\text{C}$)	638	1083
Yield Strength (GPa)	0.45	0.221
Tensile Strength (GPa)	0.48	0.27
Modulus of Elasticity (GPa)	75	124
Elongation (%)	13	55

5.2 Ballistic Impact Set-Up

The lab-scale WA projectile used in this study was composed of 93%W, 4.9%Ni, and 2.1%Fe (by wt.%). The cylindrical penetrator, with a hemispherical nose, consisted of 93% W, 4.9% Ni and 2.1% Fe by weight and had a density of 17.6 g/cm^3 . The diameter of the projectile was 0.78 cm and the length 7.8 cm, effecting an L/D ratio (length-to-diameter) of 10. The nominal properties of WHA are as follows: density- 17.6 g/cm^3 , yield strength – 1.089-1.169 GPa, ultimate strength – 1.131-1.213 GPa, and elongation – 5.8-10.6% [90]. A macrograph of the projectile along with an optical micrograph of its starting microstructure, consisting of hard tungsten particles in a ductile Ni-Fe matrix, can be seen in figure 5.1(a) and (b).

The penetrator was fired from a laboratory gun consisting of a Bofors' 40-mm gun breech assembly with a custom-made 40-mm smoothbore barrel positioned approximately 3 m in front of the targets. Impact was achieved at a striking velocity of 1.5 km/s. The geometry of both projectile and target are shown in figure 5.2.

High-speed (flash) x-ray photography was used to capture and measure various parameters at various times during the impact process. These include projectile pitch, yaw, striking velocity, residual rod length and residual rod velocity. Flash radiography is accomplished by positioning 2 pairs of orthogonal x-ray tubes in the vertical and horizontal planes along the shot line in front of the target (as illustrated in the schematic of figure 5.3). An additional pair of x-ray tubes was positioned in the horizontal plane along the shot line behind the target.

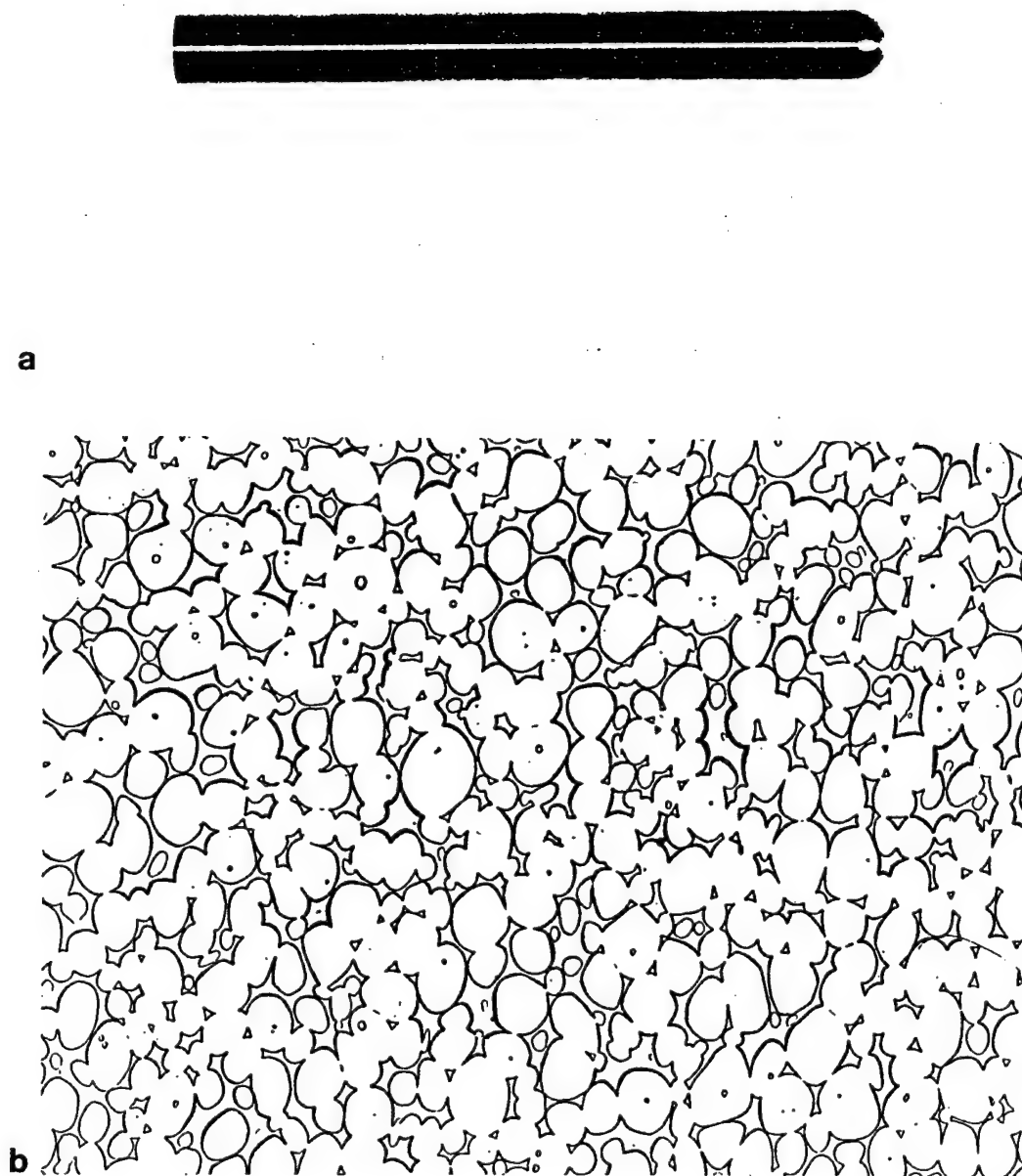


Figure 5.1: a) Macrograph of a WHA (tungsten-heavy alloy) right-circular cylinder projectile. b) Microstructure of WHA, consisting of tungsten particles embedded in a Ni-Fe matrix.

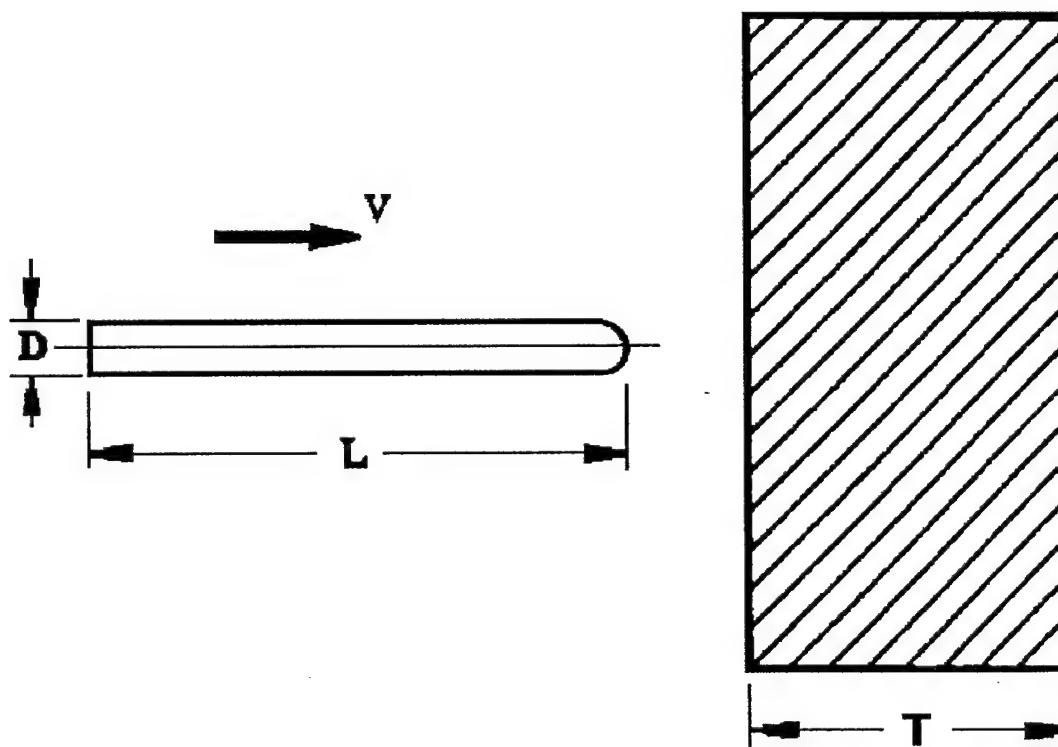


Figure 5.2: Geometrical parameters of target and projectile prior to impact.

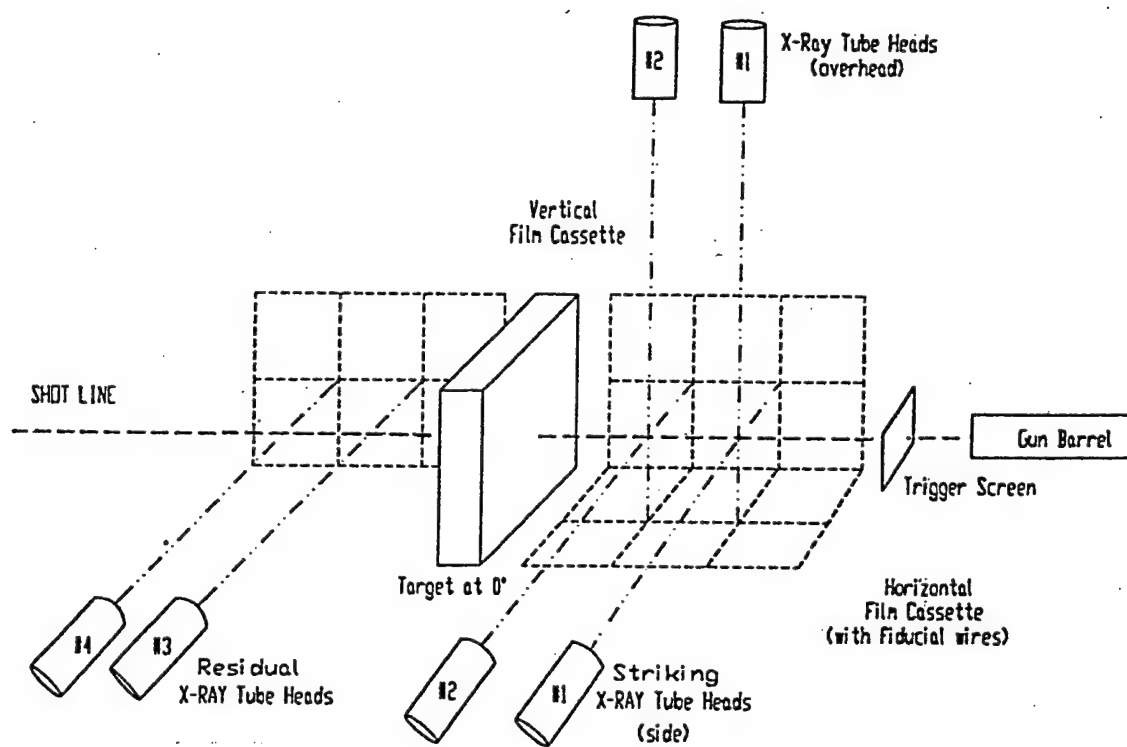


Figure 5.3: Experimental set-up for high-speed (flash) x-ray radiography [25].

5.3 Metallography

5.3.1 Macrography

Low magnification photography was taken of both targets before and after sectioning in preparation for optical microscopy. The macrographs were obtained through a Polaroid MP4+ instant camera using Polaroid type 55 film. Figures 5.4 and 5.5 reveal the surface views of the perforation entrance and exit for copper and 7039Al, respectively. The targets were sectioned in half to expose the penetration channels as shown in figure 5.6. Since 7039Al had been arranged in a two-layer configuration, the half-sections of both layers have been included in figure 5.7. The first layer consists of a softer aluminum-magnesium alloy, the second consists of the 7039 alloy.

5.3.2 Micrography

Since the residual penetration channel is cylindrical in nature, due to the geometry of the projectile, axial symmetry can be assumed for the material surrounding it. Therefore, the surface along one side of the penetration channel in the half-section of each target was chosen for microscopic analyses. The specimens were then put through a sequence of polishing steps for producing a flat, highly reflective surface.

This began with grinding, using variable speed polishing wheels, SiC abrasive papers from rough to fine mesh sizes (120-800 grit), and water as a lubricant and coolant. Next, fine polishing was achieved using a polishing cloth and alumina slurry in two particle sizes, 1 μm and 0.3 μm . As the surface is highly reflective and scratch-free at this point, it is then chemically etched to bring out contrast and microstructure. The

**a****b**

Figure 5.4: Surface view of perforation a) entrance and b) exit in the OFHC copper target perforated by a tungsten-alloy rod at a velocity of 1.5 km/s.

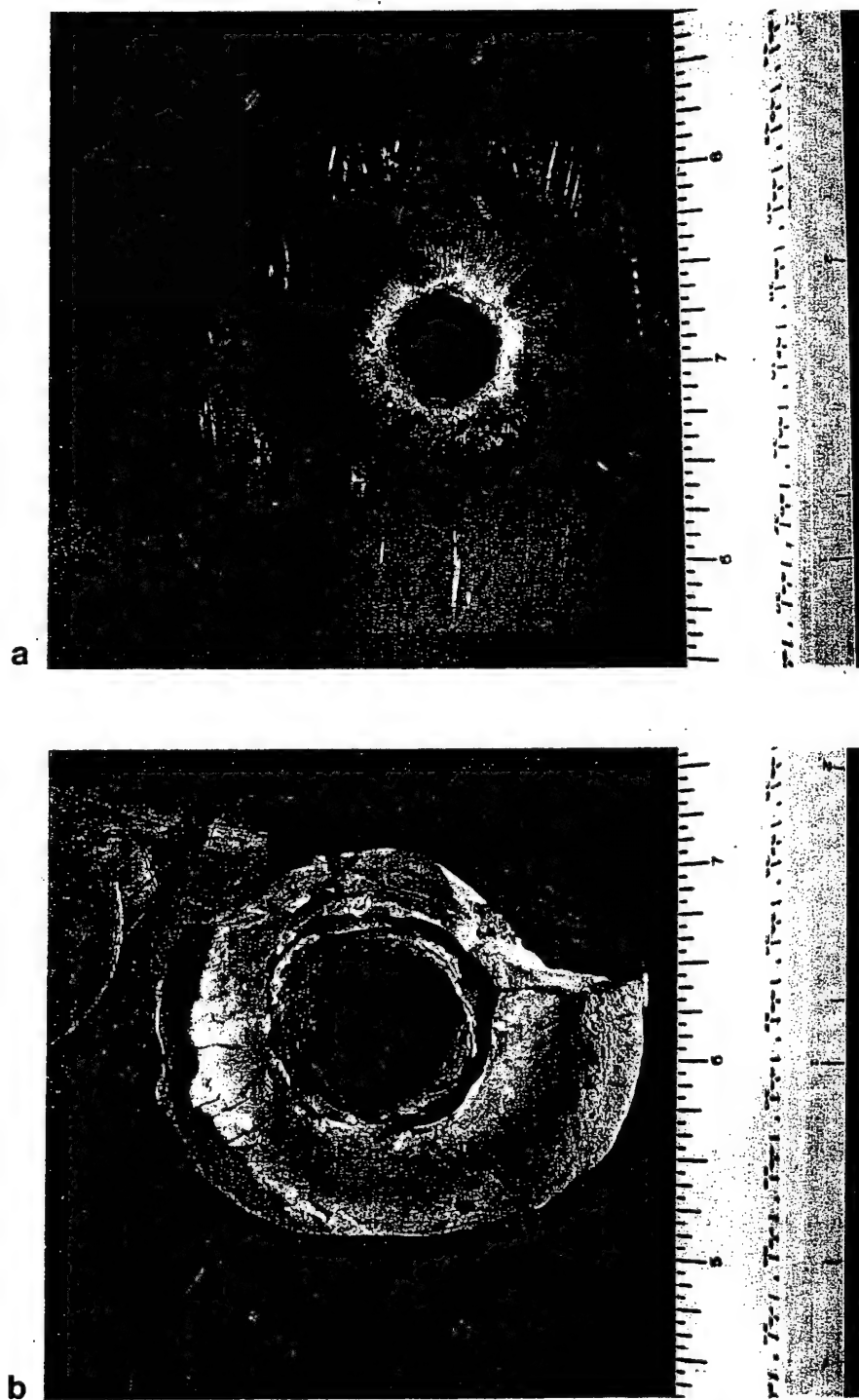
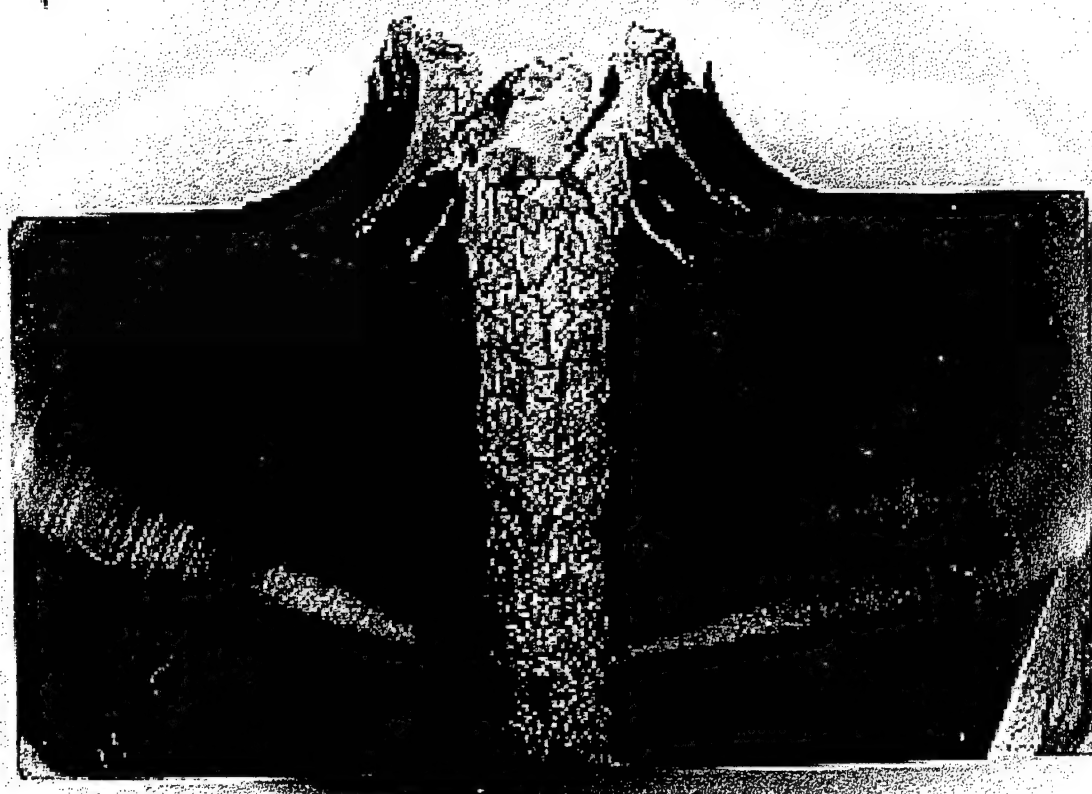
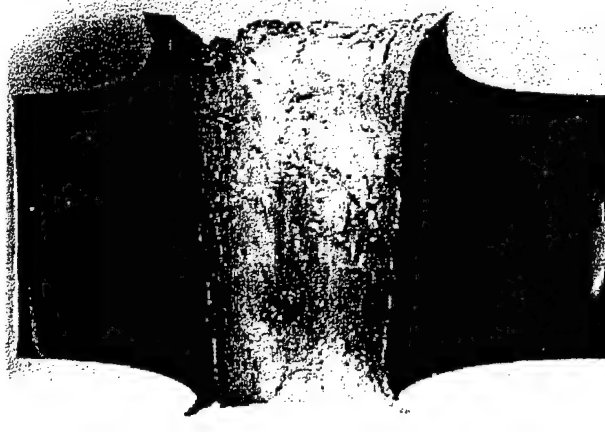


Figure 5.5: Surface view of the perforation a) entrance and b) exit in the 7039Al target plate impacted by a WHA rod at 1.5 km/s impact velocity.



a



b

Figure 5.6: Half-section views of the a) 7039 aluminum and b) copper target, revealing the penetration channels.

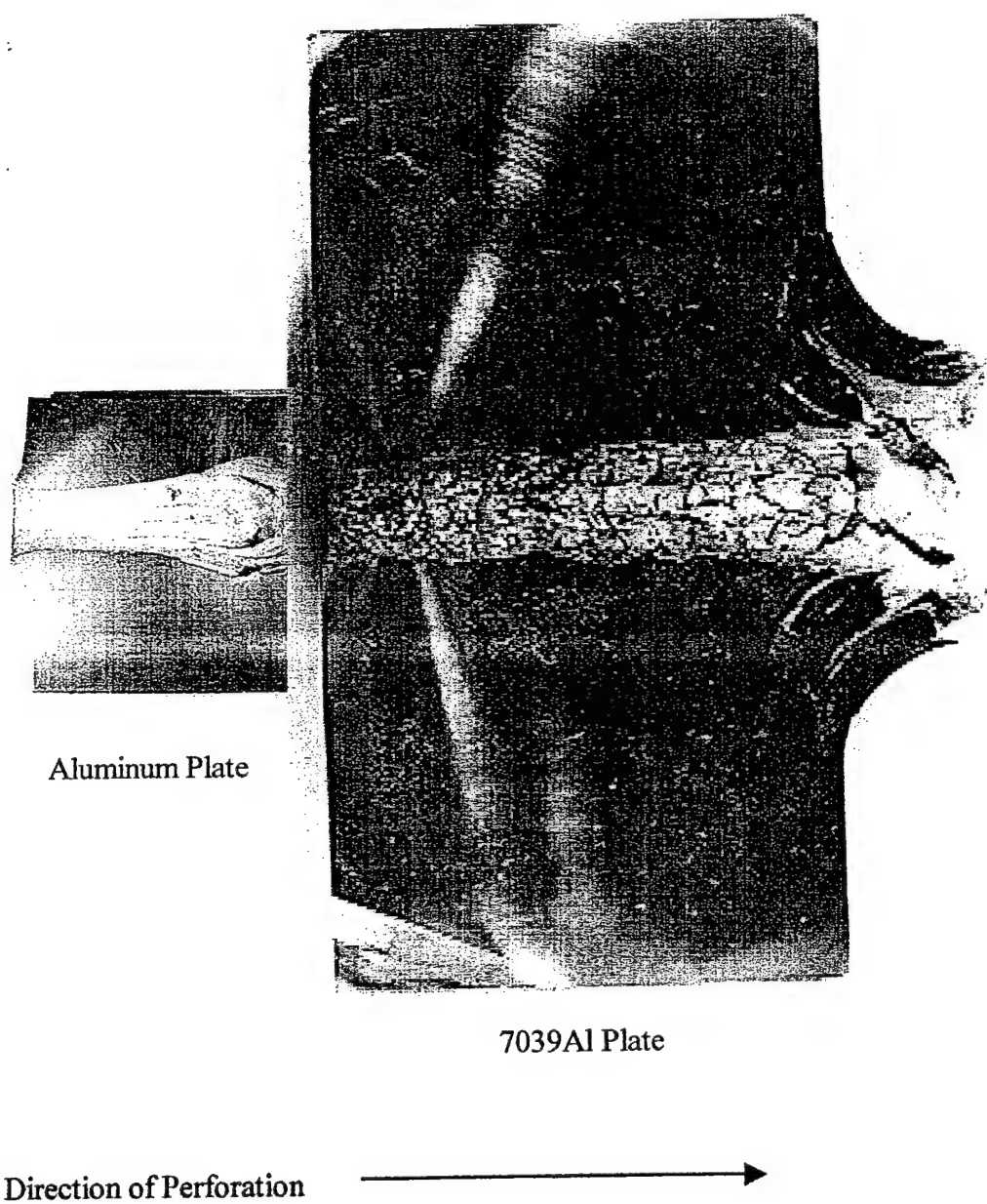


Figure 5.7: Half-sections of the residual al-mg alloy pre-target (front block), and the 7039Al primary target in a two-layer impact arrangement.

etchant for 7039Al is referred to as a modified Keller's reagent and consists of 2ml HF, 3ml HCl, 20ml HNO₃ and 175ml H₂O. Copper required an etchant containing 2g K₂Cr₂O₇, 5ml H₂SO₄, 4ml NaCl (saturated solution) and 100ml H₂O. The specimens were then rinsed in water after etching, cleansed in methanol, and then dried using an air blast. A LEICA MEF4M optical microscope was used in obtaining micrographs.

5.4 Microhardness Testing

Following optical microscopy, the specimens were polished again to produce a smooth, etch-free surface in preparation for microhardness testing. Vickers microhardness data were collected for both copper and aluminum targets using a Shimadzu HMV-2000 microhardness tester with a diamond-tipped indenter. A load of 100gf was employed in testing 7039Al, and 50gf was used for testing OFHC copper. In both cases, the load was held in contact with the surface for 10s.

A hardness number for each reading is calculated in the following manner: during application of the load, the indenter leaves a diamond-shaped impression on the surface of the sample, following removal of the load both diagonals of the diamond are measured and the average value is used to calculate the Vickers hardness number (HV) through the equation

$$HV = 2 L \sin(\alpha/2) / d^2 = 1.8544 L / d^2 \quad (23)$$

Where d is the mean diagonal (mm), L is the load in kgf and α is the angle between the opposing faces of the diagonal (136°).

In indentation hardness about two-thirds of the mean contact pressure is hydrostatic pressure, while the remaining one-third pressure produces plastic flow [91]. Thus the mean pressure P between the metal and the indenter is three times the yield stress σ_y :

$$\frac{1}{3} P \approx \sigma_y \quad \text{or} \quad P \approx 3 \sigma_y \quad (24)$$

The value of the Vickers hardness number (VHN) is only slightly less than P , and will therefore have the following relationship to yield stress (σ_y):

$$\text{VHN} \approx 3 \sigma_y \quad (25)$$

Maps of the differing zones of hardness were created for both target surfaces by taking several lines of readings which spanned the entire length of the penetration channel. Color coding has been used to distinguish between the different zones. The color scheme chosen is also similar to that of the residual stress profiles created by the hydrocode, and this allows for a reasonable comparison between the two plots.

Since yield stress is affected by the alteration of microstructure, hardness will likewise be affected proportionally, and it is in this manner that hardness testing is used to relate material changes to property changes.

5.5 Electron Microscopy

5.5.1 SEM Analysis

The topographical fracture features of the penetration channel and heavily deformed rim areas for both the copper and aluminum alloy residual targets were

observed through scanning electron microscopy (SEM). For this purpose, an ISI DS-130 SEM operating at an applied voltage of 20kV was employed.

5.5.2 TEM Characterization

Specimens for observation under the transmission electron microscope (TEM) were prepared by first sectioning a thin layer from the surface of both targets, then grinding that layer down to a 200 μ m thickness. Sample discs of 3mm diameter were punched out of the thin layer and then electro-chemically polished in a Struers Tenupol III jet polisher, until a small hole was detected.

The electron-transparent samples were then analyzed in a Hitachi H-8000 STEM operating at an accelerating voltage of 200kV. Preparation of the jetpolishing solution for copper was carried out in the following manner: 825ml H₂O and 7.5g urea were mixed together and chilled to 0°C, then 375ml ethanol and 75ml propanol were added and the solution was again chilled to 0°C, finally 300ml phosphoric was added and the solution was used at 7-10°C. The samples were polished at a high flow rate (8) until dimpling occurred, at which the flow rate was reduced to 2 until a hole appeared. Electrothinning of the 7039Al samples required a solution of 1400ml methanol and 600ml HNO₃ chilled to -20°C. Polishing occurred at a voltage of 7-12V and a flow rate of 3.

5.6 AUTODYNTM-2D Computer Simulations

Ballistic impact simulations have been performed using the AUTODYNTM Interactive Nonlinear Dynamic Analysis Software released by Century Dynamics in 1986. The AUTODYN programs, or hydrocodes, are general-purpose engineering software packages that use finite difference, finite element, as well as finite volume techniques to solve a wide variety of non-linear problems in solid, fluid and gas dynamics.

The phenomena to be studied with such a program can be characterized as highly time-dependent with both geometric non-linearities (e.g. large strains and deformations and softening, multiphase equations of state), and material non-linearities (e.g. plasticity, failure, strain-hardening and softening, multiphase equations of state) [80]. Typical defense industry applications for AUTODYN include:

- Impact / Penetration
- Armor and anti-armor systems
- Kinetic energy and chemical energy devices
- Underwater shock and explosions

The various numerical processors available in AUTODYN include:

- Lagrange processor for modeling solid continuum and structures
- Euler processors for modeling fluids, gases and large distortion
- ALE (Arbitrary Lagrange Euler) processor for specialized flow models
- Shell processor for modeling thin structural elements

- SPH (Smoothed Particle Hydrodynamics) processor for large strain / large deformation problems

A notable feature of the software is that it allows coupling between the processor types, i.e. alternative numerical processors can be selectively used to model different regions of a problem. Utilizing a more suitable processor for each region allows for a more accurate solution to the problem.

The software's interactive graphics environment allows the user to monitor results during the execution of a simulation, and also to obtain a detailed interrogation and display of the results during post processing. Figure 5.8 shows one such display, a material status plot, for the impact of an RHA (rolled homogenous armor) plate. A built-in database of parameters is provided with the program, consisting of over 250 different material models, which include combinations of various equations of state with constitutive and failure models.

An Eulerian numerical processor was chosen to model the perforation of ductile OFHC Cu by the WHA projectile. Both the Euler and SPH processor was used to model the more brittle deformation behavior of the 7039Al target. SPH, a relatively new processor still under development, is a gridless, Lagrangian method using a pseudo-particle interpolation method to compute smooth hydrodynamic variables [93]. Unlike conventional Lagrangian techniques, SPH avoids mesh tangling and is therefore much more robust in its treatment of problems with large material distortions. The Johnson-Cook constitutive model was applied to the WHA projectile (for all simulations) and the 7039Al target, while the Zerilli-Armstrong model was applied to the OFHC copper.

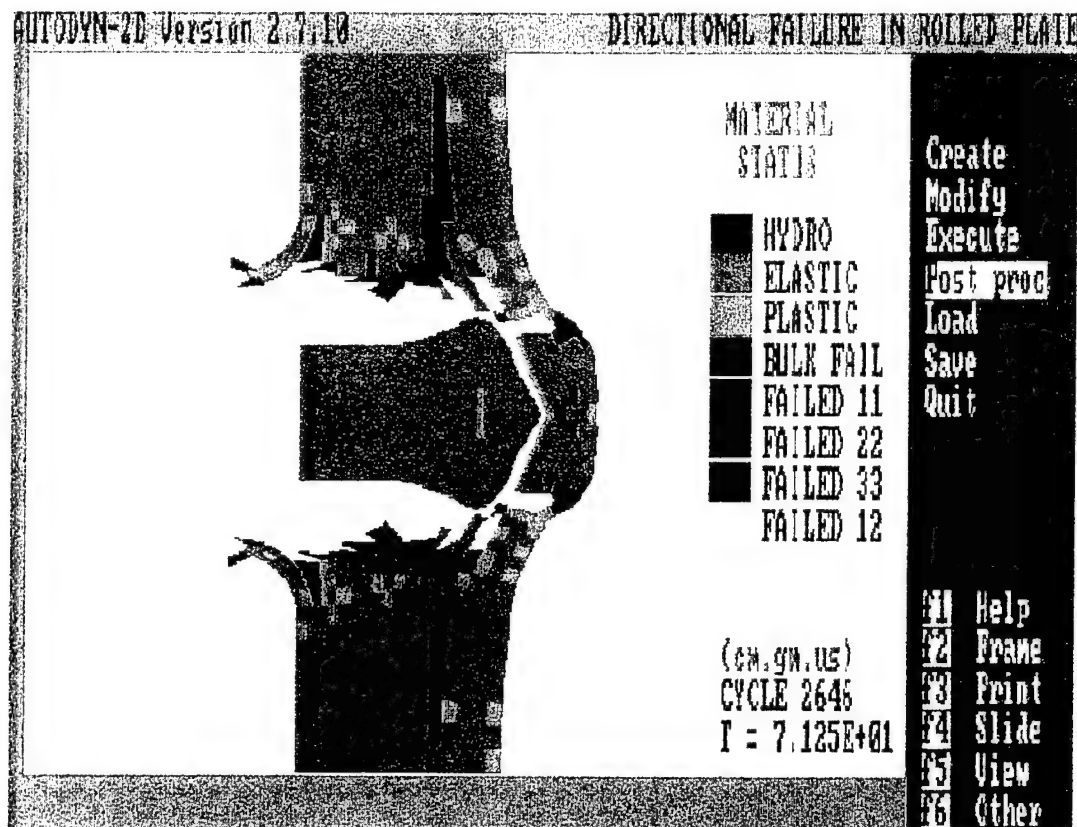
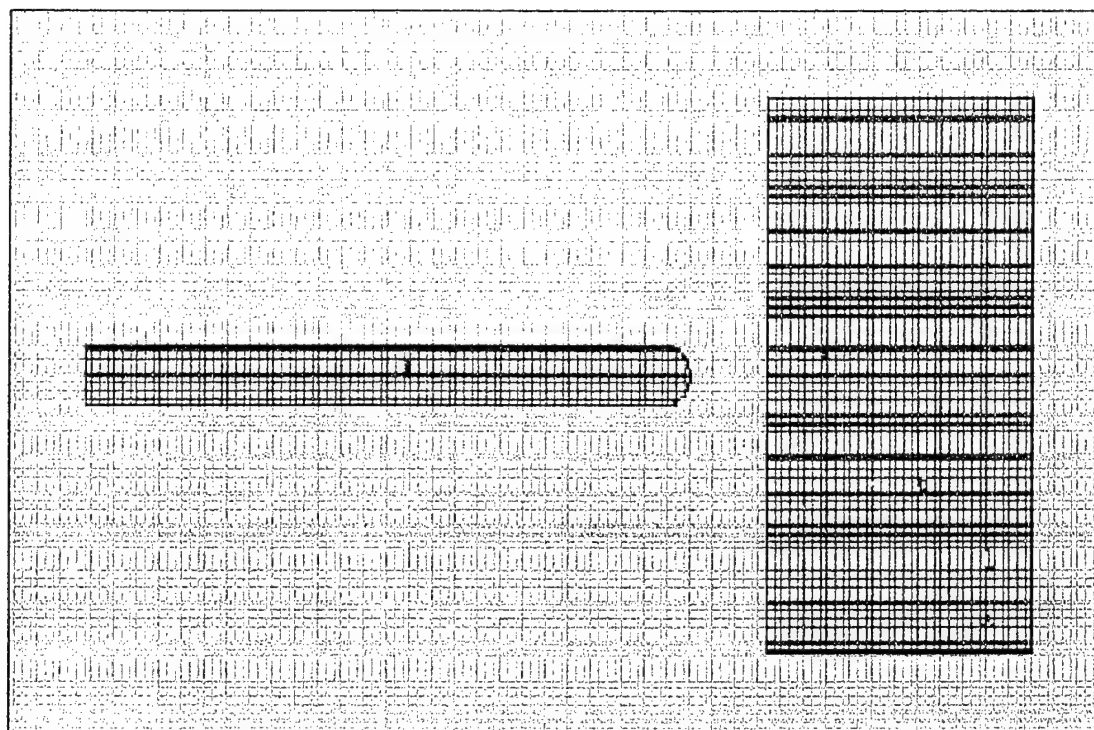


Figure 5.8: AUTODYN material status plot for the impact of an RHA plate by a WHA rod [87].

A 'Bulk' failure model, which is generally used for ductile failure, was chosen for the copper simulation. This model considers the material to behave in an isotropic manner and allows for failure when the effective plastic strain exceeds a predefined value [80]. For the simulation of aluminum in an SPH processor, a 'Principal Stress' failure model was used, while the "Hydrodynamic Tensile Limit" model was applied to simulations using an Euler processor. The Principal Stress model is used to model failure initiation which is directionally dependent, and is very appropriate for failure modes such as spalling, plugging, delamination, and petalling. The Hydro model can be used to model spalling or cavitation, and a constant hydrodynamic tensile limit is specified for the material.

The initial set-up plots for both the copper and aluminum simulations can be seen in figures 5.9 - 5.11. Following the completed simulation, residual yield stress profiles generated by the code were matched with measured microhardness plots in an effort to provide a microstructural-based validation of the hydrocode. Additional input parameters for the copper and aluminum simulations have been listed in the appendix.



Y
 X
 Axis
 3.300E100
 A.1 (cm, g, m, s)
 CYCLES
 1 = 0.000E+00

Figure 5.9: Set-up plot for the computer simulation of impact in the copper target by a WHA long-rod projectile at 1.5 km/s impact velocity.

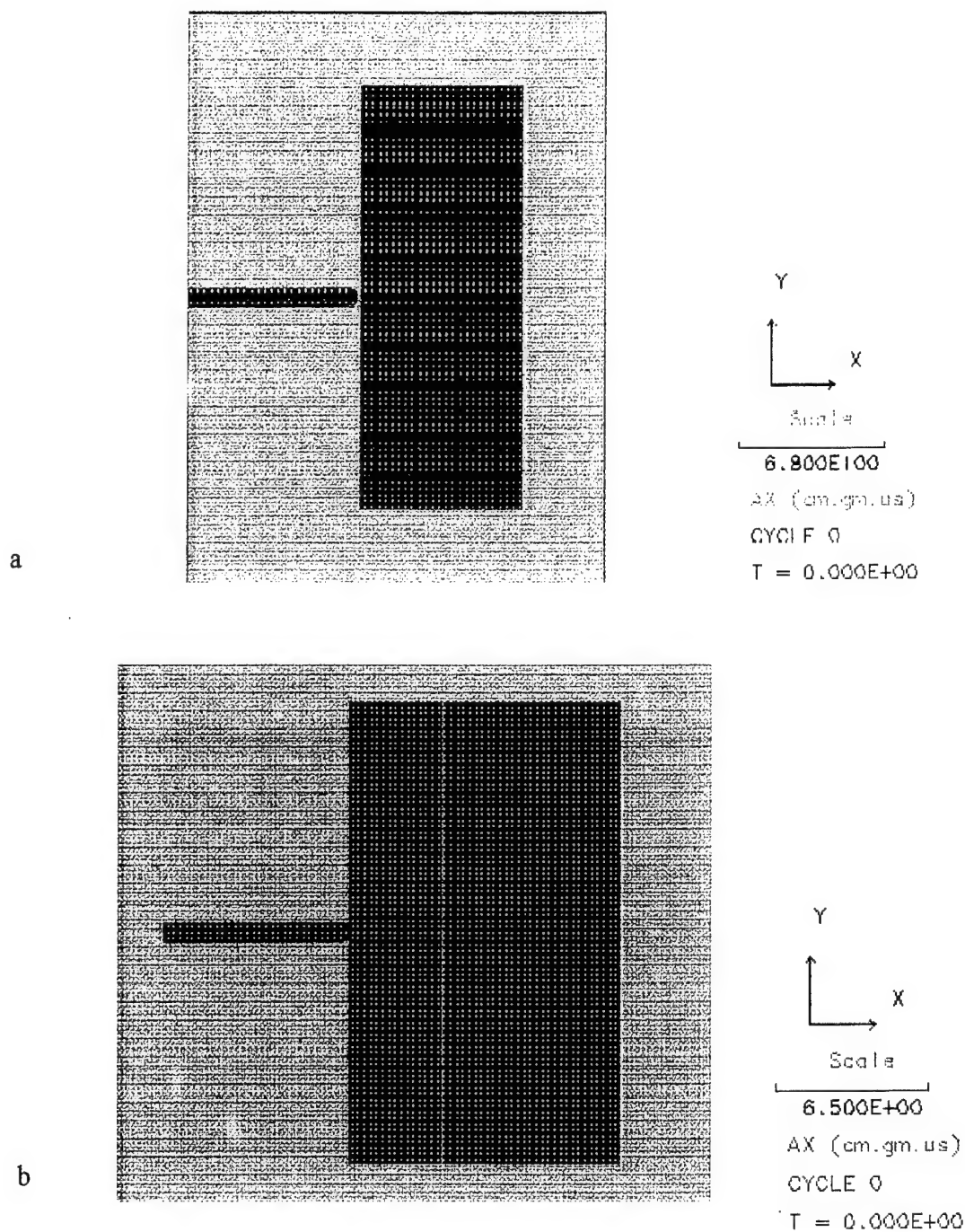


Figure 5.10: Initial set-up plot for the computer simulation of the perforation of 7039Al by a WHA long-rod projectile in the a) monolithic and b) two-layer configuration in an Euler subgrid.

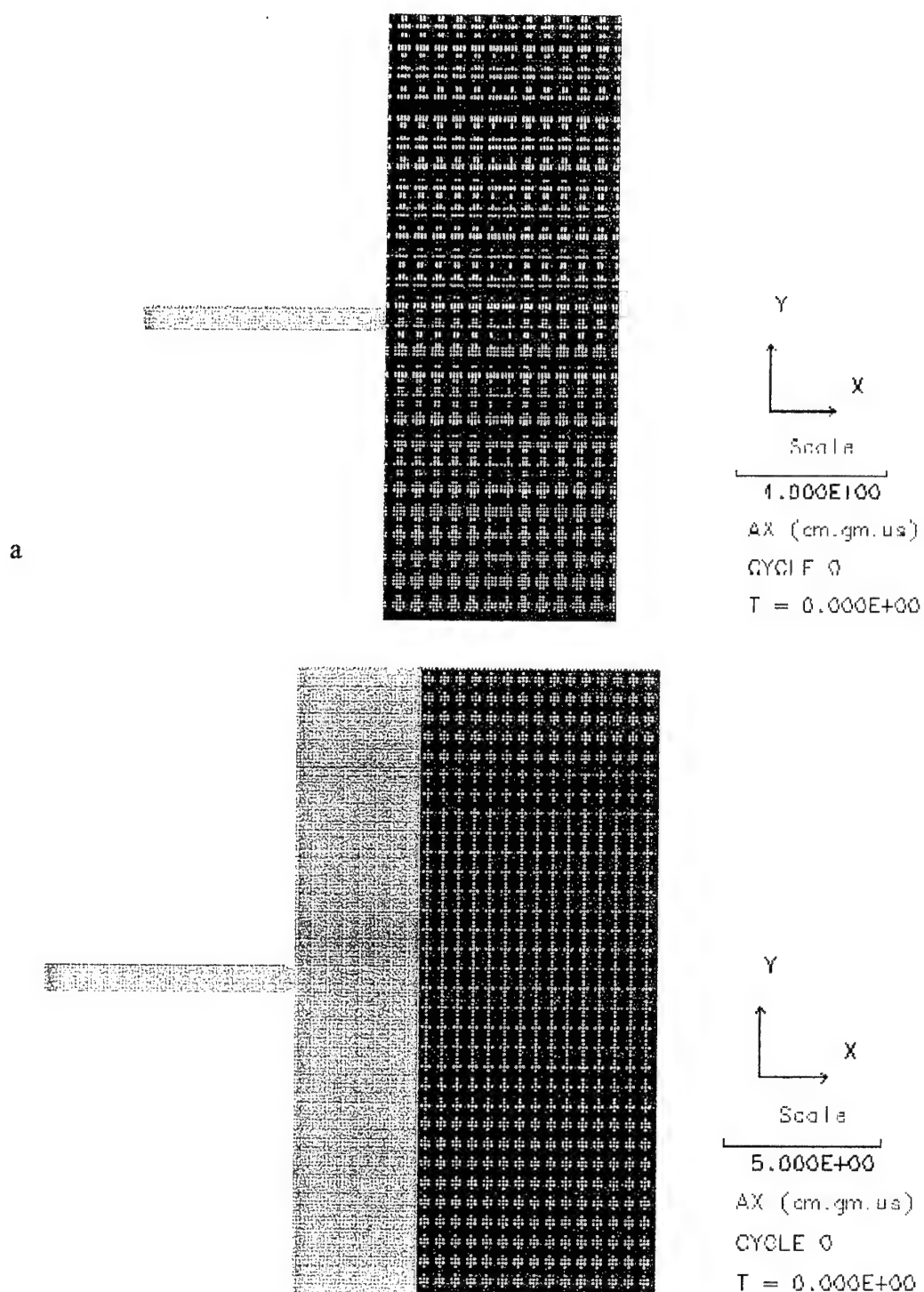


Figure 5.11: Set-up plot for the computer simulation of aluminum impact in the a) monolithic and b) two-layer configurations using the SPH subgrid.

Chapter 6

RESULTS AND DISCUSSION

The ballistic penetration/perforation of a thick metal target (or plate) is a very complex process involving many variables inherent in both target and projectile. Though many theories abound to explain the phenomena, the microstructural aspects of failure are generally ignored. An analysis at the different levels of material structure may provide invaluable information concerning the high-strain-rate failure of impacted targets, as well as contributing to the understanding of penetration mechanics. Likewise, an analysis of this nature can provide additional variables with which to validate computer hydrocodes, other than a geometry-based validation which is currently the standard practice. The results that follow include a systematic microstructural characterization of both an Oxygen-Free High-Conductivity (OFHC) copper target, and a 7039 aluminum target. The residual mechanical properties will be applied towards the validation of the AUTODYNTM hydrocode in simulating the realistic behavior of both target materials.

6.1 Macrostructural Failure Features

At the macrostructural level, the mode of deformation of the impacted copper and aluminum targets appears to be completely different. The penetration channels of the copper and aluminum half-sections are shown in figures 6.1 and 6.2, respectively. In

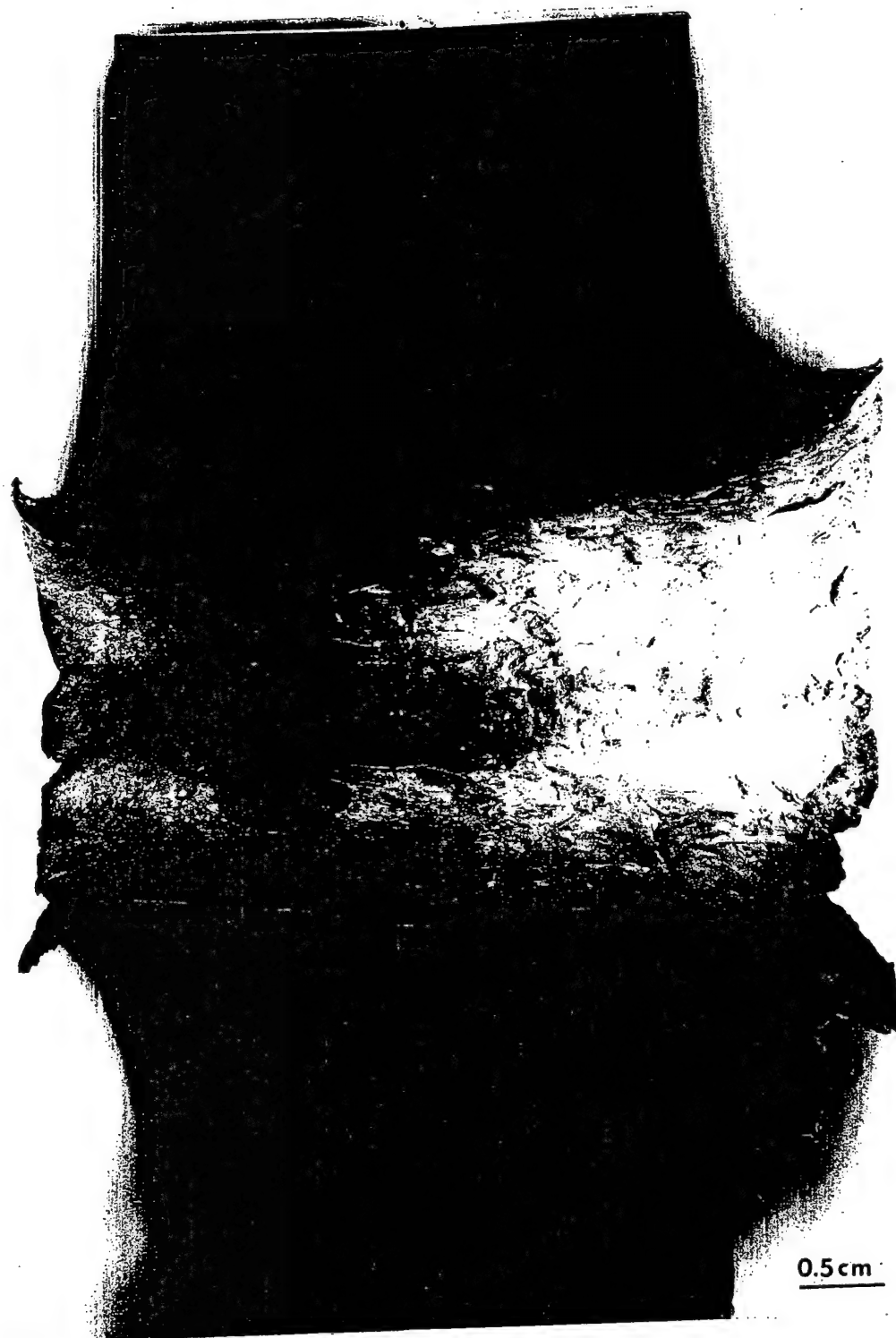


Figure 6.1: Enlarged half-section of the impacted copper target revealing the penetration channel.



Figure 6.2: Half-section of the impacted 7039Al plate; target is enlarged to show the fracture characteristics of the penetration channel.

comparison, the penetration channel of copper is much smoother and wider than that of the aluminum, the diameter at the entrance being three times the width of the projectile. There is also a rim formation at both the entrance and exit areas, indicative of ductile failure. These rim structures are similar to those observed in the hypervelocity impact cratering of OFHC copper by spherical aluminum projectiles [30,53,70-73]. The 7039 aluminum penetration channel, on the other hand, exhibits greater irregularity and is characterized by extensive brittle cracking and the formation of large shear lips where complete perforation of the target occurs. Further, there appears to be a large cavity at the exit point before the final shear lips, indicating the likelihood of spall fracture before final breakout of the projectile.

6.1.1 SEM Analysis

The scanning electron microscope (SEM) was utilized in the investigation of fracture features along the penetration channel wall of both target materials. The most striking observation from the copper crater was the presence of particles along the entire length of the penetration channel, more noticeably towards the exit half of the channel. Figure 6.3 reveals an area at the exit rim of the channel where some of the embedded particles have been identified by arrows. Chemical analysis through energy-dispersive spectrometry (EDS) showed the particles to consist of W, Ni, and Fe – all components of the WHA projectile.

The presence of the particles can be explained by considering the hydrodynamic process of impact. As the penetrator creates a cavity within the target, material at the head

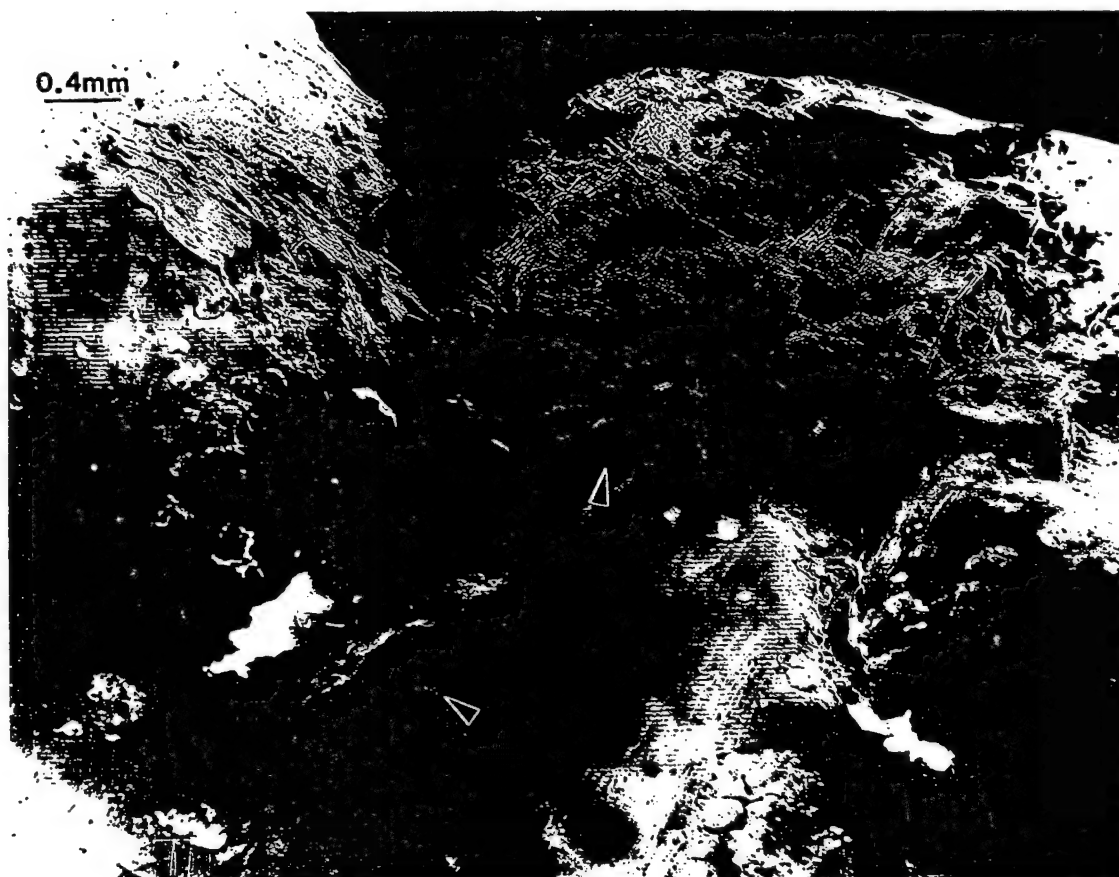


Figure 6.3: SEM view of the numerous WHA erosion products embedded along the crater wall in the region of the exit rim.

of the penetrator will undergo extensive plastic deformation and become 'back-extruded' to form a mushroomed head. Fragments from the eroding projectile head then becomes embedded in the wall of the copper crater as perforation continues. The tungsten-alloy particles are more obvious towards the latter half of the channel where erosion of the penetrator head occurs more readily.

The topography of the 7039Al penetration channel is shown in figure 6.4. The fractured surface is defined by cracking and cleavage-like features (facets), indicative of brittle-like failure. Brittle fracture is characterized by rapid crack propagation, and is devoid of the appreciable gross plastic deformation that characterizes ductile fracture [94]. As 7039Al is a hard material as a result of straining and heavy precipitation, failure under high-strain-rate conditions apparently assumes a brittle nature.

The residual target materials have offered two scenarios to be dealt with, one of ductile failure and the other of brittle-like failure. It is now necessary to observe the internal material structure on a smaller scale to determine possible mechanisms of failure, and whether or not a relationship exists between the two FCC materials.

6.1.2 Properties of Cu and 7039Al

The different failure behaviors of the materials might be better understood by looking at their individual properties. OFHC copper, a 99.99% pure copper, can be considered a rather 'soft' material (in comparison to the aluminum) with a measured microhardness of $\cong 85$ VHN (Vickers hardness number) in the initial, undeformed state. Also, the material has been annealed to produce large, equiaxed grain structures

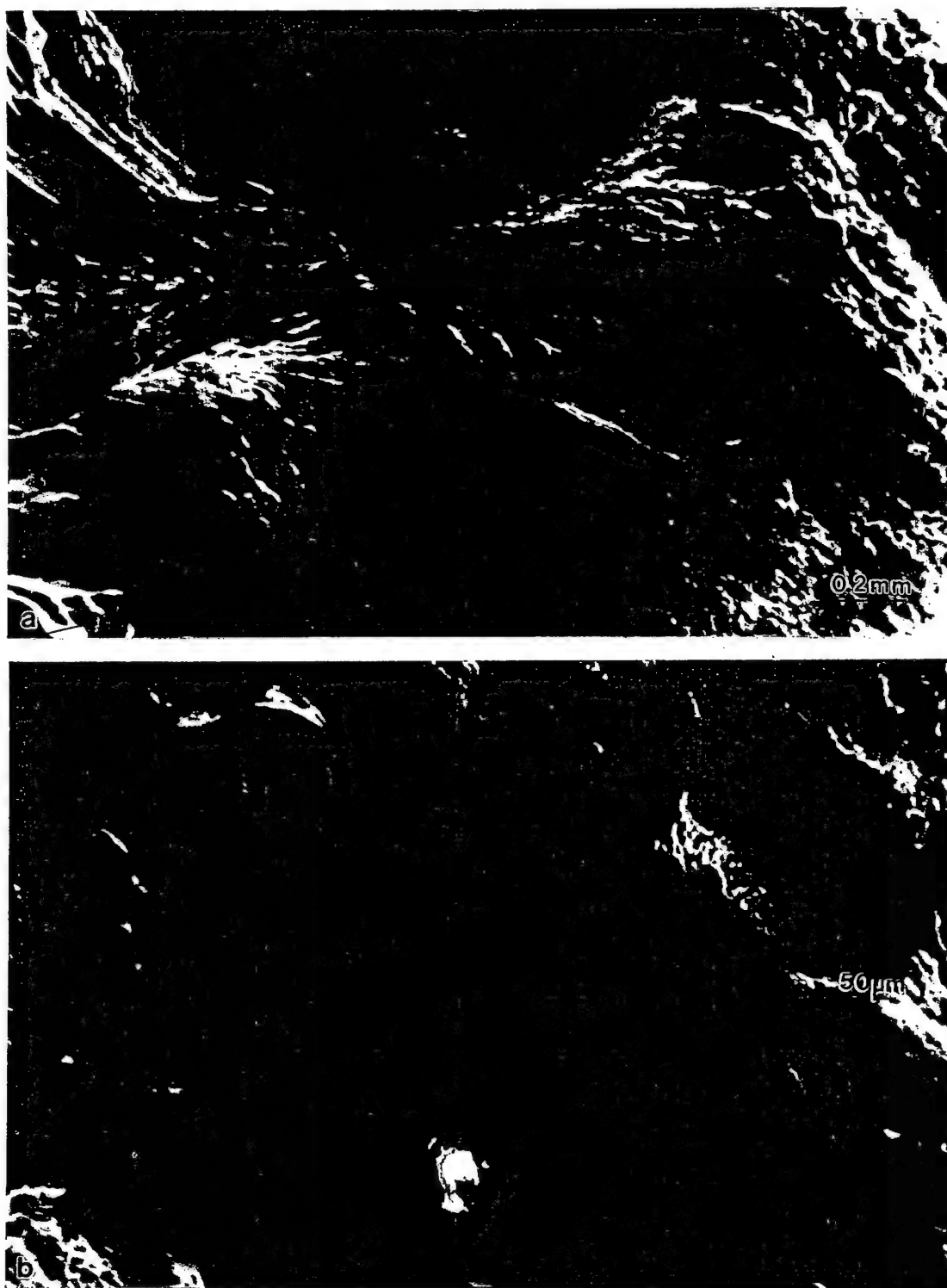


Figure 6.4: SEM views of the fracture features on the crater wall of the 7039Al showing a) cleavage as well as b) ductile dimpling.

(microstructure will be presented in the proceeding sections) contributing to the low hardness and yield stress (0.27 GPa). The composition of 7039 aluminum consists of Al, Zn, and Mg; this wrought material has been work-hardened (or strain-hardened) to a maximum limit, resulting in a yield stress of 0.48 GPa. Its hardness value (140 VHN) is one and a half times that of copper. Consequently, this material is very highly work-hardened; perhaps there is a saturation of work-hardening which does not allow for much, if any, additional slip or dislocation motion to accommodate the plastic flow involved in the penetration process.

Other differences lie in density and melting temperature. The density of copper (8.6 g/cm^3) is three times that of aluminum (2.7 g/cm^3), while its melting temperature (1356 K) is nearly twice as high as that of aluminum (877 K). The one similarity that exists between the two is the FCC (face-centered cubic) crystal structure inherent in both materials.

6.2 Microstructural Examination of OFHC Cu

6.2.1 Initial Microstructure

Copper can be considered an ideal material in the study of dynamic impact since its shock behavior has been well documented. Also, its microstructure is sensitive to pressure changes, and can be easily revealed metallographically [95].

Figure 6.5(a) reveals the microstructure of OFHC copper in its original state. The micrograph shows typical characteristics of annealed, high-purity copper such as large,

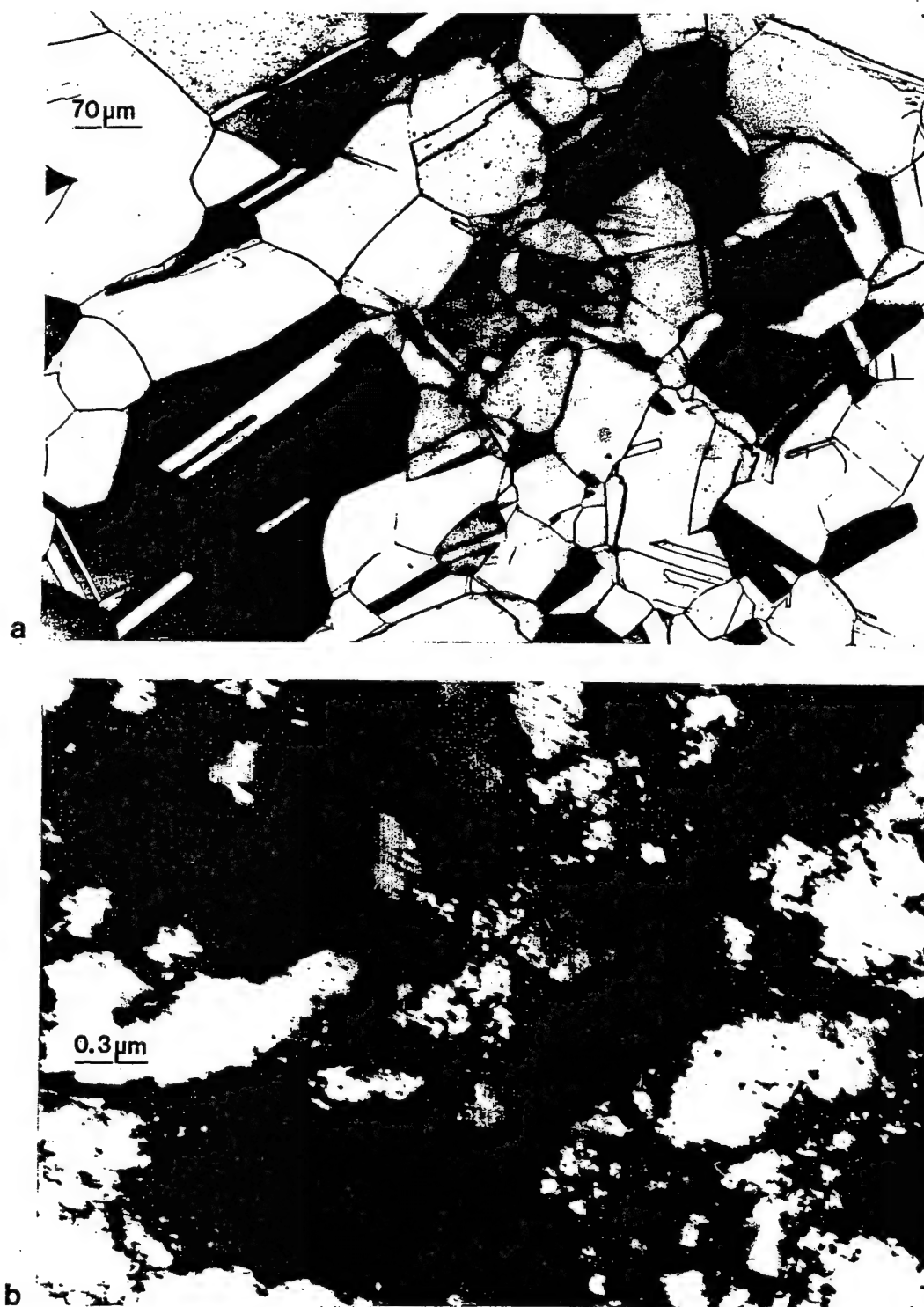


Figure 6.5: Initial microstructure characteristic of annealed copper consisting of a) large equiaxed grain structures and b) dislocations.

equiaxed grains and the presence of annealing twins. A corresponding transmission electron microscopy (TEM) image of the undeformed substructure is shown in figure 6.5(b); this displays the representative dislocation cell structure within the equiaxed grains.

6.2.2 Residual Microstructure

From the cross-section of the copper target penetration channel, a recreation of a region (microstructural map) was performed to reveal the evolution of deformation as a consequence of impact. This map begins at the edge of the crater wall (from the central region of the channel) and extends ≈ 6 mm into the surrounding material, as seen in figure 6.6. The cross-section of a WHA particle appears at the edge of the crater; this is followed by a zone of tiny, recrystallized grains directly beneath the particle.

The deformation continues with a region of heavily distorted grains, and, at a distance of 2mm from the edge of the crater, a profusion of linear bands within deformed grains. These linear bands have been characterized as microbands in previous studies involving impact cratering of copper [30,53,76]. At a distance of ≈ 6 mm from the from the channel edge, the microstructure begins to return to its original state. Though the map is a recreation of a region mid-way between the entrance and exit areas, the different zones observed are consistent along the entire length of the penetration channel.

Thus far, this evolution of microstructure is similar to that observed in hypervelocity impact studies of copper [30,53,70-73], as well ballistic impact of copper [29,76]. The exception is the observation of projectile fragments embedded along the

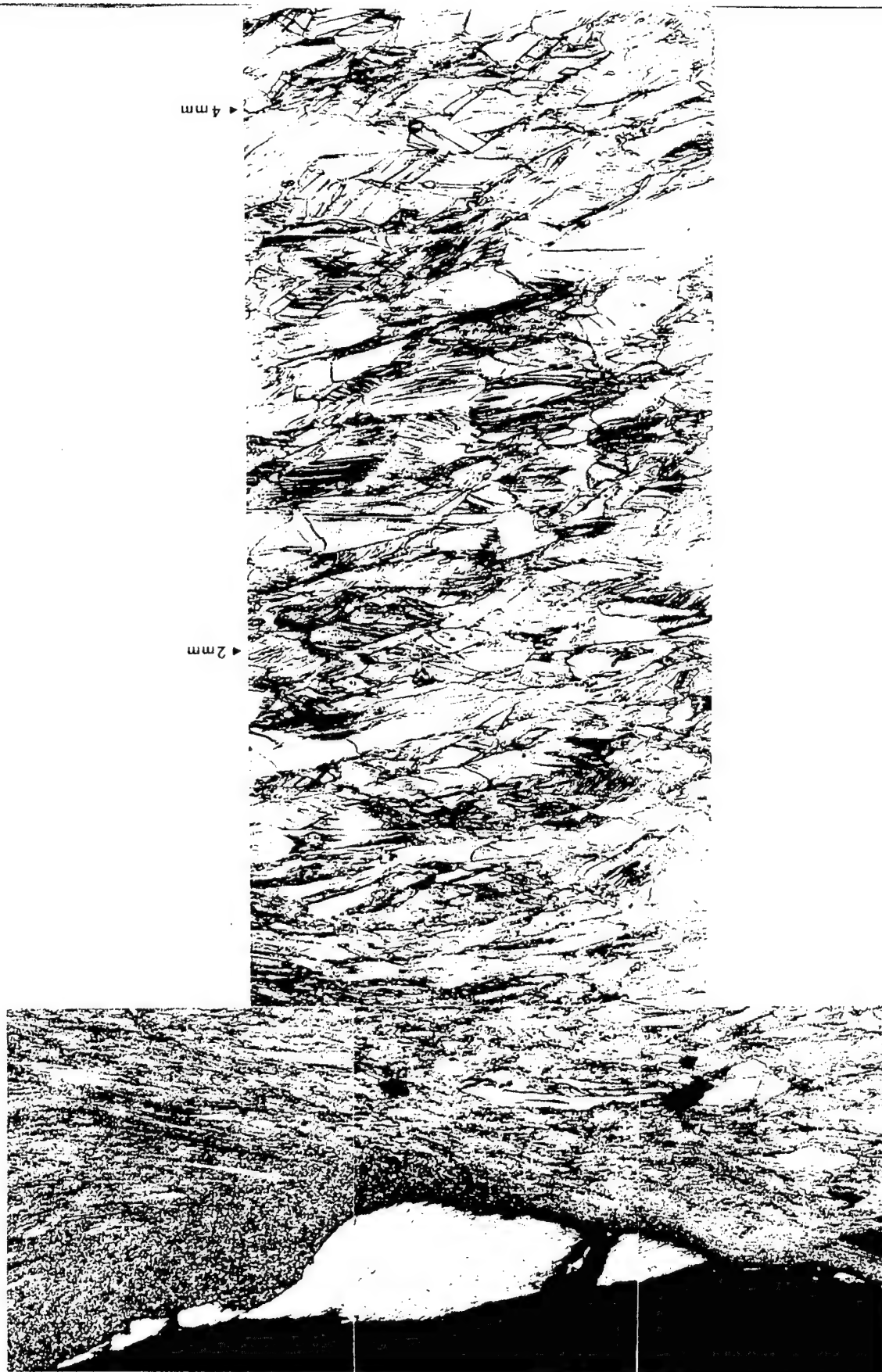


Figure 6.6: Microstructural map from a region of the residual copper target, revealing the evolution of deformation from the WFLA particle at the channel edge to 6 mm into the surrounding material.

wall of the crater. Figure 6.7(a) shows the cross-section of one such fragment at the channel wall. This micrograph clearly reveals the deformed microstructure of WHA (tungsten particles within a Ni-Fe matrix) as well as the recrystallized grains adjacent to the particle. An enlarged view of the recrystallized area is shown in figure 6.7(b). The normally narrow recrystallized zone remains so along the length of the channel, however, in the presence of WHA fragments this recrystallized region becomes highly exaggerated.

It was from such an exaggerated area that the TEM bright-field image of figure 6.8 was acquired. The highly refined, dynamically recrystallized grains of the micrograph are confirmed by the corresponding selected-area diffraction (SAD) pattern, which indicates crystallinity and large misorientations $> 10^\circ$. The term 'dynamic recrystallization' is applied in this case, since it has been generally accepted that the recrystallization process occurs during deformation, *i.e.* under concurrent conditions of high strain, high-strain-rate, and temperature. In the study of recrystallized grains within adiabatic shear bands, Hines and Vecchio [42] have concluded that the thermal component plays a much smaller role than once believed. As such, the formation of recrystallized grains should occur exclusively during deformation, by mechanical means. In the ballistic impact of copper, extreme conditions at the projectile/target interface are ideal for recrystallization. As the strain-free grains are associated with a reduction in yield stress, they may well provide an easier path for perforation by inducing solid-state flow of the target material.

Figure 6.9(a) is a reconstruction (map) of the rim cross-section from the entrance of the penetration channel, showing layers of dynamically recrystallized grains. These

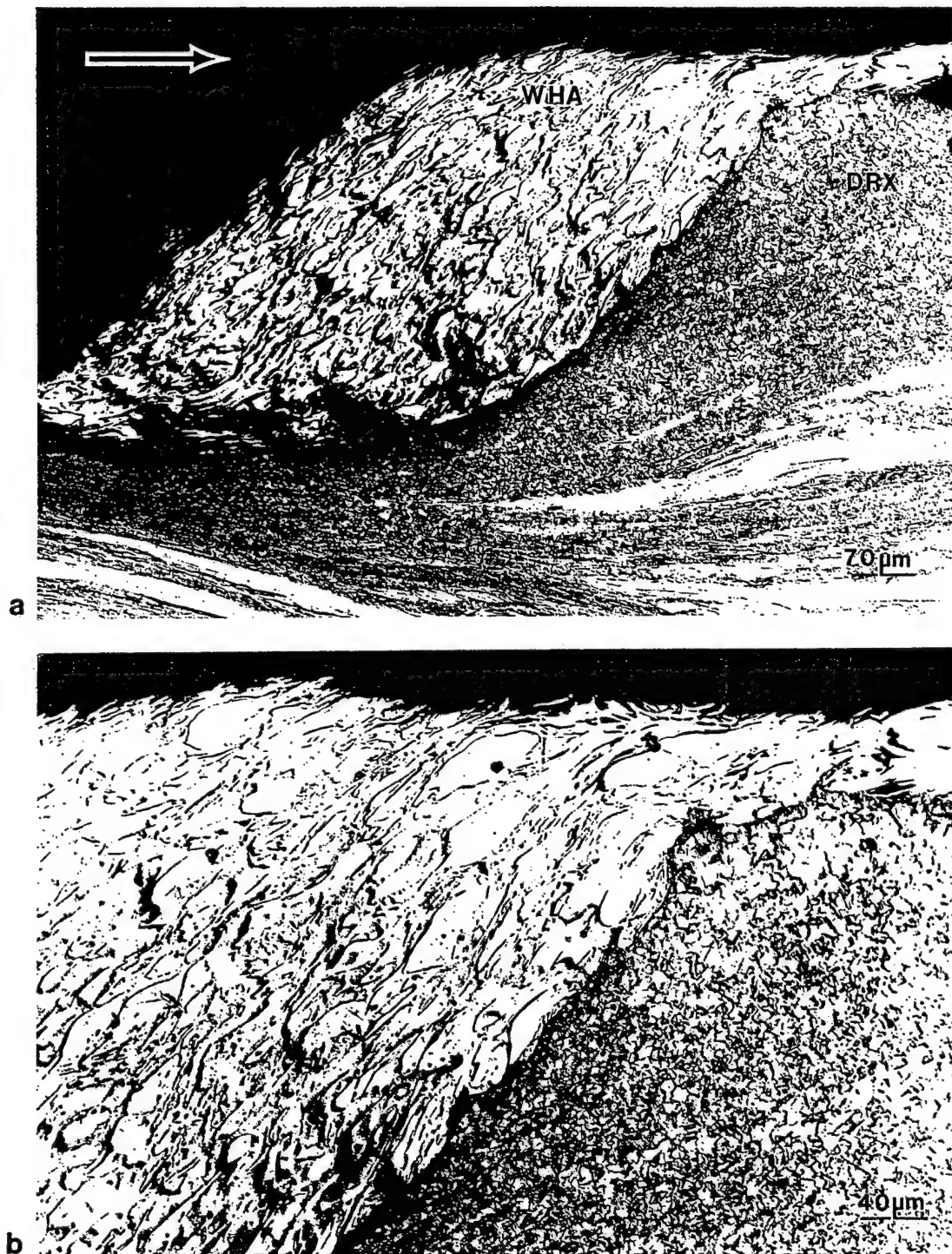


Figure 6.7: a) Cross-sectional view of a WHA erosion product along the channel wall, arrow indicates direction of perforation. b) Enlarged view of the exaggerated zone of dynamic recrystallization surrounding the particle.

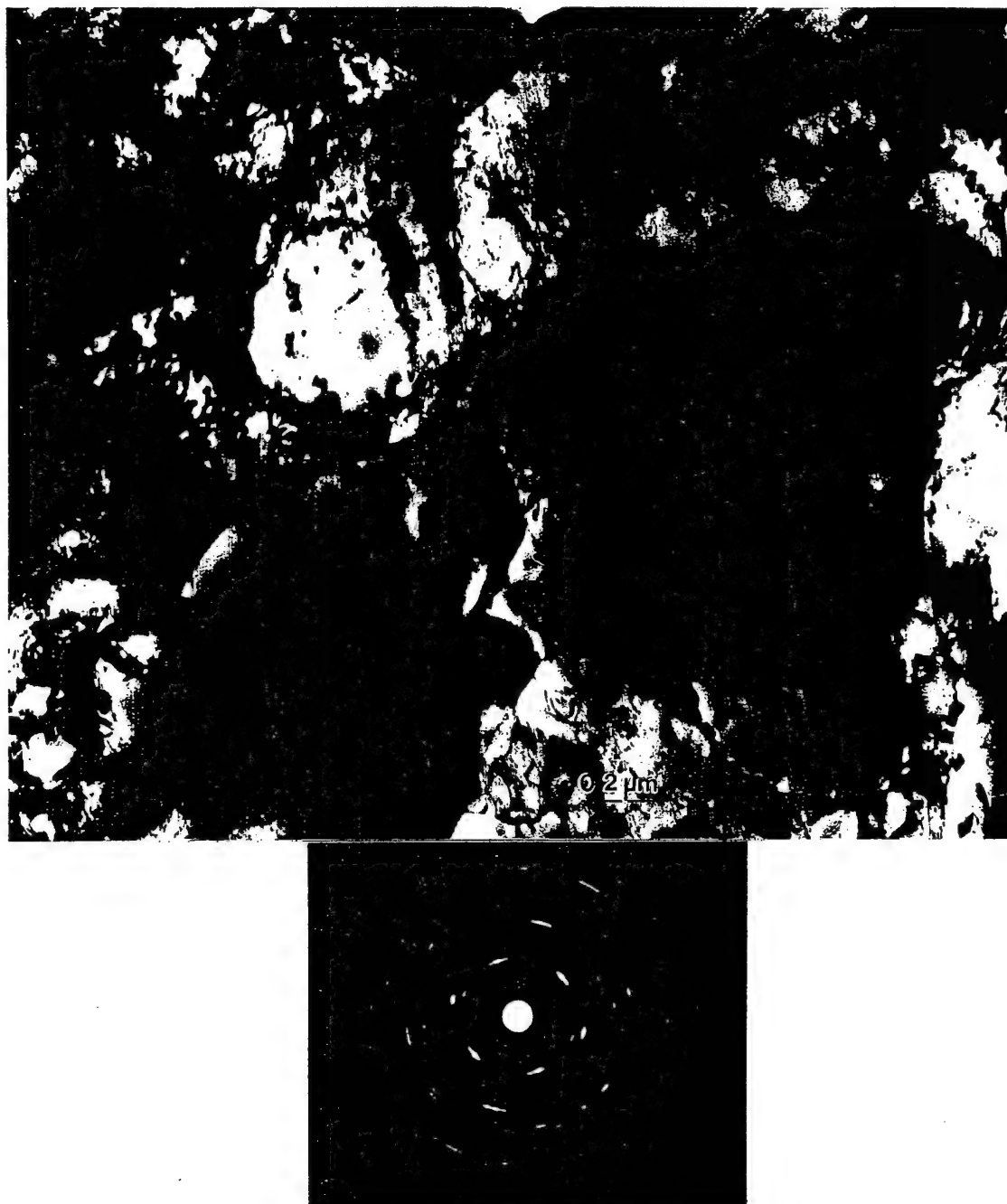


Figure 6.8: TEM bright-field image of dynamic recrystallization in 7039Al confirmed by the polycrystalline nature of the diffraction pattern.

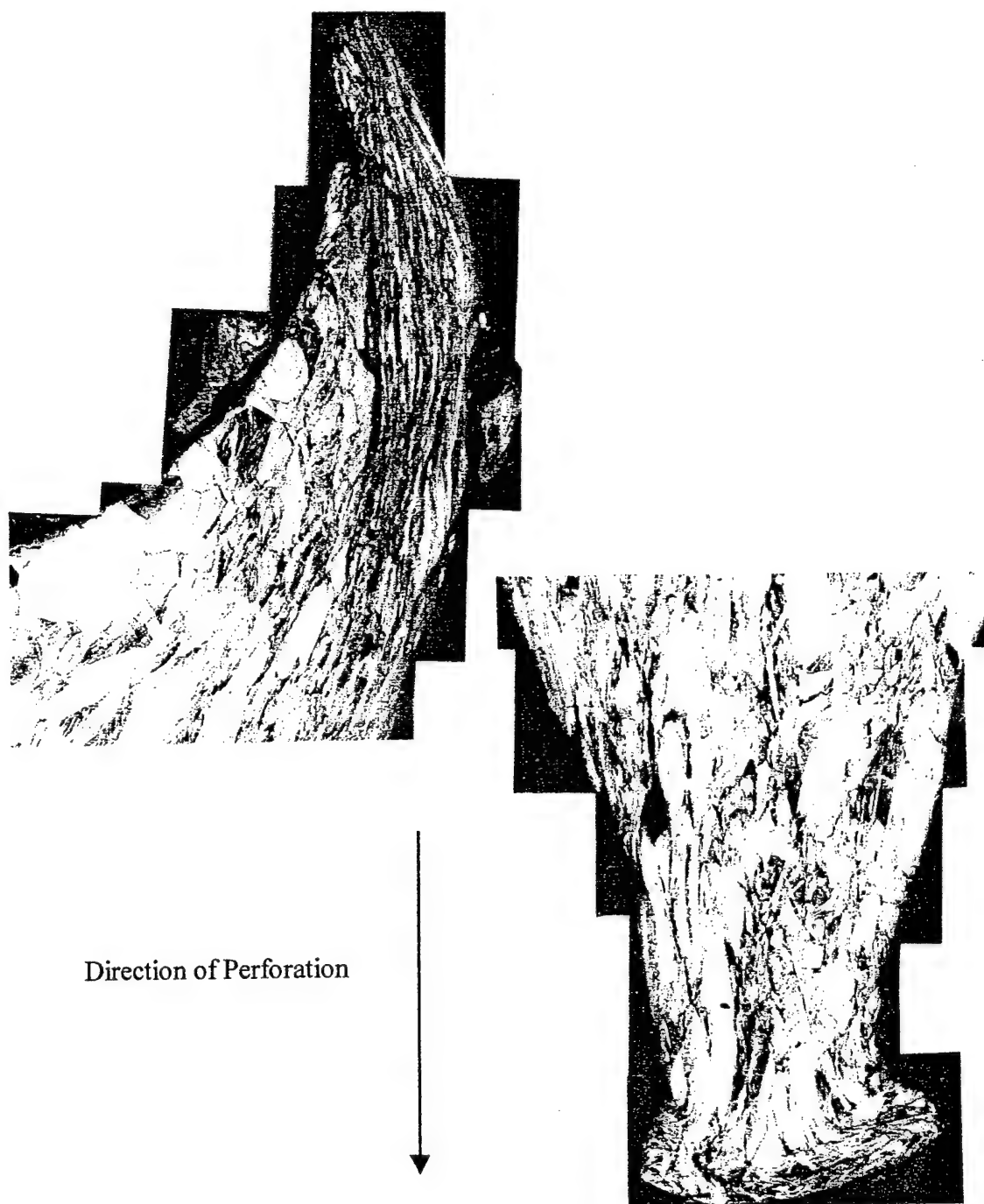


Figure 6.9: Layers of dynamically recrystallized grains are shown in the reconstruction of the copper entrance rim (left), while the reconstruction of the exit rim cross-section (right) shows very little plastic flow and more fracturing than the entrance rim.

layers of recrystallization appear to have facilitated the solid-state flow of material, opposite to the direction of penetration, to form the rim during impact. Hence, dynamic recrystallization should likewise facilitate solid-state flow in the creation of the penetration channel during perforation by the projectile. The exit rim cross-section, figure 6.9(b), reveals a somewhat different behavior from the previous. There appears to be very little plastic (solid-state) flow, which now occurs in the direction of penetration, and the material appears to be fractured from the wall.

The substructure in the region that follows the recrystallized zone consists of subgrains. Figure 6.10 was obtained from an area ≈ 1 mm from the crater edge. The diffraction pattern shows a misorientation of $6-13^\circ$, indicating a mixture of subgrains and recrystallized grains. Recrystallization is generally indicated by a large misorientation of $>10^\circ$. Figure 6.11 shows elongated subgrains found in a similar region, with misorientations in the diffraction pattern smaller than that of figure 6.10.

The linear bands observed previously in the microstructural map are primarily located in the region 2-4 mm from the edge of the channel wall. Though these features have been characterized as microbands in the previous impact studies of copper, no evidence of deformation twinning was presented. In this study, microbands have indeed been observed, as figure 6.12 illustrates. The bright field image shows a microband coincident with a (111) plane in the [110] direction for a (110) surface orientation. The corresponding dark-field image of 6.12(b) shows a reverse image of the microband from a diffraction spot with a small misorientation of $\approx 3.5^\circ$, characteristic of microbands. Bi-



Figure 6.10: TEM image showing a mixture of recrystallized grains and subgrains from an area 1 mm away from the crater edge. SAD pattern shows a range of misorientations.

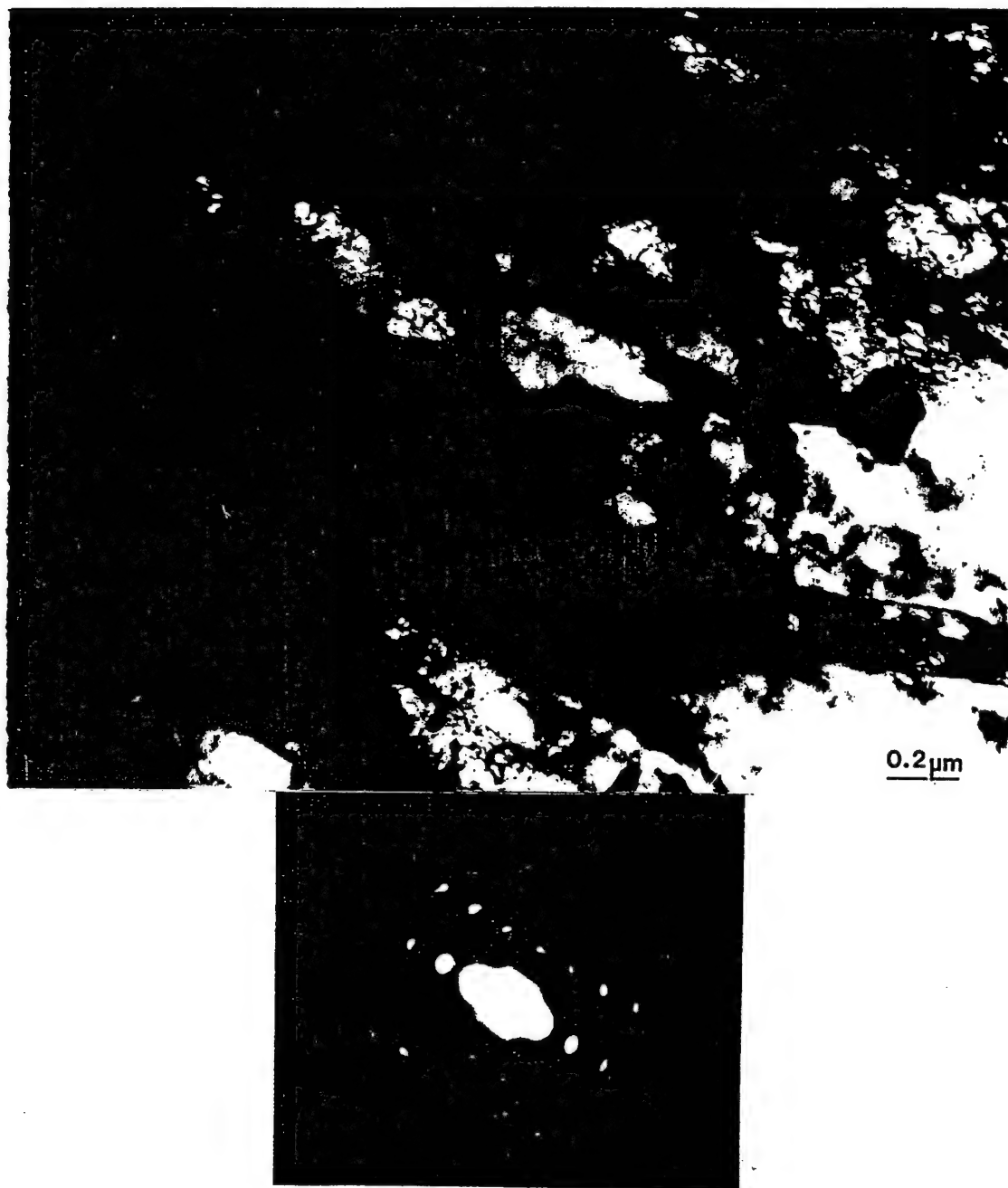


Figure 6.11: Bright-field image of elongated subgrains located 1 mm from the crater edge.

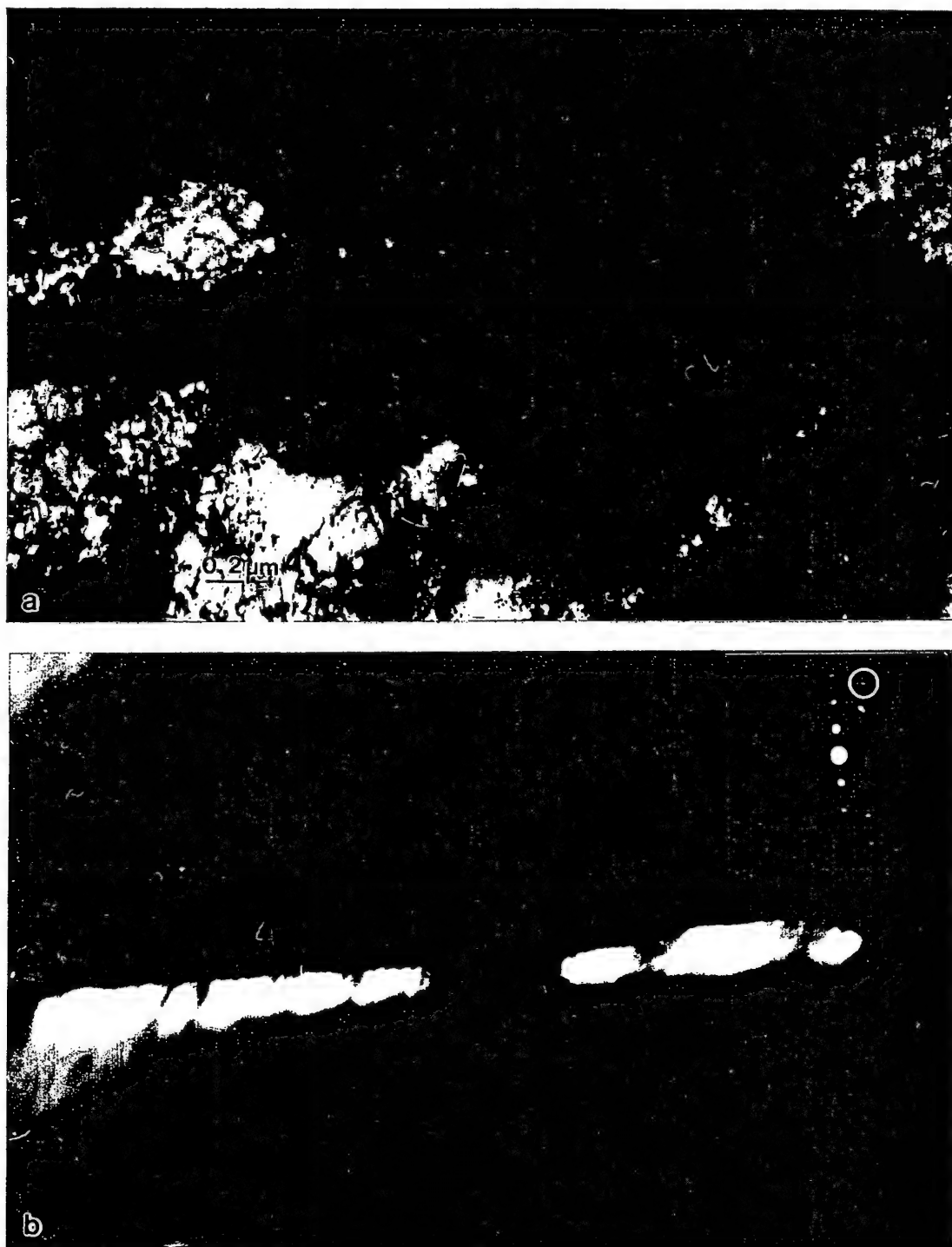


Figure 6.12: a) TEM bright-field image of a microband lying coincident with a (111) plane in the [110] direction for a (110) surface orientation. b) The dark-field image corresponding to a), obtained from the reflection circled on the SAD pattern insert.

directional microbands were also observed, as seen in figure 6.13. These microbands are formed coincident with $\{111\}$ planes along $\langle 022 \rangle$ directions for a (100) zone axis.

Remarkably, though no evidence was found in aforementioned studies, deformation twinning was also observed in the impacted copper. Figure 6.14 shows microtwins that have been intermixed with microbands, and both these structures are unambiguously confirmed by the corresponding SAD. The characteristic $\frac{1}{3}[111]$ twin spots (marked T on the pattern) are very prominent, along with the splitting of matrix reflections ($\sim 3.5^\circ$, marked M) characteristic of microband misorientation.

In light of the work by Sanchez et.al [69,75] on the oblique shock-loading of copper, it is presumed that ballistic perforation produces shock waves of a combination of oblique and spherical nature, in effect producing a microstructure consisting of microtwins and microbands. This supports the presumption that shock-deformation geometry is a critical feature in determining the occurrence of twinning. Figure 6.15 illustrates the residual microstructures of copper as a result of shock-wave geometry. For a planar shock wave of at least 20 GPa pressure, the resulting microstructure consists of twins (figure 6.15(a)), in hypervelocity impact cratering where the shock geometry appears to be spherical, the residual microstructure consists of microbands figure (6.15(b)), and in the ballistic impact of copper the nature of the oblique wave produces a combination of microbands and twinning (figure 6.15(c)). This is an important observation since it may be that similar penetration effects will be observed in elongated hypervelocity impact cratering in copper, i.e., mixtures of twins and microbands along the penetration channel.

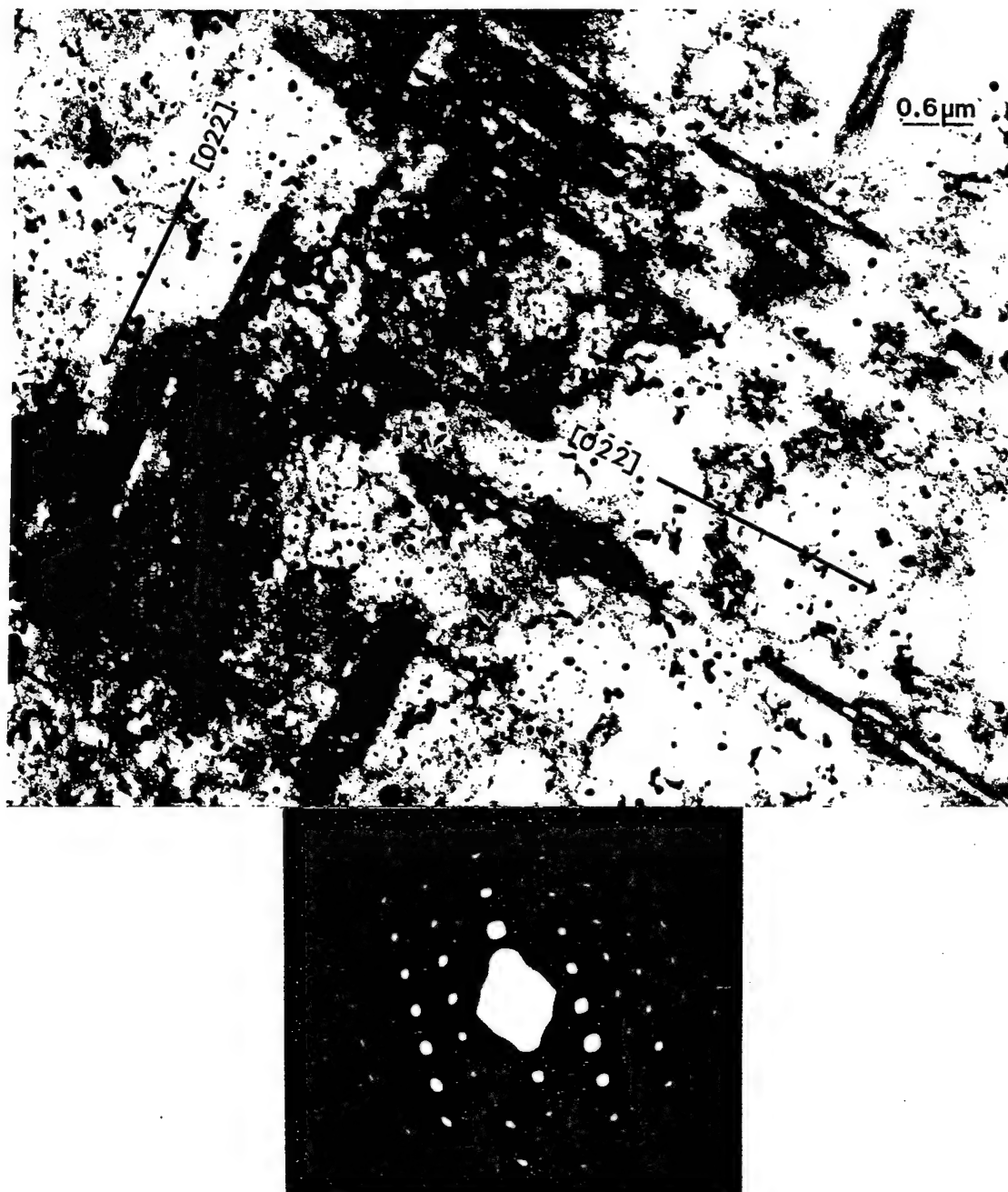


Figure 6.13: Bi-directional microbands observed in the impacted copper target. These are coincident with $\{111\}$ planes and run along $\langle 022 \rangle$ directions.



Figure 6.14: TEM image of an intermixing of microtwins and microbands in a (110) grain where the SAD pattern clearly illustrates misorientations (M) of $\sim 3.5^\circ$, as well as twin spots ($\frac{1}{3}[111]$) perpendicular to the direction of twinning marked T.

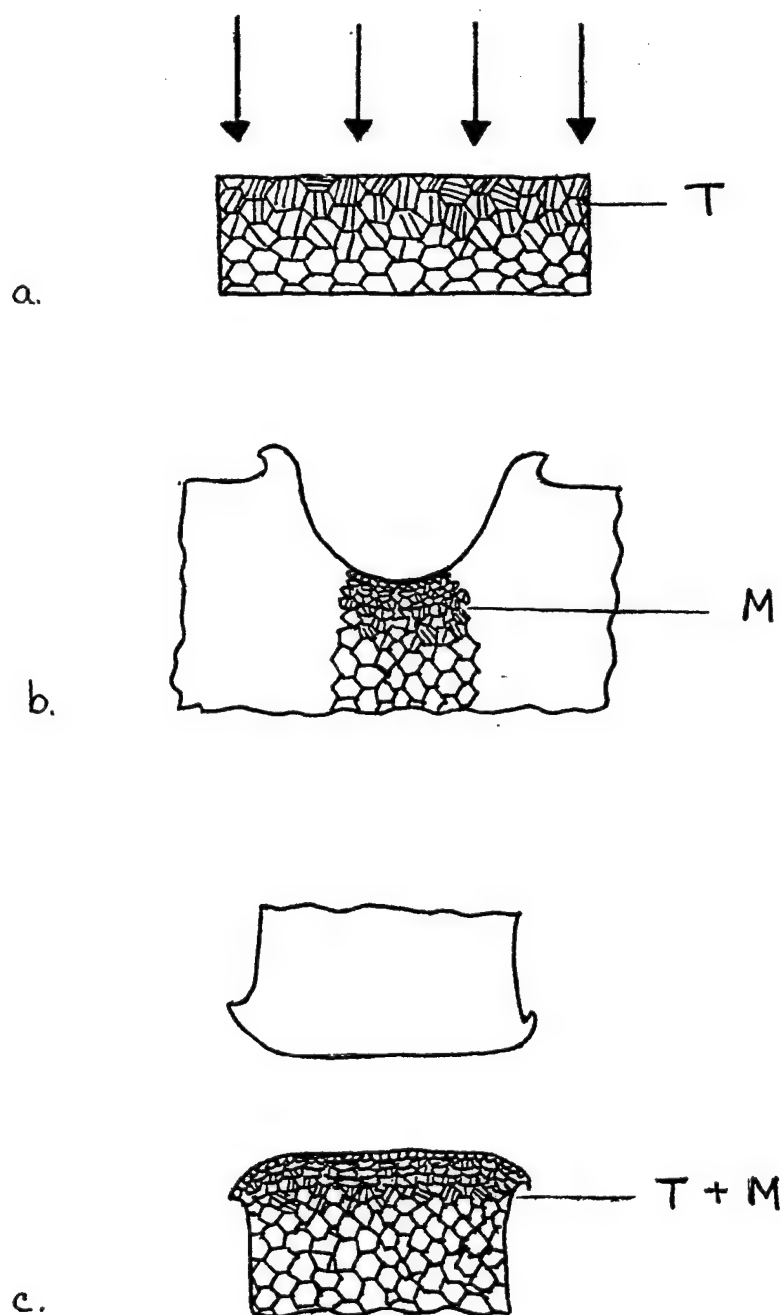


Figure 6.15: Schematic illustrating residual microstructure of copper in connection with shock geometry. a) Planar shock-loading produces twinning (T), b) hypervelocity impact cratering results in microbands (M), and c) ballistic impact by a long-rod projectile produces a mixture of microbands and twinning (M + T).

6.3 Microstructural Examination of 7039Al

6.3.1 Initial Microstructure

Unlike the annealed, lower strength starting condition of the OFHC copper target, 7039 aluminum is a wrought material that precipitation-hardened and fully work-hardened. Its undeformed microstructure is shown in figure 6.16, consisting of elongated grains (in the direction of working) interdispersed with clusters of small grains and precipitates. This may be seen more clearly in the magnified view of figure 6.16(b). The small grains become more apparent under the transmission electron microscope (figure 6.17) and precipitates of varying sizes and morphologies are also visible. With tilting of the specimen to bring dislocations into contrast, the high dislocation density (approaching saturation) as a result of work-hardening (deformation) becomes readily apparent in the grain structure of figure 6.17(b). The larger, elongated grains are shown in figure 6.18(a) and (b).

Work-hardening, or strain-hardening, occurs as a result of the plastic deformation of a metal. As the dislocation density increases due to slip, strength and hardness will increase due to the interaction of stress fields surrounding dislocations [96]. This phenomena can be described by the following equation:

$$\tau = \tau_0 + A \rho^{1/2} \quad (26)$$

where τ is the stress to move a dislocation in a matrix of dislocation density ρ , τ_0 is the stress required to move the dislocation in the same matrix with zero dislocation density, and $A \sim \mu^{1/2}$, where μ is the shear modulus of the crystal and b is the Burgers

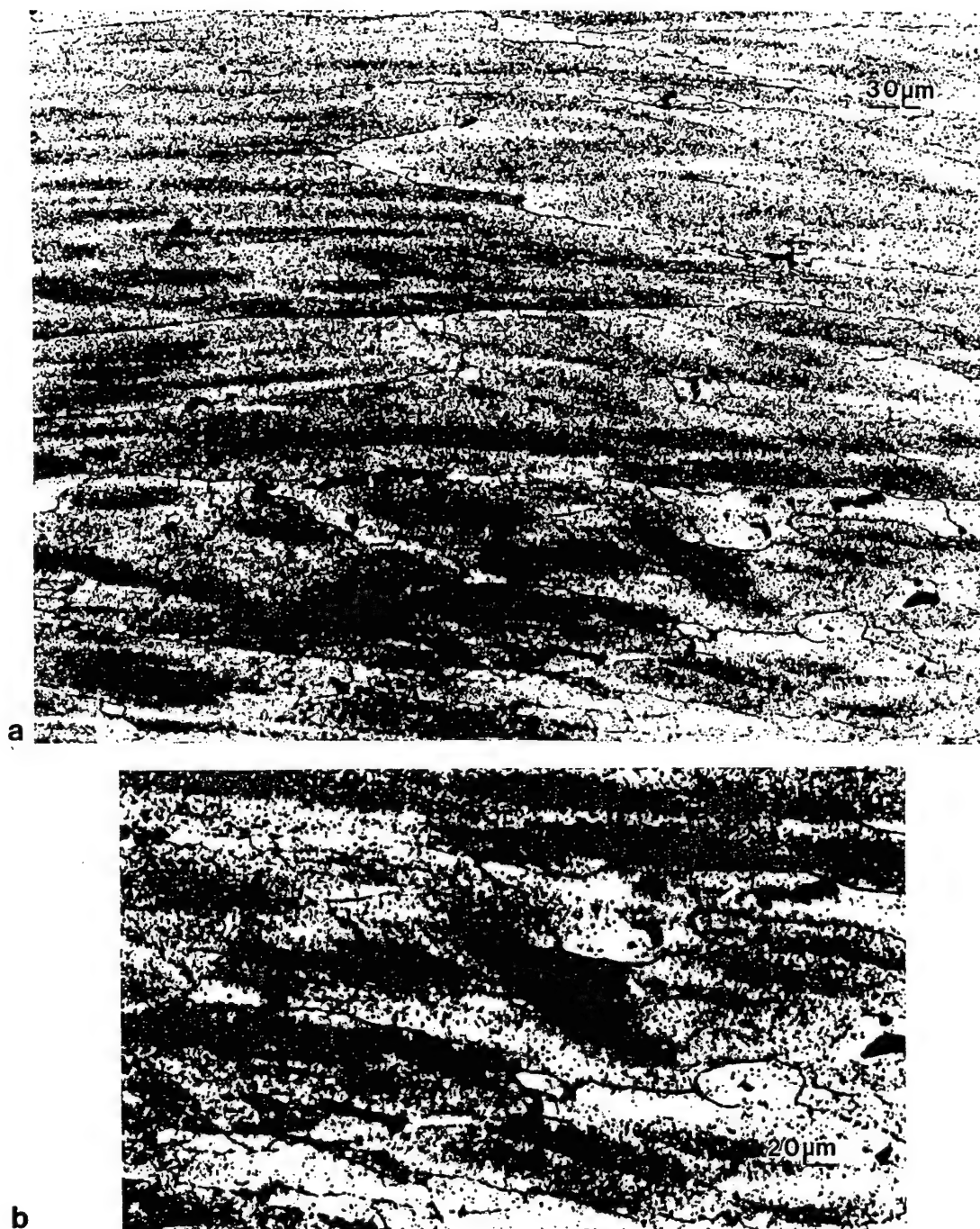


Figure 6.16: Optical view of the starting microstructure for work-hardened 7039Al showing a) elongated grains, oriented in the direction of deformation, mixed with clusters of small grains, seen more clearly in the b) enlarged view.



Figure 6.17: Micrographs of a) small grains and precipitates in the initial work-hardened microstructure of 7039Al and b) heavy dislocation density, approaching saturation, within the small grains.



Figure 6.18: a) TEM view of a large, elongated grain in the aluminum alloy. b) High dislocation density within the grain, consistent with work-hardening.

vector of the moving dislocation. Figure 6.19 shows a stress strain diagram where the positive slope of the curve in the plastic region designates work-hardening. As work-hardening reaches a maximum limit, or UTS, subsequent plastic deformation will result in fracture.

6.3.2 Residual Microstructure

During impact by the tungsten-alloy projectile, the aluminum target endures a large amount of cracking, as previously shown by the macrograph of the crater half-section in figure 6.2. A microstructural recreation of a segment of the penetration channel, close to the entrance area, is shown in figure 6.20. The direction of perforation is indicated by the arrow. From the micrograph, the extent of plastic deformation is limited to a narrow region alongside the penetration channel (~3 mm from the crater edge) where the heavily deformed region microstructure appears to 'flow' in the direction of perforation. Cracking occurs extensively along the channel wall, increasing in length and width towards the exit region.

Cracking is attributed to localized shear deformation, which propagates in the form of bands and are known as shear bands. Figure 6.21 illustrates a narrow shear band located ~4 mm from the channel wall. Shear band formation involves a rotation of the grains, towards a new orientation to accommodate the applied strains [96]. The plastic instability within the shear band is favorable for the nucleation, growth and coalescence of microcracks along the band, which induce fracture and leads to failure. Figure 6.22(a)

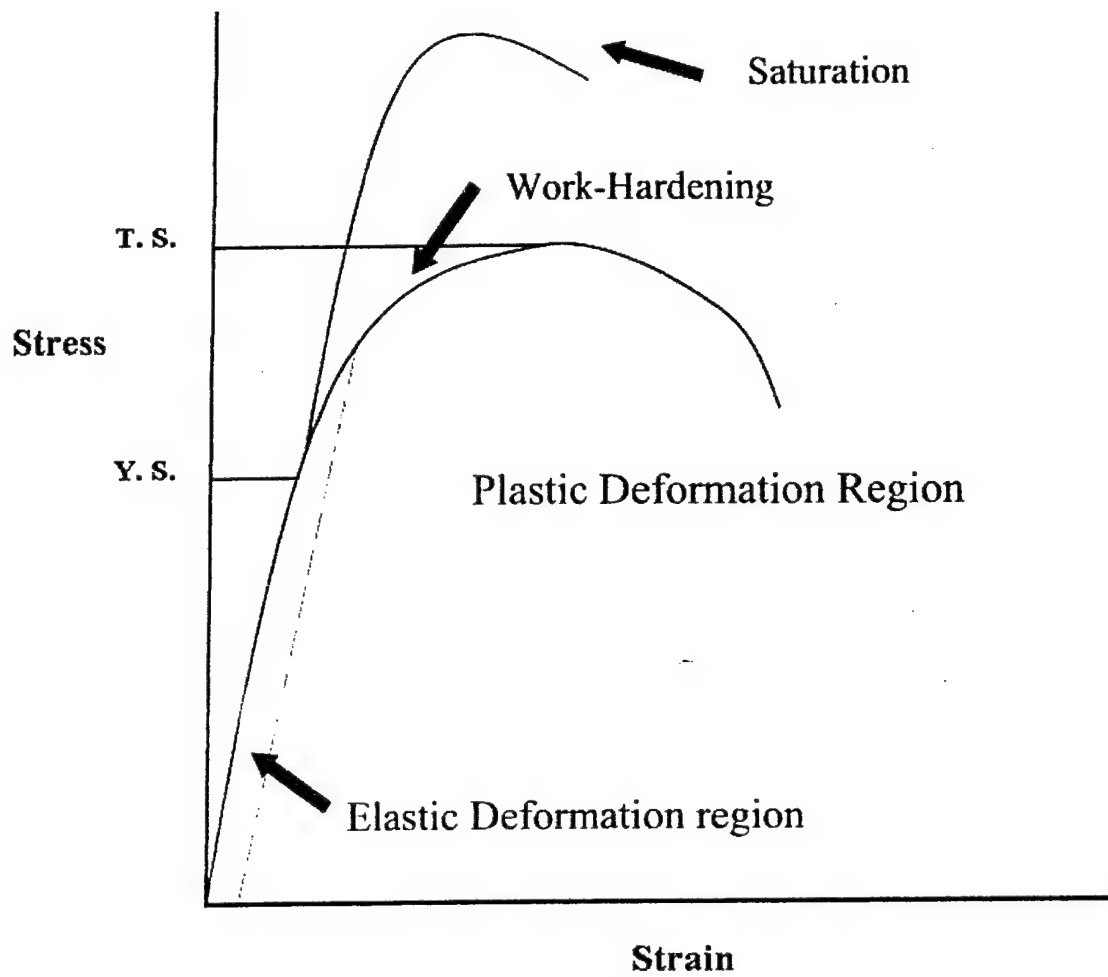


Figure 6.19: General stress-strain diagram illustrating work-hardening behavior in metals and the effect of saturation.

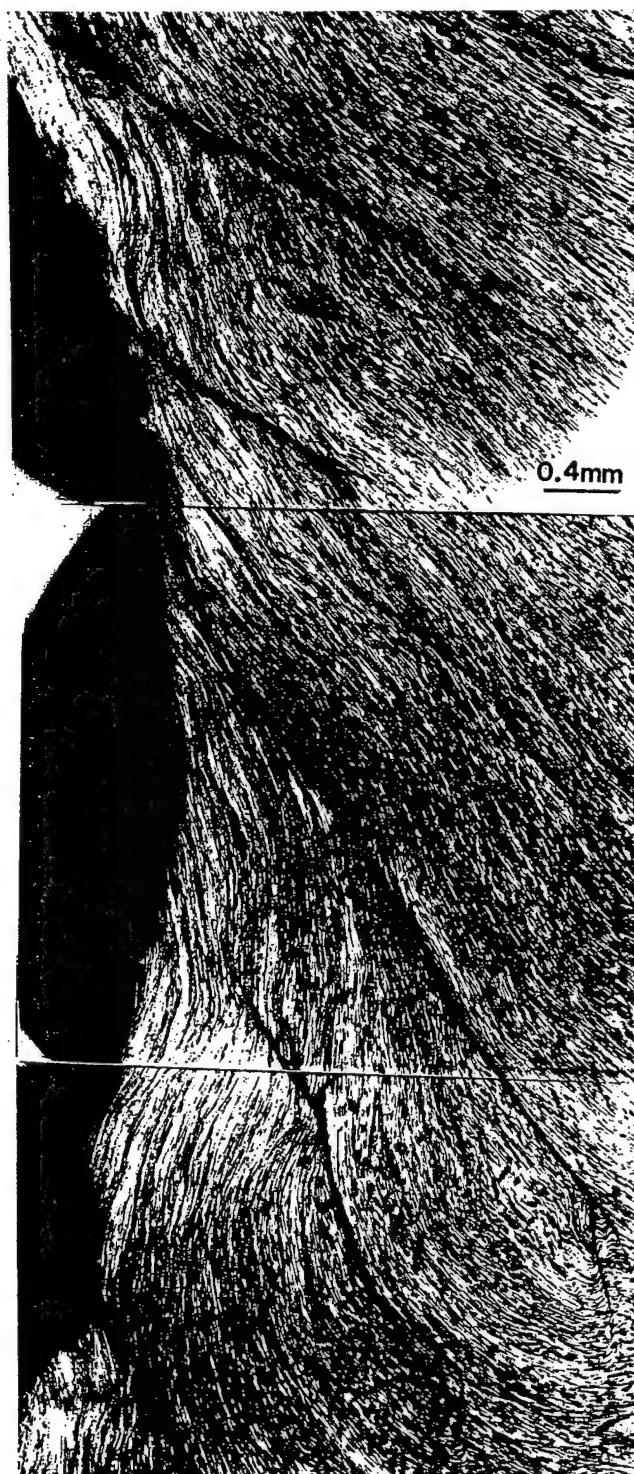


Figure 6.20: Microstructural map of a segment of the penetration channel in the residual 7039Al target. Limited plastic flow is seen close to the channel edge, also, shear bands and associated cracks are revealed.

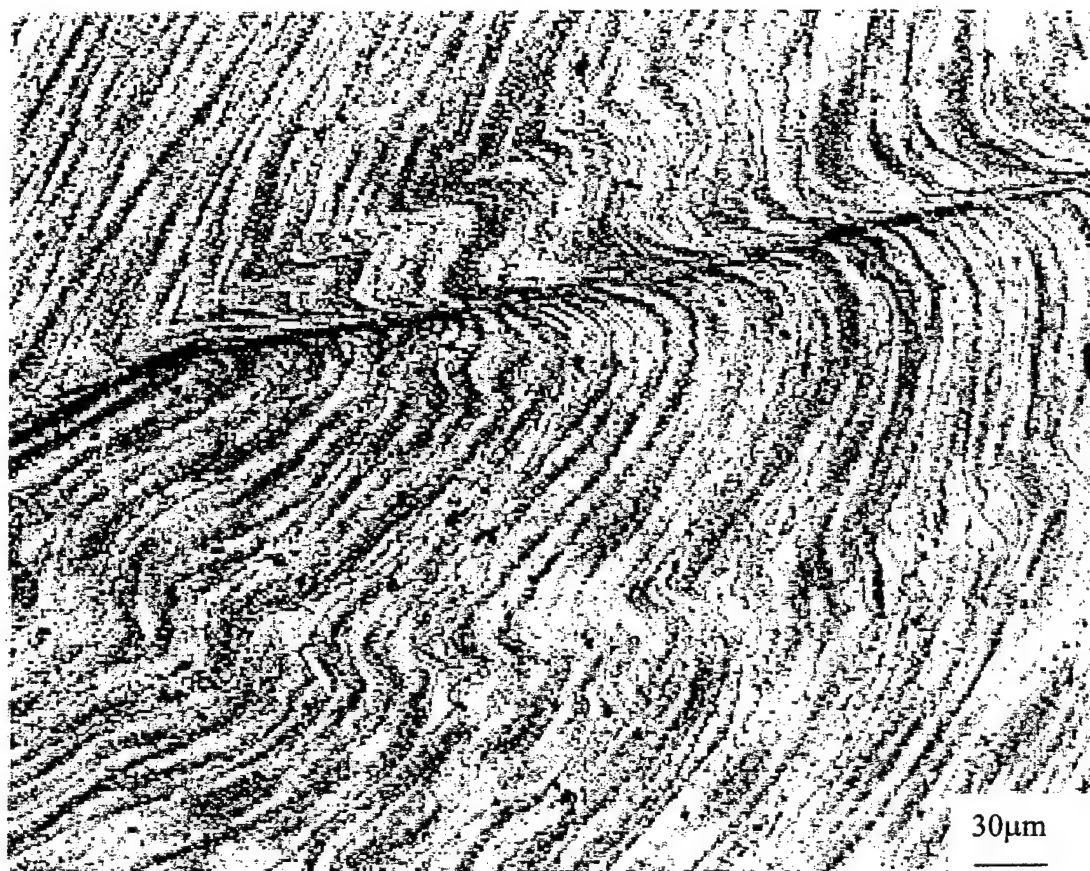


Figure 6.21: Micrograph of a narrow shear band located 4 mm from the channel wall.

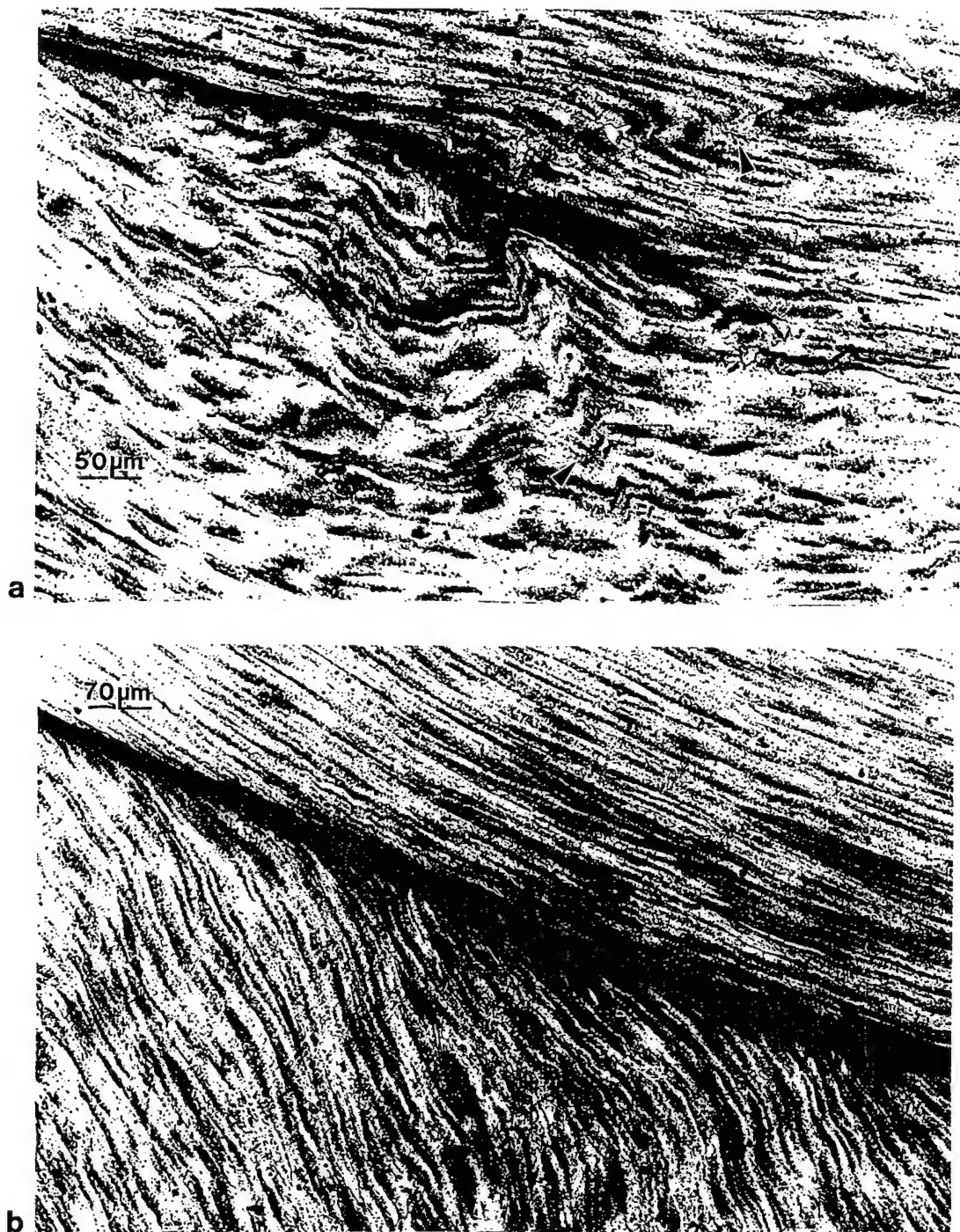


Figure 6.22: a) Optical view of two shear bands propagating in the shear direction and terminating at a crack. b) View of the re-oriented microstructure alongside a crack.

and (b) reveals the cracks associated with shear band deformation; figure 6.22(a) shows two shear bands propagating towards the shear directions and terminating at the crack.

It has recently become accepted that the large strain deformation (in shear localization) occurring at high-strain-rates and the associated temperature rise can lead to a recrystallized microstructure [97]; it was recently proposed by Hines and Vecchio [42] that this recrystallized structure develops simultaneously with deformation (dynamic recrystallization). Recrystallized grains in shear bands have been observed, through TEM analysis, in high-strain-rate testing of aluminum alloys such as an 8090 Al-Li alloy by Xu [97]. However, in the ballistic impact of metallic targets, due to a general lack of analyses at the microstructural level and non-existent analyses at the level of substructure, no evidence exists for recrystallized grains within shear bands of residual 7039Al.

In this study, locating a microscopic shear band for a 3 mm diameter thin foil specimen, then electropolishing the appropriate area to electron transparency for TEM analysis proved to be highly difficult. Figure 6.23 reveals an area of possible localized deformation, from a region ~ 3 mm from the crater wall. The corresponding SAD pattern indicates a mixture of recrystallization and subgrains.

Recrystallization was observed, however, by extracting specimens from the wall of the crater. Of the eight specimens prepared for TEM analysis, only two produced a small area of recrystallized grains, shown in figure 6.24. There is a possibility that, due to the irregularity of the channel surface, only a fine layer of recrystallization exists along the crater wall. This may be due to either the temperature rise along the channel wall

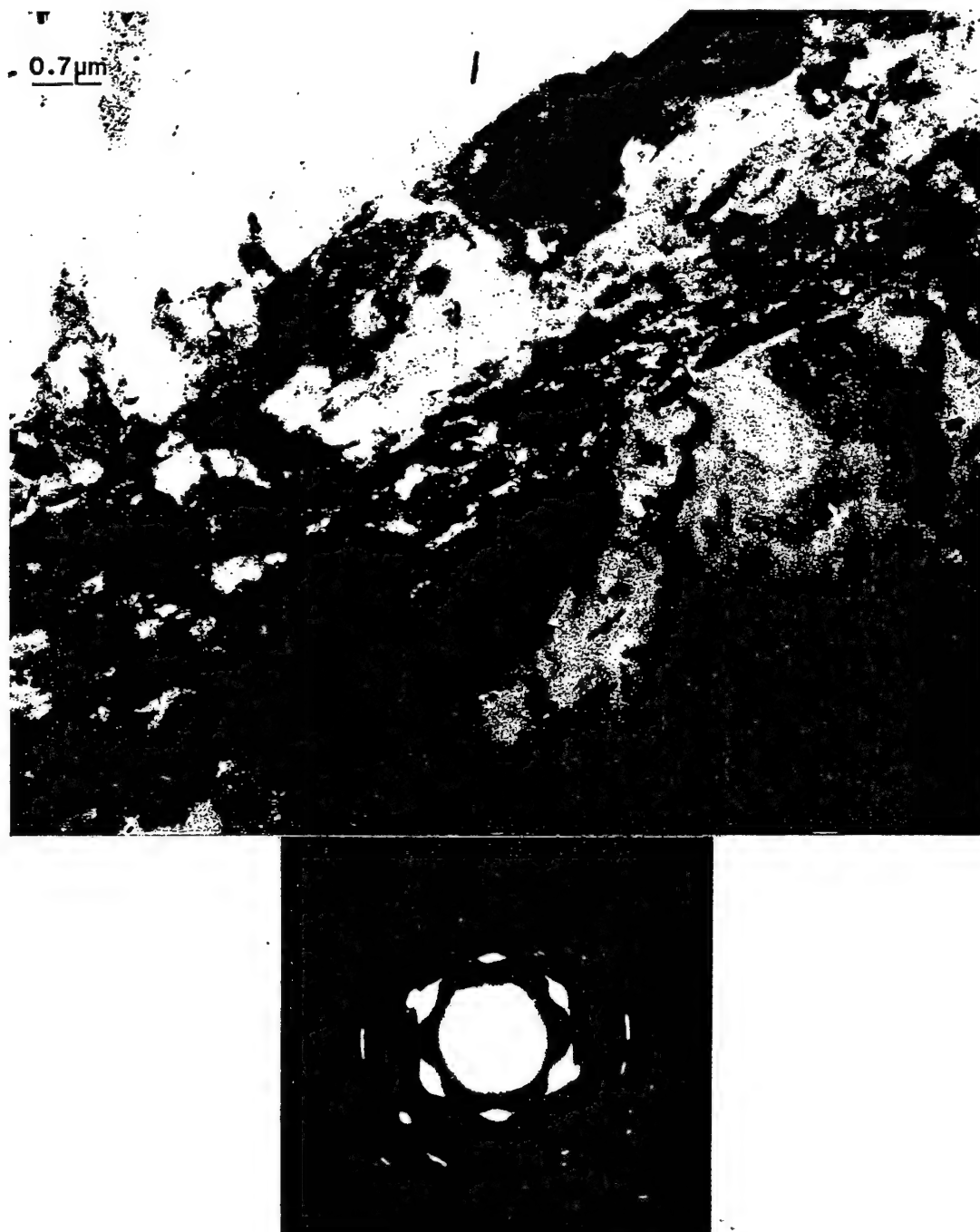


Figure 6.23: Bright-field image of a narrow region of possible localized deformation associated with a shear band. The corresponding SAD pattern shows high misorientations related to subgrains and recrystallized grains, and also shows texturing of the microstructure.

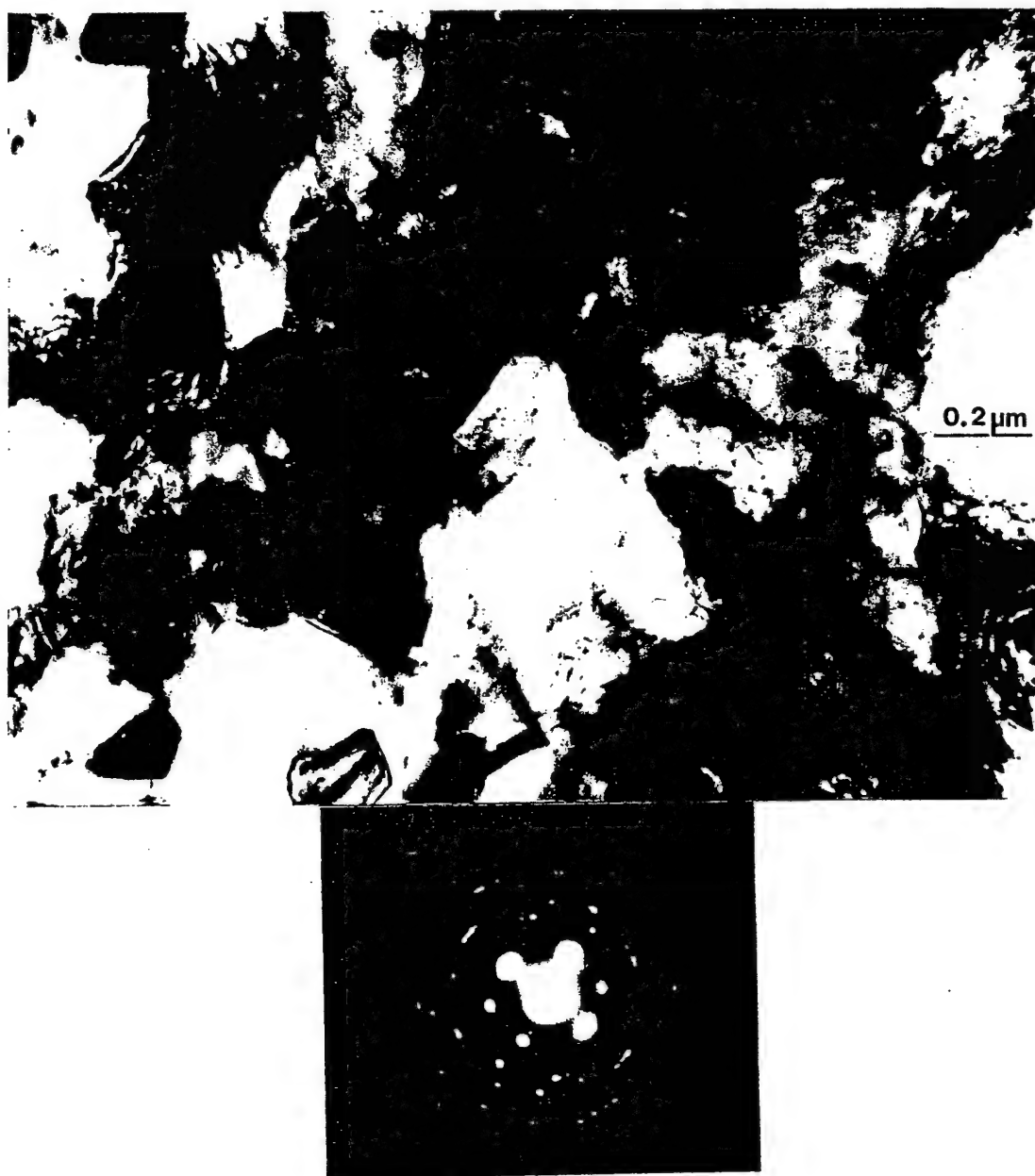


Figure 6.24: Micrograph of dynamically recrystallized grains located on the surface of the 7039Al channel. This is confirmed by the large misorientations in the corresponding SAD.

during penetration, or by mechanical means only (straining), since the large stored energies from severe work-hardening will provide a driving force for recovery and recrystallization with subsequent strains. Recovery structures were also observed on the surface of the channel wall including microbands, subgrains, and dense dislocation cells, as figures 6.25 and 6.26 illustrate.

In the region adjacent to the edge of the crater (~ 1 -2 mm away) typical microstructure consists of very dense dislocation cells as depicted in figure 6.27. The heavy dislocation density of the original work-hardened microstructure undergoes recovery, under high-strain-rate conditions, to form dislocation cells with heavy wall densities.

Localized plastic deformation of substructure in the form of microbands has also been observed close to the crater edge (at ~ 3 mm). Figure 6.28 shows a microband lying along a (111) plane in the [121] direction. The corresponding SAD reveals the diffraction spot responsible for the microband, determined by dark-field analysis, with the characteristic misorientation (3°) and width ($0.2 \mu\text{m}$) of microbands. The microband in figure 6.29 lies on a similar orientation as that of figure 6.28, in a different direction ([112] direction). This particular microstructure was not observed by Huang et.al [76], in their study of ballistically impacted 7039Al.

Unlike those examined in copper, microbands in aluminum appear to have a different morphology. Rather than form in clusters, such as it generally occurs in copper, microbands in the residual aluminum appear to form in long, continuous strings. It is highly likely that this development occurs from long, dense dislocation walls within the

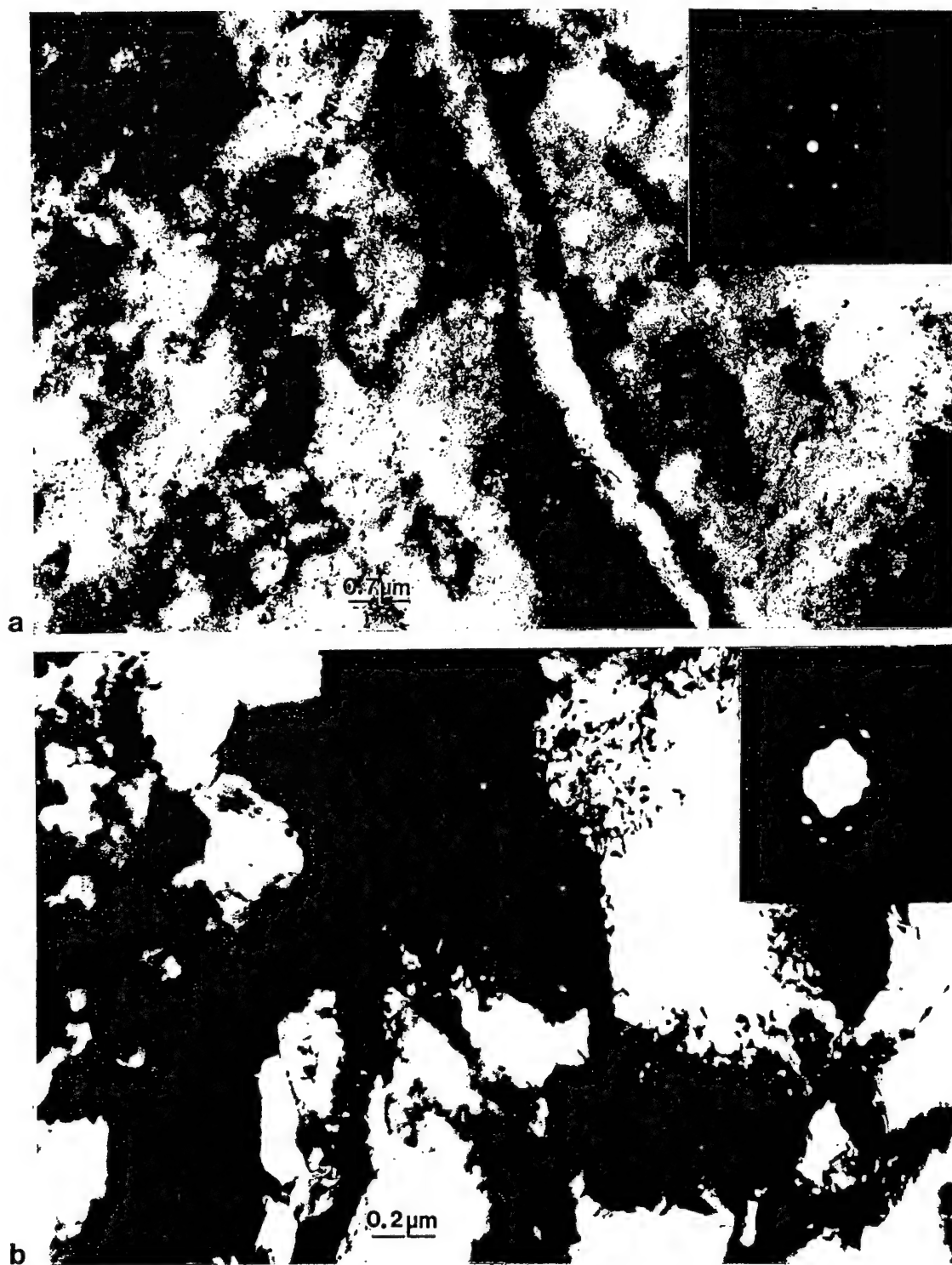


Figure 6.25: Microstructure from the surface of the 7039Al penetration channel consisting of a) microbands as well as b) recrystallized grains and subgrains.

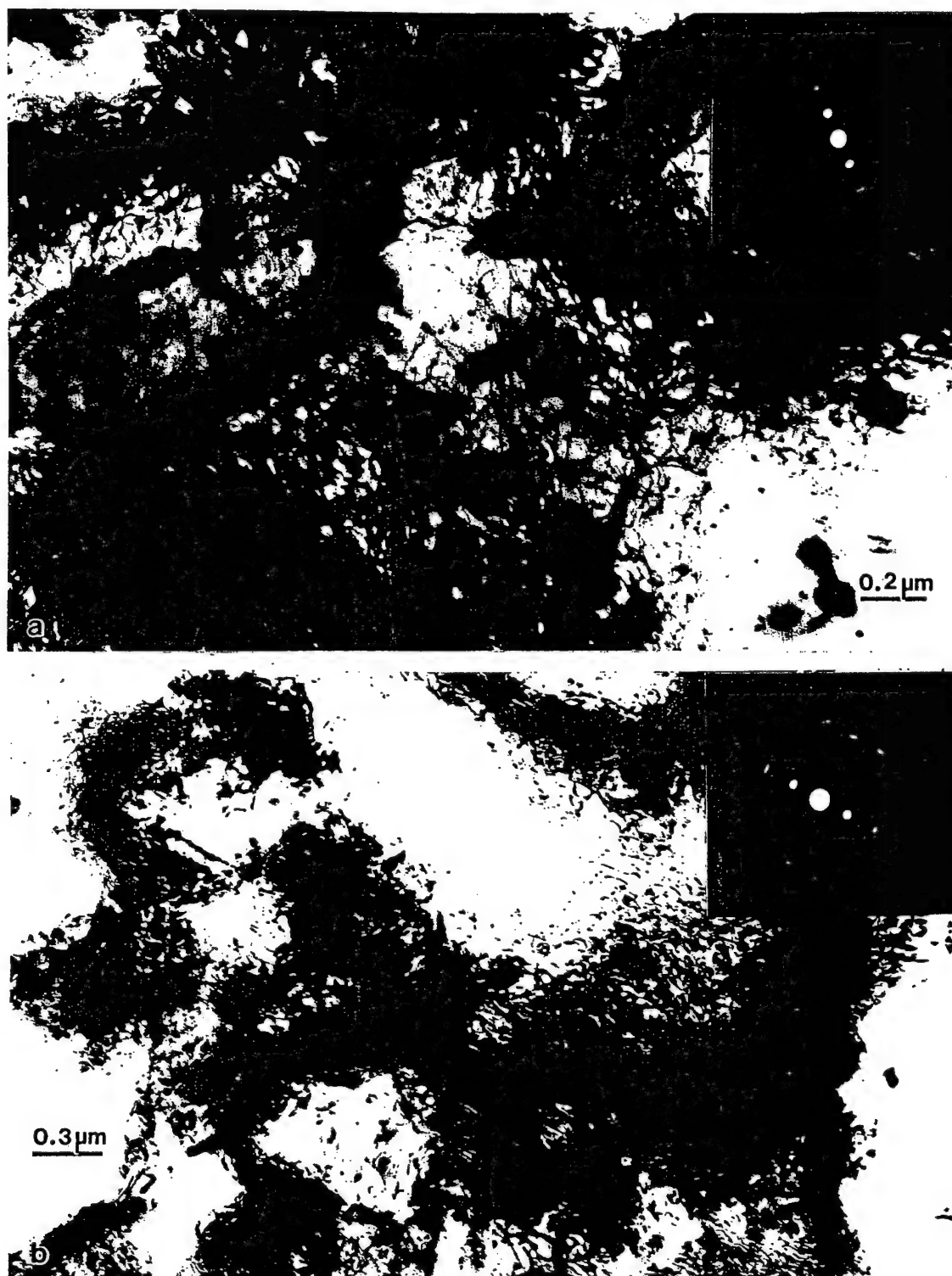


Figure 6.26: Dense dislocation cells and subgrains from the surface of the 7039Al penetration channel.

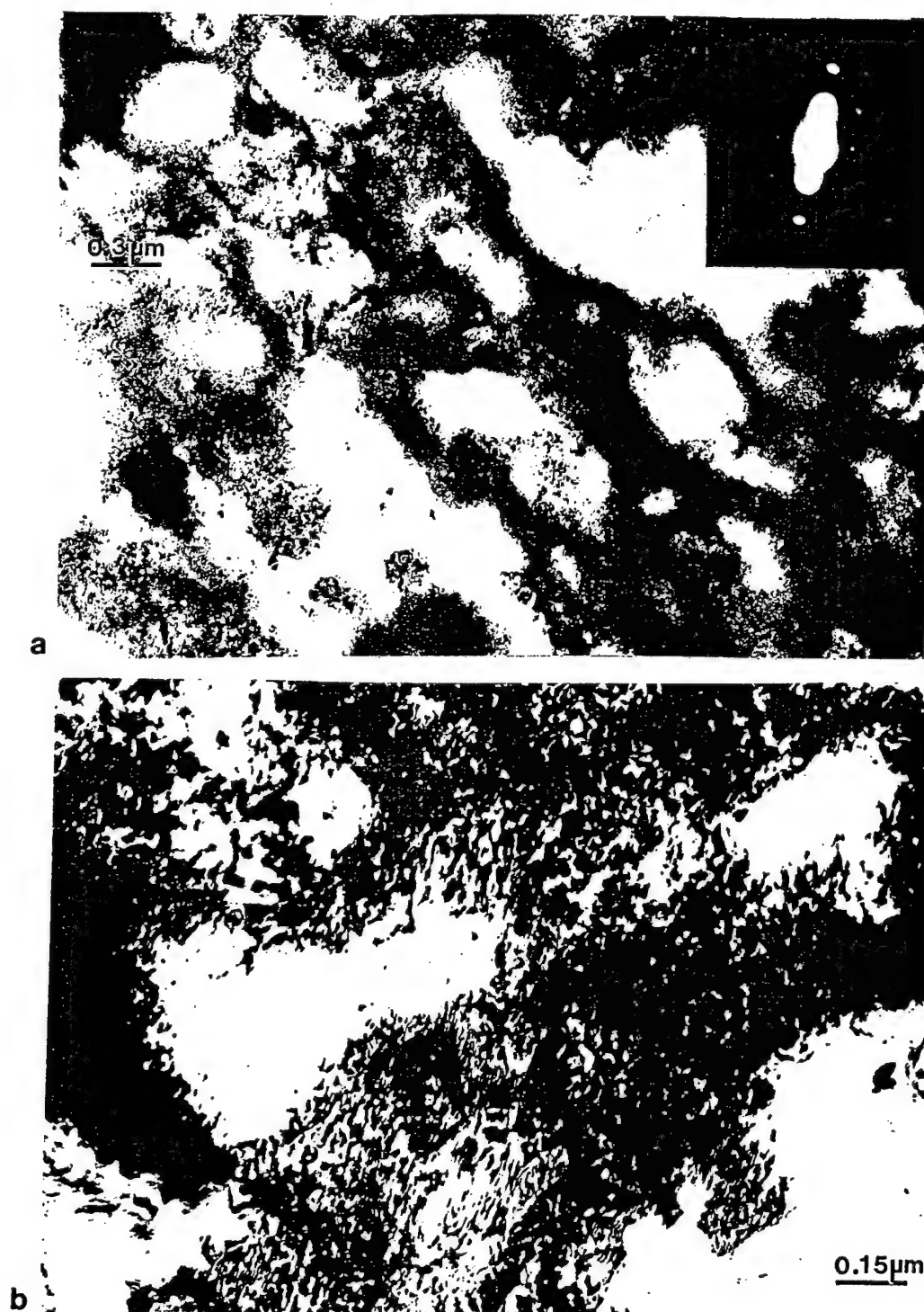


Figure 6.27: a) Dense dislocation cells observed in the region <2 mm from the channel edge.

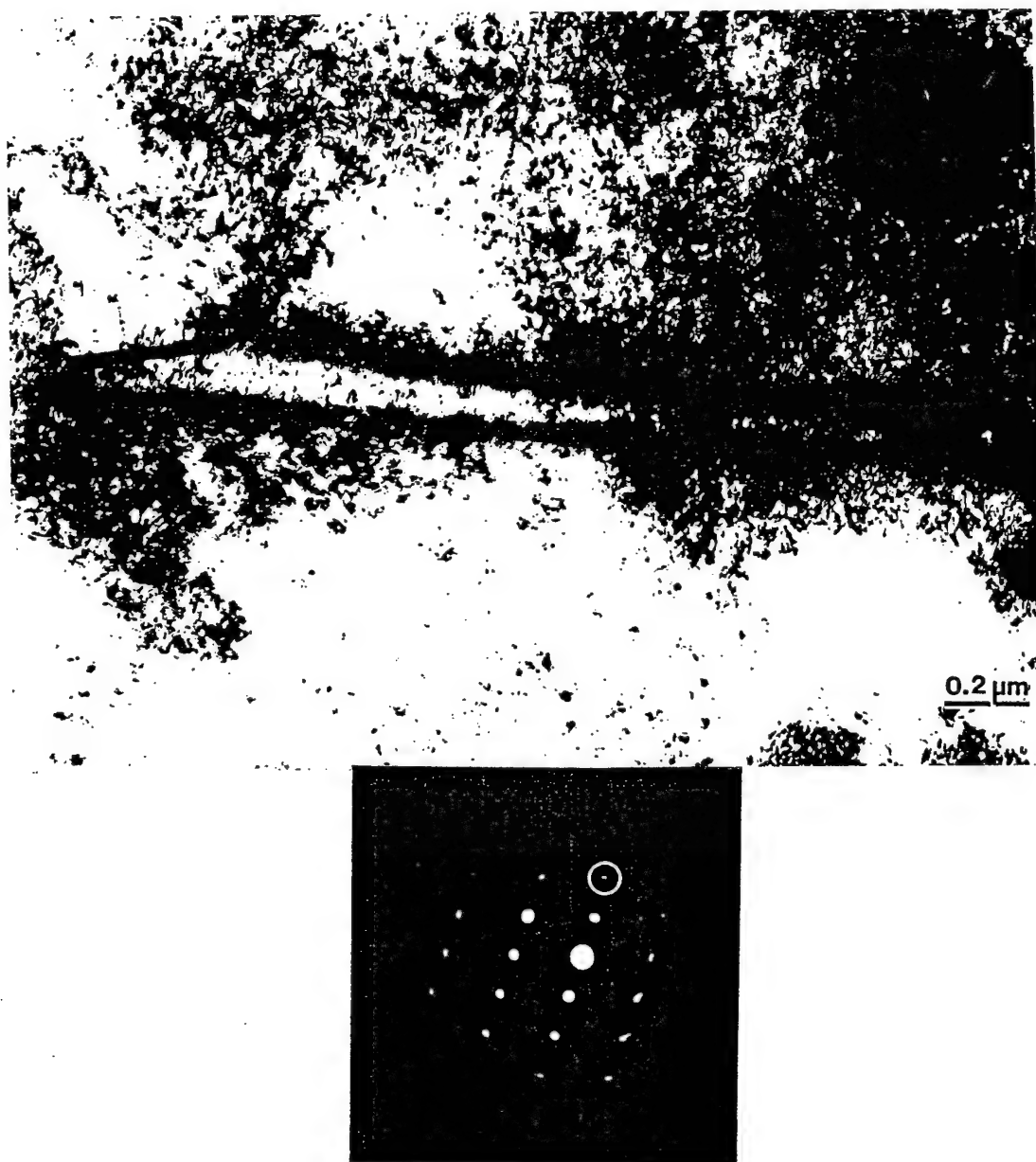


Figure 6.28: a) Bright-field image of microband parallel to the trace of a (111) plane in the [121] direction. b) The corresponding SAD pattern shows the reflection (circled) of small misorientation ($\sim 3^\circ$) characteristic of microbands.

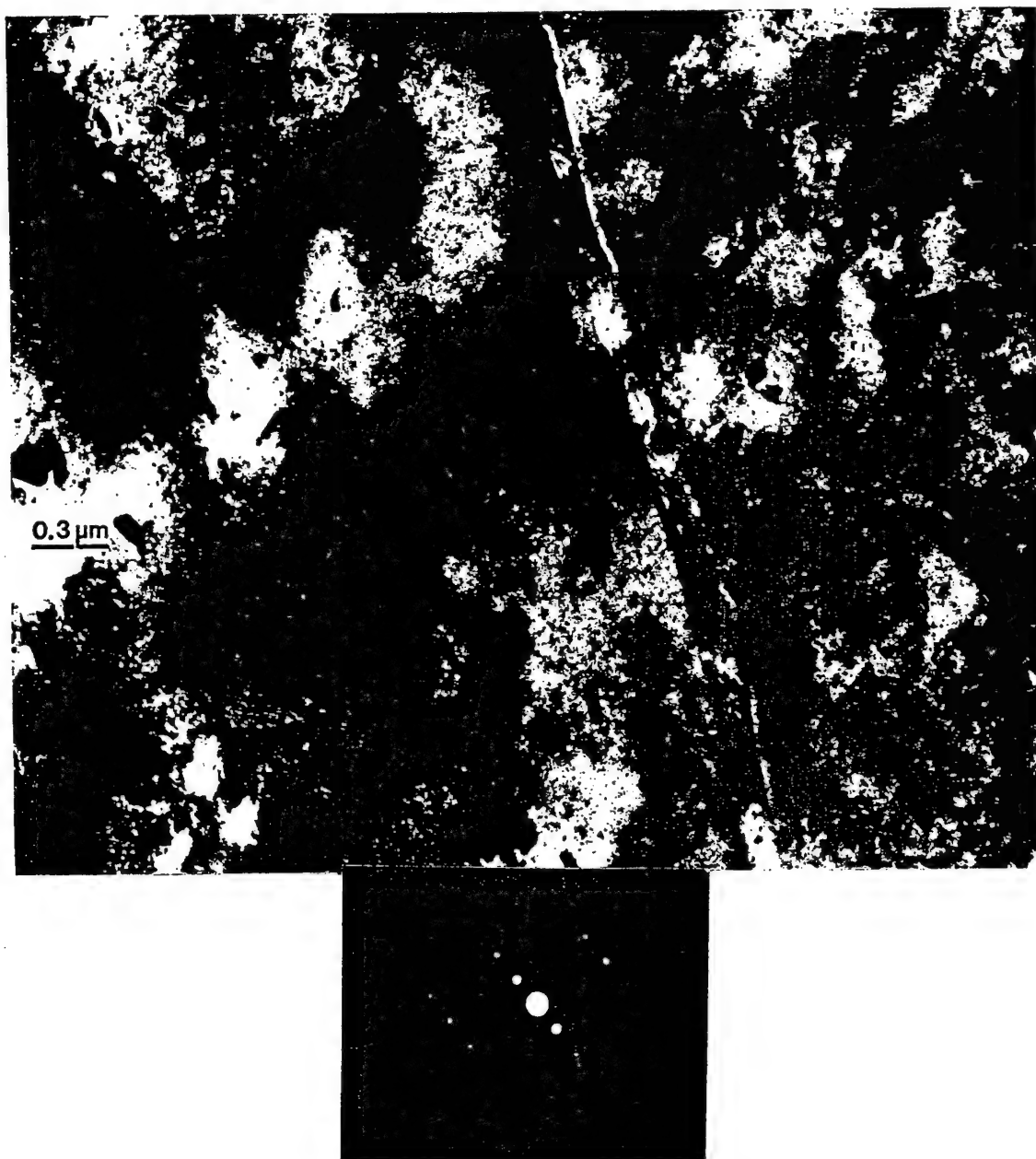


Figure 6.29: TEM image of a microband with a characteristic width ($0.2\mu\text{m}$) located 3mm from the crater edge. The SAD pattern shows a (123) zone axis, with the microband lying in the $[523]$ direction.

elongated grains. The string-like behavior was illustrated previously by figure 6.29, this is also observed in figure 6.30.

No deformation twinning was observed in the residual aluminum microstructure. This is in accordance with the high stacking-fault energy possessed by aluminum ($\sim 170 \text{ mJ/m}^2$), whereby the residual microstructure develops as a result of slip. Figure 2.9 clearly illustrates the relationship between stacking-fault energy and twinning pressure; a material with high stacking-fault energy such as aluminum would require a large critical twinning pressure for shearing of the lattice to occur.

An additional observation was made in the deformed aluminum, involving large, parallel bands in the heavily fractured regions towards the exit end of the channel, and along the shear lips. Figure 6.31 illustrates optically these linear bands within the deformed elongated grains. These are believed to be deformation bands, since they have been described in the literature as well-defined bands formed across grains in parallel sets with a typical thickness of 0.05 μm , and 1 μm spacing [98]. The misorientation across such bands have been observed to increase with the degree of deformation, while the width of the bands decrease with increasing strain. Although deformation bands are a frequent observation in single crystals, only few observations have been reported for polycrystalline materials, of which most have occurred for deformed coarse-grained materials [99,100].

Deformation bands have been observed through TEM in copper that had been cold-rolled 90% [101], though attempts to identify the bands in deformed polycrystalline aluminum have been unsuccessful [102]. Figure 6.32 shows a bright-field image from a



Figure 6.30: TEM image illustrating the long, string-like behavior of microbands in the residual 7039Al target.

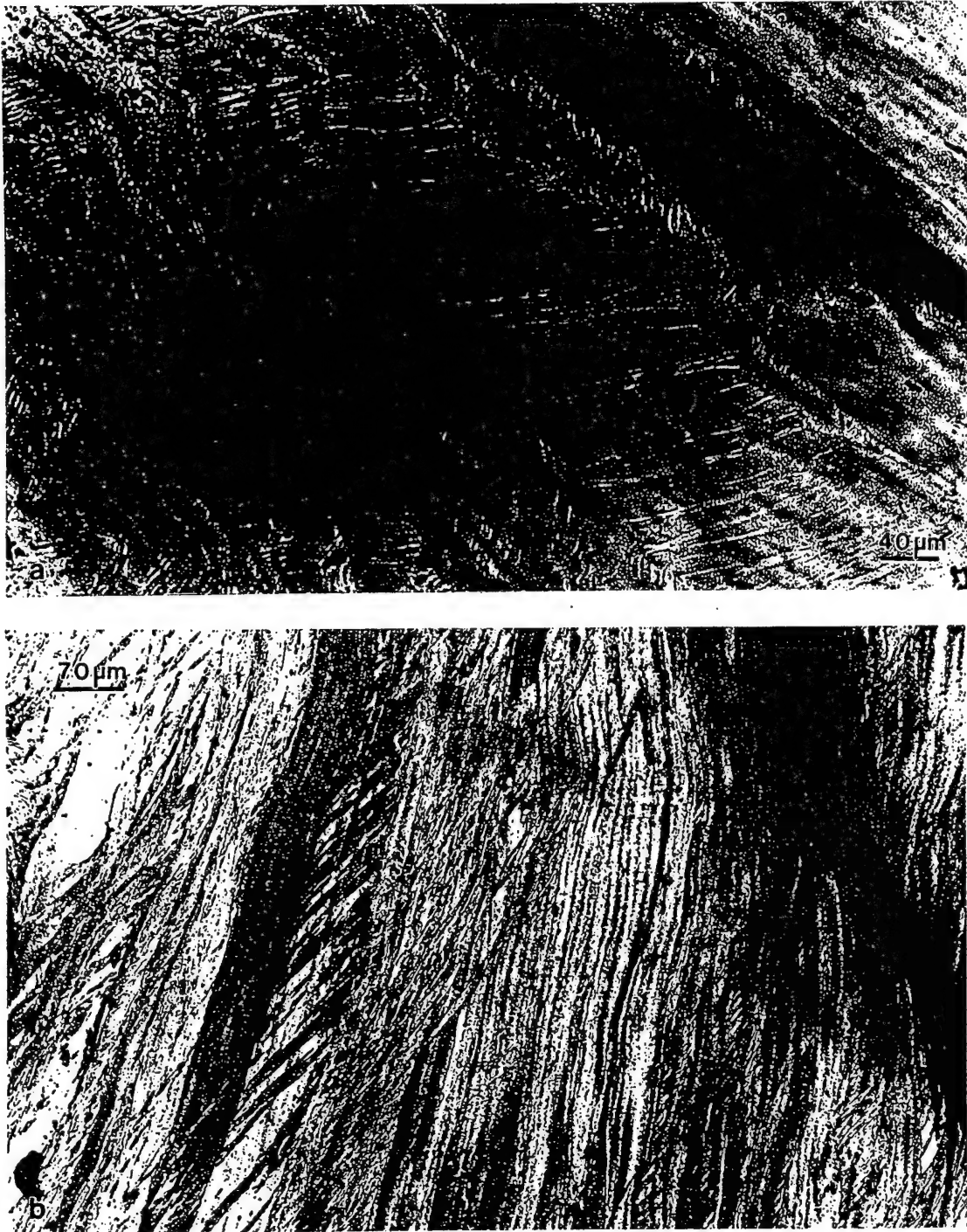


Figure 6.31: Optical view of deformation bands a) within elongated grains, and b) within the region of the fractured shear lips.

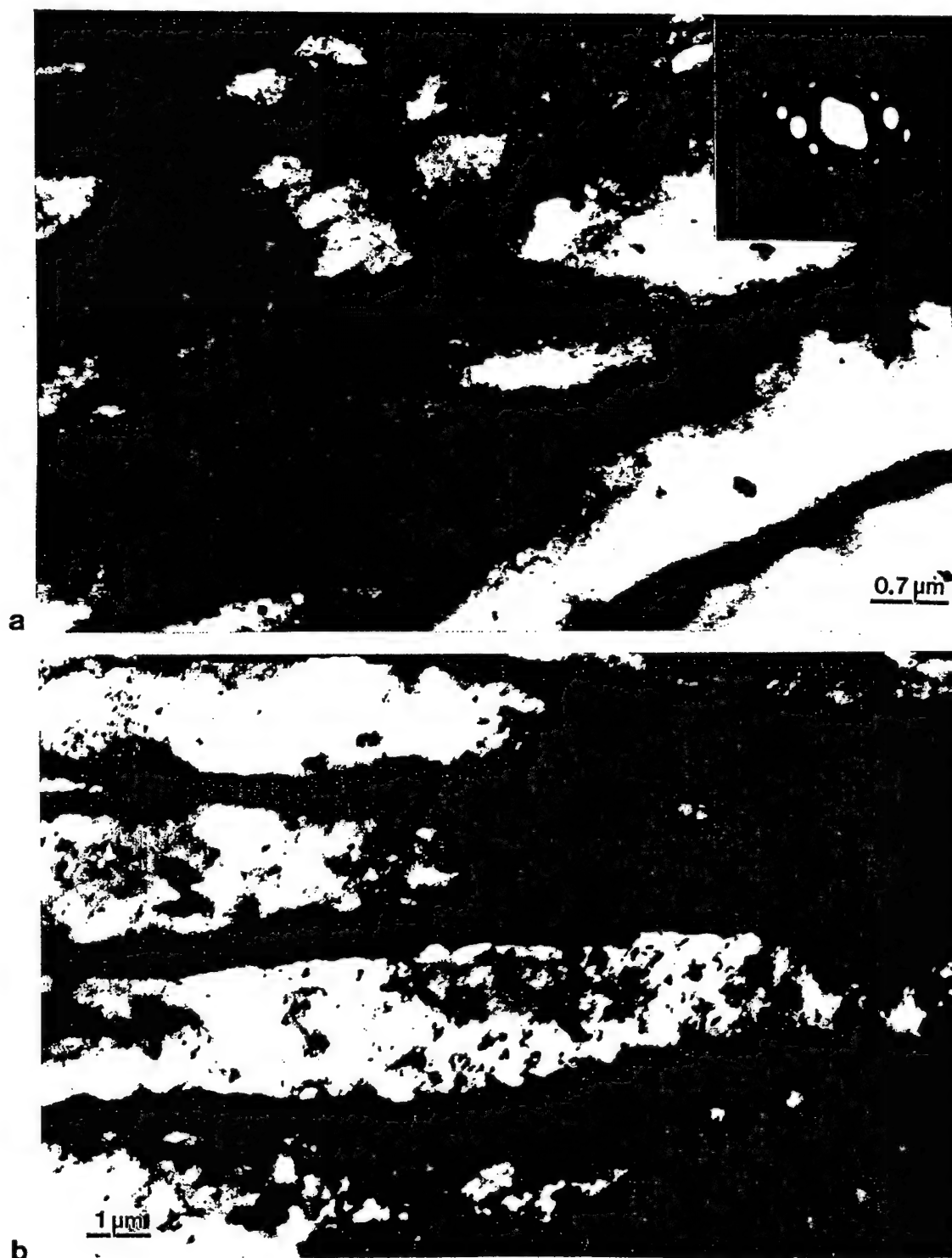


Figure 6.32: a) TEM image of band-like features that may correspond to the deformation bands observed in figure 6.33. b) SAD insert shows large misorientations associated with the microstructure.

region similar to that of figure 6.31, exhibiting band-like features that possibly correspond to the optical features of figure 6.31. The selected-area diffraction pattern shows a (112) grain surface orientation with misorientations as high as 15° . Deformation bands will accommodate a large orientation change, thus separating volumes of a common orientation, which will deform uniformly but with different combinations of slip systems [103].

6.4 Comparison of Target Deformation Behavior

It was previously seen that the dynamic deformation behaviors of the copper and aluminum alloy targets appear quite dissimilar at the macroscale, mesoscale and microscale. This is due largely in part to processing conditions, which affect the initial properties, and is also due to differences in properties that are inherent in both materials. This section will provide an in-depth comparison of the experimental results of both target materials and will relate deformation behavior to material properties.

6.4.1 Penetration Channel Analysis

A comparison of the penetration channels is shown in figure 6.33. There is a large variation in entrance and exiting diameters; Table 6.1 lists the differences between the channel geometries. Copper exhibits a large entrance diameter, 3 times that of the WHA rod diameter (0.78 cm), which increases significantly up to the exit diameter. The

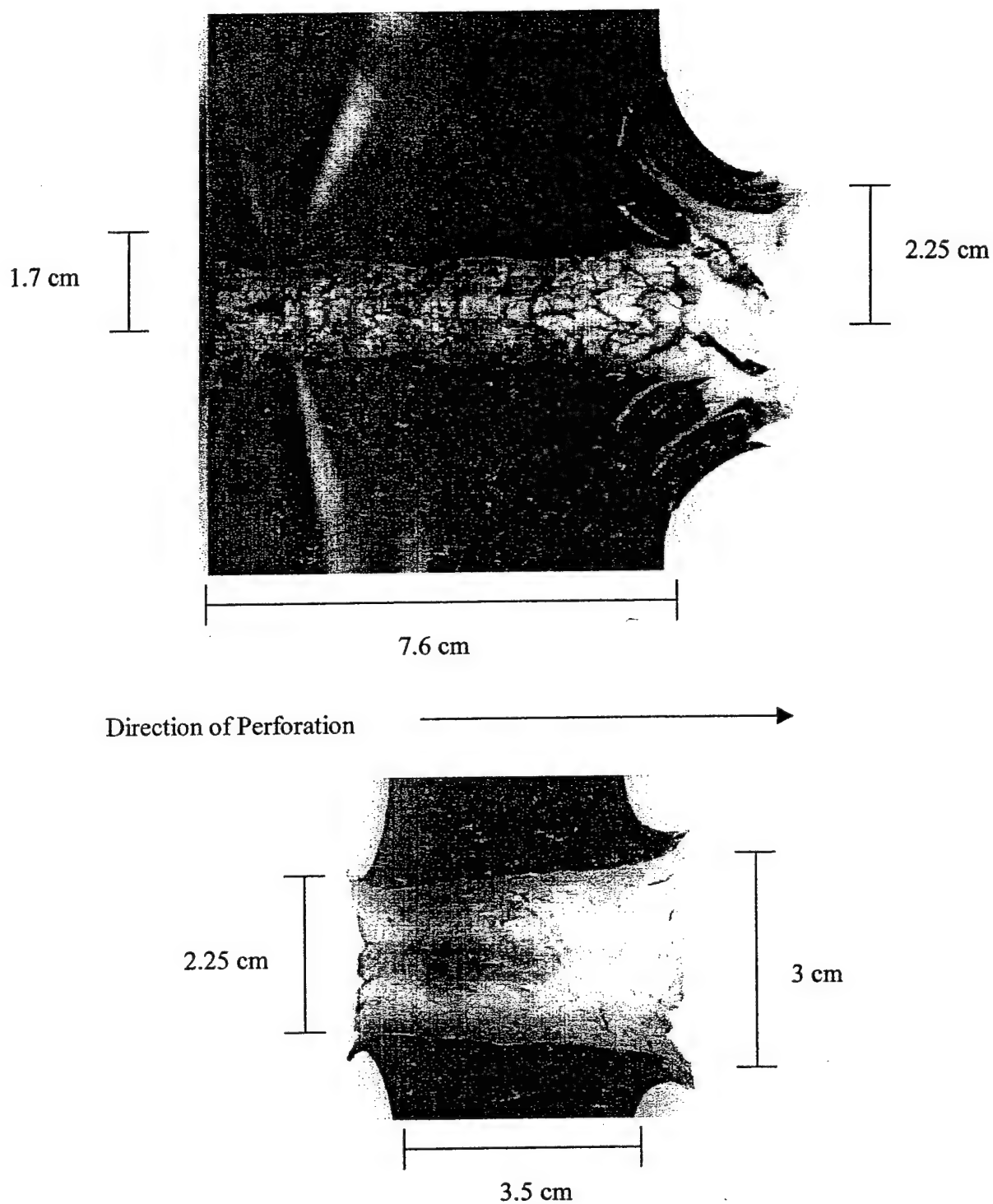


Figure 6.33: Comparison of the geometries of the penetration channels in the a) 7039Al and b) OFHC copper target.

channel is also associated with a large amount of plastic flow demonstrated by the cratering rim formation at the entrance and exit surfaces.

Table 6.1

**Comparison of Penetration Channel Geometry for the Copper
and Aluminum Alloy Target**

Geometrical Parameter	Copper Target Geometry	7039Al Target Geometry
Target Thickness (cm)	3.5	7.6
Entrance Diameter (cm)	2.25	1.7
Mid-channel Diameter (cm)	2.65	1.95
Exit Diameter (cm)	3	2.25

Channel formation in aluminum appears more complicated. The channel is not associated with ductile behavior as evident by the narrow channel diameter and substantial cracking at the breakout surface; however, there does appear to be a somewhat ductile tearing mode of failure at the exit surface resulting in large shear lips.

It is evident that a larger amount of energy is expended by the WHA projectile during perforation of the copper target. This is further substantiated by the eroded WHA fragments embedded along the channel wall. As such, it is expected that less rod erosion occurs in the impact of aluminum, and that residual rod velocity will be higher than in the case of copper impact.

The differences in penetration geometry may be explained by considering the stress-strain curves of figure 6.34(a) for the starting target materials. The severely work-hardened aluminum alloy exhibits a curve with a high tensile (T.S.) and yield stress (Y.S.). The heavy dislocation density generated during working of the metal requires a subsequent increase in flow stress to induce plastic flow. The fact that yield stress is slightly lower than tensile stress suggests that only a limited amount of deformation may be accommodated before fracture is induced. Annealed copper, with a low initial dislocation density can accommodate a much larger amount of strain before fracture.

6.4.2 Residual Microstructure Comparison

The stress-strain curves of figure 6.34(a) corroborate the gross plastic deformation of copper that occurs as a result of impact, as opposed to the limited plastic flow and highly localized deformation behavior of 7039Al. The microstructural profile of copper seen previously in figure 6.6 reveals the extent of deformation well into the material away from the channel wall. The highest degree of distortion occurs closest to the channel edge where pressures are highest during impact. Dissipation of pressure away from the channel results in an attenuation of deformed microstructure. Plastic deformation of aluminum, which was seen in figure 6.20, is optically confined to a narrow region along the channel edge and to localized bands running in the shear direction (shear bands).

Table 6.2 provides a comparison of observed microstructure and substructure as a function of distance from the channel edge. The evolution of microstructure in copper commences with a narrow zone of recrystallized grains observed along the length of the penetration

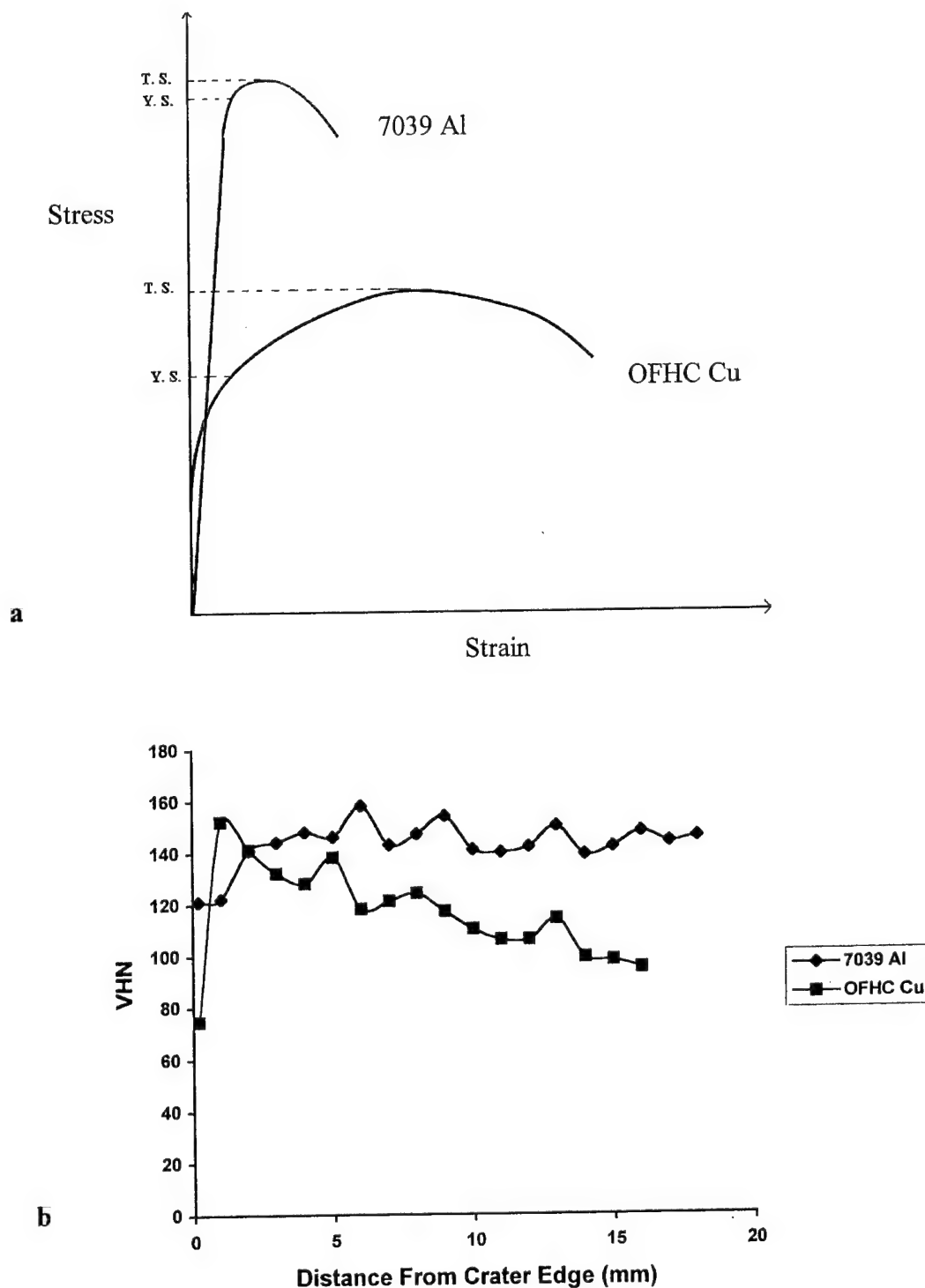


Figure 6.34: a) Stress-strain curves illustrating the different tensile behaviors of the copper and aluminum alloy starting materials. b) Comparison of hardness variations with distance from the channel wall in both residual targets.

channel. The high strains and high strain-rate in this region will result in adiabatic heating affects which appears to have reached the minimum recrystallization temperature of 200° C for copper ($T_r \approx 0.35T_m$) [104]. This is followed by a highly dense zone of planar defects (twins and microbands) and highly distorted grains resulting from shock-hardening by the high pressure affecting the region. This pressure in copper has been estimated to be ~45.5 GPa, significantly higher than the critical twinning pressure of 20 GPa [35] required for twinning in copper based on stacking fault energy. As the pressure attenuates with distance from the channel wall, so too does deformation decrease, returning to the base structure.

Table 6.2

Comparison of Deformation-Induced Microstructure

Distance from channel wall	Cu Microstructure	7039Al Microstructure
Surface of channel wall	Narrow zone (0.12 mm) of DRX	Very narrow zone of DRX - immeasurable
≤ 1 mm	Subgrains	Subgrains Dislocation cell structures Microbands
≤ 2 mm	Highly distorted grains Twins Microbands Subgrains	Dislocation cell structures Microbands Shear Bands
≤ 5 mm	↓	Microbands Deformation bands Shear Bands
≤ 10 mm	Slightly deformed grains Dense dislocation cells	Shear bands

Dynamic recrystallization on the channel surface in the aluminum alloy was observed through TEM, but not optically, suggesting an extremely narrow zone and the fact that the temperature rise may not have been sufficient for appreciable recrystallization. The recrystallization temperature for aluminum is estimated to be $0.35T_m$, or $\sim 210^\circ\text{C}$. Subgrains and microbands were also observed on the channel surface and in the narrow region of plastic flow near the channel edge. Beyond this region, little deformation of the microstructure is observed optically, save for shear bands and the appearance of deformation bands towards the cracked region of the channel. The substructure consists of microbands and dense dislocation cell structures up to 5 mm from the channel wall. Thus, unlike the well-distributed deformation in copper, plastic deformation in the aluminum alloy occurs in a localized manner. This is seen in the formation of shear bands, where local plastic deformation incurs a localized temperature rise resulting in thermal softening and failure of material in a band-like mode. It is also seen in the occurrence of microbands, which are considered to be a feature of localized plastic deformation [103]. Though deformation bands are not localized deformation per se, they are localized in regions of large strains where breakout of the projectile occurs, and these strains are accommodated by the re-orientation of portions of the grains in the form of bands. These localized shear regimes create a temperature spike and are referred to as adiabatic shear bands.

Therefore, bulk plastic deformation occurs in the copper target where slip occurs readily due to the annealed condition. Shear mechanisms also operate due to a lower stacking fault energy ($\sim 78\text{ mJ/m}^2$) than that of aluminum ($\sim 160\text{ mJ/m}^2$). The strain-hardened

and precipitation-hardened initial state of 7039Al results in a higher hardness and severely limited dislocation mobility. As a consequence, deformation is localized rather than large-scale. That is, there is no significant 'microscopic' slip and the material is forced to shear locally in order to accommodate deformation during penetration. The projectile flows through a very narrow dynamically recrystallized zone like a lubricant, but the large strains associated with the penetration are accommodated by adiabatic shear bands and the associated cracking.

Figure 6.34(b) gives a comparison of hardness variation with distance from the channel edge, where the readings were performed mid-channel on the cross-sectional surfaces of both targets. For copper, the initial drop in hardness (below base hardness of 90 VHN) corresponds to the region of dynamically recrystallized grains. This is followed by a drastic increase in hardness corresponding to the high density of planar defects, and the attenuation of deformed microstructure with distance from the channel is also reflected by the gradual decrease in hardness to the base value. The initial softening effect in the aluminum hardness plot corresponds to the narrow region of plastic deformation where recovery microstructures dominate. The hardness immediately returns to its base value (145 VHN) indicating very little deformation beyond this region.

There are several, dramatically distinct features which differentiate the penetration of copper and 7039Al targets by a WHA rod impacting at 1.5 km/s. The most apparent feature is the difference in the penetration channel size in relation to the penetrating rod diameter – almost twice as large for copper. The other obvious feature is the considerable cracking, especially at the back surface (or breakout surface) of the

7039Al in contrast to the copper target where there is no cracking. Since both materials are face-centered cubic (fcc) with relatively high stacking-fault free energies, the dislocation slip mechanisms will be similar. However, because the 7039Al is essentially fully work-hardened (fully hard), penetration will not be facilitated by dislocation slip. The copper target, on the other hand, can accommodate the strain imposed by the penetrating rod primarily through dislocation slip. Accommodation of strain also occurs through the generation of deformation microstructures (microbands, microtwins, and dislocation cells) along the penetration channel wall, and through the development of a zone of dynamically recrystallized material at the channel wall which facilitates perforation by the projectile.

Correspondingly, the 7039Al cannot accommodate any strain or strain energy (kinetic energy dissipation) associated with the projectile except in a narrow zone of dynamically recrystallized grains at the channel wall which facilitates penetration of the rod. Consequently, as the rod penetrates, there is a large strain energy gradient which accumulates ahead of the projectile. To accommodate this strain, the materials begins to form adiabatic shear bands which grow in size forming cracks, creating free surfaces which dissipate the large strain energy gradient (or kinetic energy). Since there is not appreciable slip, the penetration channel does not enlarge and the strain energy dissipates during breakout. There is, of course, some differences in penetrator erosion and interaction with the channel walls. This is apparent in the copper penetration channel where WHA erosion products were observed, especially near the exit surface, in contrast to no detectable product deposition in the 7039Al channel wall.

While in each case the projectile is accommodated by dynamic recrystallization, the accumulating strain energy cannot dissipate through homogenous slip mechanisms in the 7039Al target. Instead, heterogeneous and irregular shear bands develop to dissipate this energy. Shear bands, however, are also regions of dynamically recrystallized material, and as such the volume of recrystallized material may be similar in both residual targets.

6.4.3 Mechanisms of Failure

Dynamic recrystallization along the channel of the copper target is believed to be responsible for formation of the channel by facilitating the solid-state flow of material at the head of the projectile during perforation. It has already been seen that this solid-state flow, due to layers of recrystallized grains, is responsible for crater rim formation by the evidence in figure 6.9(a). This solid-state flow and dislocation slip in the target results in the ductile failure behavior of copper.

Though clear evidence of shear band substructure was not observed in this study, there have been numerous observations of recrystallized grains within shear bands throughout the literature [46,62-66]. Since this microstructure will have a lower flow stress than the material surrounding it, tensile stresses can initiate voids within shear bands leading to cracking and failure [105]. The shear-band initiated cracks in 7039Al results in failure that is brittle-like in nature.

Consequently, dynamic recrystallization is believed to be the mechanism of failure in the penetration of both the copper and aluminum alloy targets, but so-called

macroscopic strain is accommodated by dislocation slip in the copper while the 7039 aluminum forms adiabatic shear bands in gross localized flow regimes which becomes a precursor to failure.

6.4.4 Hardness Profiles of Cu and 7039Al

Microhardness indentations were performed over the entire cross-sectional surfaces of both targets to produce maps of hardness variations which correspond to variations in microstructure. The hardness profile of the copper target is shown in figure 6.35(a). The resulting zones of hardness correspond excellently to the evolution of deformed microstructure described previously in the residual copper. The recrystallized zone in the profile shows irregularity since the actual zone is very narrow. It does become more prominent in the vicinity of tungsten-alloy particles, however, and can therefore be measured in these areas. The zone of maximum hardness (corresponding to the high density of linear defects) is shown in red. Since axial symmetry is assumed for the materials surrounding the penetration channel, both surfaces of the half-section will share the same profile.

Since very little plastic deformation was observed in the 7039 aluminum target (only in the region 2-3 mm from the penetration channel), the corresponding hardness profile of figure 6.35(b) reveals a region of slightly lower hardness (120-135 VHN) than the base hardness (~160VHN). The fact that very little variation in hardness occurs in 7039Al, as compared to hardness in copper, corroborates the fact that deformation is highly localized.

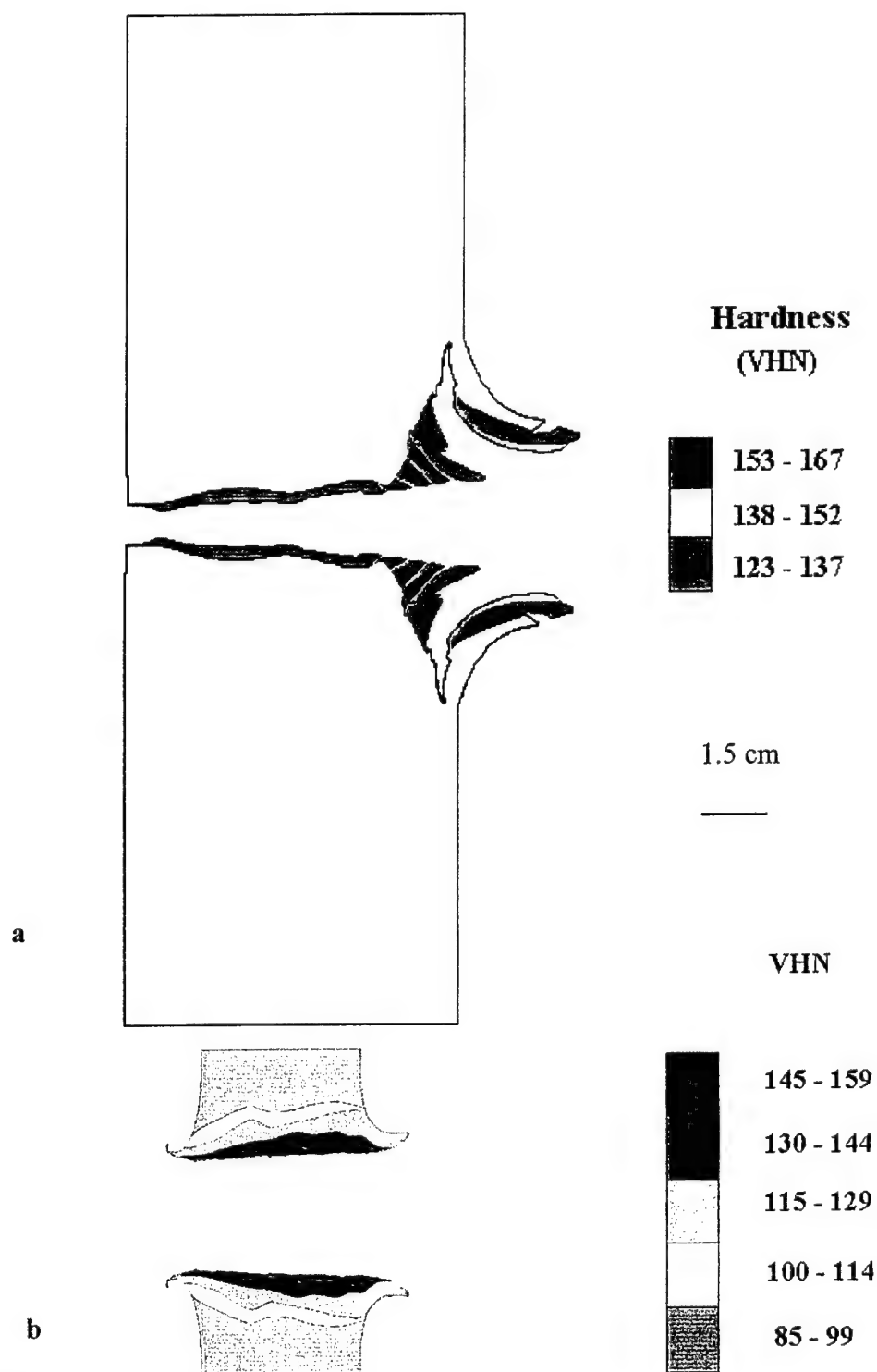


Figure 6.35: Computer generated yield stress contour plots for a) the OFHC Cu and b) 7039Al target. Aluminum shows limited variation in yield stress than Cu, consequently, deformation is localized

Since hardness can be correlated to the mechanical properties of a material, e.g. yield strength, the information furnished by the profiles can be used as additional parameters, namely property-based parameters, in the validation of the computer simulations performed by the AUTODYNTM hydrocode.

6.5 Computer Modelling of Cu

The ballistic impact of copper was modelled through the AUTODYNTM (version 4.1) two-dimensional hydrocode. An Eulerian subgrid was chosen to compute the large deformations typical of high-velocity impact. The strength model of Zerilli-Armstrong, a shock equation of state, and a bulk failure model were selected to predict the behavior of copper. For the tungsten-alloy projectile, the Johnson-Cook strength model, shock equation of state, and bulk failure model were selected. Other materials input parameters for this simulation have been listed in the appendix.

6.5.1 X-ray Radiography Validation

Flash radiography is routinely used in ballistic penetration experiments, among other impact experiments, to determine measured quantities that might be used to validate the values calculated through computer modelling of the impact event. These parameters can include the position of the depth of penetration, residual geometry of the projectile and target, and also position-time events such as time at impact and time at breakout.

Figure 6.36(a)-(b) shows a sequence of x-ray shadowgraphs for the perforation of the OFHC copper plate by the WHA projectile at 1.5 km/s impact velocity. The tungsten rod leaving the sabot at 1.5 km/s is shown in figure 6.36(a), while the figure 6.36(b) shows the projectile emerging from the rear surface of the target in debris cloud of rod and target fragments.

A comparison of the shadowgraph with the computer-simulated event is shown in figure 6.37. The simulation had been stopped at the point in which it resembled the shadowgraph of figure 6.37(b). Bearing in mind that the simulation presents a two-dimensional cross-sectional view of the impact event, it can be seen that the debris cloud formed in the simulation of figure 6.37(a) closely resembles that of the x-ray shadowgraph.

6.5.2 Geometry-Based Validation

For geometrical validation, a comparison is made between the cross-section of the residual crater and the simulated crater, shown in figure 6.38. The physical characteristics of the residual crater, such as the rim formation at the entrance and exit ends of the simulated crater, match fairly well to that of the experimental crater. Figure 6.39 shows the enlarged mapping of the exit rim formation in comparison to that of the simulated crater. In contrast to the solid-state flow at the entrance rim, which opposes the direction of perforation in the creation of a smooth rim, the exit rim appears fractured as a result of the 'stretching' of material as it flows and fails in the direction of perforation.

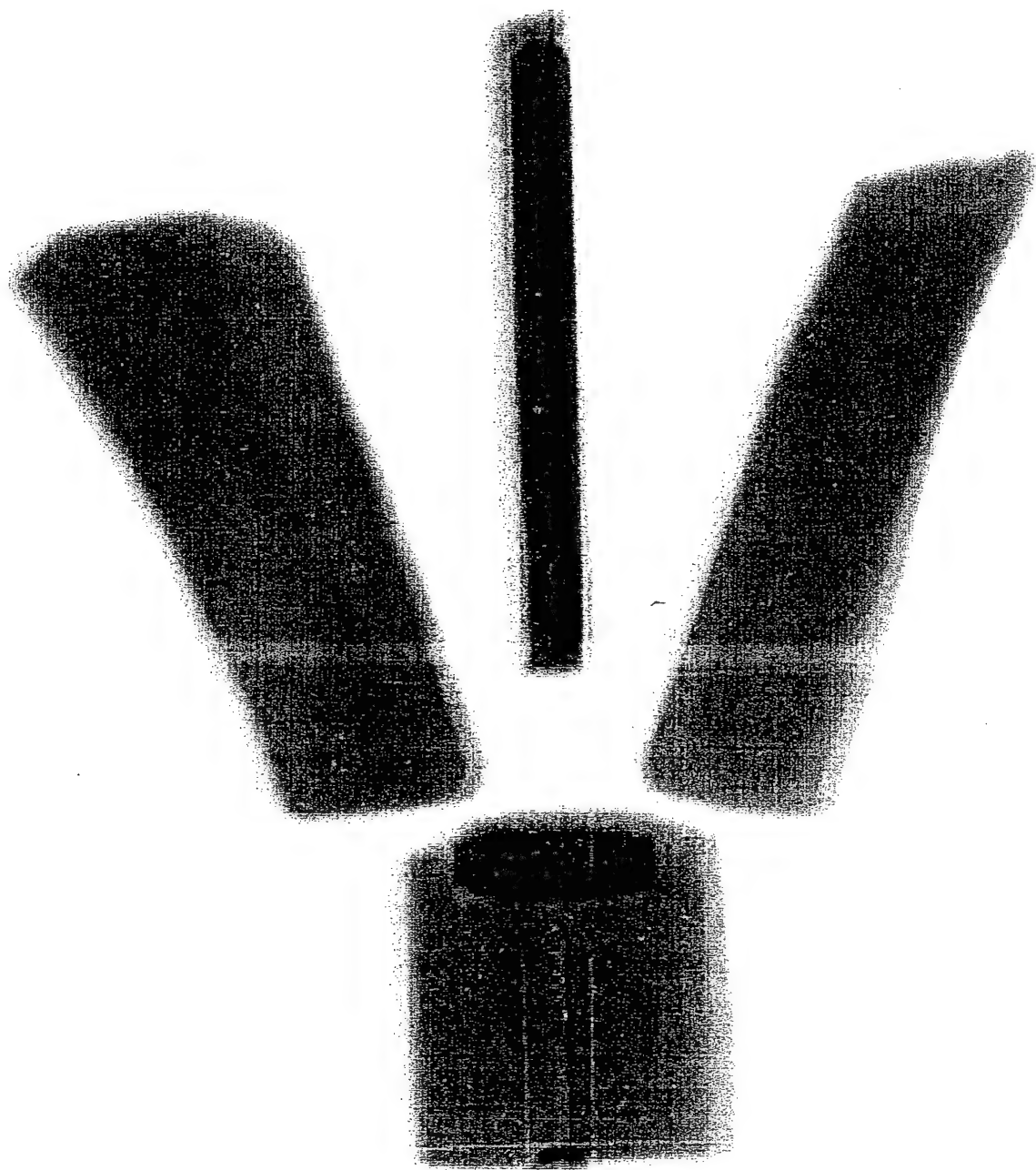


Figure 6.36: Flash x-ray radiograph sequence for a tungsten-alloy projectile perforating an OFHC copper plate at a velocity of 1.5 km/s, which begins with a) the projectile leaving the sabot at impact velocity.....

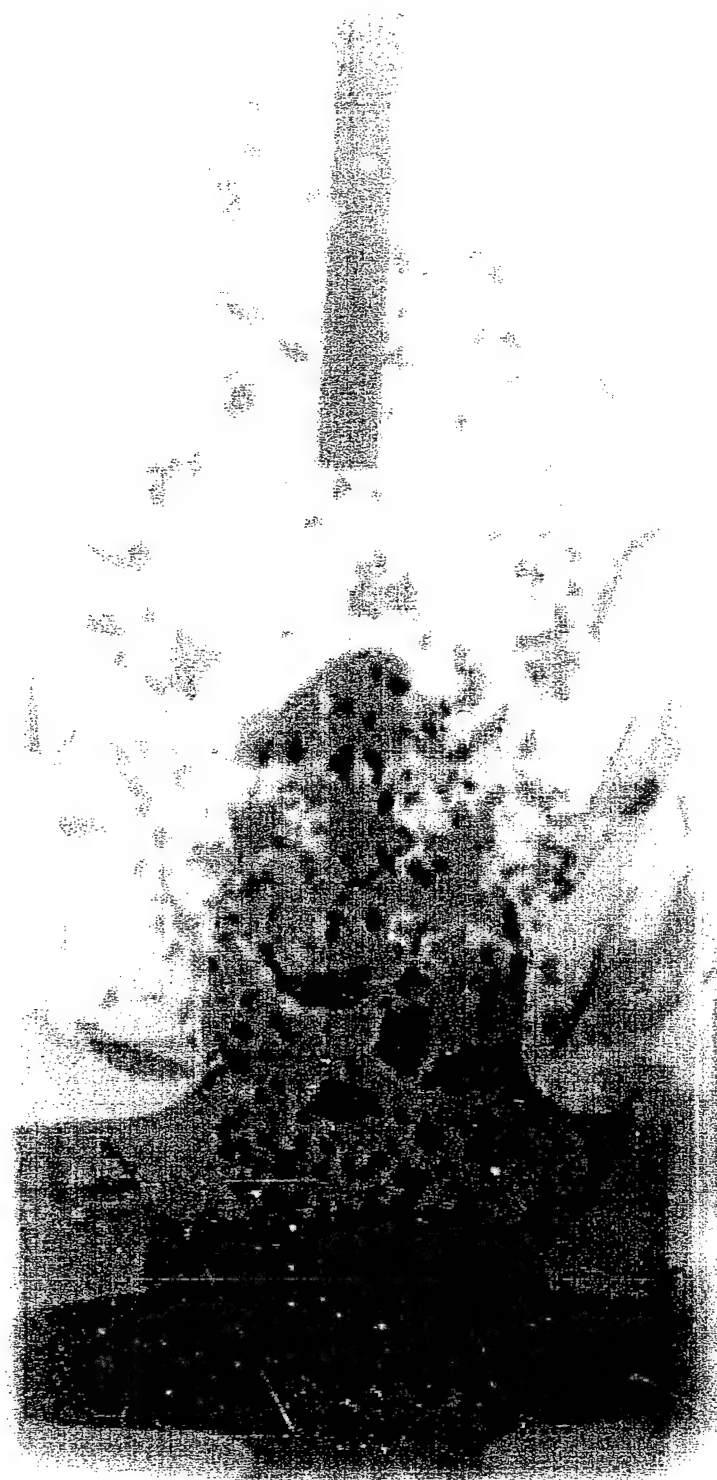


Figure 6.36: (con't) b) the tungsten-alloy rod exiting the rear surface of the target in a debris cloud.....



Figure 6.36: (con't) c) the final shape of the target alloy rod compared with the initial rod. Erosion products from the initial rod were observed to be embedded along the channel wall of the copper target.

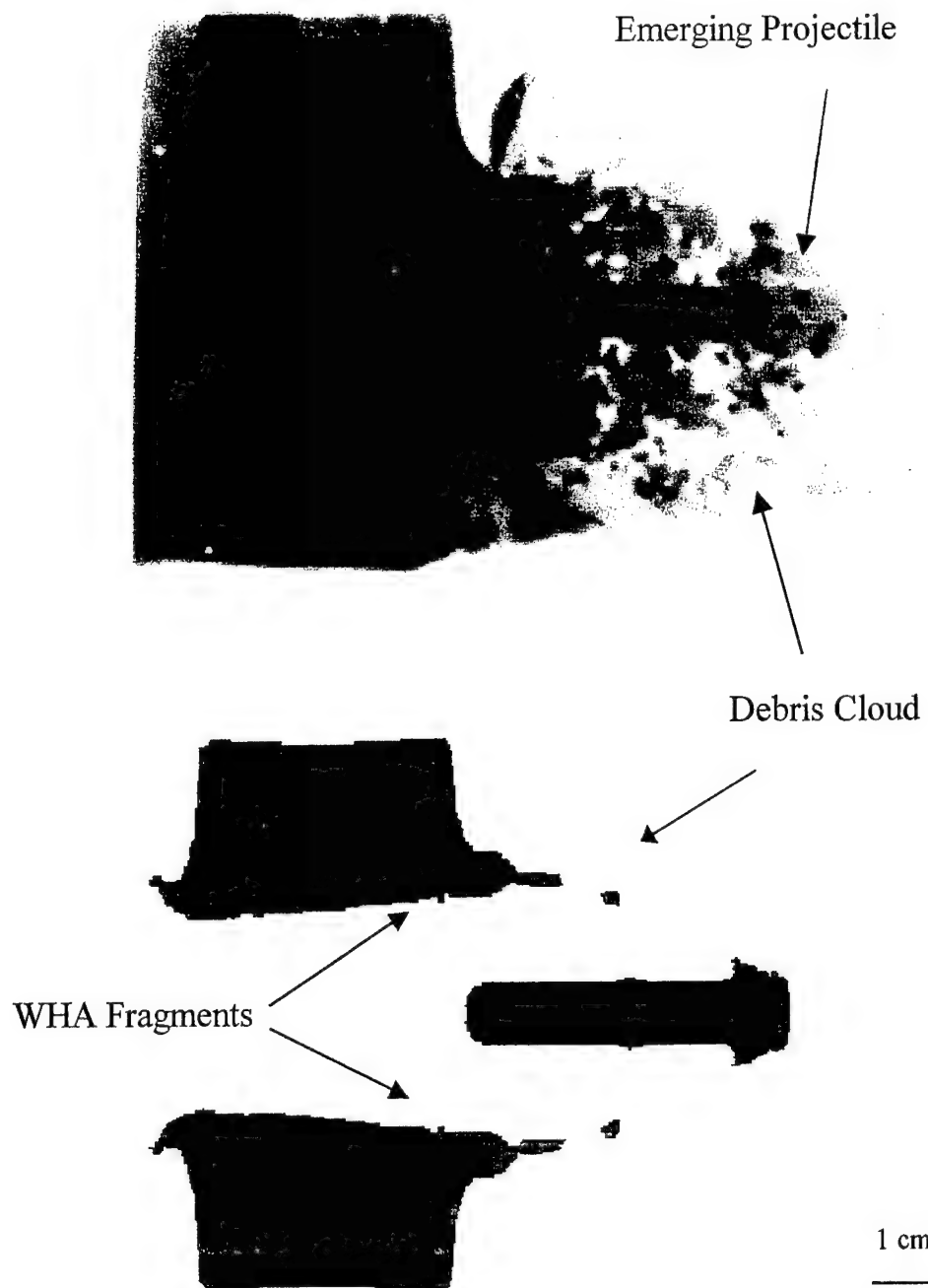


Figure 6.37: A comparison of a) the x-ray radiograph of the projectile leaving the back surface of the copper target, with b) the computer simulation of the same.

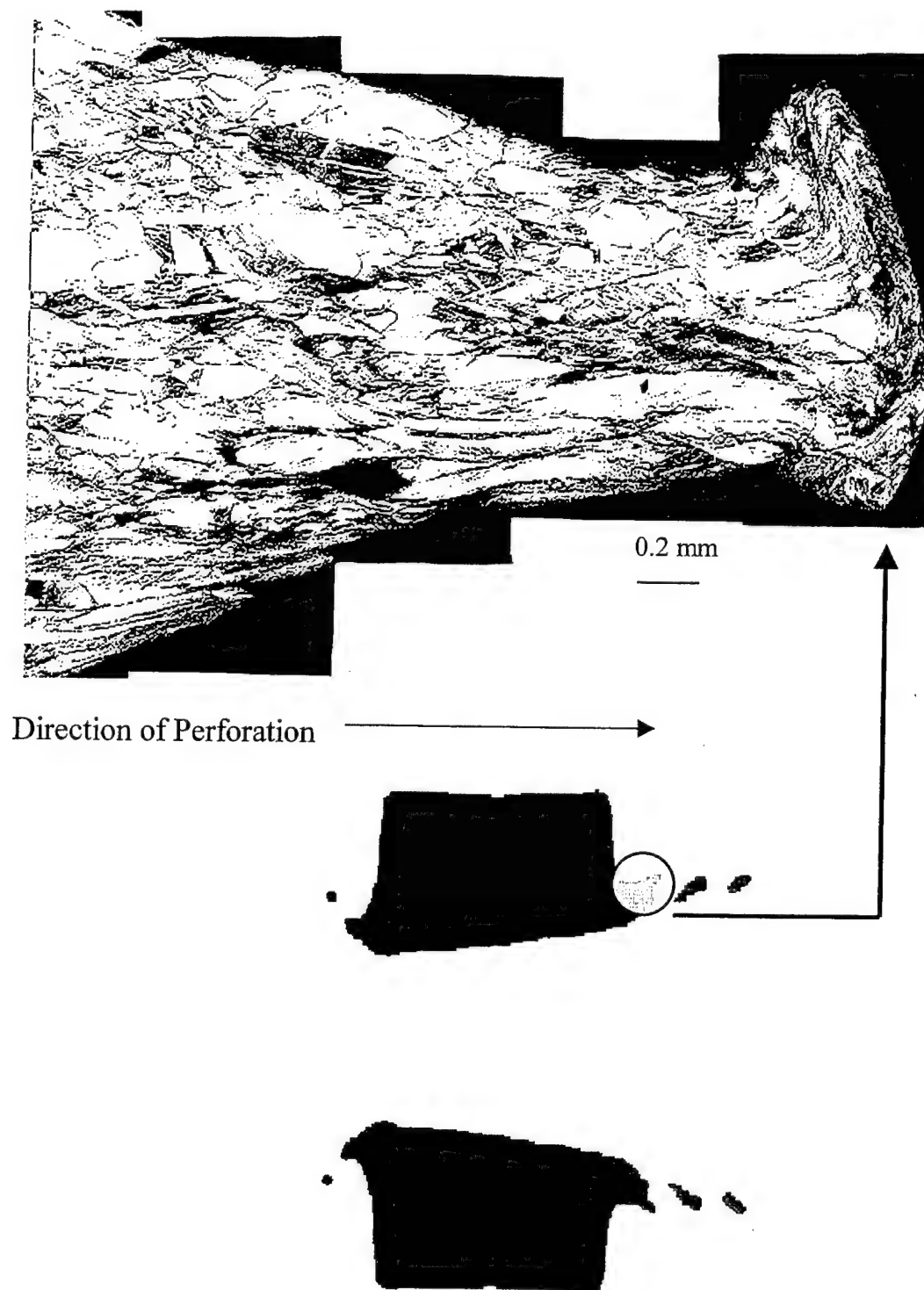


Figure 6.39: A comparison of the fracture features in the exit rim formation of the a) experimental (enlarged) and b) computer simulated crater.

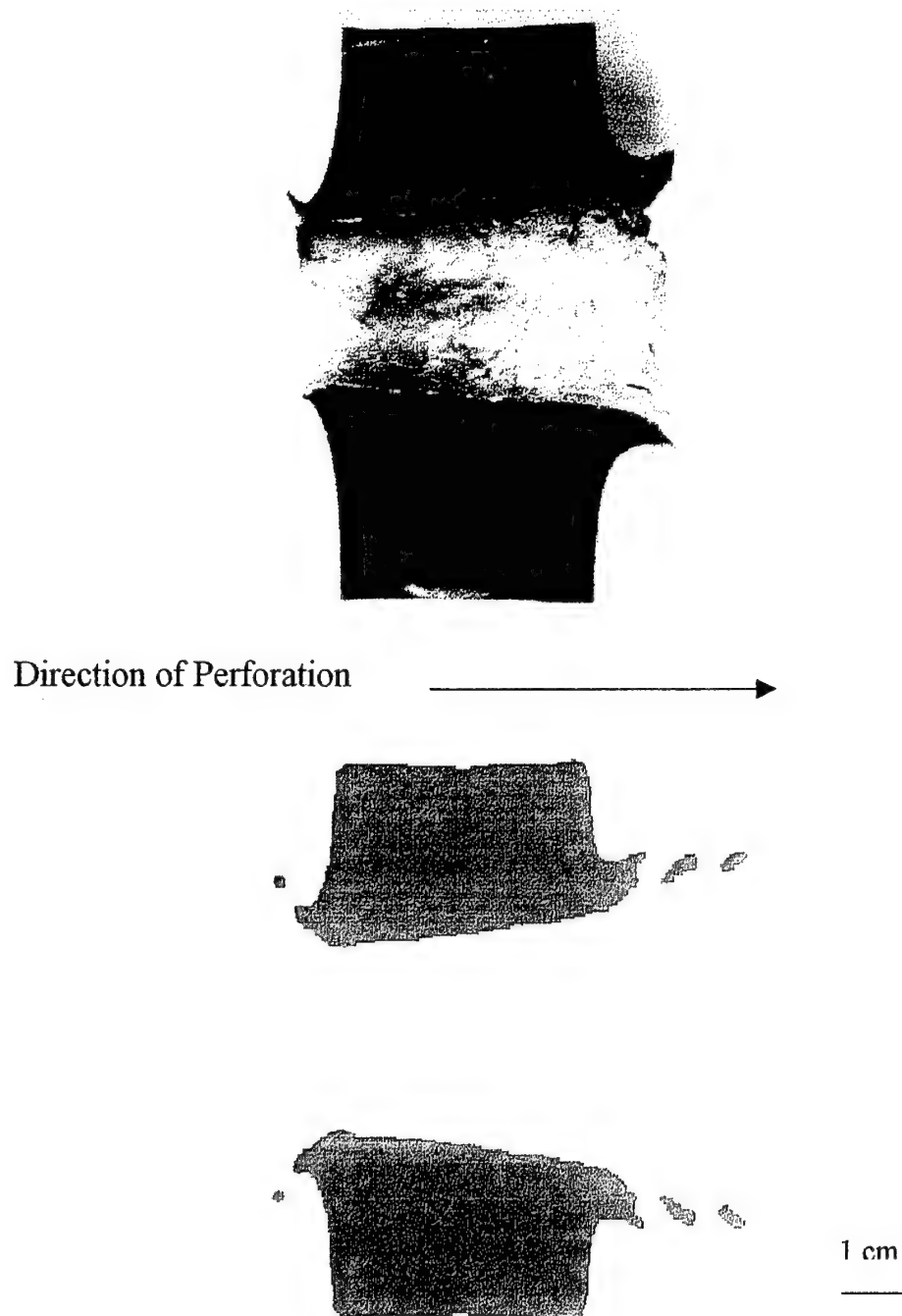


Figure 6.38: A comparison of a) the experimental half-section of the copper target and b) the computer simulated half-section.

Table 6.3 gives a comparison of geometrical parameters for the simulated and experimental residual crater. Though the simulated geometries are, on average, around 10% higher, than the experimental values, they are consistently higher; thus the ratio of exit to entrance diameter shows a rather good agreement.

The most notable feature of the simulation was the eroded tungsten-alloy (WHA) particles appearing along the crater wall, these are identified in figure 6.38(b). Remarkably, the hydrocode is capable of simulating the embedment of WHA erosion products along the channel wall (though few in number), which were identified in the SEM view of figure 6.3.

Table 6.3
Comparison of Cu Geometrical Parameters

Parameter	Experimental Results	Simulation Results
Entrance diameter (cm)	2.25	2.5
Diameter at center of crater (cm)	2.66	2.75
Exit diameter (cm)	2.82	3.2
Ratio of exit/entrance diameters	1.25	1.28
Diameter of entrance rim (cm)	2.98	3.5
Diameter of exit rim (cm)	4.02	4.75

Unfortunately, a comparison of the residual projectile, in both the simulation and the x-ray shadowgraph, revealed that a higher amount of erosion occurs in the simulation (43%) compared to that of the actual experiment (26%). Though the resultant residual

length of the simulation projectile was inaccurate, possibly due to an inadequate material description of the complex WHA microstructure, the geometry of the simulated crater shows a good agreement to the actual crater geometry; in this respect modelling of the copper target can be considered successful.

6.5.3 Property-Based Validation

A residual yield stress contour plot from the simulation is compared to the experimental hardness plot in figure 6.40, for a materials property validation. Using the conversion: $0.01 \text{ Mbar} = 1 \text{ GPa} = 100 \text{ VHN}$, it can be seen that yield stress values for the zones in the simulation and hardness profiles show a strong similarity. The evolution of yield stress in the simulation corresponds quite well to the evolution of microstructures indicated by the hardness profile. Also, there are discontinuous regions of highly 'soft' zones along the channel edge of the simulation; this can be related to the exaggerated regions of dynamic recrystallization that yields a lower hardness in the experimental crater.

6.5.3 Additional Hydrocode Predictions

The successful validation of the material modeling of copper, through geometry and a material property, gives increased confidence in analyzing additional contour plots for a better understanding of the perforation process.

Figure 6.41 shows a plot of the initial set-up for impact, where target points have been specified on the initial copper plate. All target points are located on the line of

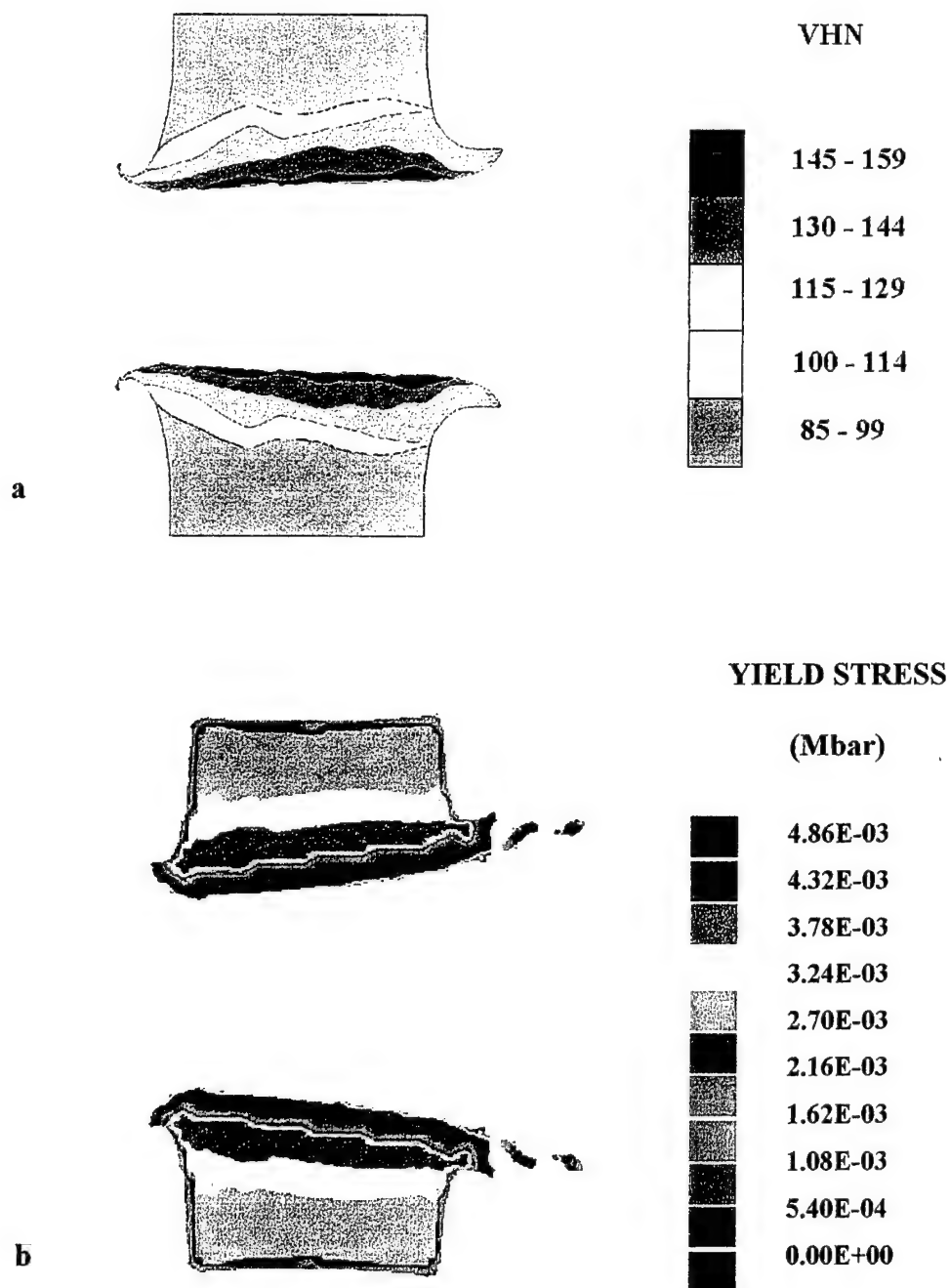


Figure 6.40: a) Copper hardness profile showing variations in hardness with respect to deformed microstructure. b) Computer simulated yield stress contour plot for comparison with a) in a validation that is based on material property.

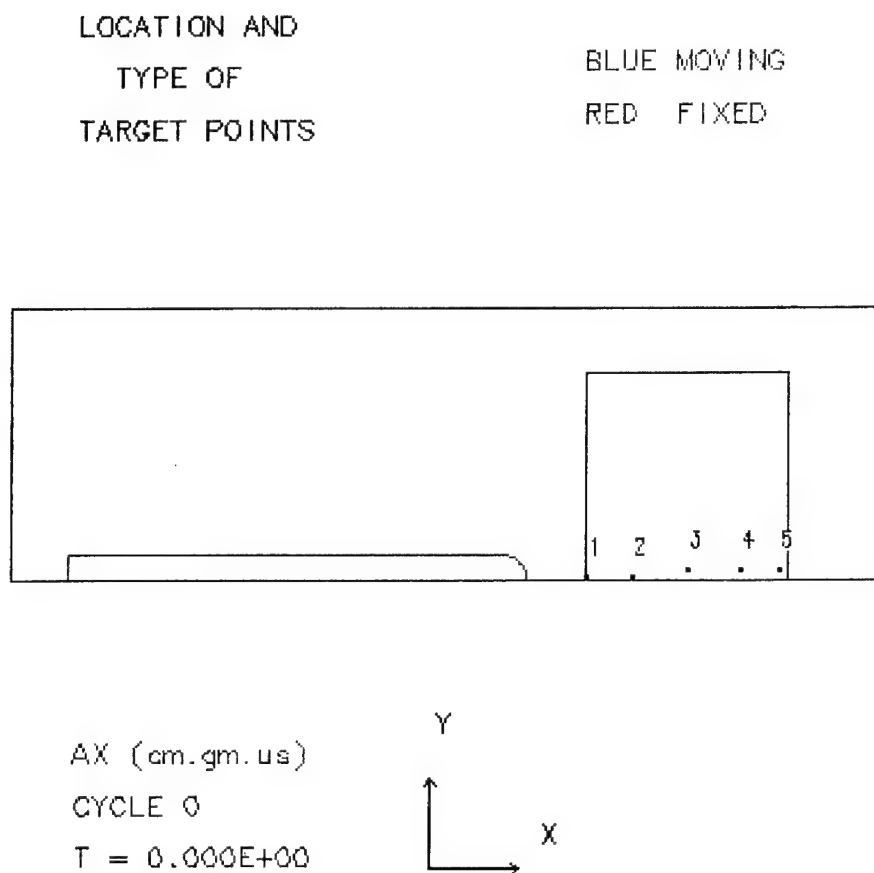


Figure 6.41: Computer plot showing the location of selected targets points on the initial copper target. The target points will provide histories for selected variables.

impact. Figure 6.42 shows history plots generated for pressure and effective plastic strain. The pressure vs. time plot of figure 6.42(a) reveals that maximum pressure occurs at the instant of impact, at a value of ~ 60 GPa, decreasing as penetration continues. In comparison, the Hugoniot pressure at impact was estimated to be roughly 45.5 GPa [30]. Effective plastic strains, shown in figure 6.42(b), appear to be consistent throughout penetration at 0.5.

The temperature vs. time history plot is shown in figure 6.43. The plot indicates that a high temperature (800 K) is reached during the initial phase of impact, and this corresponds to the high pressure experienced at the start of impact (figure 6.42(a)). Since dynamic recrystallization for copper occurs at $\approx 0.35(T_m)$, then the recrystallization temperature would be approximately 475 K, and it can be inferred from the plot that temperature is responsible for recrystallization at the beginning of the cratering process where subsequent solid-state flow of recrystallized grains results in rim features. With time, temperature decreases to below 400 K, and it is likely that other means of recrystallization will dominate, such as the high strains which are consistent throughout the penetration process (figure 6.41(b)).

6.6 Computer Modelling of 7039Al

The ballistic perforation of aluminum was likewise simulated using the AUTODYNTM software. Though the actual impact experiment involved a two-layer target configuration of a softer aluminum plate in front of the 7039Al target plate,

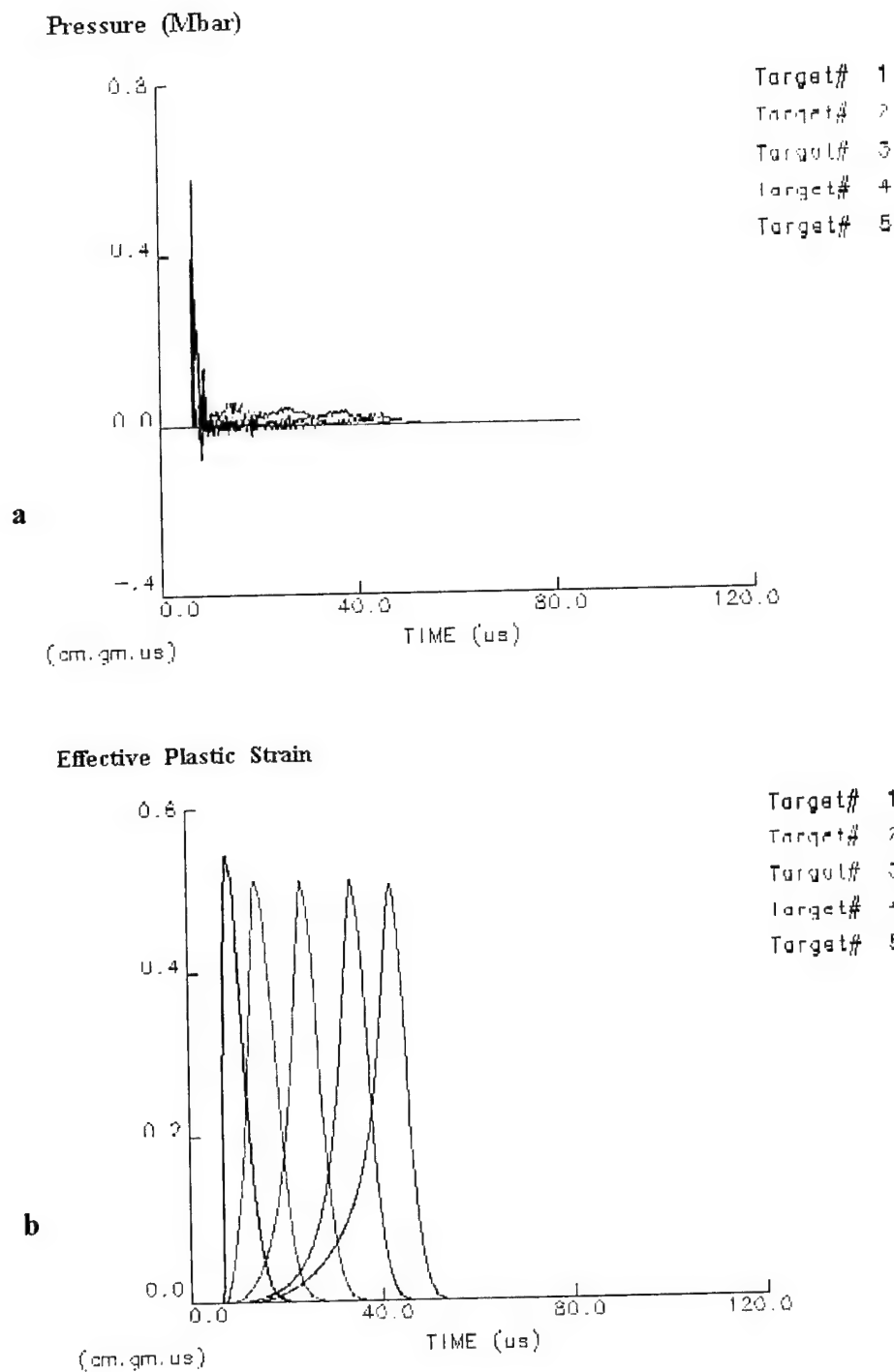


Figure 6.42: History plots of a) pressure vs. time and b) effective plastic strain vs. time showing the respective variations at the selected target points.

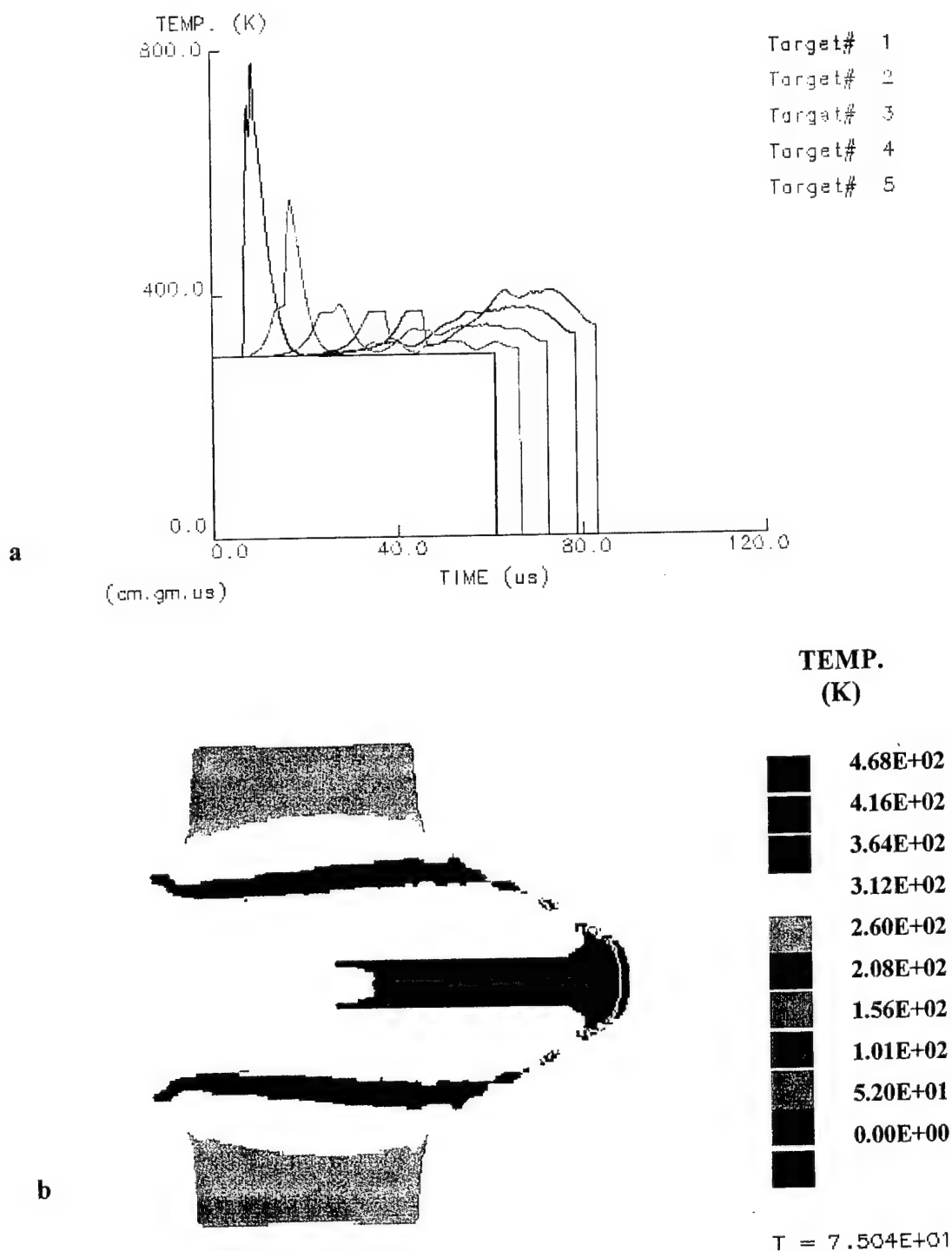


Figure 6.43: a) History plot of temperature vs. time for the perforation of copper. b) Temperature contour plot at 75 μ s after impact.

simulations were performed with the 7039Al plate in a monolithic configuration initially to determine the appropriate failure and strength parameters for the target and projectile. The same parameters were then used in the impact of the two-layer configuration. Also, two simulations were performed, one using an Eulerian subgrid, the other an SPH subgrid. The shock equation of state and Johnson-Cook strength model were incorporated into both simulations for the modeling of aluminum. Different failure models were chosen; a principal stress model was chosen to model brittle behavior for the SPH subgrid, and a Hydrodynamic Tensile Limit model was selected to model possible spalling in the Eulerian subgrid. Additional input parameters have been listed in the appendix.

6.6.1 Geometry-Based Validation of Monolithic Target

The simulation of monolithic aluminum perforation in an Euler subgrid is shown in figure 6.44(b). The experimental crater is also shown for comparison (figure 6.44(a)). Physically, the simulation appears to show a large crack near the exit surface, similar to the actual crater. However, the fractured shear lips of the simulation appear to slope downward, in contrast to the experimental crater, and there is an absence of a crack pattern at the exit end of the channel. Geometrically, the comparison of parameters in Table 6.4 for the simulated and experimental crater shows very little agreement, with the exception of the diameters at mid-channel, though in both cases the diameters increase from entrance to exit and there is irregularity in the appearance of the penetration channels in both cases. The simulation of ballistically impacted aluminum using an SPH

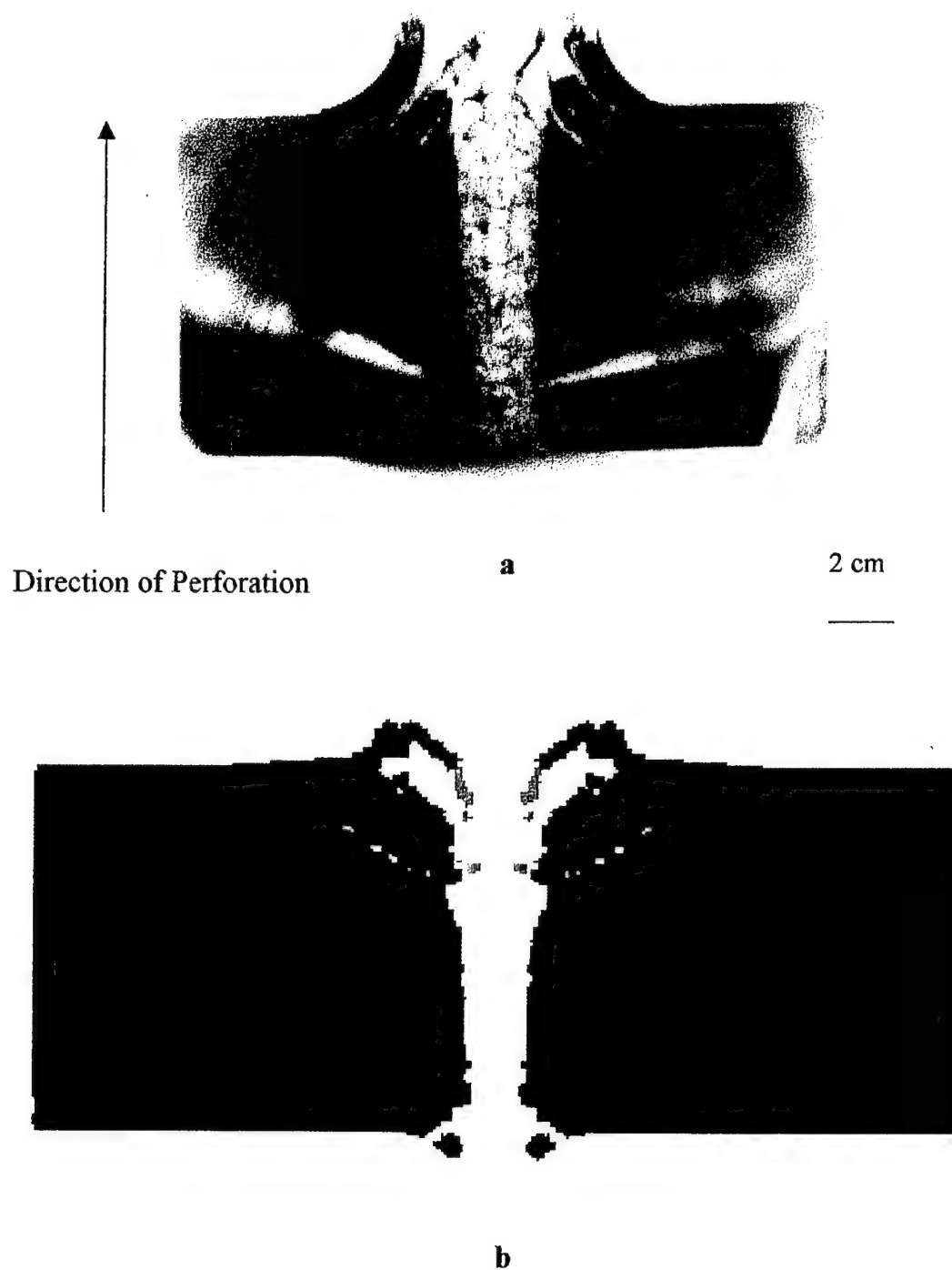


Figure 6.44: Comparison of a) the experimental 7039Al penetration half-section to b) the predicted half-section (Euler).

subgrid is shown in figure 6.45(b). The combination of subgrid and failure model (Principal Stress) seems to have an advantage over the previous simulation; a crack

Table 6.4

Comparison of Al Geometrical Parameters (Euler)

Parameters	Experimental Results	Simulation Results
Entrance diameter (cm)	1.63	2.65
Diameter at mid-channel (cm)	1.55	1.52
Exit diameter (cm)	2.17	5.1
Ratio of diameters	1.33	1.92
Width of apparent spall crack (cm)	7.76	5.1

pattern can be observed at the exit end. Up on closer inspection, however, the pattern appears to be opposite that of the actual crater. Cracks appear to be propagating away from the channel walls. Similar to the previous simulation, there is very little correspondence between the geometry of the simulation and that of the experimental ring crater. The comparison is shown Table 6.5. To determine how failure occurs during breakout of the projectile, a time-lapsed sequence of the penetration process is shown for both aluminum simulations in figure 6.46, and these are compared to the time-sequenced failure of copper. The aluminum penetration plot for the Euler simulation (figure 6.46(a)) shows that spalling does not occur as initially believed, but rather failure occurs through a plugging mode, where the material at the head of the projectile is constrained

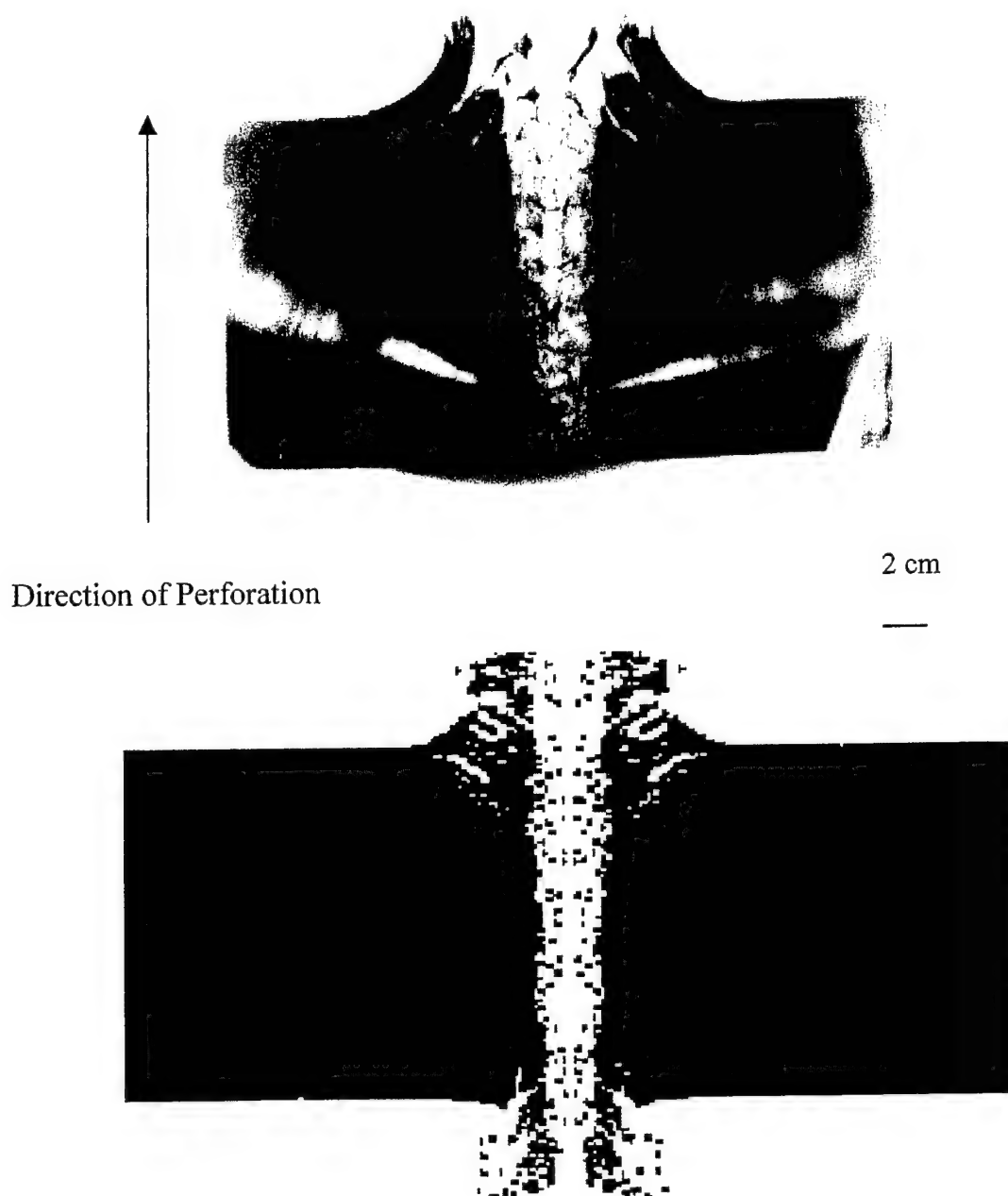


Figure 6.45: Comparison of a) the experimental 7039Al penetration half-section to b) the predicted half-section (SPH).

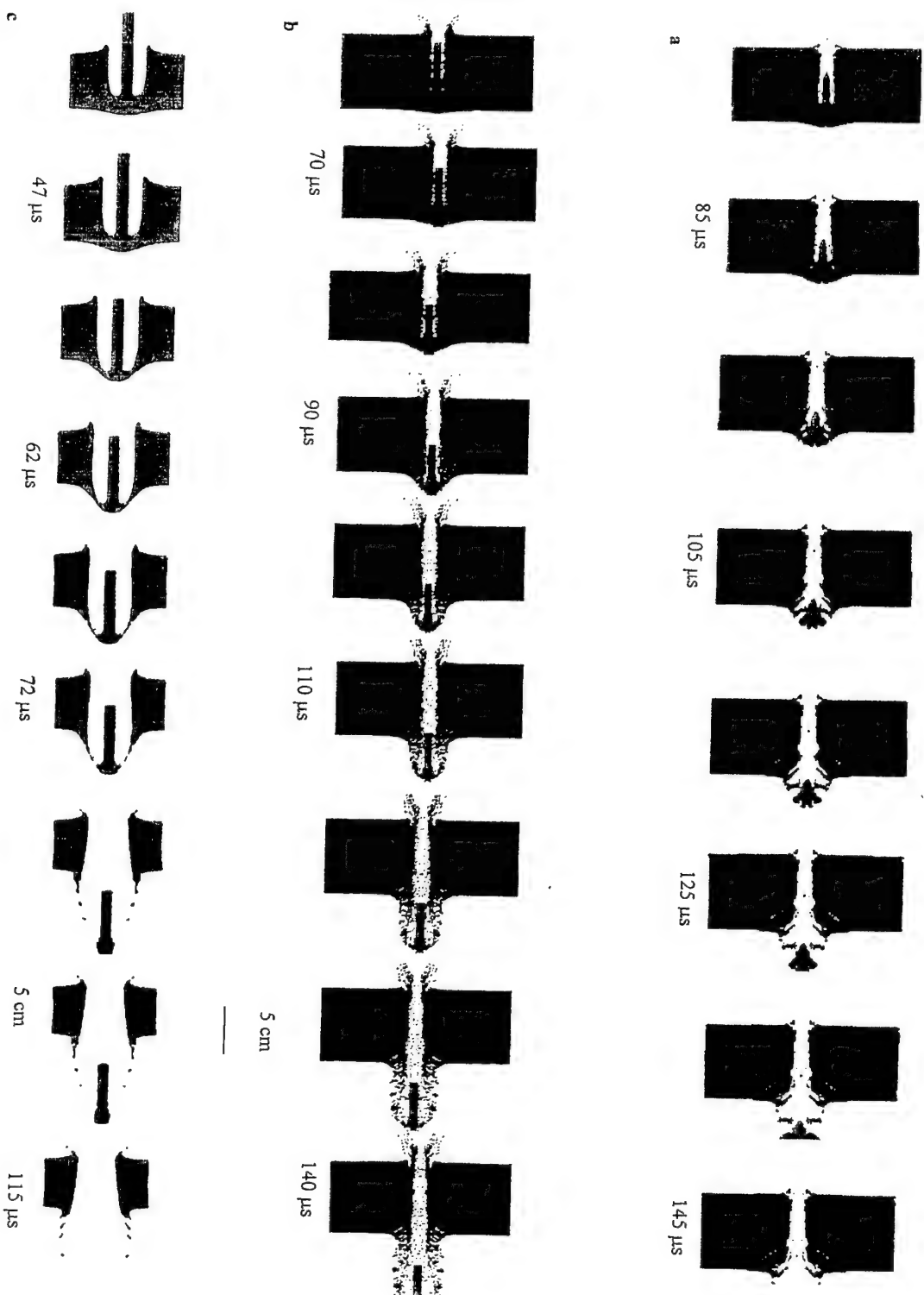


Figure 6.46: Time-sequence for the perforation of a) 7039 Al (Euler), b) 7039 Al (SPH), and c) OFHC copper.

Table 6.5
Comparison of Al Geometrical Parameters (SPH)

Parameter	Experimental Results	Simulation Results
Entrance diameter (cm)	1.63	3.17
Diameter at mid-channel (cm)	1.55	1.35
Exit diameter (cm)	2.17	1.58
Ratio of exit/entrance diameters	1.33	0.5
Width of spall crack (cm)	7.76	5.88

(through shear banding) to continue moving ahead of the projectile, resulting in a plug [106]. In contrast, the projectile completely perforates the copper target through the large plastic 'stretching' of the copper material until failure occurs.

The time-sequence plots also illustrate the incorrect erosion of the tungsten-alloy projectile. It was mentioned in the previous discussion on the simulation of copper impact that the predicted residual rod erodes almost twice as much as that illustrated by flash x-ray radiographs. In figure 6.46(a), the rod erodes almost completely, while in figure 6.46(b) the rod remains fairly intact. Either the simulation technique (Euler or SPH) or the different failure models used may have an effect on rod erosion, but it is more likely that the constitutive modelling of WHA is inadequate since both the Johnson-Cook and Zerilli-Armstrong models, when applied to the simulation of figure 6.46(a), gave similar results.

6.6.2 Property-Based Validation of Monolithic Target

Figure 6.47 shows the comparison of the residual microhardness profile for the 7039Al half-section with the yield stress contour plot generated by the simulation of aluminum impact using an Euler subgrid. The simulations are similar in that both show very little variation. However, the computer simulation shows a variation in yield stress that begins with higher values near the penetration channel which decreases to the base hardness. This is in contrast to the hardness map, which shows lower values near the channel wall, where limited plastic flow was observed, and this increases to the base hardness. Both show higher hardness at the breakout region.

Figure 6.48 gives the comparison between the experimental profile and the yield stress plot for the simulation in which an SPH subgrid was used. In the simulated plot the values near the channel wall are comparable to the experimental profile, where slight softening occurs, though the values increase further away from the channel wall and then decrease to a yield stress less than the initial value for the aluminum alloy.

The discrepancies in the geometry and property-based validation of the numerically predicted results further reinforces the idea that more variables should be involved in the validation of simulated impact for better reliability and increased confidence in using the code for further analysis of the experiment. Since it was observed that the aluminum alloy exhibits more complex deformation behavior, in the form of shear bands, it may be advisable to incorporate a constitutive model for shear banding in the 7039Al strength model. It must be emphasized that the Johnson-Cook constitutive equation is a simple curve-fitting procedure [104]. The three effects of work hardening,

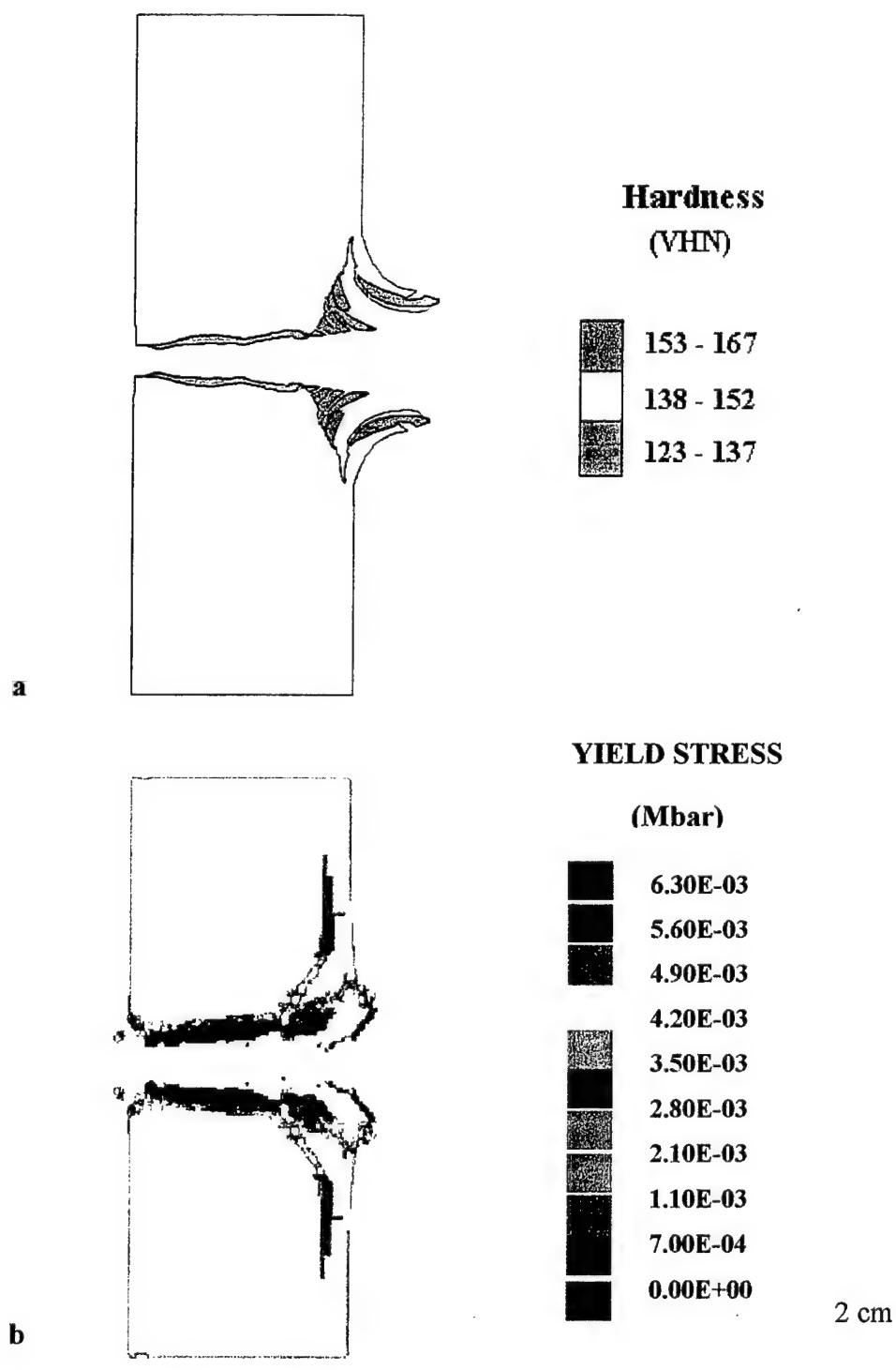


Figure 6.47: a) 7039Al hardness profile showing slight softening near the penetration edge and maximum hardness at the breakout region. b) Simulated yield stress contour plot (Euler) showing limited variation similar to a).

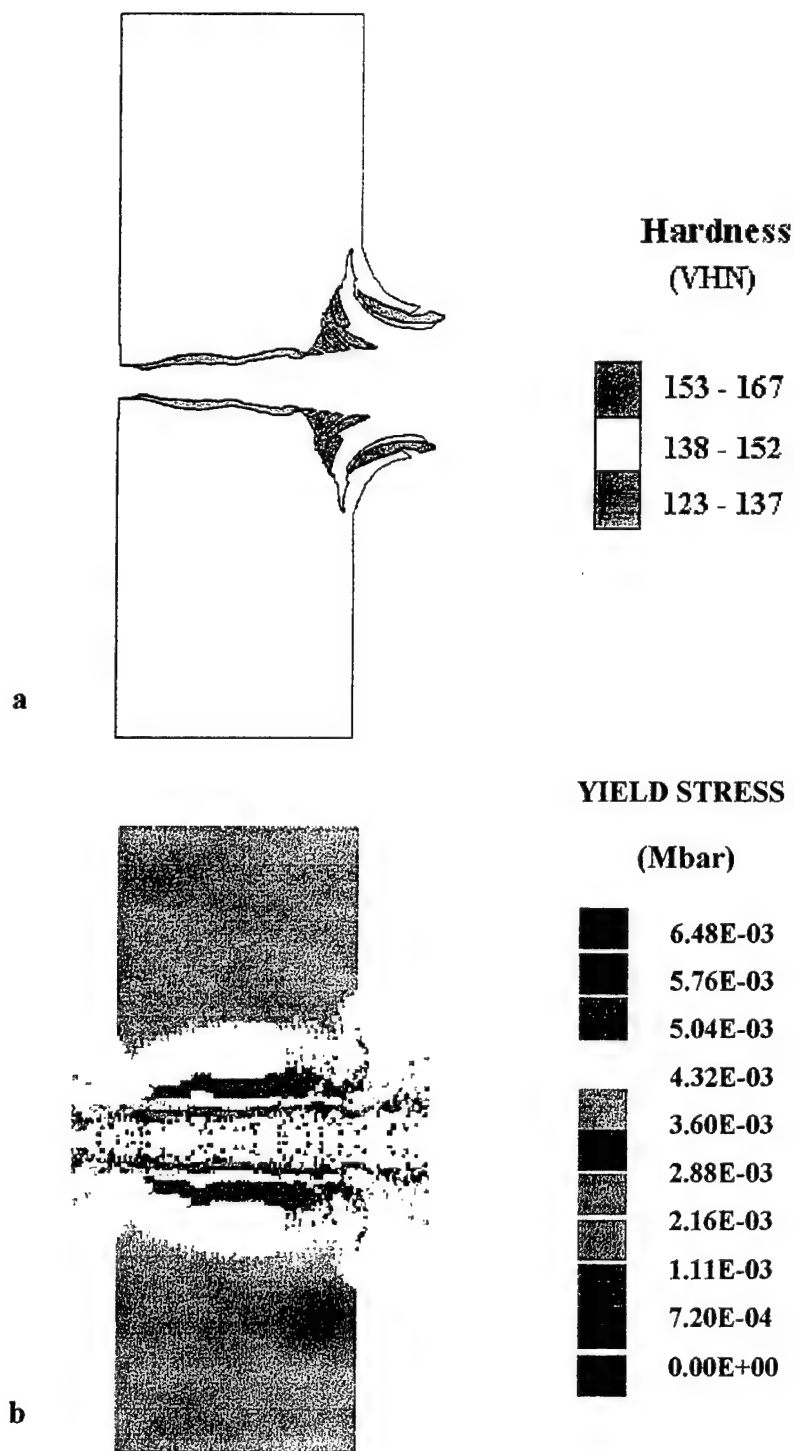


Figure 6.48: Comparison of a) 7039Al hardness profile with b) the predicted yield stress contour plot for the SPH subgrid, which shows some softening at the channel edge, but too much variation with distance from the crater.

strain-rate hardening, and thermal softening are multiplied by each other in the equation; the rate of work hardening will therefore increase with decreasing temperature and increasing strain. Modifications to the equation are necessary to account for a flow stress drop as a result of a change in mechanism (such as dynamic recrystallization) or phase change.

In fact, Andrade et al. [107] have proposed a modified Johnson-Cook equation that incorporates a flow stress discontinuity due to dynamic recrystallization (the microstructure within shear bands), that should create a more realistic representation of localized behavior. The proposed equation has the following form:

$$\sigma = (\sigma_0 + B\epsilon^n) (1 + C \log \epsilon/\epsilon_0) [1 - (T - T_r / T_m - T_r)^m] H(T) \quad (27)$$

$$H(T) = 1 / 1 - \{1 - [(\sigma_f)_{rec} / (\sigma_f)_{def}] \} u(T) \quad (28)$$

where $u(T)$ is a step function of temperature defined as:

$$u(T) = \begin{cases} 0 & \text{for } T < T_c \\ 1 & \text{for } T > T_c \end{cases} \quad (29)$$

where T_c is the temperature at which the critical phenomenon (dynamic recrystallization) occurs and $(\sigma_f)_{rec}$, $(\sigma_f)_{def}$ are the flow stresses of the material just after and prior to the critical phenomenon, respectively.

6.6.3 Impact in the Two-layer Configuration

The materials parameters used for the previous predictions of aluminum perforation were applied to the simulation of 7039Al perforation in the two-layer

configuration. The starting aluminum plate was assumed to be a softer, purer aluminum than the work-hardened 7039Al plate.

Figure 6.49 shows a comparison of the Euler simulations for 7039Al in the monolithic and two-layer configurations. The features of the starting aluminum crater match fairly well to the actual crater. However, the impact configuration alters the failure behavior of the 7039Al block. The penetration channel is wider at the entrance surface and there is less cracking in the breakout region.

Figure 6.50 shows the comparison of SPH simulations for both the two-layer and monolithic configurations. In this case the 7039Al target loses the crack pattern formed in the single target condition. In the two-layer configuration, failure becomes more complicated since both target materials will have an effect on one another and the manner in which each fails. Generating an agreeable prediction in this case would require determining the appropriate failure parameters and strength parameters (e.g. initial yield strength values) for the three materials involved. Though it has been determined, both experimentally and numerically, that modelling of the complex failure of 7039Al (and possibly the WHA) would require a specialized constitutive model to incorporate the effects of localized deformation. Irregular, localized shear is not a feature of either the Johnson-Cook or Zerilli-Armstrong constitutive relationships, as a consequence, computer simulations for the impact of 7039Al are not very accurate compared to the simulations of the copper penetration phenomena.

The results to this study point to the fact that computer simulations which are applied without adequate validation, based upon microstructures and fundamental

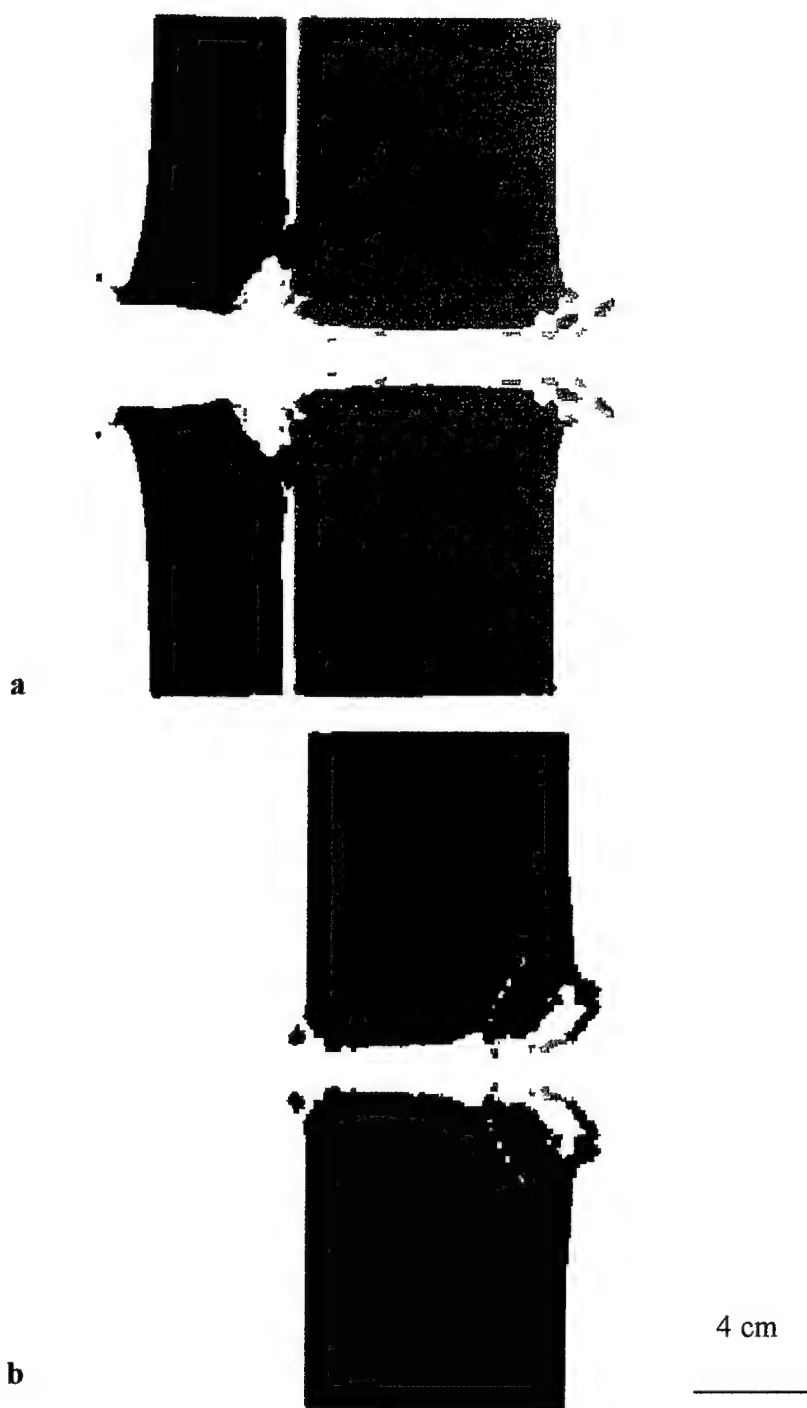


Figure 6.49: Comparison of the simulated (Euler) impact of 7039Al in the a) two-layer and b) monolithic configuration. The same parameters were used for 7039Al in both cases.



Figure 6.50: Comparison of the simulated (SPH) impact of 7039Al in the a) two-layer and b) monolithic configuration, using the same input parameters for 7039Al.

mechanisms contributing to these microstructures, may be completely erroneous. The results also point out that in order to assure valid simulations, every system must be experimentally tested. Results for one system may not apply to another even in the same crystal system; one reason being the state of the microstructure or the stage of work-hardening as in the case of 7039Al. This also applies to materials which often exhibit similar mechanical properties under normal conditions of temperature, strain, and strain rate.

Chapter 7

SUMMARY AND CONCLUSIONS

In the ballistic impact regime where long-rod kinetic energy projectiles penetrate metal plates of finite thicknesses, there is an acute lack of information regarding the material aspects of impact. The penetration/perforation phenomena associated with impact is indeed a complex process that has not yet been solved analytically, though a too great amount of emphasis has been placed on numerical simulation tools as a primary means of apprehending the subject. While advances in theoretical penetration mechanics have produced a large body of knowledge pertaining to perforation and penetration, certain aspects of the process have still not been adequately addressed.

These issues include the dynamic behavior of materials under the rigorous impact conditions of extreme strains and strain rates, as well as the nature of target deformation in terms of altered microstructure [1]. Since a specific metal target will possess a specific composition, processing history, and combinations of mechanical and physical properties, etc., general penetration theories must incorporate these in order to predict a realistic outcome of the target/projectile interaction.

A systematic study of deformation behavior at the levels of microstructure and substructure would not only aid in identifying particular failure mechanisms, but would also greatly supplement theoretical aspects of penetration/perforation for specific target materials.

In this study, a microstructural analysis and comparison was performed on two target materials perforated by a tungsten-alloy projectile at 1.5 km/s impact velocity, OFHC (Oxygen-Free High-Conductivity) copper and a 7039 aluminum alloy. Though copper would prove impractical as an armor material, it did, however, represent a contrasting system with which to make comparisons to aluminum.

Both materials possess a face-centered cubic (FCC) crystal structure, though this remained the sole similarity. Significant differences exist in processing conditions and initial properties. These include, but are not limited to, yield strength, hardness, densities, melting temperatures, and stacking fault energies. The systematic characterization of both residual targets required the use of transmission and scanning electron microscopy, metallography and microhardness testing.

The initial, annealed state of copper consisted of an equiaxed grain microstructure and dislocation cell substructure. The residual analysis revealed an evolution of microstructure that comprised the following, in successive order from the edge of the channel wall: a narrow zone of recrystallized grains, subgrains and heavily deformed grains, and a mixture of microtwins and microbands in highly distorted grains.

This is similar to the observations of residual microstructure in hypervelocity impact cratering of copper [30,52,70-73,91] and the ballistic impact of copper [29,75]. Though no evidence of deformation twinning was observed in either case. The fact that microtwins have been observed to be characteristic of the ballistic impact of copper suggests that the impact loading of a target by a projectile of cylindrical geometry is associated with oblique shock waves. Oblique shock-loading of cylindrical copper rods

by Sanchez et. al [68,74] has been shown to produce a similar intermixing of twins and microbands. Though the relationship between microtwin and microband development is still unclear, in general, it can be said that plane-wave or uniaxial deformation appears to favor twinning, the high shear mode associated with spherical shock waves produces microbands [91], and oblique shock waves are associated with mixtures of deformation twins and microbands.

In addition, the solid-state flow of material seen at the entrance rim of the residual target appears to be facilitated by layers of dynamically recrystallized grains. This solid-state flow due to recrystallized grain structures may be a plausible explanation for the development of the penetration channel. The exaggerated regions of recrystallization surrounding WHA eroded fragments lends credibility to this.

In contrast to copper, 7039 aluminum is precipitation-hardened and heavily work-hardened to produce a starting microstructure consisting of a mixture of large, elongated grains and small grains with heavy dislocation densities. Hence, the material is harder in comparison to copper, and failure occurs in a brittle-like fashion.

The residual analysis of the aluminum crater revealed a small region of plastic flow close to the channel walls. Though dynamic recrystallization was observed in this region, it may be that only a very narrow zone exists along the channel wall due to adiabatic heat effects during penetration. This narrow zone may facilitate the flow of the projectile through the target somewhat, though it is obvious that the large strains involved in the penetration/perforation process are accommodated by extensive shear banding that occurs alongside the channel walls. The microscopic evidence indicates that, unlike

copper, slip is hindered by the initial, heavy dislocation and precipitate density, and deformation therefore becomes irregular, or localized. These shear bands become precursors to cracking, which leads to a lower energy mode of failure for the aluminum alloy target. Similar to copper, the mechanism of failure is brought about by dynamically recrystallized grains (within the shear bands). The presence of recrystallized grains in adiabatic shear bands has been reported in a number of different materials [61-65]. Microbands were also observed in the deformed region, appearing in string-like configurations rather than in clusters as those in copper. This microstructure was not reported by Huang et. al [75] in a similar study of impacted 7039Al. Finally, it is believed that deformation bands have been observed in the residual microstructure, particularly in the region of the fractured shear lips (lending to the higher hardness of the region), though more evidence may be needed for irrefutable identification.

Thus, plastic deformation is well distributed in the residual copper target, resulting in an evolution of residual microstructure and failure that is ductile in nature. Whereas deformation of the aluminum alloy becomes localized, through shear banding, leading to cracking and failure that is brittle in nature. The similarity that exists between the two, however, is the observation of dynamic recrystallization in the microstructure. In copper, recrystallization appears to facilitate the solid-state flow of material necessary for crater development. In aluminum, recrystallized grains are the mechanism for shear band formation and an easy path for crack propagation. In either case, it appears that recrystallization plays a major role in initiating failure and is therefore considered the dominant failure mechanism.

Computer modelling of the ballistic impact of both materials was carried out through the AUTODYNTM hydrocode. The numerical modelling of copper was considered successful as the geometry-based validation showed that experimental values matched closely to that of simulated values. The AUTODYNTM simulation of hypervelocity impact cratering in copper had also been found to be geometrically successful by Quinones [91]. In addition, the simulated ballistic impact of copper showed a strong similarity to the actual impact of copper revealed by flash x-ray radiographs. The material property-based validation of the copper simulation was found to be successful, since the computer generated yield-stress contours correlated well to the experimental hardness contours which represented the evolution of residual microstructure. As such, additional variables contributing to the impact behavior of copper, including temperature, effective plastic strain, and pressure, can be analyzed with confidence.

Computer simulations of the aluminum alloy showed mixed results. Although the measured geometry of the experimental and simulated crater did not agree well, the physical aspects of deformation, such as narrow penetration channel and crack patterning at breakout, appeared similar. It is apparent that 7039Al is too complicated a system for accurate simulation by general constitutive models. A more complex failure model should be incorporated for the flow stress discontinuities involved in shear banding (AUTODYNTM features simpler models), and should also account for the two competing mechanisms involved in shear band formation, thermal softening and strain-hardening.

This research effort has demonstrated that a systematic analysis, at the microstructural level, of long-rod, ballistically impacted metal plates can aid considerably in the theoretical development of penetration/perforation phenomena through an understanding of material behavior. In addition, though both target plates exhibited significant differences in properties, and hence differences in deformation modes, the mechanism for failure was determined to be similar. An analysis of this nature may benefit the development of improved armors if such mechanisms can be controlled to limit failure of the target. Finally, constitutive modeling of materials in the high-strain-rate regime should be undertaken with caution, and validation of such models should involve as many variables as conceivable to ensure the reliability of the model. In closing, an investigation of residual properties will allow for a validation of the numerical model, a reliable numerical model will in turn allow for an investigation of dynamic events that are not possible in real time.

REFERENCES

1. J. S. Rinehart and J. Pearson, Behavior of Metals Under Impulsive Loads, Dover Publications, Inc., New York, 1965
2. M. A. Meyers, Dynamic Behavior of Materials, John-Wiley & Sons, Inc., New York, 1994
3. D. R. Kennedy in: Tactical Missile Warheads, J. Carleone, ed., American Institute of Aeronautics and Astronautics, Inc., 1993
4. Juan C. Sanchez, M. S. Thesis, The University of Texas at El Paso, El Paso, Tx ,1996
5. L. E. Murr, C-S. Niou, J. C. Sanchez, and L. Zernow, *Scripta Metallurgica et Materialia*, **32:1** (1995) 31-36
6. L. E. Murr, E. Ferreyra, T., S. Pappu, E. P. Garcia, J. C. Sanchez, W. Huang, J. M. Rivas, C. Kennedy, A. Ayala, and C-S. Niou, *Materials Characterization*, **37** (1996) 245-276
7. Sridhar Pappu, M. S. Thesis, The University of Texas at El Paso, El Paso, Tx ,1995
8. M. R. Lurance and D. E. Brownlee, *Nature*, **323** (1986) 136
9. <http://frontier.arl.mil/SciVis/sci.sabot.html>
10. http://www.army-technology.com/contractors/ammunition/royal_ordnance/royal3.html
11. J. Mescall in: Computational Aspects of Penetration Mechanics, J. Chandra and J. Flaherty, eds., 1983, p47

12. L. S. Magness, *Mechanics of Materials*, **17** (1994) 147-154
13. L. S. Magness and C. Lopatin in: Proceedings of the Army Symposium on Solid Mechanics, Plymouth, MA, August, 1992
14. T. W. Wright in: Computational Aspects of Penetration Mechanics, J. Chandra and J. H. Flaherty, eds., 1983, p85
15. J. A. Zukas, Impact Dynamics, John-Wiley & Sons, Inc., 1982
16. M. E. Beckman and W. Goldsmith, *Int. J. Engr. Sci.*, **16** (1978) 1
17. R. F. Recht and T. W. Ipson, *J. Appl. Mech. Trans.*, **30** (1963) 384-390
18. W. Bruchey in: Computation Aspects of Penetration Mechanics, J. Chandra and J. E. Flaherty, eds., Springer, 1983
19. G. Birkhoff, D. P. MacDougall, E. M. Pugh and G. I. Taylor, *Journal of Applied Physics*, **19** (1948) 563
20. Backman and Goldsmith, *Intl. J. Eng. Sci.*, **16** (1978) 1
21. J. P. Lambert and G. H. Jonas, Towards Standardization in Terminal Ballistics Testing: Velocity Representation, BRL-R-1852, U. S. Army Ballistics Research Laboratory, Aberdeen Proving Ground, MD, 1976
22. J. Awervuch and S. R. Bodner, *Inter. J. Mech. Sci.*, **10** (1974) 685-699
23. R. L. Woodward and M. E. de Morton, *Inter. J. Mech. Sci.*, **18** (1976) 119-127
24. R. L. Woodward, B. J. Baxter, and N. V. Scarlett, *Inter. Phys. Cont. Ser.*, **70** (1984) 525-532
25. J. M. Ravid and S. R. Bodner, *Inter. J. Engr. Sci.*, **21** (1983) 577-691
26. F. I. Grace, *International Journal of Impact Engineering*, **16:3** (1995) 419-433

27. N. L. Rupert and F. I. Grace in: Proceedings of the 1995 Conference on Metallurgical and Materials Applications of Shock-Wave and High-Strain-Rate Phenomena (EXPLOMET '95), L. E. Murr, K. P. Staudhammer, and M. A. Meyers, eds., Elsevier, NY, 1995, pp257-264
28. F. I. Grace, *International Journal of Impact Engineering*, **16**:3 (1995)
29. Wei Huang, M. S. Thesis, The University of Texas at El Paso, El Paso, Tx , 1996
30. J. M. Rivas, Ph.D. Dissertation, The University of Texas at El Paso, El Paso, Tx, 1996
31. L. E. Murr in: Materials at High-Strain-Rates, T. Z. Blazynski, ed., Elsevier Applied Science Publishers, NY, 1987
32. W. J. M. Rankine, *Phil. Trans. Roy. Soc. Lond.*, **160** (1870) 270
33. H. J. Hugoniot, *J. L'Ecale Polytech.*, **58** (1989) 3
34. A. Zurek in: Fundamental Issues and Applications of Shock-Wave and High Strain-Rate Phenomena, Proceedings of EXPLOMET 2000, K. P. Staudhammer, L. E. Murr, and M. A. Meyers (eds.), to be published
35. M. A. Meyers and L. E. Murr, eds., Shock Waves and High-Strain-Rate Phenomena in Metals, Plenum, New York, 1981
36. RH. J. McQueen, J. J. Jonas, Recovery and Recrystallization During High Temperature Deformation, R. J. Arsenault, ed., Academic Press, New York, (1975), p393-493
37. V. Raghavan in: Physical Metallurgy: Principles and Practice, Prentice Hall, New Delhi, India, 1993

38. J. A. Hines, K. S. Vecchio, and S. Ahzi, *Metallurgical and Materials Transactions*, **A29** (1998) 191-203
39. R. D. Doherty, *Metal Science*, **8** (1974) 132-142
40. J. E. Bailey and Hirsch, *Proc. Roy. Soc. Lond.*, **267A** (1962) 11-30
41. P. A. Beck and P. R. Sperry, *Journal of Applied Physics*, **21** (1950) 150
42. J. A. Hines and K. S. Vecchio, *Acta Metallurgica Materialia*, **45:2** (1997) 635-649
43. J. C. M. Li, *J. Appl. Phys.*, **33** (1962) 2958-2965
44. H. Hu in: *Recovery and Recrystallization of Metals*, V. Himmel, ed., Interscience Publishing, New York, 1963
45. R. Sandstrom, *Acta Metallurgica*, **25** (1977) 897-904
46. U. Andrade, M. A. Meyers, K. S. Vecchio, and A. H. Chokshi, *Acta Metallurgica Materialia*, **42** (1994) 3183-3193
47. L. E. Murr, J. M. Rivas, E. Ferreyra T., and J. C. Sanchez, *Microstructural Science*, **24** (1997) 121-132
48. J. C. Huang and G. T. Gray III, *Acta Metallurgica*, **37:12** (1989) 3335-3347
49. V. S. Ananthan, T. Letters, and N. Hansen, *Scripta Metallurgica*, **25** (1991) 137-142
50. S. Pappu and L. E. Murr, *Materials Science and Engineering*, **A284** (2000) 148-157
51. V. Raghavan, *Materials Science and Engineering*, 3rd ed., Prentice-Hall International, Inc., New Delhi, 1989, p136
52. L. E. Murr, C-S. Niou, E. P. Garcia, E. Ferreyra, T., J. M. Rivas, and J. C. Sanchez, *International Journal of Impact Engineering*, (1997)

53. S. A. Quinones, J. M. Rivas, E. P. Garcia, L. E. Murr, F. Horz, and R. P. Bernhard in: *Metallurgical and Materials Applications of Shock-Wave and High-Strain-Rate Phenomena*, Chpt. 36, L. E. Murr, K. P. Staudhammer, and M. A. Meyers, eds., Elsevier Science, B. V. Amsterdam, 1995, p293
54. J. H. Schmitt, J. V. Fernandes, J. J. Gracio, and M. F. Vieira, *Materials Science and Engineering*, **A147** (1991) 143-150
55. J. V. Fernandes, J. J. Gracio, and J. H. Schmitt in: *Large Plastic Deformation, MECAMET '91*, C. Teodosiu, J. L. Raphanel, and F. Sidoroff, eds., Balkema, Rotterdam, 1993, p219
56. M. A. Meyers, U. R. Andrade, and A. H. Chokshi, *Metallurgical and Materials Transactions*, **A26** (1995) 2881-2889
57. L. E. Murr, *Electron and Ion Microscopy and Microanalysis: Principles and Applications*, 2nd ed., Marcel Dekker, Inc., New York, 1991
58. L. E. Murr, ed., in: *Shock-Waves for Industrial Applications*, Noyes Publications, Park-Ridge, New Jersey, 1989
59. L. E. Murr, C-S. Niou, S. Pappu, J. M. Rivas, and S. A. Quinones, *Phys. Stat. Sol.*, (a), **149** (1995) 253-274
60. C. G. Lee, Y-J. Lee, *Scripta Metallurgica et Materialia*, **32** : 6 (1995) pp821-826
61. C. Zener and J. H. Hollomon, *J. Appl. Phys.*, **15** : 32 (1944)
62. M. A. Meyers and H-R. Pak, *Acta Metallurgica*, **34** (1986) 2493-2499
63. M. A. Meyers, G. Subhash, B. K. Kad, and L. Prasad, *Mechanics of Materials*, **17** (1994) 175-193

64. R. W. Chen, M. S. Thesis, The University of California, San Diego, CA, 1993
65. M. A. Meyers, L. W. Meyers, K. S. Vecchio, and U. Andrade, *Journal de Physique*, **1.8** (1991) 11-17
66. A. H. Chokshi and M. A. Meyers, *Scripta Metallurgica et Materialia*, **24** (1990) 605-610
67. G. E. Dieter in: Response of Metals to High Velocity Deformation, P. G. Shewmon and V. F. Zackay, eds., Interscience Publishers, Inc., New York, 1961, p409
68. L. E. Murr and J. V. Foltz, *Journal of Applied Physics*, **40** (1969) 3796
69. J. C. Sanchez, K. P. Staudhammer, and L. E. Murr in: Metallurgical and Materials Applications of Shock-Wave and High-Strain-Rate Phenomena, L. E. Murr, K. P. Staudhammer, and M. A. Meyers, eds., Elsevier Science, Amsterdam, 1995, p801
70. L. E. Murr, C.-S Niou, J. M. Rivas, S. A. Quinones and K. S. Murr, *Scripta Metallurgica et Materialia*, **27** (1992) 101-106
71. J. M. Rivas, S. A. Quinones, L. E. Murr, C.-S Niou, A. H. Advani, D. J. Manuel and R. Birudavolu, *Ibid.*, (1993) 261-281
72. S. A. Quinones, J. M. Rivas and L. E. Murr, *Journal of Materials Science Letters*, **14** (1995) pp685-688
73. J. M. Rivas, S. A. Quinones, E. P. Garcia and L. E. Murr in: Metallurgical and Materials Applications of Shock-Wave and High-Strain-Rate Phenomena, L. E. Murr, K. P. Staudhammer and M. A. Meyers, eds., Elsevier, (1995) pp313-323
74. E. Ferreyra T., M. S. Thesis, The University of Texas at El Paso, El Paso, TX (1996)

75. J. S. Sanchez, L. E. Murr, and K. P. Staudhammer, *Acta Materialia*, 45:8 (1997) 3223-3235
76. W. Huang, L. E. Murr, C-S. Niou, N. L. Rupert, F. I. Grace, and S. J. Bless, Ballistics '96: 16th International Ballistics Symposium and Exhibition, Proceedings, vol.3, American Defense Preparedness Association, Arlington, 1996, p733
77. L. E. Murr, E. P. Garcia, J. M. Rivas, W. Huang, F. I. Grace, and N. L. Rupert, *Scripta Materialia*, 37:9 (1997) 1329-1335
78. C. E. Anderson, Jr., *International Journal of Impact Engineering*, 5 (1987) 35-59
79. J. A. Zukas, J. R. Furlong, and S. B. Segletes, *Computers in Physics*, 6:2 (1992) 146-154
80. AUTODYN Theory Manual, Century Dynamics, Inc., 1998
81. F. I. Grace, *International Journal of Impact Engineering*, 16:3 (1995) 419-433
82. C. E. Anderson and S. R. Bodner, *International Journal of Impact Engineering*, 7 (1988) 9-35
83. C. E. Anderson, Jr., J. D. Walker and G. E. Hauver, *Nuclear Engineering and Design*, 138 (1992) 93-104
84. C. E. Anderson, Jr., S. A. Mullin and C. J. Kuhlman, *International Journal of Impact Engineering*, 13:1 (1993) 35-52
85. C. E. Anderson, Jr., V. Hohler, J. D. Walker and A. J. Stilp, *International Journal of Impact Engineering*, 16:1 (1995) 1
86. J. E. Raugh in: High Pressure Science and Technology, 1993, S. C. Schmidt, ed., AIP Press, NY, 1994

87. N. L. Rupert and F. I. Grace, Army Research Laboratory Report No. ARL-TR-1453, 1997
88. <http://www.matweb.com/SpecificMaterial.asp?bassnum=MC102B&group=General>
89. H. W. Pollack, Materials Science and Metallurgy, 3rd ed., Reston Publishing Company, Inc., Reston, Virginia, 1981
90. J. E. Raugh in: Proceedings of the Ballistics '93 14th International Symposium, National Defence Research Establishment, 1993
91. G. Vander Voort, Metallography: Principles and Practice, ASM International, Metals Park, Ohio, 1999, p336
92. AUTODYNTM website- http://208.55.130.87/library/image_gal/image08.html
93. D. A. Mandell, C. A. Wingate, and L. A. Schwalbe, 14th U. S. Army Symposium on Solid Mechanics, Oct. 16-18, 1996
94. ASM Handbook, Vol. 11: Failure Analysis and Prevention, ASM International, Metals Park, Ohio, 1992
95. S. A. Quinones, Ph.D. Dissertation, The University of Texas at El Paso, El Paso, Texas, 1996
96. G. Dieter, Mechanical Metallurgy, 3rd ed., McGraw-Hill Inc., New York, 1986
97. Y. B. Xu, W. L. Zhang, Y. J. Chen, L. T. Shen, Q. Liu, Y. L. Bai, and M. A. Meyers
98. A. H. Cottrell, Dislocations and Plastic Flow of Crystals, Clarendon Press, Oxford, 1953
99. S. P. Bellier and R. D. Doherty, *Acta Metallurgica*, **25** (1977) 521

100. A. A. Ridha and W. B. Hutchinson, *Acta Metallurgica*, **30** (1982) 1929
101. Y. Inokuti and R. D. Doherty, *Acta Metallurgica*, **26** (1978) 61
102. P. Faivre and R. D. Doherty, *J. Mat. Sci.*, **14** (1979) 897
103. N. Hansen, *Scripta Metallurgica et Materialia*, **27** (1992) 1447-1452
104. R. M. Brick, A. W. Pense, and R. B. Gordon, Structure and Properties of Engineering Materials, 4th ed., McGraw-Hill Book Co., New York, 1977, p83
105. M. A. Meyers, R. W. Armstrong, and H. O. K. Kirchner, eds., Mechanics and Materials: Fundamentals and Linkages, John Wiley and Sons, Inc., New York, 1999
106. Y. Bai and B. Dodd, Adiabatic Shear Localization: Occurrence, Theories and Applications, Pergamon Press, New York, 1992
107. U. R. Andrade, M. A. Meyers, and A. H. Chokshi, *Scripta Metallurgica et Materialia*, **30** (1994) 933

APPENDIX

Materials Parameters for AUTODYN-2D Simulations

Table A: Materials Parameters for the Simulation of OFHC Cu Perforation

PARAMETERS	OFHC CU TARGET	WHA ROD
Processor	Euler	Euler
Equation of State	Shock	Shock
Strength Model	Johnson-Cook	Johnson-Cook
Failure Model	Bulk strain	Bulk Strain
Reference Density (g/cm ³)	8.96E+00	1.70E+01
Gruneisen Coefficient	1.99E+00	1.54E+00
Parameter C ₁ (cm/μs)	1.29E+00	4.029E-01
Parameter S ₁	1.51E+00	1.237E+00
Parameter Quad. S ₂ (μs/cm)	0.00E+00	0.00E+00
Relative Volume, VE	0.00E+00	0.00E+00
Relative Volume, VB	0.00E+00	0.00E+00
Parameter C ₂ (cm/μs)	0.00E+00	0.00E+00
Parameter S ₂	0.00E+00	0.00E+00
Reference Temperature (K)	3.00E+02	3.00E+02
Specific Heat (C.V.)	3.83E-06	1.34E-06
Shear Modulus (Mbar)	4.60E-01	1.60E+00
Yield Stress (Mbar)	9.00E-04	1.60E-02

Table A: (Con't)

Hardening Constant (Mbar)	2.92E-03	1.77E-03
Hardening Exponent	3.10E-01	1.20E-01
Strain Rate Constant	2.50E-02	1.60E-02
Thermal Softening Exponent	1.09E+00	1.00E+00
Melting Temperature (K)	1.356E+03	1.723E+03
Ultimate Strain	8.00E-01	6.00E-01
Crack Softening, G_f (GJ/m²)	0.00E+00	0.00E+00
Or, K_c (Gd/cm^{3/2})	0.00E+00	0.00E+00

Table B: Materials Parameters for the Simulation of 7039Al Perforation (Euler)

PARAMETERS	7039Al PLATE	Al PRE-TARGET	WHA ROD
Processor	Euler	Euler	Euler
Equation of State	Shock	Shock	Shock
Strength Model	Johnson-Cook	Steinberg-Guinan	Johnson-Cook
Failure Model	Hydro	Bulk Strain	Bulk Strain
Reference Density (g/cm ³)	2.77E +00	2.707E +00	1.8167E +01
Gruneisen Coefficient	2E +00	1.97E +00	1.67E +00
Parameter C ₁ (cm/μs)	5.328E-01	5.386E -01	4.03E -01
Parameter S ₁	1.338E +00	1.339E +00	1.237E +00
Parameter Quad. S ₂ (μs/cm)	0.00	0.00	0.00
Relative Volume, VE	0.00	0.00	0.00
Relative Volume, VB	0.00	0.00	0.00
Parameter C ₂ (cm/μs)	0.00	0.00	0.00
Parameter S ₂	0.00	0.00	0.00
Reference Temperature (K)	3E +02	3E +02	3E +00
Reference Density (g/cm ³)	8.75E -06	2.707E +00	1.43E -06
Shear Modulus (Mbar)	2.76E -01	2.71E -01	1.45E +00
Yield Stress (Mbar)	4.66E -03	5E -04	1.87E -02
Maximum Yield Stress (Mbar)	0.00	6E -04	4.00E -02

Table B: (Con't)

Hardening Constant	3.43E -03	4E +02	7.7E +00
Hardening Exponent	4.1E -01	2.7E -01	1.3E -01
Strain Rate Constant	1E -02	0.00	0.00
Derivative dG/dP	0.00	1.767E +00	1.494E +00
Derivative dG/dT	0.00	-1.669E -04	-2.204E -04
Derivated Y/dP	0.00	2.608E -03	1.926E -02
Thermal Softening Exponent	1.00E +00	0.00	0.00
Melting Temperature (K)	8.77E +02	9.23E +02	2.263E +03
Hydro Tensile Limit (PMIN)	-3.5E -03	0.00	0.00
Ultimate Strain	0.00	5E -01	9E -01
Crack Softening, G_f (GJ/m²)	5E -05	0.00	0.00

Table C: Materials Parameters for the Simulation of 7039Al Perforation (SPH)

PARAMETERS	7039Al PLATE	Al PRE-TARGET	WHA ROD
Processor	SPH	SPH	SPH
Equation of State	Shock	Shock	Shock
Strength Model	Johnson-Cook	Steinberg-Guinan	Steinberg-Guinan
Failure Model	Principal Stress	Bulk Strain	Bulk Strain
Reference Density (g/cm ³)	2.77E +00	2.703E +00	1.8167E +01
Gruneisen Coefficient	2.0E +00	1.97E +00	1.67E +00
Parameter C ₁ (cm/μs)	5.328 E-01	5.24E -01	4.03E -01
Parameter S ₁	1.338E +00	1.4E +00	1.237E +00
Parameter Quad. S ₂ (μs/cm)	0.00	0.00	0.00
Relative Volume, VE	0.00	0.00	0.00
Relative Volume, VB	0.00	0.00	0.00
Parameter C ₂ (cm/μs)	0.00	0.00	0.00
Parameter S ₂	0.00	0.00	0.00
Reference Temperature (K)	3.0E +02	3E +02	3E +02
Reference Density (g/cm ³)	8.75E -06	8.85E -06	1.43E -06
Shear Modulus (Mbar)	2.76E -01	2.76E -01	1.45E +00
Yield Stress (Mbar)	4.66E -03	2.9E -03	1.87E -02
Maximum Yield Stress (Mbar)	0.00	6.8E -03	4E -02
Hardening Constant	3.43E -03	1.25E +02	7.7E +00

Table C: (Con't)

Hardening Exponent	4.1E -01	1E -01	1.3E -01
Strain Rate Constant	1E -02	0.00	0.00
Derivative dG/dP	0.00	1.8E +00	1.494E +00
Derivative dG/dT	0.00	-1.7E -04	-2.204E -04
Derivativd Y/dP	0.00	1.8908E -02	1.926E -02
Thermal Softening Exponent	1E +00	0.00	0.00
Melting Temperature (K)	8.77E +02	1.22E +03	2.263E +03
Tensile Failure Stress (Mbar)	2.5E -03	0.00	0.00
Maximum Shear Stress (Mbar)	3E-03	0.00	0.00
Ultimate Strain	0.00	5E -01	7E -01
Crack Softening, G_f (GJ/m²)	7E -05	0.00	0.00

CURRICULUM-VITAE

Christine Kennedy was born on April 30, 1971 in Chonburi, Thailand. The eldest daughter of Joe Keith Kennedy and Luckie Kennedy, she has traveled to and lived in four different countries and six states in the U.S. She graduated from Andress High School in El Paso, TX, in 1989. She received her Bachelor of Science degree in Metallurgical Engineering in 1995 from the University of Texas at El Paso and subsequently entered the Graduate School at the University of Texas at El Paso, receiving her Master of Science (M.S.) degree in Metallurgical and Materials Engineering in December of 1997.

Permanent address: 10781 Pleasant Hill Drive
El Paso, Texas 79924

This dissertation was typed by Christine Kennedy.

PUBLICATIONS

1. C. Kennedy, S. Pappu, and L. E. Murr, *Dislocation substructures in tungsten-alloy ballistic penetrators*, Electron Microscopy 1998 – Proceedings of the 14th International Congress on Electron Microscopy (ICEM 14), vol. II, Aug. 31 – Sept. 4, 1998, Cancun, Mexico, pp. 67-68
2. C. Kennedy, L. E. Murr, S. Pappu and D. Kapoor, *Microstructural Analysis and Comparison of Mechanically Alloyed and P/M Processed W-HfC and W-Ir-HfC Ballistic Penetrator Rods*, Advanced Particulate Materials and Processes, 1997, Proceedings of the 5th International Conference on Advanced Particulate Materials and Processes, F. H. Froes, ed., Metal Powder Industries Federation, West Palm Beach, FL, 1997, pp. 227-234
3. C. Kennedy, R. Avalos, A. A. Bujanda, and L. E. Murr, *Tungsten-heavy alloy ballistic rod penetration into a copper target: microstructural analysis and computer simulations*, in: Fundamental Issues and Applications of Shock-Wave and High-Strain-Rate Phenomena, Proceedings of EXPLOMET 2000, K. P. Staudhammer, L. E. Murr, and M. A. Meyers (eds.), to be published
4. S. Pappu, C-S. Niou, C. Kennedy, L. E. Murr, L. DuPlessis, and M. A. Meyers, *High-Strain-Rate Behavior of Pure Tantalum in Explosively Formed Penetrator and Shaped Charge Regimes*, Chap. 59 in: Metallurgical and Materials Applications of Shock-Wave and High-Strain-Rate Phenomena, L. E. Murr, K. P. Staudhammer, and M. A. Meyers, eds., Elsevier Science, B. V., Amsterdam, 1995, pp. 495-502
5. S. Pappu, C. Kennedy, and L. E. Murr, *Observations of Deformation Twins in a Shock-Loaded Ta-2.5%W Liner and a Recovered EFP Slug Using Transmission Electron Microscopy*, Ballistics '96, Vol. 2, Proceedings of the 16th International Ballistics Symposium and Exhibition, American Defense Preparedness Association, 1996, pp. 593-602
6. S. Pappu, C-S. Niou, C. Kennedy, and L. E. Murr, *A Study and Comparison of Microstructures in Ta and Ta-W Starting Liners and a Pure Ta Explosively Formed Penetrator*, Microstructural Science **23** (1996) 259-26
7. S. Pappu, C. Kennedy, L. E. Murr, and M. A. Meyers, *Deformation Twins in a Shock-Loaded Ta-2.5%W Precursor Plate and a Recovered Ta-2.5%W Explosively Formed Penetrator*, Scripta Mater. **35** (1996) 959-965

8. S. Pappu, C. Kennedy, L. E. Murr, L. S. Magness, and D. Kapoor, *Microstructure analysis and comparison of tungsten alloy rod and [001] oriented columnar-grained tungsten rod ballistic penetrators*, Materials Science and Engineering: A262, 1999, 115-128
9. L. E. Murr, E. Ferreyra T., J. G. Maldonado, E. A. Trillo, S. Pappu, C. Kennedy, J. De Alba, M. Posada, D. P. Russell, and J. L. White, *Materials Science and Metallurgy of the Caribbean Steel Drum - Part 1: Fabrication, deformation phenomena, and acoustic fundamentals*, accepted for publication in J. Mater. Sci
10. L. E. Murr, S. Pappu, C. Kennedy, C-S. Niou, and M. A. Meyers, *Tantalum Microstructures for High-Strain-Rate Deformation: Shock Loading, Shaped Charges, and Explosively Formed Penetrators*, in: Tantalum, E. Chen, A. Crowson, E. Lavernia, W. Ebihara, and P. Kumar, eds., TMS, Warrendale, PA, 1996, pp. 145-155
11. L. E. Murr, E. Ferreyra T., S. Pappu, E. P. Garcia, J. C. Sanchez, W. Huang, J. M. Rivas, C. Kennedy, A. Ayala, and C-S. Niou, *Novel Deformation Processes and Microstructures Involving Ballistic Penetrator Formation and Hypervelocity Impact and Penetration Phenomena*, Materials Characterization 37 (1996) 245-276
12. L. E. Murr, M. A. Meyers, C-S. Niou, Y. J. Chen, S. Pappu, and C. Kennedy, *Shock-Induced Deformation Twinning in Tantalum*, Acta Mater. 45:1 (1997) 157-175
13. L. E. Murr, E. Ferreyra T., J. G. Maldonado, E. A. Trillo, C. Kennedy, J. De Alba, M. Posada, D. P. Russell, and J. L. White, *Metallurgy of the Caribbean Steel Drum*, accepted for publication in Percussion Notes: Focus on Research, April 1999
14. E. Ferreyra T., J. G. Maldonado, L. E. Murr, S. Pappu, E. A. Trillo, C. Kennedy, M. Posada, J. De Alba, R. Chitre, and D. P. Russell, *Materials Science and Metallurgy of the Caribbean Steel Drum - Part 2: Heat treatment, microstructures, hardness profiles, and tuning effects*, accepted for publication in J. Mater Sci.
15. E. Ferreyra, L. E. Murr, S. Pappu, J. G. Maldonado, and C. Kennedy, *Effect of Heat Treatment on the Multi-Harmonic Tuning and Acoustics of the Caribbean Steel Drum*, to be published in the proceedings of Heat Treat '98, ASM International Materials Park, OH

16. L. E. Murr, C-S. Niou, E. Ferreyra T., S. Pappu, C. Kennedy, S. A. Quinones, J. M. Rivas, R. J. Romero, and J. G. Maldonado, in: *Developments in Materials Characterization Technologies: Proceedings of the 28th Annual Technical Meeting of the International Metallographic Society*, ASM International, Materials Park, OH, 1996, pp. 1-13
17. O. Valerio F., C. Kennedy, L. E. Murr, D. Brown, S. Pappu, B. M. Nowak and J. C. McClure, *Microstructural Characterization of Friction-Stir-Welded As-Cast Aluminum Plate and a Cast 50% Cold-Rolled Plate*, Proceedings of the IV Congreso Internacional De Materiales Y XIX Encuentro De Investigacion Metalurgica, M. M. Cisneros G., M. Martinez G. and J. E. Pacheco M., eds., Saltillo, Coahuila, Mexico, 1997, pp. 286-295
18. O. Valerio F., C. Kennedy, L. E. Murr, D. Brown, S. Pappu, B. M. Nowak and J. C. McClure, *Microstructural Issues in a Friction-Stir-Welded Aluminum Alloy*, Scripta Materialia 35:5 (1998) 703-708

PRESENTATIONS

1. "Deformation Twinning in Shock-Loaded Tantalum", double presentation by C. Kennedy and L. E. Murr, Materials Science and Engineering Seminar Series, University of Texas at El Paso, Sept. 5, 1995
2. "Microstructural Features of Some Penetrator Materials", C. Kennedy, S. Pappu, C-S. Niou, and L. E. Murr, Spring Meeting of the Texas Society for Electron Microscopy, Texas A&M University, College Station, TX, March, 1996
3. "Microstructural Analysis and Comparison of Mechanically Alloyed and P/M-Processed W-HfC and W-Ir-HfC Penetrator Rods", C. Kennedy, L. E. Murr, S. Pappu, and D. Kapoor, 126th TMS Annual Meeting and Exhibition, Orlando, FL, Feb. 9-13, 1997
4. "Microstructural Analysis and Comparison of Mechanically Alloyed and P/M Processed W-HfC and W-Ir-HfC Ballistic Penetrator Rods", C. Kennedy, L. E. Murr, S. Pappu and D. Kapoor, 5th International Conference on Advanced Particulate Materials and Processes, West Palm Beach, FL, April 7-9, 1997
5. "Metallurgical Aspects Involved in the Fabrication of a Musical Steel Drum", C. Kennedy, S. Pappu, E. Trillo, J. Maldonado, E. Ferreyra, M. Posada, L. E. Murr, J. De Alba and R. Chitre, Cancun '97, International Materials Research Congress, Cancun, Mexico, Sept. 1-4, 1997
6. "Dislocation Substructures in Tungsten-Alloy Ballistic Penetrators", C. Kennedy, S. Pappu and L. E. Murr, The Oklahoma Microscopy Society and the Texas Society for Electron Microscopy Joint Spring Meeting, Kingston, OK, Apr. 2-4, 1998
7. "Dislocation Substructures in Tungsten-Alloy Ballistic Penetrators", C. Kennedy, S. Pappu, and L. E. Murr, 14th International Conference on Electron Microscopy (ICEM 14), Cancun, Mexico, Aug. 31 – Sept. 4, 1998
8. "Tungsten-heavy Alloy Ballistic Rod Penetration into a Copper Target: Microstructural Analysis and Computer Simulations", C. Kennedy, R. Avalos, A. A. Bujanda, and L. E. Murr, EXPLOMET 2000: Fundamental Issues and Applications of Shock-Wave and High-Strain-Rate Phenomena, Albuquerque, NM, Julne 18-22, 2000